Silicon Based Materials for Energy Related Technologies

Zur Erlangung des akademischen Grades Doktor-Ingenieur (Dr. -Ing.)
Genehmigte kumulative Dissertation von M. Sc. Dragoljub Vrankovic aus Gradiska, Bosnien
Dezember 2017 - Darmstadt – D17

TECHNISCHE
UNIVERSITÄT
DARMSTADT

Disperse
Feststoffe

Silicon Based Materials for Energy Related Technologies
Silicium basierte Materialien für energiebezogene Technologien

Genehmigte kumulative Dissertation von M. Sc. Dragoljub Vrankovic aus Gradiska, Bosnien
Darmstadt, Technische Universität Darmstadt

1. Gutachten: Prof. Dr. Ralf Riedel
2. Gutachten: Prof. Dr. Gian Domenico Soraru̇

Tag der Einreichung: 12.12.2017
Tag der Prüfung: 01.03.2018

Darmstadt — D 17

Erklärung zur Dissertation

Hiermit versichere ich, die vorliegende Dissertation ohne Hilfe Dritter nur mit den angegebenen Quellen und Hilfsmitteln angefertigt zu haben. Alle Stellen, die aus Quellen entnommen wurden, sind als solche kenntlich gemacht. Diese Arbeit hat in gleicher oder ähnlicher Form noch keiner Prüfungsbehörde vorgelegen.

Darmstadt, den 12. Dezember 2017

(Dragoljub Vrankovic)

The presented cumulative dissertation summarizes the essential scientific findings reported to the scientific community in the following peer-reviewed articles and as a patent. The reports itself [1] – [7] are enclosed in the Chapter *Publications* at the end of this work.

[1] **D. Vrankovic**, L.M. Reinold, R. Riedel, M. Graczyk-Zajac, Void-shell silicon/carbon/SiCN nanostructures: toward stable silicon-based electrodes, *Journal of Materials Science* **51** (2016) (12) 6051.

[2] **D. Vrankovic**, K. Wissel, M. Graczyk-Zajac, R. Riedel, Novel 3D Si/C/SiOC nanocomposites: toward electrochemically stable lithium storage in silicon, *Solid State Ionics*, **302** (2017) 66.

[3] K. Wissel, **D. Vrankovic**, G. Trykowski, M. Graczyk-Zajac, Synthesis of 3D silicon with tailored nanostructure: Influence of morphology on the electrochemical properties, *Solid State Ionics*, **302** (2017) 180.

[4] J. Rohrer, **D. Vrankovic**, D. Cupid, R. Riedel, HJ. Seifert, K. Albe, M. Graczyk-Zajac, Novel Si- and Sn-containing SiOCN-based nanocomposites as anode materials for lithium ion batteries: synthesis, thermodynamic characterization and modelling, *International Journal of Materials Research*, **108** (2017) (11) 920.

[5] **D. Vrankovic**, M. Graczyk-Zajac, C. Kalcher, J. Rohrer, M. Becker, C. Stabler, G. Trykowski, K. Albe, R. Riedel, Highly Porous Silicon Embedded in a Ceramic Matrix: A Stable High-Capacity Electrode for Li-Ion Batteries, *ACS Nano*, **11** (2017) 11409.

[6] M. Storch, **D. Vrankovic**, M. Graczyk-Zajac, R. Riedel, The influence of pyrolysis temperature on the electrochemical behavior of porous carbon-rich SiCN polymer-derived ceramics, *Solid State Ionics* **315** (2018) 59.

Patent:
[7] **D. Vrankovic**, M. Storch, C. Schitco, M. Graczyk-Zajac, R. Riedel, Solvent assisted synthesis of micro/mesoporous ceramics from preceramic polymers, German Patent registration DE 10 2016 116 732 A1.

Table of Contents

List of Abbreviations

AK	Arbeitskreis/Working group
ATR	Attenuated total reflection
BET	Brunauer, Emmett and Teller
BF	Bright-field
BJH	Barrett-Joyner-Halenda
a_i	Chemical activity of the component i
C_a	Anode specific capacity
C_c	Cathode specific capacity
CCS	Carbon capture and Sequestration
CE	Cycling efficiency
CNTs	Carbon nano-tubes
C_{irr}	Irreversible capacity
C_{rev}	Reversible capacity
C_{th}	Theoretical capacity
C_{total}	Total capacity of a Li-ion battery full-cell
DBE	Dibutyl ether
DMC	Dimethyl carbonate
DVB	Divinylbenzene
DVT	Divinyltiophene
E	Electromotive force/difference in half-cell potential
E°	Standard electrode potential
EC	Ethylene carbonate
EDS	Energy-dispersive X-ray spectroscopy
e.g.	Of example
EMF	Electromotive force
F	Faraday's constant (96485.3365 C·mol^{-1})
FTIR	Fourier transformed infrared spectroscopy
ΔG	Change in Gibb's free energy
ΔG°	Change in standard Gibb's free energy
GCPL	Galvanostatic cycling with potential limitation
GF	Glass fibres
η	Coulombic efficiency
ΔH_{ads}	Adsorption enthalpy
HAADF-STEM	High-angle annular dark-field scanning transmission electron microscopy
HTT1800	Commercially available polyorganosilazane, Clariant GmbH, Germany
HRTEM	High-resolution transmission electron microscopy
i	Current density
IUPAC	International union of pure and applied chemistry
K	Equilibrium constant
L_a	Lateral size of the carbon-nanodomains
LCO	Lithium cobalt oxide
LFP	Lithium iron phosphate
LIBs	Lithium ions batteries
$LiPF_6$	Lithium hexafluorophosphate
Li-S	Lithium-sulphur batteries
LMO	Lithium manganese oxide
MAS-NMR	Magic angle spinning nuclear magnetic resonance (spectroscopy)
MD Simulations	Molecular dynamic simulations
MOFs	Metal-organic frameworks

n	Number of electrons
NCA	Nickel cobalt aluminium oxide
NMC	Nickel manganese cobalt oxide
NMP	N-methyl-2-pyrrolidone
NMR	Nuclear magnetic resonance (spectroscopy)
NP	Nanoparticles
p	Specific power
P	Power
PDC	Polymer-derived ceramic
PHPS	Commercially available perhydropolysilazane, AZ Electronic Materials
PMS MK	Commercially available polyorganosilsesquioxane, Wacker-Belsil, Germany
PVDF	Polyvinylidene fluoride
q	Specific charge capacity
Q_m	Mass specific capacity contribution of the inactive components of a Li-ion battery full-cell, in $\mathrm{mAh \cdot g^{-1}}$
R	Gas constant ($8.314\ \mathrm{J \cdot mol^{-1} \cdot K^{-1}}$)
Ref.	Reference
RD-684a	Commercially available polyorganosiloxane, Starfire Systems Inc, USA
SEI	Solid electrolyte interface
SEM	Scanning electron microscopy
SiCN	Silicon carbonitrtide
SiOC	Silicon oxycarbide
SSA	Specific surface area
T	Temperature
TEM	Transmission electron microscopy
TGA	Thermogravimetric analysis
TPV	Total pore volume
$\mathrm{T_{pyr}}$	Temperature of pyrolysis
$U°$	Standard cell voltage
ΔV	Change in volume
W	Specific energy density
wt.%	Weight percent
XRD	X-ray diffraction

1. Introduction

The continuously increasing energy demands of modern society impose new challenges to existing environmental problems notably, the climate change by greenhouse gas emissions. Reaching a global warming "well below 2 °C" by 2050 requires fast actions to reduce the use of fossil fuels. Among all hydrocarbon fuels only natural gas faces a moderately secure position as a bridge to a low-carbon future. Gas has lower emissions than oil and coal, but is still a carbon-based fossil fuel with limited availability. For its extensive use, a significant development of Carbon Capture and Sequestration (CCS) technologies is required. The so-called "green carbon" technology enables the usage of carbon-based sources with high efficiency and in an environmentally friendly manner. Additionally, the green carbon strategy preserves carbon resources for high-value chemicals rather than to use them for direct combustion with low efficiency [8, 9]. In any scenario, a new energy economy based on (solar) hydrogen as energy carrier will develop [8, 10].

An important challenge of renewable energy sources is their inaccessibility/lower output at a certain time of a day or a year. This implies efficient and cheap energy storage as the main aspect in the green economy scheme. The development of rechargeable batteries over the past 150 years from lead-acid cells in the 1850s to Li-ion batteries (LIBs) in the 1990s is considered as driving force for technological progress [11-17].

The Li-ion cell, originally designed and commercialised by Sony in the 1990s, consists of a graphite anode, a metal oxide cathode and a liquid electrolyte. In the past decades, scientific and technological progress enabled a significant improvement in the safety, performance and lifetime of the cells but almost no progress concerning basic electrochemical processes has been made. Currently, there is a strong demand for higher energy densities to satisfy the significantly increased energy consumption of portable electronics, to extend the driving range of electric vehicles and to provide safe, high capacity reservoirs for renewable energy. The low energy density of Li-ion cells causes limited driving range. The large amount of raw materials required raises the price of the battery and limits their application in electrical grids. Thus, the research is nowadays focused on increasing the energy density of cathode and anode active materials, while diminishing their price. A real break-through is, however, expected from new battery chemistries, beyond intercalation [11, 12].

In this work, new materials with a tailored microstructure and composition are developed and tested in the green energy technology. In the first part, the detailed study of silicon-based nanocomposites stabilising the Si anode in a half-cell is presented. The improvement of the intrinsically poor cycling stability of silicon opens up the possibility to use alloying-type anodes long-awaited for post-lithium-ion batteries. The second part of this thesis discloses a *de novo* invented synthesis route for porous Si-based ceramics using simple chemical tools. The highly efficient and cost-effective method provides hierarchically porous materials also suitable for, e.g., CO_2 gas capture and storage.

2. Fundamentals

This chapter deals with lithium-ion batteries and the fundamentals of their working principle. Various materials and governing chemistries will be introduced. The focus will be on challenges related to the use of silicon as anode material. In addition, it describes the concept of polymer-derived ceramics (PDCs), with the focus on composites based on PDCs as matrix material. It also includes a brief overview of porous ceramics used for energy applications.

2.1. Lithium-ion battery

2.1.1. Basic concepts and electrochemical principles

This chapter introduces the working principle of the lithium-ion battery together with the basic electrochemical equations and concepts [18, 19].

“A battery can be defined as a system that uses electrochemical reaction to directly convert the chemical energy of an electrode material into electric energy” [19]. In general, batteries can be classified as primary and secondary batteries. Primary batteries are used only once and subsequently disposed, while secondary batteries allow for recharging or multiple use, respectively. Looking more closely, a battery usually consists of one or more interconnected electrochemical cells. For large-scale applications, the electrochemical cells are grouped into separate modules. The cells form a battery system together with interconnecting circuits, safety and temperature management.

An electrochemical cell consists of two electrodes, denoted as cathode and anode, the current collectors, the electrolyte, the separator and the housing. Due to the reversible process at both electrodes, secondary batteries are by convention named after their function during the discharge process. Thus, the more negative electrode is called an anode and the more positive electrode is called a cathode. Lithium secondary batteries are based on lithium ions (Li^+) migrating between the cathode and the anode through an organic electrolyte, while electrons migrate via an external circuit. A schematic drawing of a secondary Li-ion cell is shown in Figure 1. Eq. 1 describes the electrode reactions during charge/discharge, with the graphite anode and $LiCoO_2$ cathode. The charge process consists of imposing the external voltage/current promoting the oxidation of the cathode and the release of lithium ions. The electrons transferred via external circuit reduce the anode, and lithium ions are inserted for the charge equilibration. During discharge, the anode is oxidised, while the Li-ions are released into the electrolyte. The electrons are supplied to the external circuit. The charge carriers are transferred to the cathode which is subsequently reduced.

$$LiCoO_2 \underset{\text{Discharge}}{\overset{\text{Charge}}{\rightleftarrows}} Li_{1-x}CoO_2 + xLi^+xe^-$$

Positive electrode

$$6C + xLi^+ + xe^- \underset{\text{Discharge}}{\overset{\text{Charge}}{\rightleftarrows}} C_6Li_x$$

Negative electrode

$$LiCoO_2 + C \underset{\text{Discharge}}{\overset{\text{Charge}}{\rightleftarrows}} Li_{1-x}CoO_2 + CLi_x \qquad \text{Eq. 1}$$

Overall cell reaction

The basics of battery electrochemistry

The intrinsic voltage of electrochemical cells at equilibrium is controlled by the Nernst equation. The Nernst equation can be derived from the Gibbs free energy relationship shown in Eq. 2 [18, 19].

$$\Delta_r G = -nFE \qquad \text{Eq. 2}$$

where n is the number of electrons involved in the oxidation/reduction reaction, F is the Faraday constant, and E is the cell voltage (also known as electromotive force (emf)).

Knowing that $\Delta_r G = \Delta_r G^o + RT \ln Q$, it follows after division of both sides by $-nF$ that:

$$E = -\frac{\Delta_r G^o}{nF} - \frac{RT}{nF} \ln Q$$

where $Q = \prod_i a_i^{v_i}$ and $E^o = -\frac{\Delta_r G^o}{nF}$ leads to:

$$E = E^o - \frac{RT}{nF} \ln Q \qquad \text{Eq. 3}$$

When considering the following electrochemical reaction:

$$aA + bB = cC + dD$$

Eq. 3 can be rearranged and the voltage of the system can be expressed by:

$$E = E^o - \frac{RT}{nF} \ln \frac{[C]^c [D]^d}{[A]^a [B]^b} \qquad \text{Eq. 4}$$

where E^0 is the standard electrode potential, R is the gas constant, T is the absolute temperature in Kelvin, [A]-[D] are the concentrations of each species, and a-d the corresponding stoichiometric coefficients.

When the reaction reaches equilibrium, Q becomes equal to K, where K is the equilibrium constant of the cell reaction. It is important to note that the chemical reaction at equilibrium does not generate a potential difference between the electrodes of a galvanic cell. This allows to set $E = 0$ and $Q = K$ in the Nernst equation (Eq. 3) leading to

$$\ln K = \frac{nFE^{o}}{RT} \qquad \text{Eq. 5}$$

The specific charge capacity q describes the amount of charge stored (released) per mass/volume of reactants during the operation of the battery (Eq. 6). The unit of q is ampere-hour per kilogram/liter ($Ah{\cdot}kg^{-1}$; $Ah{\cdot}L^{-1}$).

$$q = \frac{zF}{m} \qquad \text{Eq. 6}$$

The specific energy density W is derived from the change in Gibbs free energy per mol of reaction, divided by the mass of the reactants as shown in Eq. 7. The unit is watt-hour per kilogram ($Wh{\cdot}kg^{-1}$).

$$W = \frac{zF \cdot \Delta E^{o}}{m} \qquad \text{Eq. 7}$$

The energy that can be derived per unit of time is defined as the power P of a battery and shown in Eq. 8. When the power is considered per mass of the electrochemical cell, it is referred to as the specific power p and is defined according to Eq. 9. The unit of p is watt per kilogram ($W{\cdot}kg^{-1}$).

$$P = i \cdot E \qquad \text{Eq. 8}$$

$$p = \frac{i \cdot E}{m} \qquad \text{Eq. 9}$$

The coulombic efficiency η is defined as the ratio between the recovered and the inserted charge according to Eq. 10. It is important to note that the irreversible losses during the first cycle are generally caused by the formation of the so called Solid Electrolyte Interface (SEI) and the trapping of Li-ions in the electrode material.

$$\eta = \frac{q_{delithiation}}{q_{lithiation}} \cdot 100\ \% \qquad \text{Eq. 10}$$

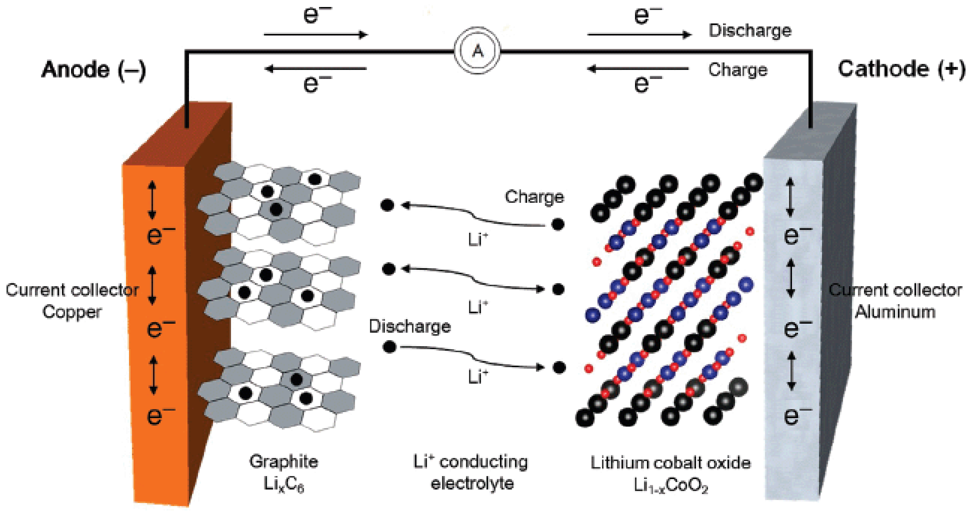

Figure 1: Schematic drawing of the lithium-ion cell. Lithium ions shuttle between electrodes through electrolyte, while electrons are transferred via external circuit. Reproduced from Ref. [19] with permission of the WILEY-VCH.

2.1.2. Material aspects

The electrodes used in current LIBs comprise of a material responsible for the storage of the lithium ions, a binder and a conducting agent (denoted as additives). Typical active materials used as cathode (Table 1) include the initially developed $LiCoO_2$ (LCO) and $LiMn_2O_4$ (LMO). Since $LiNi_xMn_yCo_{1-x-y}O_2$ (NMC) has the same R3-m layered structure as LCO, it is a promising alternative due to the higher stability against thermal overoxidation. Another widely investigated and highly competitive material with a layered R3-m structure is $LiNi_{0.80}Co_{0.15}Al_{0.05}O_2$ (NCA). Its main advantage over LCO is the much higher capacity. $LiFePO_4$ (LFP) with an olivine structure and good thermal stability is the perfect candidate for high rate applications. Each of the listed materials displays different and unique features qualifying them for different applications. Table 1 gives a brief summary of the main properties, including some advantages/disadvantages, and the common application at the present time [11, 19-23].

As anode material, graphite (natural and artificial) is frequently commercially used. It also serves as a universal reference in evaluating new anode materials. Apart from graphite, there is a wide variety of anode materials electrochemically active for lithium storage at low potentials. Depending on the storage mechanism, they can be classified into three different categories: i) intercalation, ii) alloying and iii) conversion materials. Graphite stores lithium ions by intercalating them between graphene layers during lithiation, getting reduced in the process. Additionally, the stacking order in the graphitic host material along c-direction changes from ABAB to AAAA. The highest stoichiometry at room temperature is LiC_6, which results in the theoretical capacity of 372 $mAh \cdot g^{-1}$ [11, 19, 23, 24].

Table 1: Properties of various cathode materials used in the commercial lithium ion battery. Reproduced from Ref. [23] with permission of the Journal of The Electrochemical Society.

Cathode Material	Midpoint voltage vs. Li (C/20)	Specific Capacity	Advantages	Disadvantages	Applications
LCO	3.9	155	In common use, good energy	Moderate charged state thermal stability	Mainly smaller portable electronics
LMO	4.0	100-120	Very good thermal stability, inexpensive, very good power capability	Moderate life cycle, lower energy	Higher power applications such as power tools and electric motive power
NCA	3.7	180	Very good energy, good power capability, good life cycle	Moderate charged state thermal stability, sensitive to moisture even in discharged state	Excellent for motive power and premium electronic applications
NMC	3.8	160	Very good combination of properties (energy, power, life cycle and thermal stability)	Patent issues	Both portable and high-power applications including power tools and electric vehicles
LFP	3.4	160	Very good thermal stability and life cycle, good power capability	Lower energy, special preparation conditions, patent issues	Mainly used in high power such as power tools and energy storage applications

The specific capacities of the anode and cathode materials, together with their operating voltages, are the main factors contributing to the energy density of a rechargeable battery. Concerning the calculation of the total cell capacity (C_{total}), the mass specific contribution Q_m of the inactive cell components (binder, separator, electrolyte, outer cases, etc.) also has to be taken into account [25]:

$$C_{total} = \left(\frac{1}{C_a} + \frac{1}{C_c} + \frac{1}{Q_m}\right)^{-1}$$

In order to enhance the total cell capacity, it is either possible to increase the specific capacities of the active materials or to diminish the contribution of inactive cell components. Inactive cell components, including binders, separators, outer cases and the major components of the electrolyte (solvent, salt), appear to have little room for further improvement [11]. Accordingly, for a breakthrough new redox reactions, beyond conventional intercalation, between charge-carrier ions and new host materials have to be investigated. Rather limited energy densities are characteristic of intercalation-based materials due to the relatively small number of crystallographic sites for storing charge-carrier ions. Thus, electrodes that are based on solid-state (alloying and conversion) or gas-phase reactions attract interest. In the first part of this work the main emphasis will be therefore on electrodes which are based on the alloying mechanism to store lithium ions, more specifically to silicon based nanocomposites.

2.1.3. Silicon alloying anodes and nanocomposites

Silicon and silicon oxide (SiO_x)-based materials have been considered to be promising alternatives to graphite for the next generation of Li-ion batteries. Compared to the commercially used graphite, Si has quite a low working potential (< 0.5 V versus Li/Li^+) a about ten times higher specific capacity (3579 $mAh \cdot g^{-1}$ for $Li_{15}Si_4$) [25-29].

Despite these advantages, large volume changes (> 280 %) during alloying/dealloying with lithium hinder the commercial application of silicon-based anodes. Volume expansion results in the disintegration of the electrode followed by the loss of the electric contact between the active material and the current collector, inevitably causing the capacity to fade. Furthermore, it also leads to an unstable solid-electrolyte interface (SEI) which causes the thickening of the SEI and, hence, a low Coulombic efficiency (CE) [30, 31]. Several advanced nanomaterial-design strategies have been developed to mitigate the volume expansion and to insure a stable SEI on the silicon electrode. To address only the most prominent: (i) keeping the size of silicon nanoparticles below a threshold value (about 150 nm) [32], (ii) embedding nanosilicon particles into an active or inactive matrix [33-41], (iii) synthesis of nanosilicon-carbon composites with free volume around the silicon particles [25, 42-46], (iv) chemical bonding of silicon nanoparticles to a binder or conductive additive [47-53], (v) preparation of nanowires, nanotubes, nanostructured particles [54-57], etc. These approaches indeed have led to a significant improvement of the life cycle and the specific capacities. However, complex preparation procedures and expensive starting materials, together with a relatively low electrode mass loading, still limit their practical application.

A promising approach concerning the fundamental problems of Si as anode was reported by Bao et al. [58]. It was shown that the reduction of SiO_2 in the presence of magnesium leads to nanostructured Si. Significant amount of work has been done ever since in order to optimize this procedure and to prepare nanostructured porous silicon materials for battery applications [59-64]. The generated porosity results in a large surface area accessible to the electrolyte, a short Li-ion diffusion path and void spaces necessary for volume expansion, ultimately leading to an effective release and/or homogeneous strain-stress distribution within the structure. Lin et al. [65] showed that temperatures as low as 250 °C are sufficient to prepare crystalline Si nano-particles in high yields using aluminothermic or magnesiothermic reduction. Extensive research focusing on optimizing the procedure and choosing raw materials suitable for cost effective production of nanostructured silicon [66-68] has been conducted since.

However, the use of nanostructured materials causes new challenges due to their high specific surface area and reduced particle size [29, 69]. Although high surface-to-volume ratios can boost the transfer of lithium from the solvent to the active material achieving high rates and solve issues caused by volume changes, such electrodes at the same time suffer from a poor volumetric storage capacity.

Even though high surface area is an inherent feature of nanostructured materials, the electrode/electrolyte surface area need to be tuned by engineering their secondary structures. Embedding nanostructured silicon in an inexpensive matrix, capable of providing sufficient ion and charge transfer, achieving additional storage capacity and acting as electrolyte-blocking layer could be a promising solution to the abovementioned problems with nanostructured silicon. Primary Si nanoparticles have the necessary void space required to mitigate volume changes while μm-sized secondary particles, composed of Si and matrix material, help to reduce the specific SEI.

2.2. Polymer-derived ceramics

2.2.1. General background

Preparation of advanced, polymer-derived ceramics (PDC) by pyrolysis of organo-silicon preceramic polymers attracted great interest in the past decades. This method allows for a synthesis of complex ceramic systems that are generally not accessible through other classical methods like the powder route or chemical vapour deposition (CVD). Furthermore, the micro/nanostructure of the final ceramic product can be designed and tailored at the molecular level. Choosing suitable preceramic polymers allows for the preparation of ceramic products without the need for additives or sintering agents. Well-established polymer forming techniques could be used to obtain complex ceramic shapes [70].

Historically, synthesis of non-oxide ceramics from molecular precursors was first reported by Ainger and Herbert [71] and by Chantrell and Popper [72] in the early 1960s. However, the first practical transformation of preceramic polymers to ceramic products came almost one decade later, when Verbeek, Winter and Mansmann [73-75] succeeded in the preparation of small-diameter Si_3N_4 and SiC ceramic fibres from polysilazane, polysiloxane and polycarbosilane precursors. Similarly, in the 1970s, Yajima reported on the innovative process of preparing SiC-based ceramic fibres by the thermolysis of polycarbosilanes [76-78]. Further achievements in the 1980s allowed for the fine tuning of the ceramic microstructure by controlling the chemical compositions of polyorganosilicon precursor [79-81]. In order to compete with traditional ceramics, PDCs have to acquire specific properties (novel composition or particular shapes) and have to be affordable and easy to implement in industrial processes. After the early studies on the classical binary (Si_3N_4, SiC) or ternary (SiCO, SiCN) ceramics, significant efforts have been made to develop quaternary and multinary component ceramics. Introducing additional constituents into the ternary framework (B, Al, Hf, Zr, Ti, etc.) made it possible to achieve an exceptionally high resistance to temperature and oxidation or to impart certain functionalities to the ceramic (electrical conductivity, ferromagnetic behaviour, etc.) [82-101]. PDCs additionally proved their versatility as suitable materials for energy storage. This aspect will be addressed in more details in Chapter 2.2.2 and Chapter 2.2.3.

SiOC and SiCN belong to the family of polymer-derived ceramics made from the preceramic organosilicon polymers with the general formula shown in Figure 2. The composition and microstructure of the final ceramics obtained after pyrolysis in a controlled atmosphere (inert or reactive gasses) strongly depend on the class of silicon-based polymers employed. This makes it possible to prepare various chemical compositions by the tuning of the molecular structure of the preceramic polymer. Another important step in the preparation of PDCs is crosslinking. It allows for an increase of the ceramic yield by inhibiting the fragmentation and the loss of the components with a low molecular weight during pyrolysis. Depending on the preceramic polymer, crosslinking can be achieved through: thermal crosslinking, addition of chemical reagents (catalysts or peroxides), free radical initiation, UV-curing, exposition to moisture and oxygen [102, 103]. The final step in the preparation of the ceramic product is pyrolysis at temperatures $\geq$ 800 °C [104].

SiOC ceramics are generally prepared from crosslinked polysiloxanes. As an alternative, the sol-gel processing is also widely applied. Hereby, functionalized silicon monomers are reacted to form a gel which is subsequently converted into a ceramic. The sol-gel method also allows for a precise tailoring of composition. However, poor scalability limits its commercial application [105-130]. During pyrolysis in inert atmosphere, the silicon oxycarbide network is formed from Si-centred tetrahedral sites with O and C atoms sitting at the corners bridging two or more Si-tedrahedra [111]. Furthermore, carbon/silica enriched regions are created depending on the carbon content in the final ceramic. A part of the carbon atoms segregates forming a sp^2-hybridised carbon, often called "free carbon" phase [107, 131-134]. TEM studies and electrical conductivity measurements showed that depending on the amount of segregated carbon, either carbon nano-domains or a percolating carbon network will form [135-137]. Latter frequently occurs in the so called "carbon-rich" ceramics, in which the content of carbon typically exceeds 20 wt.% [104]. The chemical composition of the SiOC matrix can be expressed as: $SiC_xO_{2(1-x)} + yC_{free}$ where $SiC_xO_{2(1-x)}$ represents the chemical composition of the amorphous SiOC matrix, and yC_{free} the carbon phase [119].

Similar to SiOC, SiCN ceramics can be prepared from crosslinked polysilazanes or polysilylcarbodiimides. During pyrolysis in an inert atmosphere, polysilazane converts to an amorphous ceramic consisting of a "mixed bonds" configuration (similar to SiOC ceramics discussed above), with tetrahedrally coordinated silicon atoms bonded to carbon/nitrogen in configurations ranging from SiC_4 via SiC_3N, SiC_2N_2 and $SiCN_3$ to SiN_4. In contrast, the pyrolysis of polysilylcarbodiimides leads to the formation of an amorphous nanocomposite comprised of Si_3N_4, SiC and a segregated carbon phase [104, 138-142].

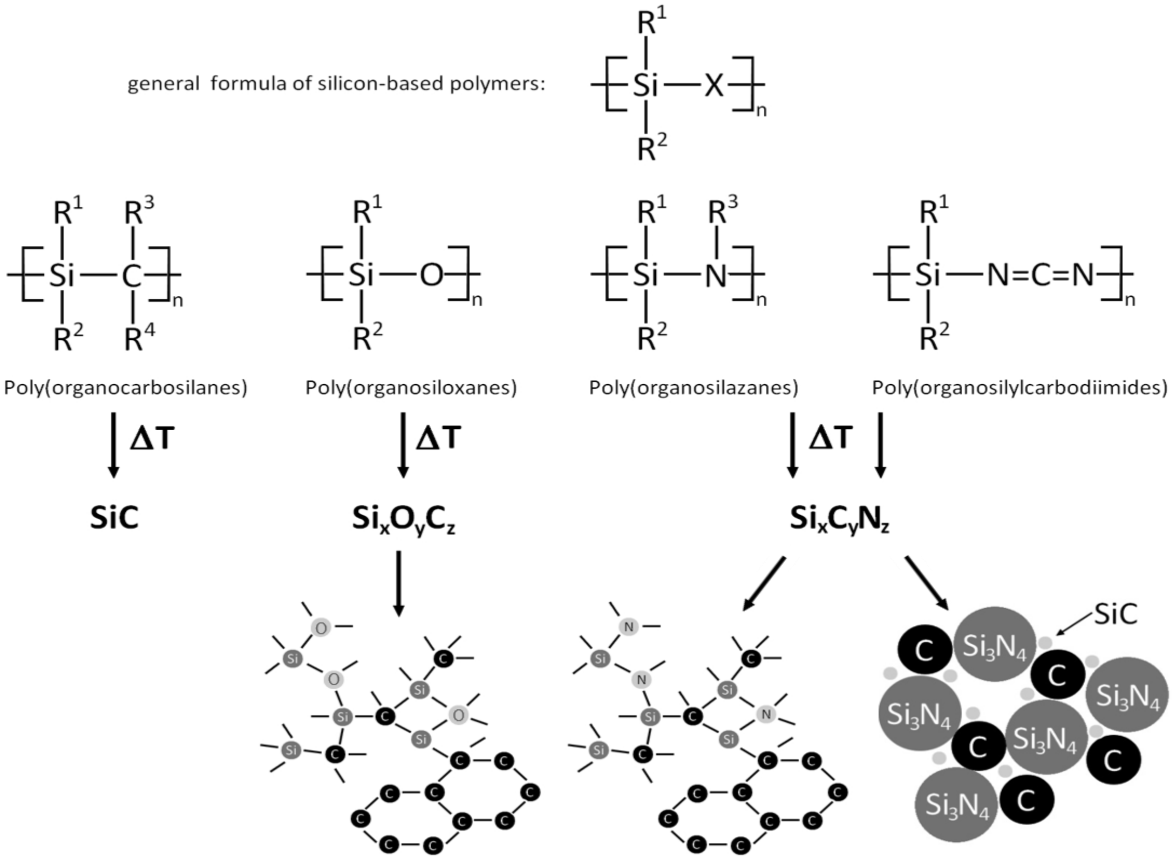

Figure 2: Chemical formulas of different organosilicon polymers and schematic representations of the corresponding microstructure after pyrolysis [70, 104, 131, 138].

2.2.2. SiOC and SiCN as an active insertion host

In the past two decades, SiOC and SiCN attracted a lot of attention as perspective Li-ion storage hosts. The pioneering work of Dahn`s group [143-149] showed that it is possible to achieve first cycle reversible capacities up to 560 and 640 mAh·g^{-1} for SiCN and SiOC, respectively.

Among the various SiOC chemical compositions tested ever since, ceramics with an exceptionally high carbon content proved to be the most promising. They exhibited the highest gravimetric capacities (up to 900 mAh·g^{-1}), good rate capabilities (up to 200 mAh·g^{-1} at 2C rate) and reliable cycling stability of more than 200 cycles [150-164]. The major drawback of SiOC anodes is the low first cycle Coulombic efficiency of ~70%. Furthermore, a large hysteresis, namely the difference in the extraction and insertion potential, significantly limits the electrochemical performance of the cell [165-167]. Even though the mechanism of Li-ion storage in SiOCs is still not fully explored, three electrochemically active sites have been identified by ^{7}Li-MAS-NMR measurements [150, 151, 153, 168-171]. Major contributions are assigned to interstitial sites and edges of the carbon layers, while another part of the Li-ions are stored in the micropores. Moreover, the similarity of the voltage profiles of carbon-rich SiOC ceramics and amorphous carbon confirms that the major Li-ion storage sites are within the free carbon phase of the ceramic microstructure [150, 158, 161, 172]. According to the results of ab-initio studies, amorphous SiOC network impacts Li insertion in SiOC by lowering the chemical potential (energy levels) of carbon [173, 174].

In comparison to SiOC ceramics, little work has been done on polymer-derived SiCN ceramics as anode material since the first publication in late 1990s [143]. Almost one decade later, Kolb et al. reported on commercially available polysilazane (VL20) as a precursor for SiCN based electrodes [175]. The reported capacities of 39 $mAh\cdot g^{-1}$ indicated that the obtained ceramics are almost inactive for lithiation. However, composites based on the VL20 polysilazane and graphite showed reversible capacities of 474 $mAh\cdot g^{-1}$ being 30% higher than the capacity obtained for the reference electrode (graphite). Significantly improved electrochemical properties of composite materials have also been reported in the following years for SiCN-based electrode materials [161, 176-183]. Single-source precursor derived SiCN ceramics also showed a stable electrochemical behavior with reversible capacities up to ~300 $mAh\cdot g^{-1}$ [184-187]. Reinold et al. [188], reported the excellent performance of carbon-rich SiCN materials and discussed the influence of the microstructure of the ceramic on the electrochemical performance. Solid state NMR studies on carbon-rich SiCN clearly identified the free carbon phase as the main lithium storage site [189, 190].

Currently, it is accepted that replacing oxygen with nitrogen in PDCs renders Si-ceramic network less attractive for lithium ions, leading to an almost complete electrochemical inactivity of the carbon-poor SiCN ceramics. In contrast, the more ionic character of Si-O bond in SiOC ceramics leads to very high initial lithiation capacities even at low carbon content. However, it is important to note that carbon-poor ceramics show no cycling stability (almost all Li-ions are trapped irreversibly in ceramic matrix). When carbon-rich systems are considered, significant differences between SiOC and SiCN ceramics have been observed. The carbon phase has no significant impact on the first cycle lithiation and delithiation capacities of SiOC, whereas for SiCN the capacity increases with the carbon concentration until a threshold value is reached (~50 wt.% of carbon). The carbon-rich ceramics generally exhibit high cycling stabilities and high reversible capacities [161, 163, 164, 168, 176, 189].

In summary, a better understanding of the Li storage sites in silicon oxycarbide and carbonitride glasses is of vital importance for overcoming the existing limitations of this anode type, while maintaining its advantages.

2.2.3. SiOC and SiCN as stabilizing matrix

Graczyk-Zajac et al. and Feng et al. showed that graphite or CNTs embedded into the SiCN strongly improves electrochemical performance, particularly at high current rates [176, 178, 179, 183, 190, 191]. These investigations have revealed that the ceramic SiCN phase prevents the exfoliation of graphite and thus stabilizes the electrode material during cycling. Furthermore, highly disordered carbon derived from potato starch/divinyl benzene embedded into the Si(O)CN matrix proved to have good capacities and rate capabilities [180, 181]. Similar behaviour was observed when SiOC ceramics were used as matrix materials for: graphite [192], CNTs [193, 194] or graphene [195]. Kaspar et al. [196] reported on preparing SiOC/Sn nanocomposites by the single-source synthesis method. Polysilsesquioxane Wacker-Belsil PMS MK (resulting in low carbon content SiOC ceramic) and polysiloxane Polyramic RD-684a (resulting in carbon-rich SiOC ceramic) have been functionalized with tin(II)acetate. The carbon-rich ceramic/tin composite showed great cycling stability and rate capability with initial cycle reversible capacities of 651 mAh·g^{-1}.

Embedding Si in a PDC-based matrix makes it possible to accommodate the stress caused by alloying with lithium. Reinold et al. [197] reported on the advantage of using polymer-derived SiCN ceramic as an inactive matrix for crystalline silicon nanopowder (30-50 nm). The authors stated a protective character of the SiCN matrix in terms of SEI stabilisation for samples prepared at 1100 °C. However, no discussion about cycling stability nor capacities was provided. Kaspar et al. [198] and Liu et al. [199] prepared composite materials based on silicon nanoparticles dispersed in a polymer-derived and sol-gel derived SiOC matrix, respectively. Kaspar et al. used polyorganosiloxane Polyramic RD-684a (PolyR) mixed with either crystalline (30-50 nm) or amorphous (36 nm) silicon and pyrolysed under argon at 1100 °C. The samples obtained exhibited a strong difference in stability depending on the silicon nanopowder used. The sample based on the amorphous silicon showed a capacity retention of 88% after 100 cycles, while the electrode containing crystalline silicon rapidly broke down due to the rupture of the ceramic matrix. Liu et al. prepared their composites by the sol-gel method. Electrochemical studies of the prepared composites showed a rapid capacity decay; only 73% of the initial values were recovered after only 30 cycles.

2.2.4. Porous polymer-derived ceramics for energy applications

Over the last decade, immense research has been focused on the synthesis and application of hierarchically organized porous materials [200, 201]. This subject became a hot topic and it will continue to gain interest due to the variety of important applications of porous and high surface area materials as sensors, chemical reactors, electrodes, gas storage media, molecular sieves, membrane supports, lightweight structural materials, thermal insulators, bioimplants, etc. [202, 203]. In this chapter, a brief introduction to porous materials and their main applications are presented. Special focus is given to the CO_2 capture together with a short summary of the most important findings on porous PDCs as anode materials.

According to IUPAC [204], a porous solid contains pores (cavities, channels or interstices) which are deeper than they are wide, while the size of the pore is defined as the distance between two opposite walls of the pore (diameter of cylindrical pores, width of slit-shaped pores). Pores smaller than 2 nm are termed micropores, pores with sizes between 2 – 50 nm are mesopores, and pores larger than 50 nm are macropores. A material containing pores of two or more length scales is referred to as a material with *hierarchical porosity* [202]. The combination of different pore sizes offers unique properties. Micro- and mesopores impart high surface areas and pore volumes which provide size and shape selectivity, while bigger pores ($>$ 50 nm) facilitate the mass transport to active sites [200-202, 205].

The applicability of porous materials depends not only on their pore size and size distributions, but also on their microstructural characteristics. The total amount of pores, their accessibility (ratio of closed to open pores), tortuosity, interconnectivity, and most importantly, the chemical composition of the porous material are the main factors which determine their potential application. Furthermore, processability in terms of shaping (fibres, monoliths, etc.), as well as thermal and chemical stability have to be considered. Therefore, the development of porous materials with controllable structures/composition and tuneable pore architecture is required to provide advances in the fields of chemical, material and biological engineering [200, 202, 206, 207]. In this context, much progress has been achieved recently with respect to materials applicable at room temperature, such as porous carbons, mesoporous silicates, organic and metal-organic frameworks (MOFs). However, many applications require porous materials with enhanced resistance to temperatures beyond 500 °C and corrosive environments [202, 203, 206, 208-211]. In a review entitled “In Praise of Pores”, Colombo strongly underlined the advantages of synthetic porous ceramics over metallic or polymeric components for high temperature applications [207].

Materials for CO_2 capture and separation

Carbon dioxide (CO_2) capture is regarded as one of the biggest challenges of the 21st century. Carbon capture and storage (CCS) involves CO_2 capture from power plants, followed by compression, transport and permanent storage. The capture step of CCS represents approximately two thirds of the total cost of CCS [212-214]. Coal-fired power plants, which are the largest source of CO_2 emission, produce flue gas at $\sim$1 bar with a CO_2 concentration of less than 15% [215]. Industrial postcombustion capture occurs under well established “wet-scrubbing” technology based on a primary alkanolamine. The reaction is well documented in literature [216, 217]. The main advantage of this technology is that it is commercially mature and can easily be adapted to existing power plants. However, it suffers from a number of drawbacks which include: (i) the high amount of energy required to regenerate the solvent, (ii) the need of inhibitors to control corrosion and oxidative degradation due to residual oxygen, and (iii) increased costs due to the chemical degradation of the solvent (presence of by-products such as SO_x and NO_x) [218]. Consequently, there is a need to develop a thermally and chemically stable material with a high-adsorption value and a moderate heat of adsorption.

Alternative technologies for the CO_2 capture are based on the storage of CO_2 in light-weight solid materials involving two mechanisms: (i) chemisorption, where CO_2 molecules interact chemically with functional groups (e.g., metal sites or amines) forming strong bonds, and (ii) physisorption, where CO_2 molecules adsorb less strongly in pores. Materials with a chemisorption mechanism adsorb CO_2 selectively even in the presence of other gases having advantages over materials, which operate via physisorption mechanisms [219, 220]. However, these advantages are counteracted by high-energy costs associated with the activation, regeneration, and recycling of the sorbent. In addition, the selectivity of chemisorption tends to monotonically decrease with the increasing loading of sorbate [221].

The main demands to achieve a high CO_2 capture based on the physisorption mechanism are [222-225]:

- *High adsorption capacity larger than 1* $\mathrm{mmol{\cdot}g^{-1}}$ [226]
- *Moderate heat of adsorption* $(-\Delta H_{ads}) \sim < 50\ \mathrm{kJ{\cdot}mol^{-1}}$
- *Selectivity of* CO_2 *over common industrial gases* [219, 227-229]

Other requirements are low cost and the availability of raw materials, fast kinetics of sorption and desorption, mechanical strength, thermal and chemical stability of the solid adsorbent. The presence of micropores, i.e., pores with the size < 2 nm, is one of the key features a material has to have in order to perform efficiently as capture material or a gas separation membrane (if operated by a size exclusion mechanism). Zeolites were reported as promising adsorbents due to their enhanced adsorption properties. However, their low selectivity for CO_2/N_2 and their high regeneration temperature still present important drawbacks. Ordered mesoporous silica may be a candidate due to an appropriate und tuneable porosity and good thermal and mechanical properties [220]. However, its adsorption capacities are not high enough, particularly at low pressures. Metal-organic frameworks (MOFs) attracted significant interest in the recent years, but still require significant research effort [225]. Microporous carbonaceous materials fulfil almost all of the above requirements [223].

The very recent work of Marszewska et al. [230] has clearly demonstrated that microsporosity as well as mesoporosity play an important role in enhancing the CO_2 storage capacity. Mesoporosity improves mass transfer allowing for faster CO_2 equilibration. Thus, the current research strongly focuses on the improvement of the pore structure and surface area by introducing hierarchical porosity.

Apart from the introduction of hierarchical porosity the chemical modification of the pore surfaces is important. The CO_2 capture capacity is enhanced by the presence of basic nitrogen-containing groups, together with hierarchical mesostructures, which include a high BET surface, a stable framework, and the presence of a large number of micropores, as well as small amount of mesopores [219, 220, 231-233]. However, these experimental results have been questioned by MD simulations [234] and the experimental work of Adeniran and Mokaya [235], suggesting that mainly the pore size determines the capacity of CO_2 adsorption, while N-doping plays a minor role.

Porous polymer-derived ceramics as electrode for Li-ion battery

Silicon-based polymer-derived ceramics (PDCs) inherit thermal stability [104, 131] in line with high electrical conductivity [161, 163] for carbon-rich PDCs. Furthermore, porous carbon-rich SiOC ceramics proved to have exceptional electrochemical properties especially at high current densities [154, 156, 162, 236]. Pradeep et al. [236] reported that porous SiOC ceramics with designed porosity deliver more than 900 $mAh \cdot g^{-1}$ at C and 200 $mAh \cdot g^{-1}$ at 20C current rate. At present, PDCs with a stable porosity at temperatures higher than 700 °C are synthesized employing fillers, foaming additives, supercritical drying, or sacrificial agents [237-239]. This renders the process difficult and cost demanding. Hence, improving the ceramic transformation step to accomplish the direct formation of porous materials from molecular preceramic polymers without aforementioned constraints is of great scientific and technological interest.

3. Cumulative part of the thesis

In this part the major scientific findings reported in the publications [1-7] are summarized and discussed in the context of a commercial silicon-based anodes.

Chapter 3.1 presents a short summary of the results obtained during the systematic study of Si-based nanocomposites. The emphasis is on the cycling stability and the Coulombic efficiency of the investigated composites, representing the most important challenge of the silicon-based electrode. Different composite design strategies are developed during this work in order to overcome intrinsically poor cycling stability of silicon anodes. Experimental studies and molecular dynamic simulations reveal a clear dependence of the composite morphology on the electrochemical stability. Chapter 3.2 brings a detailed description of a newly developed synthesis route for the preparation of porous polymer-derived ceramics. Highly porous ceramic materials are obtained after a single step synthesis without the necessity to employ fillers, foaming additives, supercritical drying, reactive pyrolysis atmosphere or sacrificial agents. Finally, successful tests of the porous ceramics as an anode material in LIBs and CO_2 capturing medium are presented.

3.1. Silicon based composites

The content of this chapter is published in:

[1] **D. Vrankovic**, L.M. Reinold, R. Riedel, M. Graczyk-Zajac, Void-shell silicon/carbon/SiCN nanostructures: toward stable silicon-based electrodes, *Journal of Materials Science* **51** (2016) (12) 6051.

[2] **D. Vrankovic**, K. Wissel, M. Graczyk-Zajac, R. Riedel, Novel 3D Si/C/SiOC nanocomposites: toward electrochemically stable lithium storage in silicon, *Solid State Ionics*, **302** (2017) 66.

[3] K. Wissel, **D. Vrankovic**, G. Trykowski, M. Graczyk-Zajac, Synthesis of 3D silicon with tailored nanostructure: Influence of morphology on the electrochemical properties, *Solid State Ionics*, **302** (2017) 180.

[4] J. Rohrer, **D. Vrankovic**, D. Cupid, R. Riedel, HJ. Seifert, K. Albe, M. Graczyk-Zajac, Novel Si- and Sn-containing SiOCN-based nanocomposites as anode materials for lithium ion batteries: synthesis, thermodynamic characterization and modelling, *International Journal of Materials Research*, **108** (2017) (11) 920.

[5] **D. Vrankovic**, M. Graczyk-Zajac, C. Kalcher, J. Rohrer, M. Becker, C. Stabler, G. Trykowski, K. Albe, R. Riedel, Highly Porous Silicon Embedded in a Ceramic Matrix: A Stable High-Capacity Electrode for Li-Ion Batteries, *ACS Nano*, **11** (2017) 11409.

In the present chapter, the influence of a composite morphology on the cycling behavior of elemental silicon will be discussed. Polymer-derived SiCN/SiOC ceramics are employed as the stabilizing matrix in order to protect silicon during the alloying process and stabilize the SEI. First, an experimental method allowing to form a necessary void space around silicon particles is established. This concept is further developed while replacing the dense Si particles by highly porous ones. This method opens more possibilities for composite preparation, allowing for a fine tuning of the morphology in order to finally provide excellent electrochemical performances.

3.1.1. Discussion

In order to overcome the great challenge imposed by the inherent nature of silicon electrodes and to mitigate volume expansion during lithium insertion/extraction, we have systematically designed core-shell structures around silicon nanoparticles. Figure 3 depicts a schematic representation of the preparation route. The synthesis procedure consists of the following steps: i) coating with fructose-derived carbon, ii) embedding of silicon covered with carbon in a ceramic matrix and iii) the introduction of cavities around silicon particles. Coating with fructose-derived carbon is applied in order to increase electronic conductivity of the prepared composite and insure electrochemical activity of silicon. In the second step, a partial burning of carbon leads to the formation of voids around silicon particles providing the free volume required during lithiation. Polymer-derived SiCN with a low carbon content is applied to ensure stable shell and to protect silicon from the contact with an electrolyte. Figure 4 shows TEM micrographs confirming that silicon particles are successfully coated with carbon prior to the embedding in SiCN ceramic. The results of EDS analysis (Figure 4b) show that the silicon nanoparticle is covered with a native silica layer. However, it is challenging to distinguish the amount of carbon (or void) around the silicon particle after the heat-treatment in air. One should note that the coating of silicon nanoparticles, prior to embedding, hinders agglomeration and allows for uniform distribution in the matrix. Furthermore, TEM study confirms the presence of voids around the Si nanoparticles. Electrochemical studies demonstrate an improvement of the cycling stability compared to the pure silicon electrodes. No large cracks of the matrix after 100 cycles have been identified. Nevertheless, this procedure allowed for a minor improvement in the cycling stability, which rendered this approach inefficient. In order to further improve the cycling stability, the capacity and the Coulombic efficiency of silicon-based composites, a simplified approach was developed, where the accommodation volume is introduced in primary silicon particles.

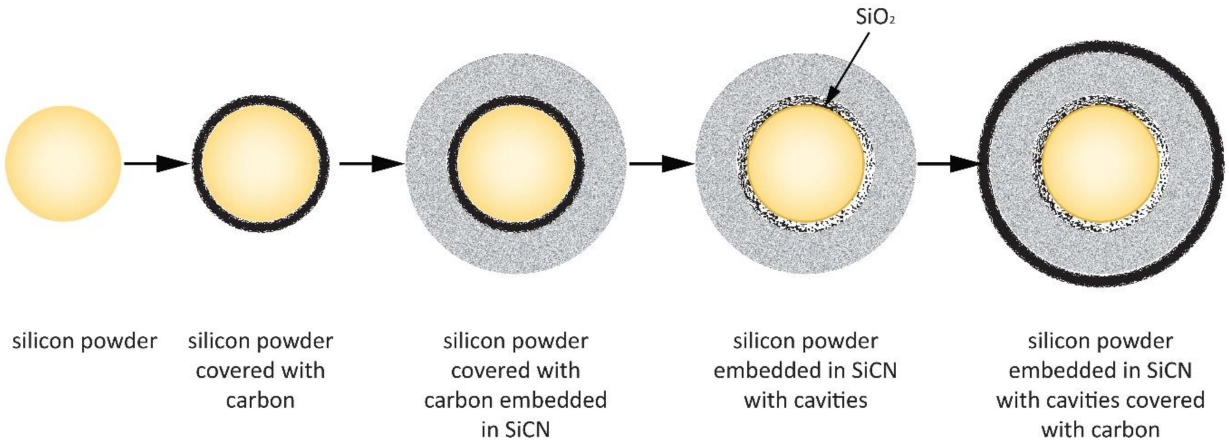

Figure 3: Schematic of composites preparation using the void-shell method. Commercially available silicon is firstly dispersed in a solution of fructose forming carbon coating at 600 °C. In the second step, C-coated silicon (Si/C) is mixed with the preceramic commercial polymer HTT1800 and pyrolyzed at 1100 °C, leading to the embedding of Si/C particles in a silicon carbonitride (SiCN) matrix. In the next step, carbon is partially outburned at 600 °C in air, leading to free space around silicon particles. Finally, the obtained composite is coated with fructose-derived carbon carbonized at 1100 °C. Reproduced from Ref. [4] with permission of the International Journal of Materials Research.

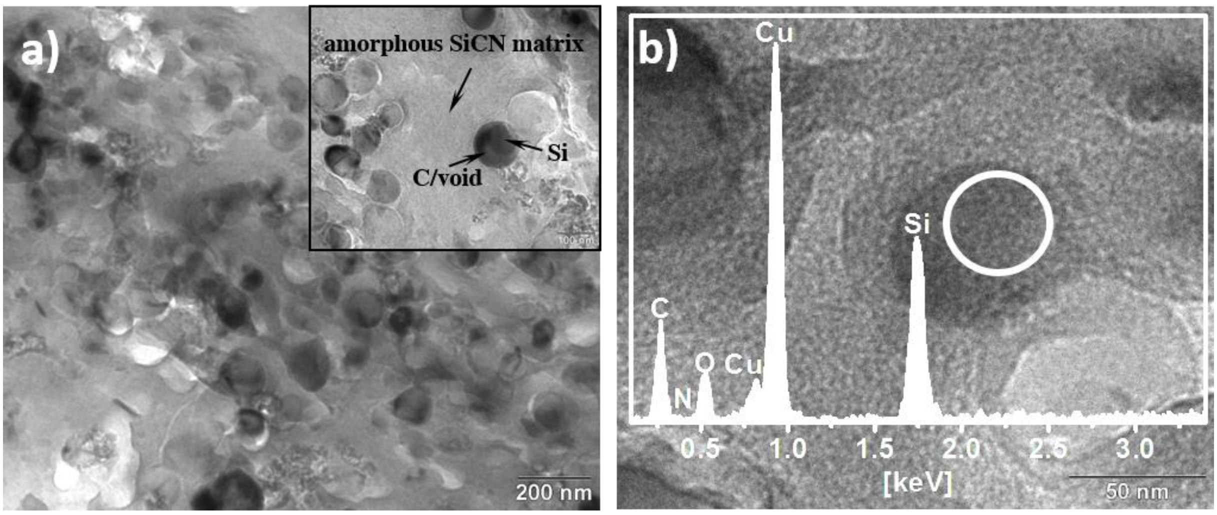

Figure 4: Microstructural characterization of the composites obtained by the void-shell method. (a,b) TEM and selected area EDS analysis of a cross section of the final composite. TEM micrographs confirm the presence of silicon particles covered by carbon dispersed in SiCN ceramic. Coating with carbon prior to embedding in ceramic matrix helps to suppress agglomeration of silicon nanoparticles. EDS analysis confirms a partial outburning of carbon around Si particles. Reproduced from Ref. [1] with permission from the Journal of Materials Science.

In the newly developed approach, nanostructured (porous) crystalline (Si_{tc}) and amorphous (Si_{sa}) silicon synthesized via magnesiothermic reduction reaction route were used as starting material for the composite preparation. To ensure electronic conductivity and to suppress agglomeration, the porous silicon was coated with fructose-derived carbon and then embedded into the polymer-derived SiOC ceramic. The primary silicon particles show highly developed open porosity (Figure 5) confirming results obtained by N_2 physisorption measurements (SSA for Si_{tc} and Si_{sa} of 198 and 623 m^2g^{-1}, respectively). Furthermore, X-ray diffraction and Raman spectroscopy measurements of the final composites show that the crystallinity of Si_{tc} as well as the amorphous character of Si_{sa} primary silicon particles are preserved.

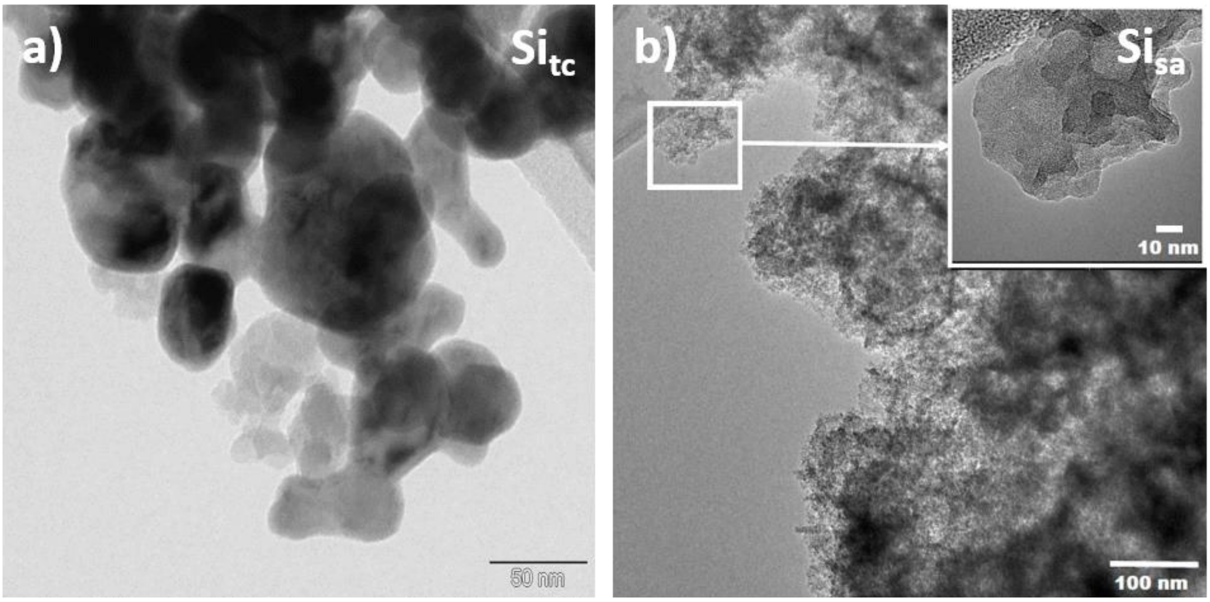

Figure 5: Microstructural characterization of silicon prepared by two-chambers and salt-assisted method. (a,b) TEM micrographs of porous Si_{NP} derived by employing two different synthesis routes, namely the two-chambers (Si_{tc}) and the salt-assisted (Si_{sa}) methods. Both TEM micrographs highlight the mesoporous texture of primary silicon particles. Significantly higher SSA found by N_2-physisorption measurements for Si_{sa} is also visible on the corresponding TEM micrograph. Si_{tc} and Si_{sa} are further used as the starting material for composite preparation. Reproduced from Ref. [3] with permission from the Solid State Ionics.

Systematic electrochemical investigations demonstrate that the best results are achieved for porous silicon embedded into the matrix consisting of carbon and SiOC ceramic with a stable cycling behavior over 50 cycles, good Coulombic efficiencies and stable capacities of 575 $mAh{\cdot}g^{-1}$ and 500 $mAh{\cdot}g^{-1}$ for Si_{tc} and Si_{sa}, respectively.

Finally, the optimal route to synthesize the composite consisting of highly porous silicon stabilized in a SiOC matrix has been developed. This approach combines a fairly easy preparation procedure with the excellent electrochemical performance of the composite. Figure 6 presents a schematic picture of the preparation route of Si/C/SiOC composites, which is defined through three major steps. First, highly porous silicon is synthetized by $AlCl_3$ assisted aluminothermic or magnesiothermic reduction of silica followed by washing of the reaction byproducts. Apart from in-house synthesized silica nanoparticles, the up-scaling potential of the developed method is underlined by the usage of commercially available glass fibers (GFs) as silicon precursor. The prepared Si samples consist of partially crystalline (< 10%) and phase-pure silicon obtained at 220 °C. TEM (Figure 7) and N_2-physisorption measurements of the silicon nanoparticles (NPs) show a highly developed texture of the silicon samples independently of the method employed. However, when GFs are used as raw material, bigger pores are developed compared to mesoporous NPs as shown by SEM investigations (Figure 8). In the second step, the porous silicon is coated with fructose-derived carbon and subsequently, in the final step, embedded in polymer-derived SiOC. The complete coverage of primary silicon particles by a SiOC matrix is confirmed with Raman spectroscopy. Electrochemical studies of all prepared composites show an exceptionally high Coulombic efficiency of 99.5%, and a capacity retention of nearly 100% of over more than 100 cycles. Rate capability tests confirm an outstanding composite stability. Furthermore, it should be pointed out that all electrodes have a relatively high areal mass loading of more than 2 mg·cm^{-2}. For practical use as a battery material, a high areal mass loading is required, although a low areal mass loading helps to achieve better performance.

In order to elaborate the impact of the initial silicon morphology on electrochemical properties, molecular dynamic simulations (MD) were employed. MD simulations show that at the maximum Li content the macroscopic expansion remains well below that of dense silicon. For the investigated system, a maximum volume change of just 25% versus the expected 280% for a dense sample is found. Initial lithiation does not affect the macroscopic volume of silicon particles until the critical Li content is reached. Critical Li content generally scales with the initial porosity, underlying the importance of the porous morphology of the primary silicon particles. Additionally, once the critical lithium content reached, Si undergoes significant elastic softening during Li insertion, allowing for the embedding SiOC matrix to counteract the inherent expansion to a large extent and preserve electrode integrity.

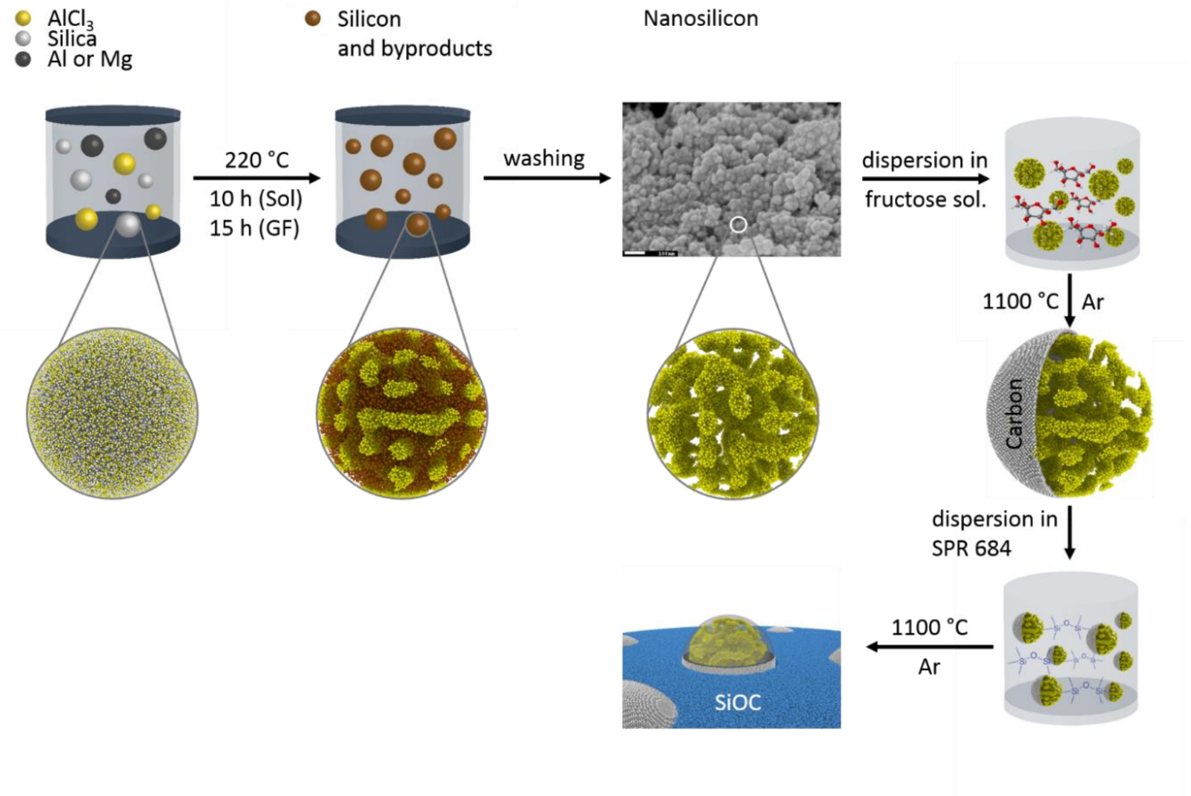

Figure 6: Schematic of composite preparation using silicon derived by $AlCl_3$-assisted aluminothermic or magnesiothermic route. Silica nanoparticles and glass fibres are first reduced by alumino/magnesiothermic reduction at 220 °C. The obtained Si is then washed in H_2O and etched in HCl to remove reaction byproducts. The porous Si is further dispersed in a solution of fructose which forms a carbon coating after carbonization at 1100 °C. In the last step, the C-coated porous Si is mixed with the preceramic commercial polymer SPR 684a and pyrolysed at 1100 °C. After pyrolysis, the final composite where C-coated porous Si is embedded in a silicon oxycarbide (SiOC) matrix is obtained. The final composite is further tested as a potential anode for LIBs. Reproduced from Ref. [5] with permission from the ACS Nano.

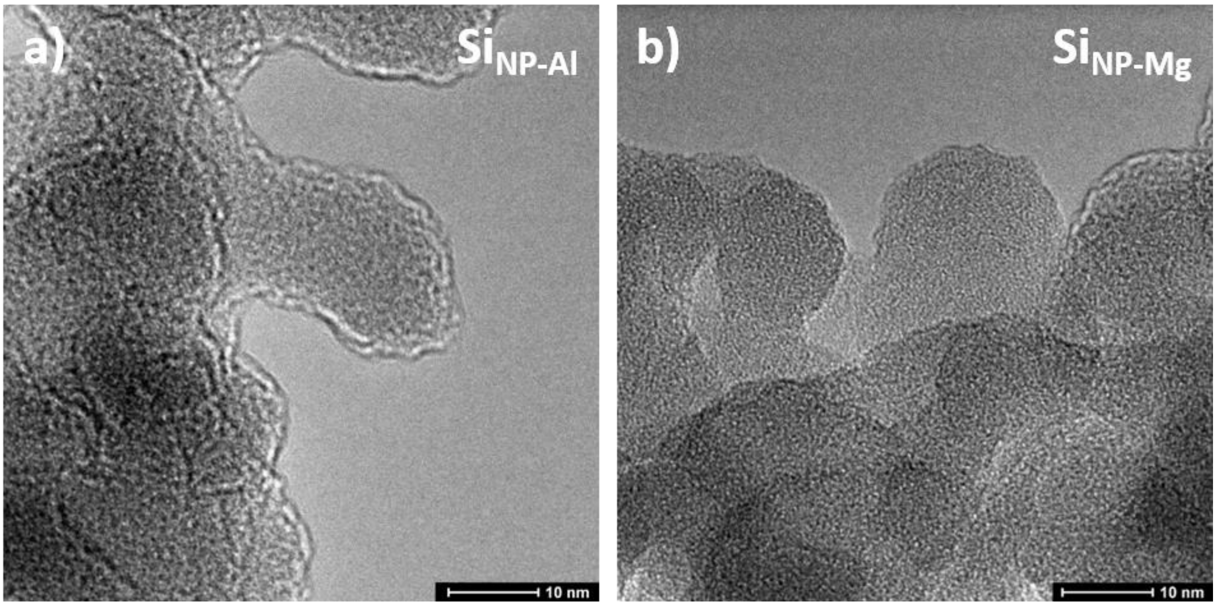

Figure 7: Microstructural characterization of silicon derived by $AlCl_3$-asisted aluminothermic and magnesiothermic route. (a,b) TEM micrographs of porous Si_{NP} derived by employing two different synthesis routes, namely the aluminothermic (Si_{NP-Al}) and the magnesiothermic (Si_{NP-Mg}) reduction reactions. Both TEM micrographs highlight the mesoporous texture of the primary silicon particles. Si_{NP-Al} and Si_{NP-Mg} are further used as the starting material for the composite preparation. Reproduced from Ref. [5] with permission from the ACS Nano.

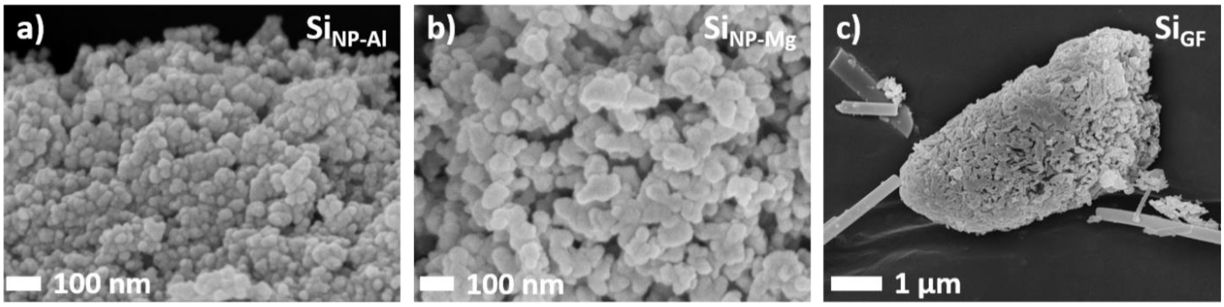

Figure 8: Microstructural characterization of silicon derived by $AlCl_3$-asisted aluminothermic and magnesiothermic route. (a,b) SEM micrographs of porous Si_{NP} derived by employing two different synthesis routes, namely the aluminothermic (Si_{NP-Al}) and the magnesiothermic (Si_{NP-Mg}) reduction reactions. SEM micrographs of Si nanoparticles show the particle size of 50-60 nm as well as the partial coalescence of Si_{NP-Mg}. (c) SEM micrographs of microsized silicon fibres demonstrate the macroporous texture after reduction reaction. The investigated porous silicon nanoparticles and microsized fibres are further used as the starting material for composite preparation. Reproduced from Ref. [5] with permission from the ACS Nano.

Figure 9 shows a comparison of the achieved Coulombic efficiencies and the retained capacities over the different composite design strategies elaborated in this PhD work. Over the years, a steady improvement of the electrochemical performance for silicon-based anode materials has been achieved. The superior properties of the latest composite materials are rationalized through a few different aspects: first, the proposed method ensures a sufficient accommodation volume within silicon particles in the open porosity, making it possible to minimize the stresses evolved during silicon lithiation. An effective ionic and electronic transport is ensured by the conductive fructose-derived carbon present in the pores and around silicon particles. Finally, the encapsulation in the SiOC ceramic which stabilizes the volume expansion and minimizes the SEI formation provides the required protection against the electrolyte, which leads to excellent electrochemical properties.

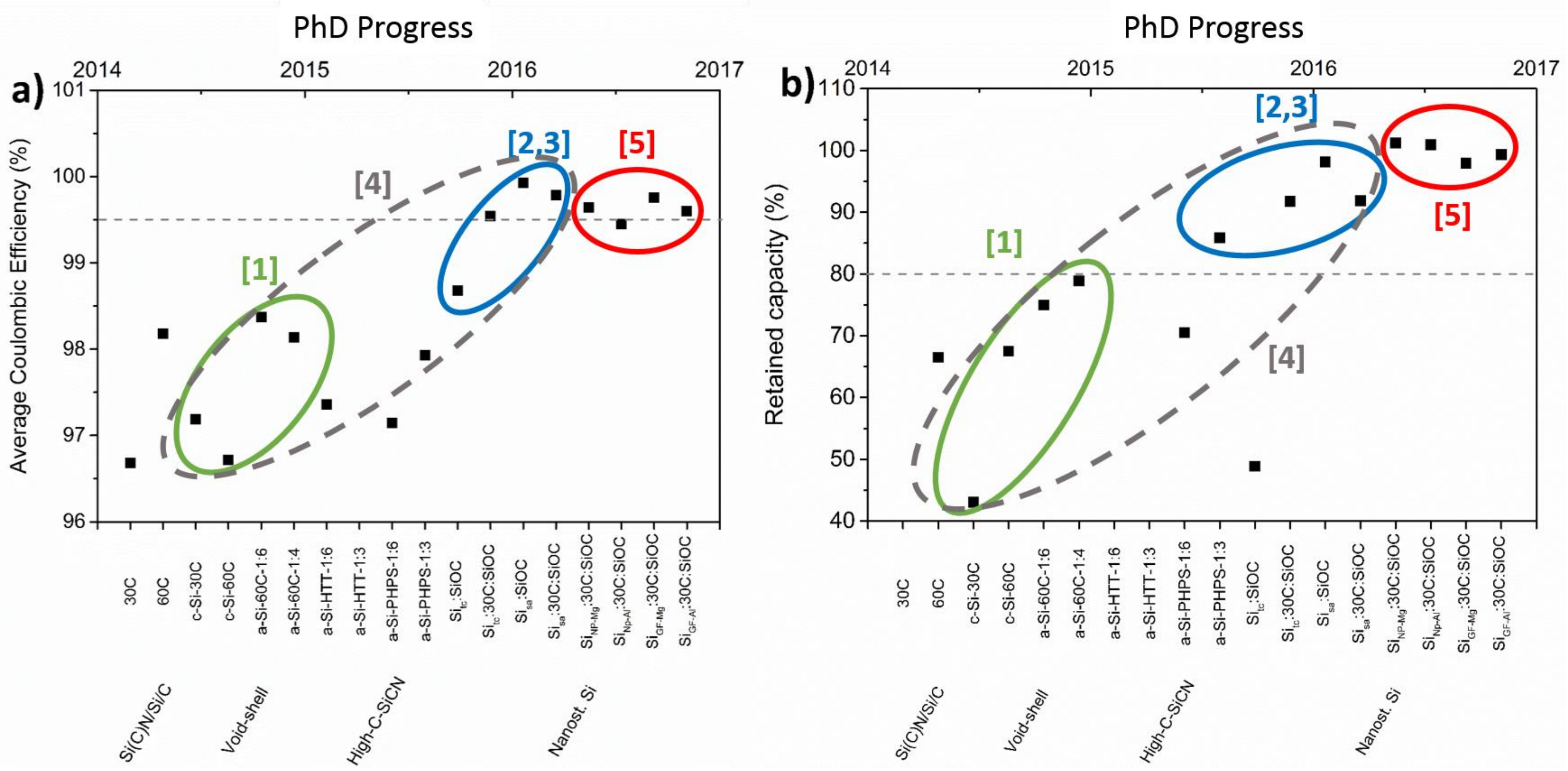

Figure 9: Comparison of the achieved Coulombic efficiencies and the retained capacities over the different composite design strategies elaborated in this dissertation. (a,b) The average Coulombic efficiency over 100 cycles and retained capacities after 100 cycles (50 cycles for composites based on Si_{tc} and Si_{sa} silicon) show a steady improvement over the years. This implies the development of mature composite design strategies bringing Si anodes closer to application. Apart from the composites discussed in detail within the frame of the PhD work, this comparison also includes intermediate materials, which were critical for the systematic development of the composite design. Four categories are defined, namely Si(C)N/Si/C, void-shell, high-C-SiCN and nanostructured Si. For each category a few most prominent samples are presented. **Si(C)N/Si/C** stands for samples where Si nanoparticles are generated in-situ by pyrolysis of PHPS under argon atmosphere, and subsequently coated with fructose derived carbon. 30C and 60C stands for the amount of carbon around obtained nanocomposite in wt.%. **Void-shell** depicts a group of composites with empty space around Si generated by the out-burning of the carbon shell around commercially available dense silicon nanoparticles. c-Si/a-Si denote crystalline and amorphous silicon used as starting material. 1:6, 1:4 or 1:3 describes the ratio of Si to matrix. In the case of **High-C-SiCN** composites, an exceptionally high amount of carbon was introduced to the preceramic polymer through a chemical reaction with divinylbenzene (DVB). Commercially available amorphous dense Si nanoparticles was used as silicon source. The **nanostructured silicon** approach stands for all composites based on porous silicon particles as starting material. The index next to Si defines the corresponding synthesis route.

3.1.2. Statement of personal contribution

[1] **D. Vrankovic**, L.M. Reinold, R. Riedel, M. Graczyk-Zajac, Void-shell silicon/carbon/SiCN nanostructures: toward stable silicon-based electrodes, *Journal of Materials Science* **51** (2016) (12) 6051.

The initial idea behind this work was developed together with my former colleagues Dr. Lukas Mirko Reinold and Dr. Jan Kaspar. Further development and optimization was done by myself. Most of the experimental work and data analysis was carried out by myself, except Thermogravimetric analysis (TGA) which was done by Dipl.-Ing. Claudia Fasel (AK Prof. Riedel) and Transmission electron microscopy (TEM) done by Dipl.-Ing. Ulrike Kunz (AK Prof. Durst). The manuscript was written by myself and revised and approved of by Dr. Magdalena Graczyk-Zajac and Prof. Ralf Riedel.

[2] **D. Vrankovic**, K. Wissel, M. Graczyk-Zajac, R. Riedel, Novel 3D Si/C/SiOC nanocomposites: toward electrochemically stable lithium storage in silicon, *Solid State Ionics*, **302** (2017) 66.

The idea behind this work was developed by myself. Most of the experimental work was carried out by M. Sc. Kerstin Wissel during her master thesis. M. Sc. Kerstin Wissel worked under my co-supervision during the entire time. In particular, I supported the engineering of a high temperature stable reactor required for the sample preparation. I have also assisted M. Sc. Wissel in the optimization of sol-gel synthesis and the microstructural characterization (except TEM, Dipl.-Ing. Ulrike Kunz, AK Prof. Durst), composite preparation, electrode processing, electrochemical measurements, as well as data evaluation and interpretation. The manuscript was written by myself. Dr. Magdalena Graczyk-Zajac and Prof. Ralf Riedel revised and approved the manuscript before publication.

[3] K. Wissel, **D. Vrankovic**, G. Trykowski, M. Graczyk-Zajac, Synthesis of 3D silicon with tailored nanostructure: Influence of morphology on the electrochemical properties, *Solid State Ionics*, **302** (2017) 180.

The idea behind this work was developed by myself. Most of the experimental work was carried out by M. Sc. Kerstin Wissel during her master thesis. M. Sc. Kerstin Wissel worked under my co-supervision during the entire time. In particular, I supported the engineering of a high temperature stable reactor required for the sample preparation. I have also assisted M. Sc. Wissel in the optimization of sol-gel synthesis and the microstructural characterization (except TEM, Dipl.-Ing.

Ulrike Kunz, AK Prof. Durst), composite preparation, electrode processing, electrochemical measurements, as well as data evaluation and interpretation. The manuscript was written by M. Sc. Kerstin Wissel and revised by myself. Dr. Magdalena Graczyk-Zajac and Prof. Ralf Riedel revised and approved the manuscript before publication.

[4] J. Rohrer, **D. Vrankovic**, D. Cupid, R. Riedel, HJ. Seifert, K. Albe, M. Graczyk-Zajac, Novel Si- and Sn-containing SiOCN-based nanocomposites as anode materials for lithium ion batteries: synthesis, thermodynamic characterization and modelling, *International Journal of Materials Research*, **108** (2017) (11) 920.

My PhD thesis has been realised within the SPP 1473 WeNDeLIB. This priority program finished at the end of 2016. The above publication summarizes the results obtained in the 6-year funding period. My contribution to this work consists of describing the methods of Si stabilization within the SiCN/SiOC matrix, which have been developed by myself.

[5] **D. Vrankovic**, M. Graczyk-Zajac, C. Kalcher, J. Rohrer, M. Becker, C. Stabler, G. Trykowski, K. Albe, R. Riedel, Highly Porous Silicon Embedded in a Ceramic Matrix: A Stable High-Capacity Electrode for Li-Ion Batteries, *ACS Nano*, **11** (2017) 11409.

The idea behind this work was developed by myself. A part of the experimental work was carried out by B. Sc. Malin Becker during her bachelor thesis. B. Sc. Malin Becker worked under my co-supervision during the entire time. In particular, I supported the development of molten salt assisted synthesis, the optimization of sol-gel synthesis, microstructural characterization (except TEM, Dr. Grzegorz Trykowski, Torun, Poland), composite preparation, electrode processing, electrochemical measurements, as well as data evaluation and interpretation. Additionally, extensive electrochemical measurements and detail structural analysis were performed by myself after B. Sc. Malin Becker left the group. Molecular dynamic simulations were done by Dr. Jochen Rohrer (AK Prof. Albe). The manuscript was written by myself. Dr. Magdalena Graczyk-Zajac, Dr. Jochen Rohrer, Prof. Karsten Albe and Prof. Ralf Riedel revised and approved the manuscript before publication.

3.2. Porous polymer-derived ceramics as energy storage materials

The content of this chapter is partially published in:

Patent:

[7] **D. Vrankovic**, M. Storch, C. Schitco, M. Graczyk-Zajac, R. Riedel, Solvent assisted synthesis of micro/mesoporous ceramics from preceramic polymers, German Patent registration DE 10 2016 116 732 A1.

[6] M. Storch, **D. Vrankovic**, M. Graczyk-Zajac, R. Riedel, The influence of pyrolysis temperature on the electrochemical behavior of porous carbon-rich SiCN polymer-derived ceramics, *Solid State Ionics* **315** (2018) 59.

In the present chapter, a novel synthesis procedure allowing to prepare porous ceramic materials with a tailored porosity is introduced. The general description of the invented procedure has been filed as a patent. Here, the details of the developed synthesis with the emphasis on the role of di-n-butyl ether (DBE) in pore formation is addressed. Furthermore, the influence of the pyrolysis temperature/atmosphere and the DBE concentration on the texture of the final ceramic is elaborated. Finally, the influence of the pyrolysis temperature on the electrochemical properties is addressed.

3.2.1. Experimental methods

In order to produce the amorphous C-rich porous SiCN ceramics the polymer precursor, the solvent and the carbon source divinylbenzene (DVB, Sigma Aldrich, UK) were used. Perhydropolysilazane dissolved in di-n-butyl ether (PHPS in DBE, AZ Electronic Materials) was used as a polymer precursor. The precursors were mixed and refluxed at 120 °C for six hours in order to enable the hydrosilylation reaction of the DVB with the preceramic polymer and to obtain the preceramic intermediate. Additionally ~10 ppm of Pt(0)-1,3-divinyl-1,1,3,3-tetramethyldisiloxane, diluted in xylene (Sigma–Aldrich, UK) were added to reaction mixture as a catalyst.

The aforementioned preceramic intermediate was pyrolysed in a quartz tube in a programmable horizontal furnace under flowing argon using heating and cooling rates of 100 $°C \cdot h^{-1}$. Material processing is divided into three parts, focusing on variation of the crosslinking temperature and time, the pyrolysis atmosphere as well as the temperature of ceramization. The prepared samples are listed, with the corresponding pyrolysis parameters, in Table 2.

As a reference, the PHPS was reacted with divinylbenzene following the before mentioned procedure without the presence of di-n-butyl ether. The denomination of the samples follows the scheme: “obtained ceramic – temperature of ceramization” (e.g. SiCN 900 for a crosslinking step at 250 °C with a three-hour dwelling time and further pyrolysis at 900 °C in argon atmosphere). After pyrolysis, the samples were ground by hand and milled using a zirconia grinding beaker and a rocker mill “MM 400” (Retsch GmbH, Germany) for an hour at a frequency of 30 Hz. Subsequently the powders were sieved to particle size < 40 μm. All the steps of material preparation and storage, apart from milling and printing, took place in argon atmosphere.

The chemical structure of the pure polymer precursor, the crosslinking agent (divinylbenzene, DVB), DBE, together with reaction products was assessed by FT-IR spectroscopy. The FTIR spectra were measured with a Varian 670-IR – spectrometer (Varian, Inc., USA), in attenuated total reflection mode (ATR) in the wave number range from 550 cm^{-1} to 4000 cm^{-1}.

Thermogravimetric analysis (TGA) was employed to monitor polymer to ceramic transformation and pore formation. TGA was performed with STA 449C Jupiter (Netzsch Gerätebau GmbH, Germany) coupled with a FTIR-spectrometer Bruker Tensor 27, allowing for the measurement of the mass change as well as the evolution of produced gasses. The analysis was performed under a constant argon gas flow (Air Liquide, purity ≥99.5%) of 30 $mL \cdot min^{-1}$. The temperature program was set close to the conditions used during pyrolysis with a heating rate of 20 $°C \cdot min^{-1}$ from room temperature up to 1100 °C.

Nitrogen (N_2) adsorption was performed at 77 K using an Autosorb-3B (Quantachrome Instruments, USA). Before the measurements, the samples were preheated at 150 °C for 24 h under vacuum. Using the obtained N_2-adsorption isotherms, the specific surface area was determined from the linear Brunauer-Emmett-Teller (BET) plots; the relative pressure p/p_0 was between 0.05 and 0.3. The amount of vapor adsorbed at a relative pressure of $p/p_0 \approx 1$ was used to determine the total pore volume [240]. The micropore volume was determined using the de Boer's t-plot analysis [241]. The Barrett-Joyner-Halenda (BJH) method was applied to access the pore size distribution [240].

The chemical composition of the prepared Si(O)CN samples was analysed by hot-gas extraction, using a Leco-200 carbon analyser and Leco TC-436 N/O analyser (both Leco Corporation, USA) for the determination of the carbon and oxygen content, respectively. The amount of silicon was calculated as the difference to 100 wt.% of the sum of the analysed wt.% values of carbon and oxygen, assuming a negligible amount of hydrogen and no other elements present in the samples.

MAS-NMR measurements were performed on the Bruker Avance III 700 MHz spectrometer operating at a proton frequency of 700.24 MHz. ^{29}Si NMR spectra were recorded with the following parameters: single pulse sequence, ^{29}Si frequency: 139.1 MHz, $\pi/8$ pulse length: 2.5 μs, recycle delay: 100 s (sufficient time to get fully relaxed spectra), 1k scans, external secondary reference: DSS. 3.2 mm zirconia rotors filled with samples were spun at 8 kHz.

Table 2: Overview of the prepared samples including the corresponding pyrolysis atmosphere, crosslinking temperature/holding time and ceramization temperature/holding time.

Denomination	Atmosphere	Crosslinking		Ceramization	
		Temperature (°C)	Time (h)	Temperature (°C)	Time (h)
SiCN 700	argon	250	3	700	3
SiCN 800	argon	250	3	800	3
SiCN 900	argon	250	3	900	3
SiCN 1100	argon	250	3	1100	3
SiCN 1400*	argon	250	3	1400	3
SiCN 900-AV	argon - vacuum	250	3	900	3
SiCN 900-V	vacuum	250	3	900	3
SiCN 900 – 2% DBE	argon	250	3	900	3
SiCN 900 – 4% DBE	argon	250	3	900	3
SiCN 900 – DRY	argon	250	3	900	3

** Pyrolysis of SiCN 1100 and subsequent thermal treatment in argon at 1400 °C for 3 h.*

CO_2 adsorption measurements were performed at 0 and 25 °C by an ASAP-2000 automated volumetric analyser (Micromeritics, USA) using the same outgassing procedure mentioned for N_2-adsorption.

An X-ray powder diffraction was performed on the prepared powders using a STOE STADI P (STOE, Germany) equipped with monochromatic Mo-K_α radiation in transmission geometry using capillaries and flat-sample configuration.

Micro-Raman spectra were recorded with the confocal micro-Raman spectrometer Horiba HR 800 (Horiba, Japan), using an Ar-Ion laser with the wavelength of 514.5 nm. Spectra were recorded in the Raman shift range from 0 to 4000 cm^{-1}.

Transmission electron microscopy (TEM) studies were performed with a 200 kV electron microscope (JEOL JEM-2100) with an ultra-resolution pole piece (Cs = 0.5 mm) and a Schottky field-emission gun. Bright-field (BF) and high-resolution TEM (HRTEM) images were recorded by a CCD camera (Gatan Ultrascan 1000). High-angle annular dark-field scanning transmission electron microscopy (HAADFSTEM) was performed in the same operated microscope. The HAADF-STEM images were recorded by the JEOL ADF detector. The camera length was 8 cm and the incident beam probe size was ~0.2 nm.

For electrochemical testing, the prepared powders were mixed with 5 wt.% of Carbon Black Super P® (Timcal Ltd., Switzerland) as conducting additive and 10 wt.% of polyvinylidene fluoride (SOLEF® PVDF, Solvay, Germany) dissolved in N-methyl-2-pyrrolidone (NMP, BASF, Germany) as a binder. Additional NMP was added to adjust the viscosity of the mixture. The obtained slurry was printed on the rough side of a copper foil (10 μm, Copper SE-Cu58 (C103), Schlenk Metallfolien, Germany) by doctor blade technique and dried at 40 °C for 24 h. Electrodes of 10 mm diameter were cut out of the coated copper foil and dried at 80 °C under vacuum in a Buchi oven for 24 h. The dried electrodes were transferred without further contact with air to a glove box (MBraun, Germany) for cell assembly (Swagelok® type cell). The counter/reference electrode with a diameter of 10 mm was cut out of a metallic lithium foil (99.9% purity, 0.75 mm thickness, Alfa Aesar, Germany). QMA (Whatmann TM, UK) was used as a separator. As electrolyte 180 μL of 1M $LiPF_6$ dissolved in EC:DMC-1:1 (Solvionic, France) was used. For gravimetric capacity calculation, the mass of active material was used. The active electrode mass excludes the mass of the carbon black and PVDF used in electrode preparation. The testing was performed with the VMP multipotentiostat (BioLogic Science instruments, France) at the charging/discharging rate of 18 $mA\cdot g^{-1}$ to about 2 $A\cdot g^{-1}$ between 0.005 and 3 V.

3.2.2. Results and discussion

The method developed

Figure 10 shows a schematic representation of the new synthesis which results in highly porous carbon-rich SiCN ceramic. Perhydropolysilazane (PHPS), divinylbenzene (DVB), and di-n-butyl ether (DBE) are used as the starting reaction mixture. The hydrosilylation reaction at 120 °C in the presence of Karstedt`s catalyst leads to a solid, crosslinked preceramic. The ceramics with mixed micro/meso/macroporosity are obtained after the thermal treatment at $T > 700$ °C. The adsorption/desorption isotherms (nitrogen, -196 °C) together with the calculated cumulative pore volume/pore size distribution vs. pore diameter of the samples pyrolysed at 500, 700, 800, 900, 1100 and 1400 °C are presented in Figure 11. The samples are denoted SiCN T_{pyr}, for details please refer to the Table 2 in the experimental section. Table 3 summarises the specific porosity data measured by means of N_2-adsorption and calculated using Brunauer, Emmett and Teller (BET) approach and t-method. The N_2-adsorption isotherms (Figure 11ab) indicate the mainly mesoporous character of all materials according to the IUPAC classification [204]. The N_2 uptake above $P/P_0 = 0.9$ reveals the presence of large meso-and macro-pores. The absence of a well-defined saturation plateau is attributed to the porosity generated by the agglomeration of the powdered sample. The high specific surface area (SSA) of 504 $m^2\cdot g^{-1}$ of SiCN 500 is rationalized by the presence of micopores (≤ 2 nm) as indicated by the t-method and by the large amount of small mesopores. The organic-to-inorganic transformation at temperature beyond 700 °C leads to the partial/complete closure of the micropores and the corresponding decrease of the SSA down to 169 $m^2\cdot g^{-1}$ at 900 °C. Small mesopores (< 4 nm) remain stable throughout the pyrolysis process up to 1100 °C and do not sinter as shown by the pore size distribution (PSD) curves (Figure 11cd) and the stable total pore volume (TPV) values (Table 3). The sintering of small mesopores occurs at 1100 °C as indicated by the further decrease in the SSA (104 $m^2 \cdot g^{-1}$) and the TPV. Increasing the pyrolysis up to 1400 °C leads to a carbothermal reaction followed by the significant increase in the SSA (446 $m^2 \cdot g^{-1}$), TPV and the micropore volume (Table 3). Nevertheless, it should be noted that the carbothermal reaction results in a porosity present in the free carbon phase, whereas at lower T_{pyr} the pores are localized in the ceramic. Figure 12a shows the comparison of the N_2-adsorption isotherms of SiCN 900 and SiCN 900-DRY synthesized with and without DBE in starting polymer mixture, respectively. SiCN 900-DRY shows a nonporous character with the SSA of 13 $m^2 \cdot g^{-1}$ (Table 3), while in the presence of DBE the mesoporous ceramic is obtained. Figure 12b shows the comparison of the N_2-adsorption isotherms and cumulative pore volume curves (insert) of the ceramics obtained at the pyrolysis temperature of 900 °C with a different concentration of the DBE in the starting reaction mixture (SiCN 900-2% DBE and SiCN 900-4% DBE). Both ceramics present entirely different textures in comparison to the material prepared in diluted conditions SiCN 900, Figure 12bd. The N_2 adsorption isotherms of SiCN 900-2% DBE and SiCN 900-4% DBE indicate the absence of macropores/large mesopores (no N_2 uptake after $p/p_0 = 0.9$). Only small mesopores (< 4 nm) contribute to the TPV of SiCN 900-2%DBE, as shown in the cumulative pore volume graph. The presence of micropores is also confirmed (Table 3) in line with the SSA of 72 $m^2 \cdot g^{-1}$. SiCN 900-4% DBE displays the increase of the SSA to 143 $m^2 \cdot g^{-1}$ and in the micro-/mesopore volume. Thus, the simple change in DBE concentration provides a powerful tool to tailor the ceramic microstructure and opens the possibility to influence pore size and hierarchy.

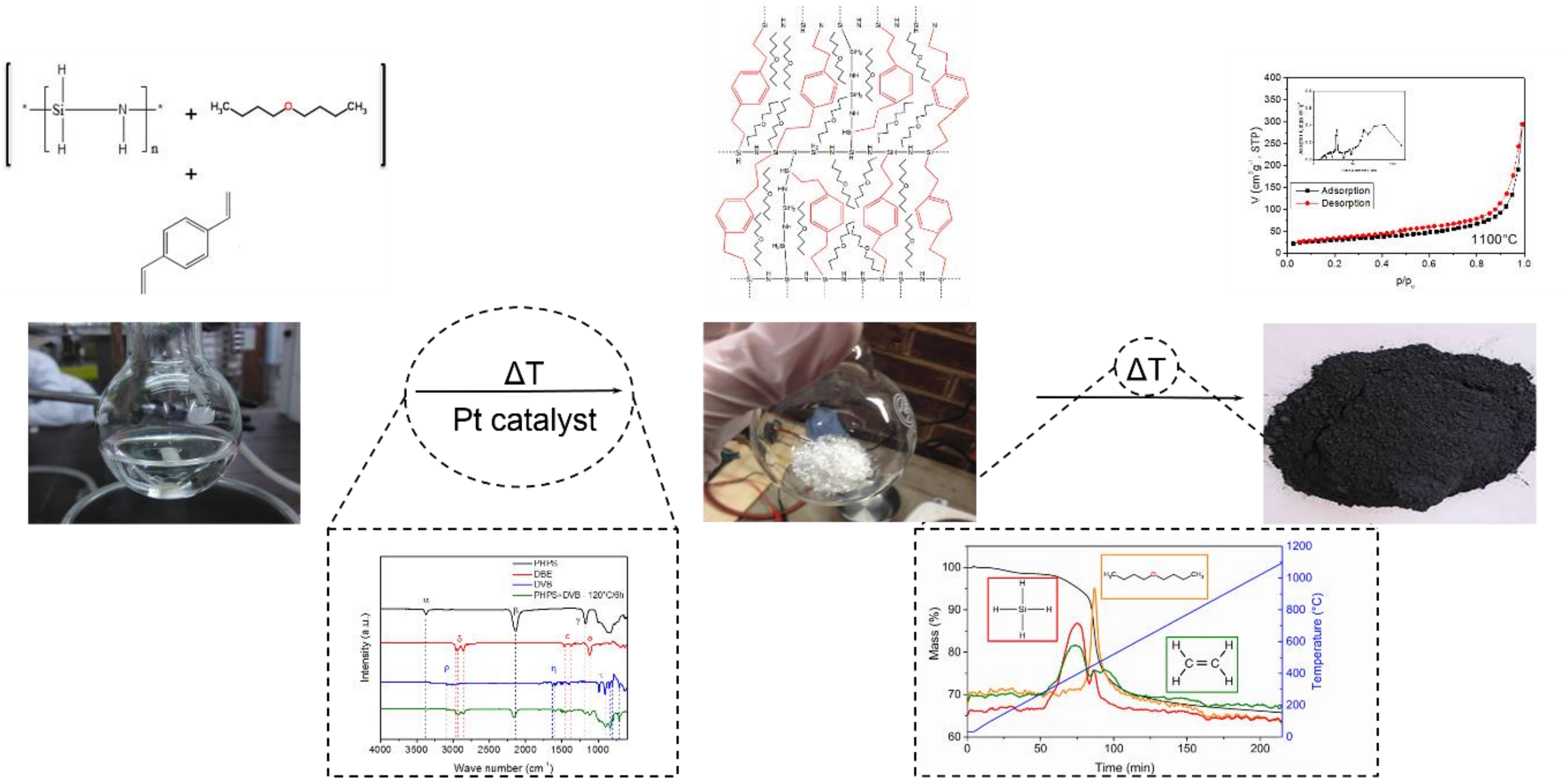

Figure 10: Schematic representation of the synthesis procedure yielding highly porous carbon-rich SiCN ceramic. The reaction mixture consisting of perhydropolysilazane (PHPS), divinylbenzene (DVB), and di-n-butyl ether (DBE) are used as the starting point. The hydrosilylation reaction is carried at 120 °C in the presence of Karstedt`s catalyst and monitored by FTIR analysis. The obtained solid, crosslinked preceramic is pyrolysied at T > 700 °C in order to obtain micro/meso/macroporous ceramic. Pore formation and role of DBE is assessed by TGA coupled with FTIR spectroscopy.

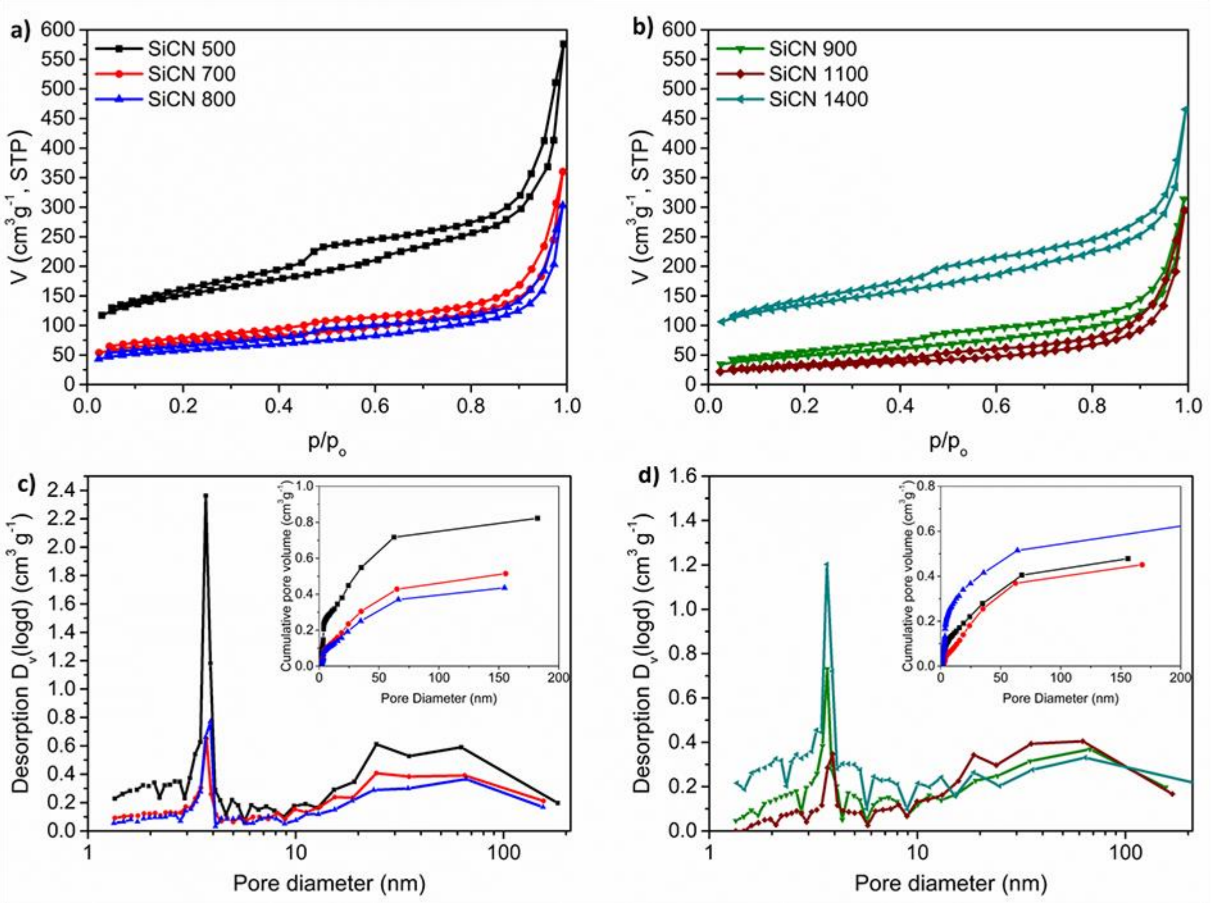

Figure 11: Evolution of porosity with the pyrolysis temperature. (a,b) Nitrogen physisorption measurements of SiCN ceramics obtained after pyrolysis at 500, 700, 800, 900, 1100 and 1400 °C. The N_2-adsorption isotherms indicate the mainly mesoporous character of all materials. The N_2 uptake above $P/P_0 = 0.9$ reveals the presence of large meso-and macropores in all samples. (c,d) The calculated cumulative pore volume/pore size distribution vs. pore diameter curves highlight the stable porosity over the entire range of pyrolysis temperatures.

Table 3: Overview of the specific porosity data measured by N_2-adsorption and calculated using Brunauer, Emmett and Teller (BET) approach, Barrett, Joyner and Halenda (BJH) and t-method.

Sample	SSA (m^2/g)	Total Pore Volume (cm^3/g)	Micropore Volume (cm^3/g)	Isotherm Type	Pore Diameter (nm)
SiCN 500	504	0.90	0.08	IV	3.7
SiCN 700	235	0.56	0.01	IV	3.7
SiCN 800	194	0.47	0.01	IV	3.9
SiCN 900	169	0.48	0	IV	3.6
SiCN 1100	104	0.46	0	IV	3.9
SiCN 1400	446	0.72	0.10	I/IV	3.6
SiCN 900 – 2% DBE	72	0.07	0.03	I/IV	4.0
SiCN 900 – 4% DBE	143	0.16	0.06	IV	3.7
SiCN 900 - DRY	13	0	0	-	-
SiCN 900 - AV	125	0.47	0	IV	3.7
SiCN 900 - V	72	0.1	0.02	I/IV	3.4

Figure 12c presents the N_2-adsorption isotherms and the cumulative pore volume curves (insert) recorded for a sample entirely pyrolyzed under vacuum (SiCN 900-V) and a sample hat-treated under argon up to 500 °C and then pyrolyzed under vacuum (SiCN 900-AV). Vacuum applied to the entire process of the pyrolysis leads to a significantly reduced amount of large meso- and macro-pores and to a formation of micropores (Table 3, Figure 12d). The amount of small mesopores is barely influenced. On the contrary, switching to vacuum first at 500 °C does not significantly influence porosity, namely only a slight decrease in the amount of small mesopores is detected, resulting in the decrease of SSA from 169 $m^2 \cdot g^{-1}$ for SiCN 900 to 125 $m^2 \cdot g^{-1}$ for SiCN 900-AV, while large meso- and macro-pores stay unaffected (Figure 12d). It signifies that the pore formation takes place mainly below 500 °C. This finding provides an important hint regarding the understanding of the mechanism of pore formation which is addressed in the next chapter.

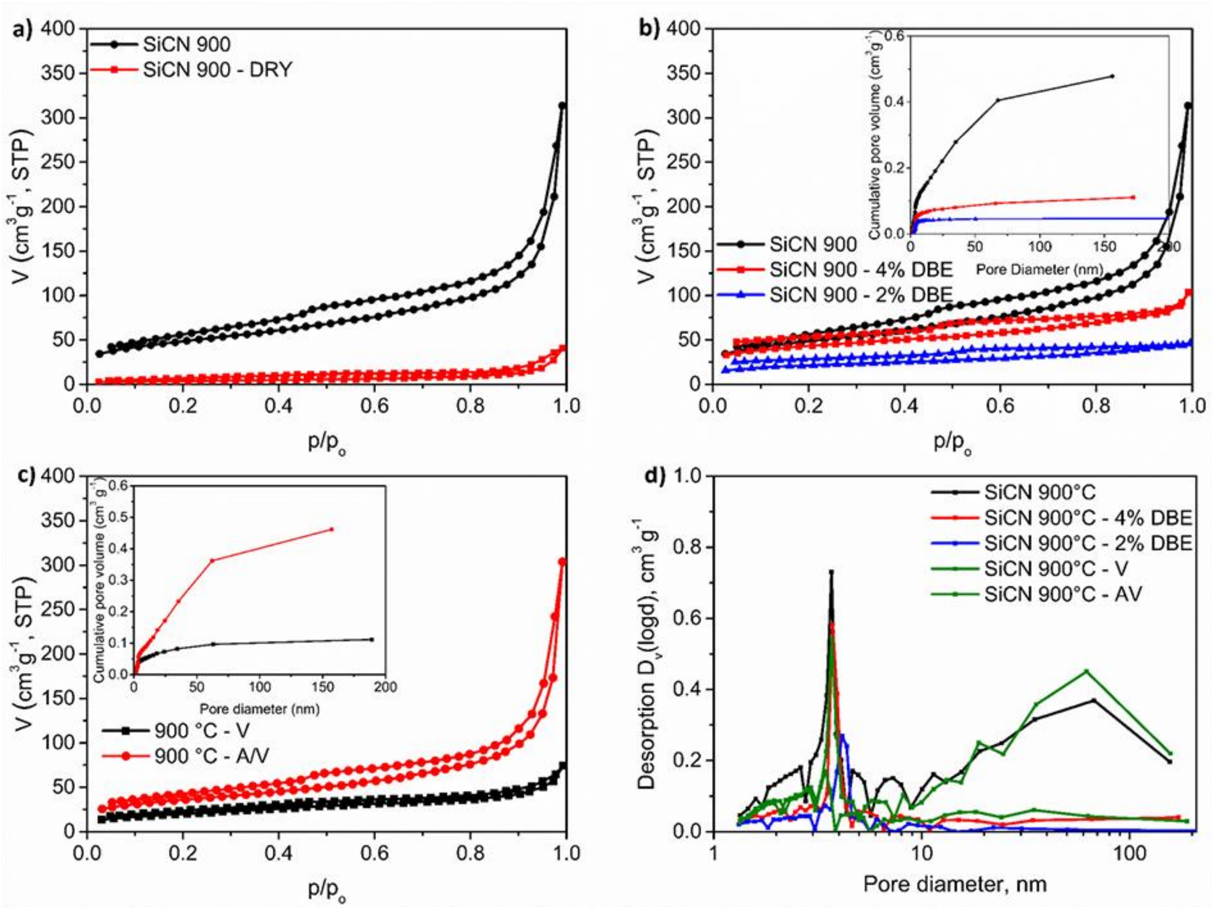

Figure 12: Influence of DBE concentration and pyrolysis atmosphere on porosity characteristics. (a) Nitrogen adsorption isotherms of SiCN 900 and SiCN 900-DRY synthesized with and without DBE in the starting polymer mixture display significant difference in porosity. SiCN 900 shows mesoporous character while SiCN 900-DRY is dense. (b) Nitrogen adsorption isotherms together with cumulative pore volume curves show a clear dependence of the final porosity on the DBE concentration. Macropores/large mesopores are absent in SiCN 900-2% and SiCN 900-4% DBE. c) N_2-adsorption isotherms and the cumulative pore volume curves recorded for a sample entirely pyrolyzed under vacuum (SiCN 900-V) and a sample heat-treated under argon up to 500 °C and then pyrolyzed under vacuum (SiCN 900-AV). Pyrolysis under vacuum exclusively leads to a significantly reduced amount of large meso- and macropores and to the formation of micropores. (d) Comparison of pore size distribution (PSD) curves underlying the potential of the invented method to tailor the porosity by varying the DBE concentration/pyrolysis atmosphere.

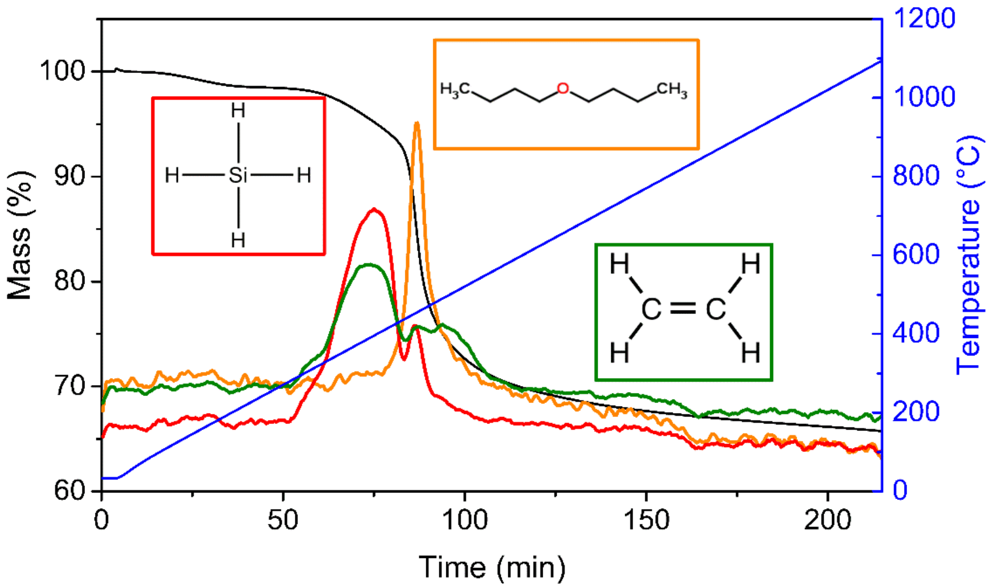

Figure 13: Elaboration of the preceramization mechanism in the presence of DBE. TGA coupled with FTIR spectroscopy is performed on the thermally crosslinked (250 °C for 3h) preceramic gel in order to monitor the preceramization. The thermal evolution of the crosslinked polymer starts at 400 °C, accompanied by degassing of SiH_4 and C_2H_4. DBE quits the system at 450 °C, namely the temperature 300 °C higher than its boiling point, leading to a major mass loss.

Mechanism

The analysis of specific data regarding the porosity of the samples prepared at various conditions provides an indication that the thermal treatment below 500 °C in the presence of DBE leads to the stable porosity of the ceramic at higher temperatures of pyrolysis. We analysed the conversion from polymer to ceramic in the presence of DBE by means of Fourier transformed infrared spectroscopy (FTIR) and thermogravimetric analysis (TGA) combined with FTIR in order to get the insights into the mechanism of pore formation.

In order to monitor the process of preceramization and to assess the pore formation, TGA coupled with FTIR spectroscopy is performed on the thermally crosslinked (250 °C for 3h) preceramic gel (Figure 13). Besides the loss of mass, the temperature program and integrated FTIR signals for SiH_4, DBE and C_2H_4 are displayed, in dependence of the measured time, and shown in Figure 13. The TGA shows the first minor mass loss around 200 °C (~2%), attributed to the CO_2 desorption from the sample. Note that no degassing of DBE (boiling point 141 °C) is recorded. The thermal evolution of the crosslinked polymer starts at 400 °C, accompanied by degassing of SiH_4 and C_2H_4, as confirmed by FTIR. The grafted divinylbenzene groups (vinyl units bonded to one Si atom) are partially eliminated in this temperature range [107, 139]. These gaseous species originate from the opening of the crosslinked preceramer structure as shown by the integrated FTIR data (Figure 13). ***First at 450 °C, namely the temperature 300 °C higher than its boiling point, DBE quits the system, leading to a major mass loss (~18%).*** The further increase in the temperature of pyrolysis leads to a slow but continuous mass loss (~8%) up to 800 °C due to degassing of C_2H_4, SiH_4 and DBE.

Ex-situ FTIR spectra of the pure polymer precursor, crosslinking agent DVB, DBE together with reaction products are recorded in order to follow the hydrosilylation reaction (Figure 14a). The main adsorption bands of the spectra are labelled with Greek letters and listed in Table 4. The characteristic bands of the "as-received" chemical precursors are in good agreement with their chemical structure shown in Figure 10. The FTIR spectrum of a chemically reacted intermediate shows the presence of residual Si-H (2140 cm^{-1}) and N-H (1170 cm^{-1}) units despite the stoichiometric amounts of the substrates used. This indicates an incomplete hydrosilylation reaction, explained by a steric hindrance [242, 243]. However, a considerable decrease in the intensity of Si-H, N-H and C=C vibrations confirms the occurrence of the hydrosilylation reaction. The chemically reacted intermediate was subjected to pyrolysis with additional crosslinking step at 130 or 250 °C for 3 h. FTIR spectra were recorded after crosslinking steps at 130 and 250 °C as well as at 500 and 900 °C, in order to follow the thermal evolution of the chemically reacted intermediate. The spectrum of the sample crosslinked at 130 °C shows no significant changes compared to the chemically reacted PHPS-DVB (Figure 14b). Crosslinking at 250 °C leads to a decrease in the intensities of the Si-H, N-H and C=C bands, confirming a more advanced hydrosilylation reaction in comparison to the material crosslinked at 130 °C. The SiCN 500 reveals low intensity bands around ~3000 cm^{-1} and ~1580 cm^{-1} originating from remaining hydrocarbons. The N-H (~3370 cm^{-1}) and Si-H (~2150 cm^{-1}) bands decrease further but do not vanish due to the steric hindrance impeding the reaction. The broad region of overlapping bands below 1100 cm^{-1} increases further, indicating the ongoing ceramization. Note that the vibration bands arising from di-n-butyl ether functional groups diminish when thermal crosslinking in tubular furnace is done at 130 °C. However, they are still present at 250 °C. Furthermore, the presence of DBE traces in the sample thermally treated at 500 °C could be observed by the low intensity bands at ~1130, ~1370 and ~2970-2870 cm^{-1}. We attribute the presence of DBE in the material at 500 °C (360 °C above boiling point) to a trapping of the solvent during the chemical reaction of the preceramic polymer with DVB, leading to the solvent encapsulation in the three-dimensional preceramer structure. The release of DBE takes place only after the crosslinked structure breaks due to undergoing ceramization. We suggest that at temperatures higher than DBE boiling point conditions close to supercritical are generated by encapsulated gaseous DBE, which in turn leads to a much higher stability of the produced porosity.

At 900 °C no bands originating from N-H, Si-H nor DBE are identified by FTIR. Remaining bands from the carbon and the silicon network are overlapping in the region below 1600 cm^{-1}. No chemical reaction between polymer/crosslinking agent and DBE takes place since no oxygen-containing bands are identified in the SiCN 900 by means of FTIR, despite the use of the oxygen containing solvent. The absence of chemical interaction is also confirmed by the fact that DBE quits the system as an entire molecule, not decomposed into fragments (see TGA-FTIR analysis). The chemically inert nature of DBE with respect to PHPS/DVB opens a variety of possibilities to tailor the chemical composition of porous ceramic while tuning the composition of a crosslinking agent/preceramic polymer.

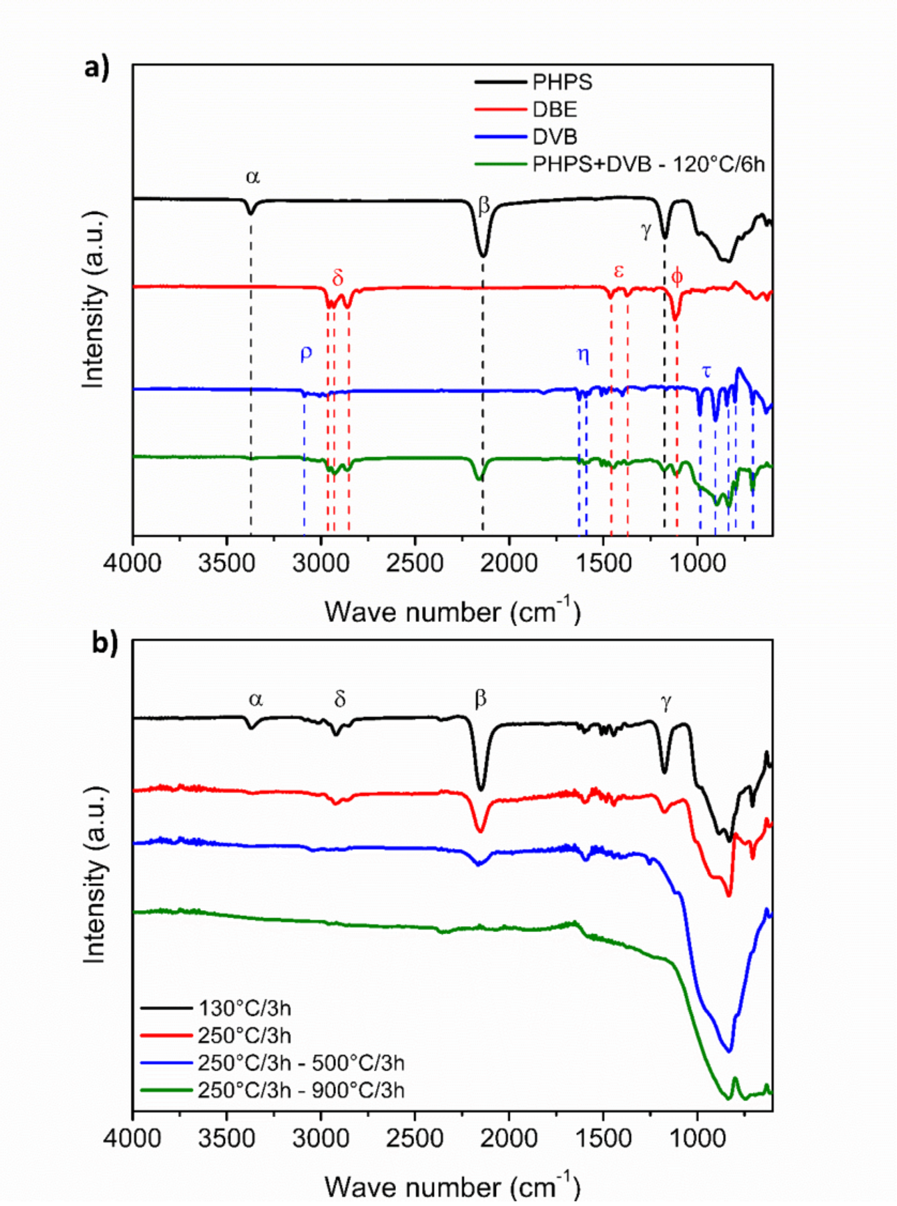

Figure 14: Hydrosilylation reaction monitored by *ex-situ* FTIR analysis. (a) FTIR spectra of the pure polymer precursor, crosslinking agent DVB, DBE together with reaction products. The characteristic bands of the "as-received" chemical precursors are in good agreement with their chemical structure. An incomplete hydrosilylation reaction is shown by the presence of residual Si-H and N-H units in the FTIR spectrum of a chemically reacted intermediate. (b) FTIR spectra of the chemically reacted intermediate after crosslinking steps at 130 and 250 °C as well as at 500 and 900 °C. Presence of the Si-H, N-H and C=C bands at 130, 250 and 500 °C indicates an incomplete hydrosilylation reaction, rationalized by a steric hindrance. At 900 °C no bands originating from N-H, Si-H nor DBE are identified by FTIR indicating ongoing ceramization.

Table 4: Overview of the bands observed by FTIR analysis with bond type and originating substance corresponding to Figure 14.

Wave Number (cm^{-1})	Label	Bond Type [244-246]	Substance
~ 3370	α	N-H	PHPS
~ 2140	β	Si-H	PHPS
~ 1170	γ	N-H	PHPS
~ 995		Si-N	PHPS
~ 2970 – 2870	δ	C-H (stretch)	DBE
~ 1465	ε	$-CH_2-$ (bend)	DBE
~ 1370	ε	$-CH_3$ (bend)	DBE
~ 1130	Φ	C-O-C	DBE
~ 3090 – 2970	ρ	$R-HC=CH_2$ (stretch) aromatic ring	DVB
~ 1630 – 1400	η	C=C $R-HC=CH_2$ aromatic ring	DVB
~ 990, ~ 905	τ	$R-HC=CH_2$	DVB

The microstructure of porous ceramic

HAABF (high-angle annular bright-field)-STEM micrographs of SiCN 800 and SiCN 1100 are presented in Figure 15ab respectively. The intensity/contrast in HAABF-STEM image can be correlated to local chemical composition or variation in thickness. Micrographs presented in Figure 15 show noticeable contrast variations indicating highly developed sample texture. The lack of clear difference between the two samples confirms the presence of stable porosity at 1100 °C, as observed in N_2-adsorption measurements.

Figure 15c presents a TEM micrograph of sample SiCN 1100. The segregation of partially ordered carbon (also shown by well-defined D and G Raman bands, Figure 16) is clearly visible on the surface of the amorphous ceramic. This finding is consistent with the X-ray diffraction study (Figure 17), revealing no reflexes for materials pyrolyzed below 1300 °C. At 1400 °C, a carbothermal reaction takes place and the first reflexes corresponding to ß-SiC are identified (Figure 17). For the detailed discussion on the Raman spectroscopy and X-ray diffraction results please refer to Chapter 3.2.5.

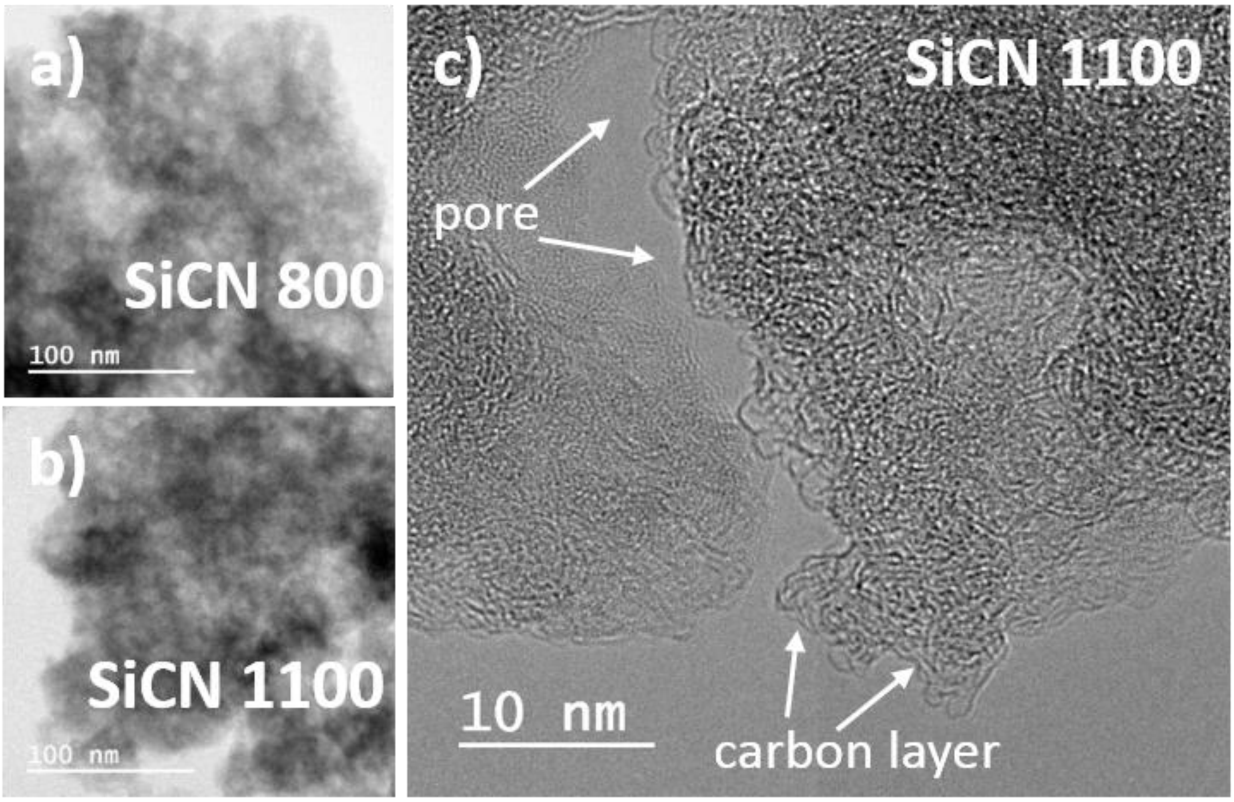

Figure 15: TEM micrographs of porous SiCN 800 and SiCN 1100 ceramics. (a,b) HAABF (high-angle annular bright-field)-STEM micrographs of SiCN 800 and SiCN 1100 indicate highly developed texture independent of the pyrolysis temperature. (c) TEM micrograph of SiCN 1100 showing the segregation of partially ordered carbon on the surface of amorphous ceramic and confirms the presence of stable porosity at 1100 °C.

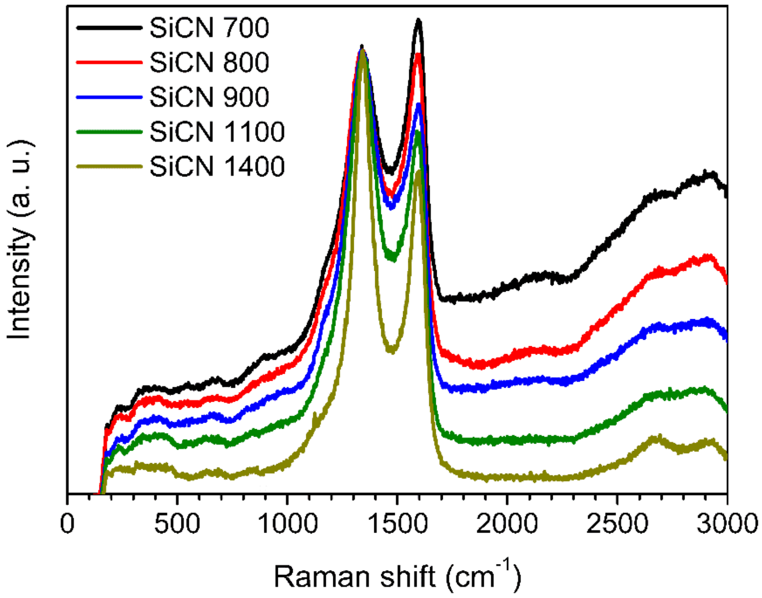

Figure 16: Evolution of Raman spectra with pyrolysis temperature. The results indicate that the carbon phase in SiCN ceramic matrix undergoes structural organization with increasing pyrolysis temperature.

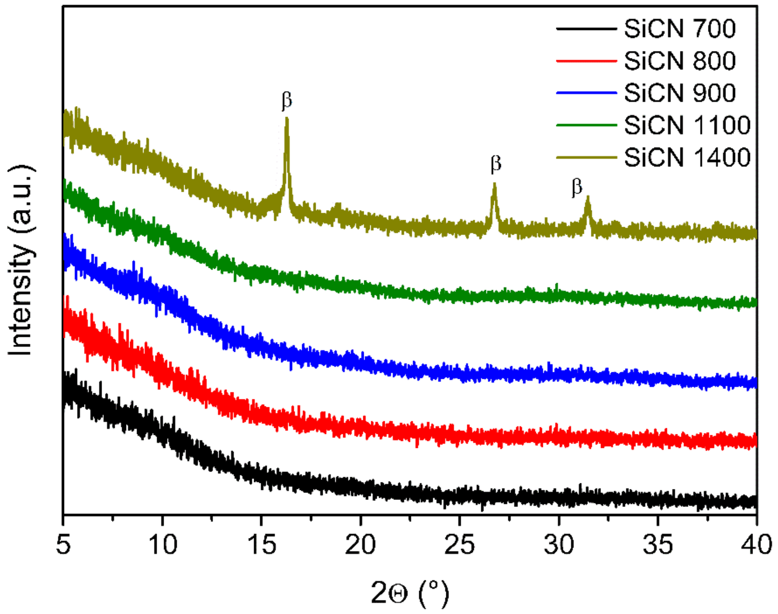

Figure 17: Evolution of the ceramic crystallinity with pyrolysis temperature. The X-ray diffraction patterns reveal the amorphous nature of the samples prepared at 700, 800, 900 and 1100 °C. At 1400 °C, crystallisation of ß-SiC occurred during the carbothermal reaction. Pronounced broadening indicates the presence of nano-SiC crystallites.

Stability of porous ceramics

Outburning

The carbon-rich SiCN ceramics have been subjected to thermal treatment at 600 °C in humid laboratory air (outburning) in order to assess the pore stability versus sintering and oxidation. The tests consisted of four heating cycles of 8, 8, 16 and 32 h with subsequent cooling to room temperature. The porosity was characterized by means of N_2-adsorption after each cycle and the results obtained are summarized in Figure 18. The microstructure of the outburned samples SiCN 800 and SiCN 1100 is presented in Figure 19.

Figure 18 presents the evolution of BET SSA, TPV and MPV with the time of outburning under ambient atmosphere for SiCN 800 and SiCN 1100. SiCN 1400 outburned for 8 h is shown as reference sample. SiCN 800 and SiCN 1100 demonstrate a significant increase in SSA, TPV and MPV due to carbon outburning within the ceramic. A corresponding decrease in carbon content is shown by the results of the elemental analysis, Table 5. The micropores in SiCN 1400 are located in the carbon phase which is oxidized during the process of outburning, thus SiCN 1400 after outburning shows a decrease in BET SSA and a complete closure of micropores. In SiCN 800 and SiCN 1100, porosity is present in the ceramic, thus outburning of the free carbon dispersed in the ceramic matrix leads to the increase in pore volume. For the possible material application in oxidative conditions, stable porosity is required underlining the importance of the stability of SiCN 800 and SiCN 1100. Their resistance against oxidation and sintering is further indicated by nearly constant BET SSA values up to 32 h at 600 °C. First after 64 h oxidative testing, a minor decrease in BET SSA, TPV and MPV has been found.

TEM micrographs (Figure 19) confirm the complete absence of segregated carbon on the surface of the ceramics. HAABF-STEM micrographs (Figure 19ab) present the highly developed texture of SiCN 800_O and SiCN 1100_O, similar to those of the materials before outburning (compare Figure 15). SiCN 1100 after outburning consists of 23 wt.% of SiC and 77 wt.% of SiO_2 as recalculated according to [128] from EA data, Table 5. ^{29}Si SSMAS NMR measurement of the outburned SiCN 1100 (insert Figure 19c) is in the full agreement with EA data, revealing only SiC_4 (< 30 ppm) and SiO_4 (~110 ppm) with no SiN_4 units present in the ceramic.

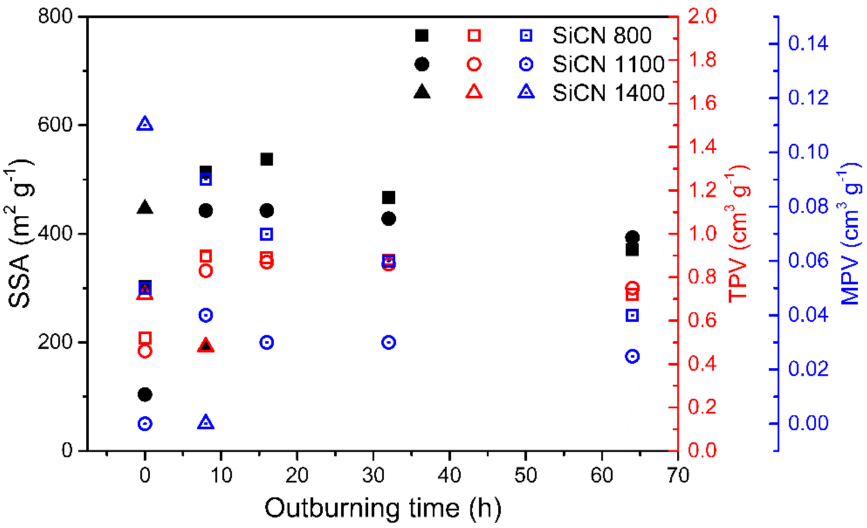

Figure 18: Oxidation stability of porous carbon-rich SiCN ceramics against outburning in air at 600 °C assessed by N_2-adsorption measurements. The tests consisted of four heating cycles of 8, 8, 16 and 32 h with subsequent cooling to room temperature. The evolution of BET SSA, TPV and MPV with the time of outburning under ambient atmosphere for SiCN 800 and SiCN 1100 is presented. SiCN 1400 outburned for 8 h is shown as reference sample. SiCN 800 and SiCN 1100 demonstrate a significant increase in SSA, TPV and MPV due to carbon outburning. Resistance against oxidation and sintering is indicated by nearly constant BET SSA values up to 32 h at 600 °C. First after 64 h oxidative testing, a minor decrease in BET SSA, TPV and MPV has been found. SiCN 1400 after 8h outburning shows a decrease in BET SSA and a complete closure of micropores.

Table 5: Oxidation stability of porous ceramics at 600 °C assessed by elemental analysis. Overview of the values obtained by elemental analysis for pristine and outburned samples.

Sample	**Nitrogen (wt.%)**	**Oxygen (wt.%)**	**Carbon (wt.%)**	**Si (wt.%)**
SiCN 800	12.1	2.0	49.7	36.2
SiCN 800 outburned	~1.0	50.5	< 1	47.5
SiCN 1100	11.0	6.5	49.4	33.1
SiCN 1100 outburned	~1.0	41.2	6.6	51.2

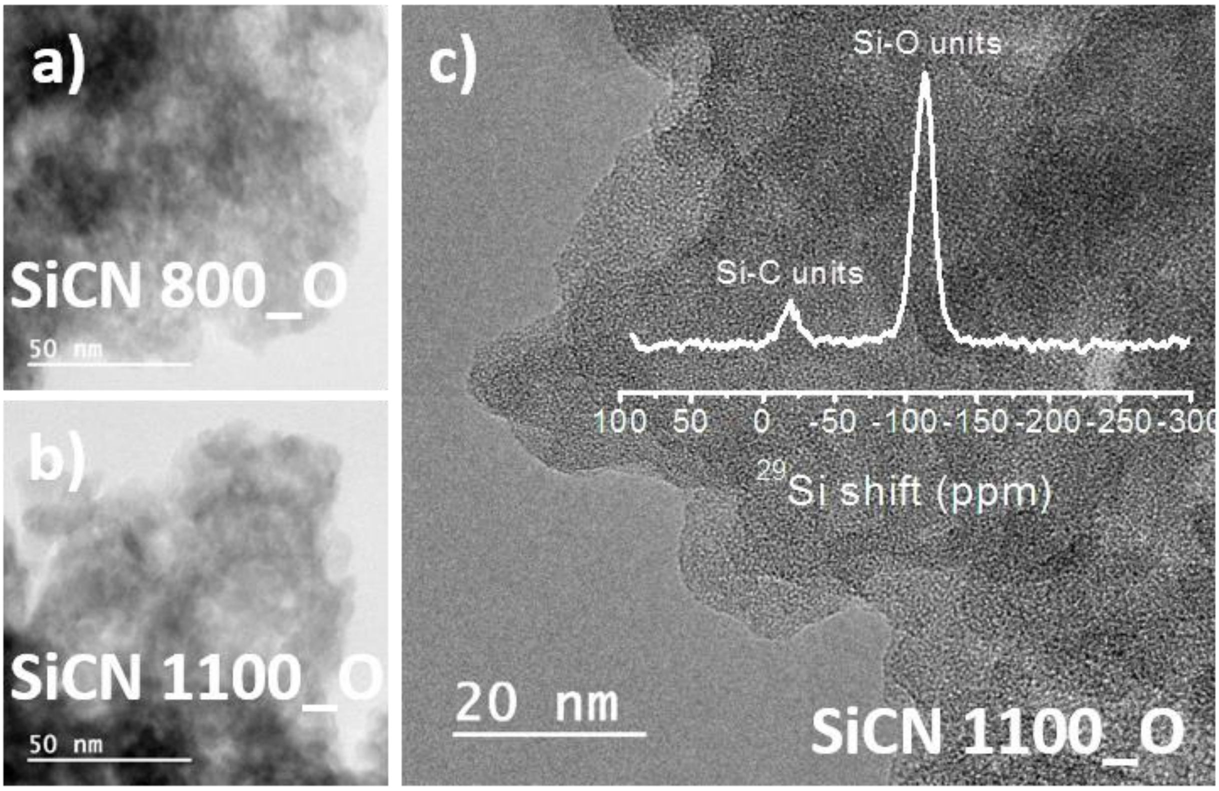

Figure 19: Oxidation stability of porous ceramics at 600 °C assessed by TEM and ^{29}Si SS NMR measurements. (a,b) HAABF (high-angle annular bright-field)-STEM micrographs of SiCN 800_O and SiCN 1100_O indicate a highly developed texture independent of the pyrolysis temperature and outburning time. This confirms the presence of stable porosity after 64 h of oxidative testing, as observed in N_2-adsorption measurements. (c) TEM micrograph of SiCN 1100_O shows no segregated carbon on the surface of the amorphous ceramic and confirms the presence of a stable porosity. ^{29}Si SSMAS NMR measurement of the outburned SiCN 1100 (insert) reveals only SiC_4 (< 30 ppm) and SiO_4 (~110 ppm) tetrahedra with no SiN_4 units present in the ceramic.

The stability of the SiCN 800 ceramic has been also examined upon prolonged (> 60 days) contact with humid ambient air. SiCN ceramics pyrolyzed at $T < 1000$ °C are prone to react with oxygen from atmospheric air upon prolonged exposition. The developed porosity of the material may enhance this process, and the presence of nitrogen in the ceramic is of crucial importance for the possible applications of the material, e.g. for CO_2 capture. Figure 20 shows the ^{29}Si NMR spectra of the SiCN 800 after both, short and prolonged exposition to ambient air. Due to the variety of the possible inner-substitutions in the vicinity of Si in the $Si(C_mN_nO_p)$ moieties, the deconvolution and detailed assignment of the NMR peaks are purely speculative. Thus, we attempt to generally address the structures present in the SiCN 800 together with their evolution with the exposition time. The NMR peak at δ_{Si} = -30 – -50 ppm is attributed to the nitrogen rich $SiCN_3$ - SiN_4 tetrahedra. The less negatives (0 – -30 ppm) shifts correlate strongly with the C content and are attributed to SiC_4 moieties. The more negatives NMR shift at -110 ppm corresponds to SiO_4 tetrahedra.

The signal of silicon coordinated with oxygen is already visible in the non-exposed sample, with 13.7 wt.% of SiO_2 calculated from the EA results (Table 5). This increase in oxygen content, in comparison to the pristine material with 3.8 wt.% of silica estimated by EA, originates from the long NMR measurements in the non-hermetically sealed rotor. In parallel, the amount of Si_3N_4 decreases from 30.2 to 26.4 wt.%. Prolonged exposition to air does not significantly affect the SiN_4 moieties, but rather lead to the transformation of Si-O-C units to SiO_4 tetrahedra.

Note, that the material pyrolyzed at 800 °C contains a variety of $Si(C_mN_nO_p)$ $(m+n+p=4)$ units. Nevertheless, the applied simplification allows for deriving general trends. The evolution of the composition with time of the exposition in air can be followed in Table 6.

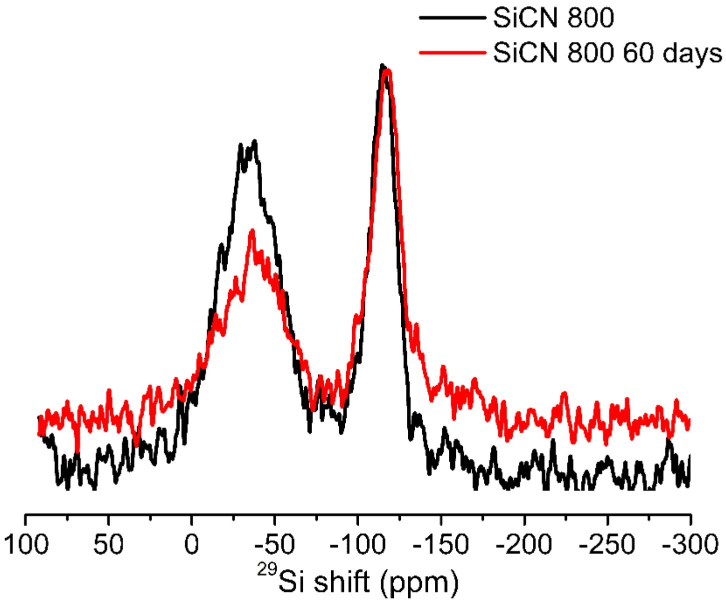

Figure 20: Oxidation stability of porous ceramics against ambient atmosphere assessed by ^{29}Si SS NMR measurements. The stability of the SiCN 800 ceramic has been examined upon prolonged (> 60 days) contact with ambient humid air. Apart from initial reaction with oxygen shown by the presence of SiO_4 (~110 ppm) units, no significant changes in the materials upon holding in air have been identified.

Table 6: Oxidation stability of porous ceramics at room temperature (elemental analysis). Overview of the values obtained by elemental analysis for pristine samples and those exposed to ambient humid air.

Sample	**SiO_2 (wt.%)**	**SiC (wt.%)**	**Si_3N_4 (wt.%)**	**C (wt.%)**
SiCN no air contact	3.8	23.2	30.2	42.8
SiCN 800 NMR	13.8	11.7	26.4	48.1
SiCN 800 3 days	22.7	9.3	23.5	44.5
SiCN 800 2 months	28.4	3.4	21.6	46.6

Applications

CO_2 capture

The CO_2 capture capacity is significantly enhanced by the presence of basic nitrogen-containing groups, together with hierarchical mesostructures, which include a high BET surface, a stable framework, and the presence of a large number of micropores as well as small amount of mesopores [219, 220, 231-233]. Thus the SiCN 800 ceramic has been examined with respect to the CO_2 capture. Figure 21 presents the CO_2 adsorption-desorption isotherm at 25 °C of SiCN prepared at 800 °C. 1.5 mmol CO_2 per gram of sorbent is adsorbed at 1 bar pressure. At 0 °C the adsorption equals 1.9 mmol CO_2 per gram of sorbent. These values are comparable with those reported for commercial carbons and zeolite frameworks [247, 248]. Note, that the adsorption and desorption branches of the isotherm overlap perfectly. It signifies the absence of irreversible reactions, namely no CO_2 chemisorption. This in turn confirms again the chemical stability of the investigated porous SiCN ceramic.

Electrochemical performance

The electrochemical performance of the selected samples is reported in Chapter 3.2.4. In this chapter the impact of the pyrolysis temperature on the electrochemical properties of porous carbon-rich polymer-derived silicon carbonitride (SiCN) ceramic was rationalised with respect to the microstructural evolution of the free carbon.

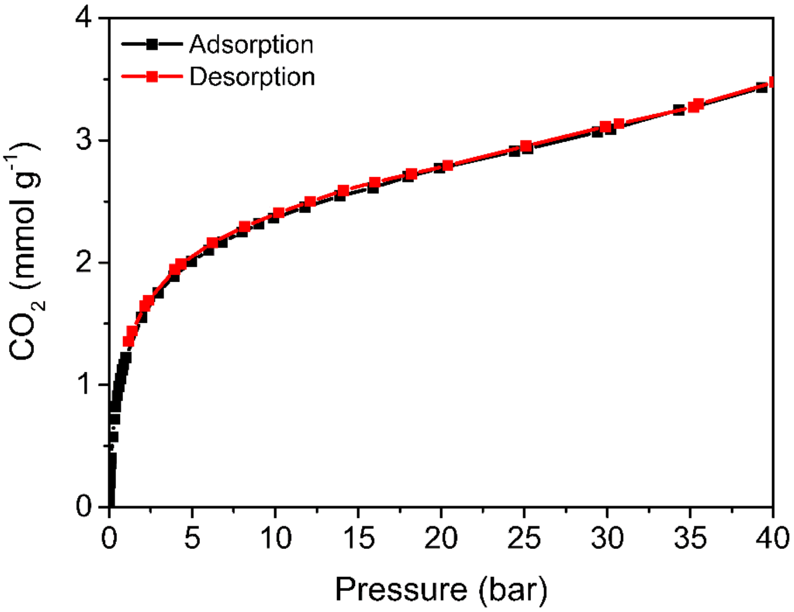

Figure 21: CO_2 capture capabilities of SiCN 800 at 25 °C. The adsorption and desorption branches of the isotherm overlap perfectly signifying the absence of irreversible reactions, e.g. CO_2 chemisorption.

3.2.3. Statement of personal contribution

[7] **D. Vrankovic**, M. Storch, C. Schitco, M. Graczyk-Zajac, R. Riedel, Solvent assisted synthesis of micro/mesoporous ceramics from preceramic polymers, German Patent registration DE 10 2016 116 732 A1.

The idea behind of this work was developed by myself and the unique synthesis procedure was filed as a patent. Most of the experimental work and data analysis was carried out by myself, except Thermogravimetric analysis (TGA) which was done by Dipl.-Ing. Claudia Fasel (AK Prof. Riedel) and Transmission electron microscopy (TEM) done by Ph. D. Cheuk-Wai Tai (Stockholm, Sweden).

3.2.4. The influence of the pyrolysis temperature on the electrochemical behaviour of porous carbon-rich SiCN polymer-derived ceramics

Within this Chapter, the impact of the pyrolysis temperature on the microstructural development and electrochemical properties of selected porous carbon-rich polymer-derived silicon carbonitride (SiCN) ceramics is addressed. The nature of the free carbon phase at each pyrolysis temperature is characterized in detail and correlated with Li-ion storage capabilities. In addition, the evolution of textural properties of investigated ceramic in line with its influence on the electrochemical lithium insertion/extraction are presented.

3.2.5. Results and discussion

Porous carbon-rich silicon carbonitride ceramics were prepared according to the method discussed in Chapter 3.2.1 at the pyrolysis temperature (T_{pyr}) of 900, 1100 and 1400 °C in argon atmosphere. Figure 22 presents the X-ray diffraction patterns revealing the amorphous nature of the samples prepared at 900 and 1100 °C. At 1400 °C a crystallisation of SiC is detected. Three broad reflexes (marked with ß in Figure 22) arising at 2Θ angles of 16.3, 26.7 and 31.4° are attributed to a β-SiC formed during carbothermal reaction. Pronounced broadening of the observed XRD reflections indicates small SiC crystallites caused by the ongoing crystallisation. The onset in crystallisation at 1400 °C is in good agreement with the former work of Mera et al. [139].

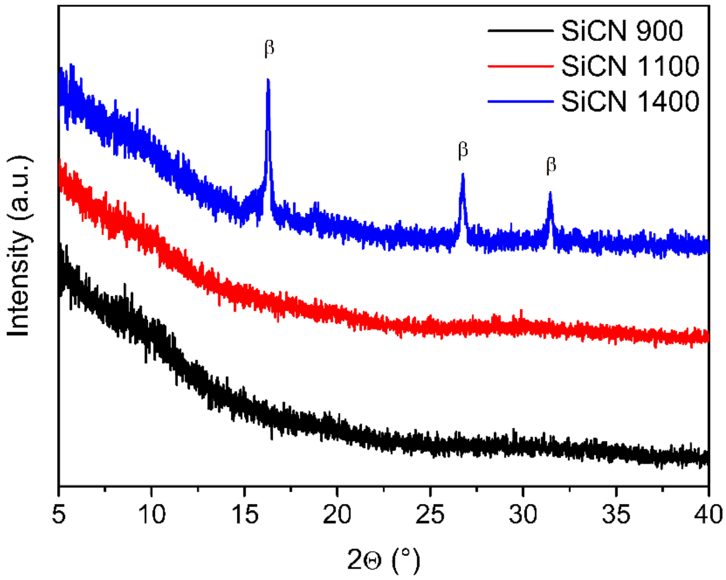

Figure 22: Crystallisation behaviour of the selected porous SiCN ceramics. The X-ray diffraction patterns reveal the amorphous nature of the samples prepared at 900 and 1100 °C. At 1400 °C a crystallisation of ß-SiC is detected. Reproduced from Ref. [6] with permission from the Solid State Ionics.

Nitrogen physisorption measurements reveal steady decrease in BET specific surface area (SSA) and total pore volume (TPV) with increasing T_{pyr} up to the temperatures the carbothermal reaction sets in. The carbothermal reaction leads to the partitioning and decomposition of Si-network causing the formation of new pores and implying the increase of SSA and TPV. However, this newly developed porosity is mainly located in the carbon phase. The detailed discussion on the porosity evolution with the pyrolysis temperature is included in the Chapter 3.2.2.

Raman spectroscopy was used to analyse microstructure of the carbon phase in the SiCN matrix for samples prepared at 900, 1100 and 1400 °C. Free carbon is considered as the major lithium storage site within the SiCN ceramic [161, 176, 188, 249, 250], thus, it is of great importance to understand evolution of its microstructure induced by change of the pyrolysis temperature. In the recorded spectra the D-band is the strongest band showing the disordered nature of the free carbon phase (Figure 23a). Figure 23b-d presents the deconvolution of the Raman spectra into G, D1, D2, D3 and D4 bands according to Sadezky et al. [251]. The less pronounced G-band together with strong D3-band suggest a highly amorphous nature of the carbon confirming the results obtained by X-ray diffraction studies. The observed shift of D3-band from ~1500 to ~1545 cm^{-1} suggests that the carbon phase consist of mixture of sp^2 and sp^3 bonded carbon as well as carbon bonded to silicon atoms [252]. With increasing pyrolysis temperature the D3-band decreases in intensity as shown by an increase of the I(D)/I(D3) ratio from 2.85 for the 900 °C sample to 3.95 for 1100 °C and 8.68 for the 1400 °C sample. In parallel, G-band increases in intensity with pyrolysis temperature as it is revealed by the decrease of the I(D)/I(G) ratio from 2.35 for the 900 °C sample to 1.95 for the 1100 °C and to 1.60 for the 1400 °C sample. Additionally the carbon cluster size L_a

increases from 1.87 nm for the 900 °C sample to 2.74 nm for the 1400 °C sample. These results indicate that with increasing pyrolysis temperature carbon phase in SiCN ceramic matrix undergoes structural organization as well as a loss of hydrogen [245, 253]. In consequence, higher organisations of carbon results in a decrease of available Li-ion storing sites and leads to lower overall capacities [159, 254].

In order to get an overview on the lithium storage properties of the porous SiCN ceramics, the samples pyrolysed at 900, 1100 and 1400 °C have been selected for electrochemical tests. Figure 24ab shows the extended cycling performance and the corresponding Coulombic efficiencies (CE) of investigated materials. Capacity losses and poor CE observed for all samples in the first few cycles are attributed to formation of solid electrolyte interface (SEI) and irreversible trapping of Li-ions in the porous structure. The SiCN 900 shows a steady increase of capacity up to 534 mAh·g^{-1}, which is rationalized by an enhanced storage due to an activation of the porous structure [255]. When pyrolysis temperature is increased to 1100 °C constant discharge capacities of 280 mAh·g^{-1} over hundred cycles are obtained. The sample prepared at 1400 °C shows a decrease in capacity until 40th cycle, followed by stable capacity of only 168 mAh·g^{-1}.

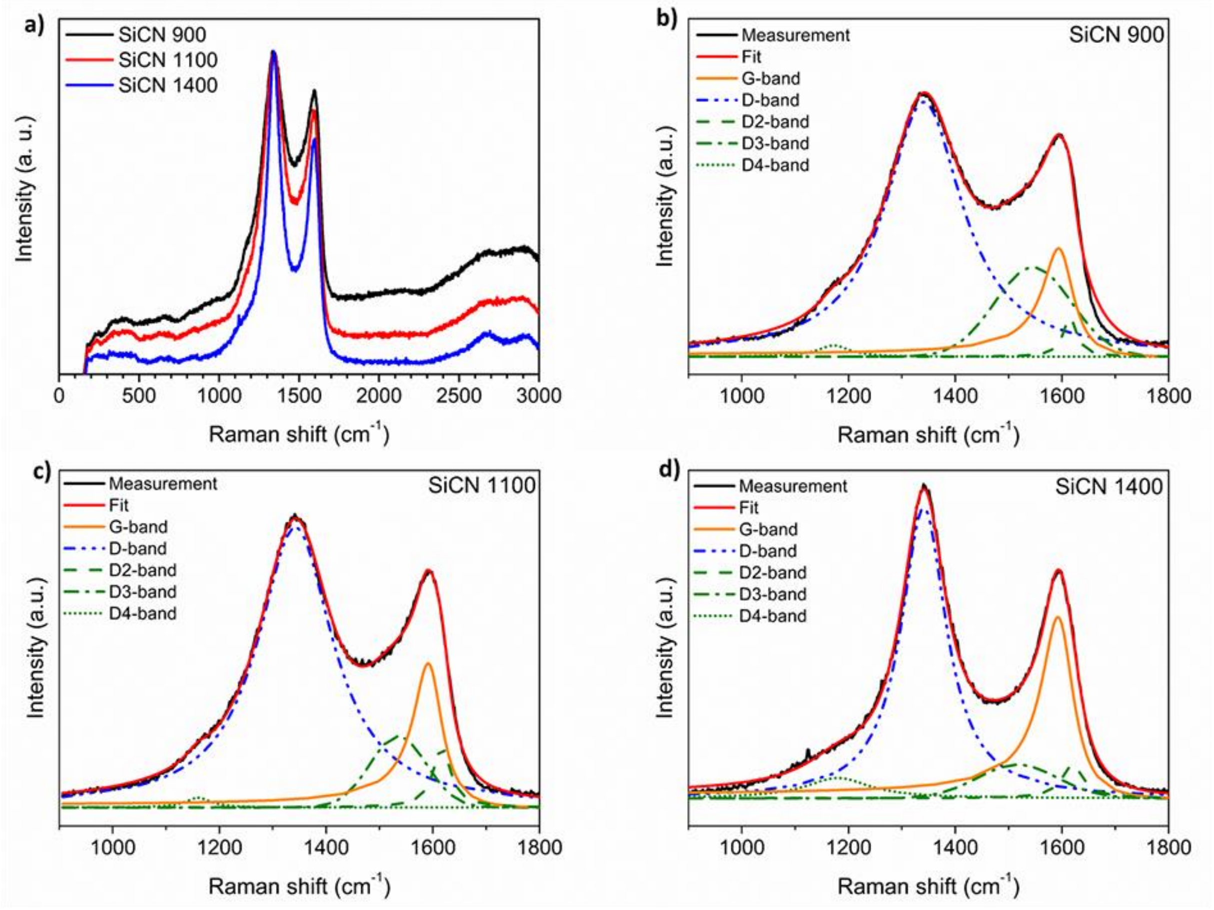

Figure 23: The microstructure of the carbon phase assessed by Raman spectroscopy. (a) Raman spectra of the samples pyrolyzed at 900, 1100 and 1400 °C. (b-d) The deconvolution of the Raman spectra into G, D1, D2, D3 and D4 bands according to Sadezky et al. [251]. Reproduced from Ref. [6] with permission from the Solid State Ionics.

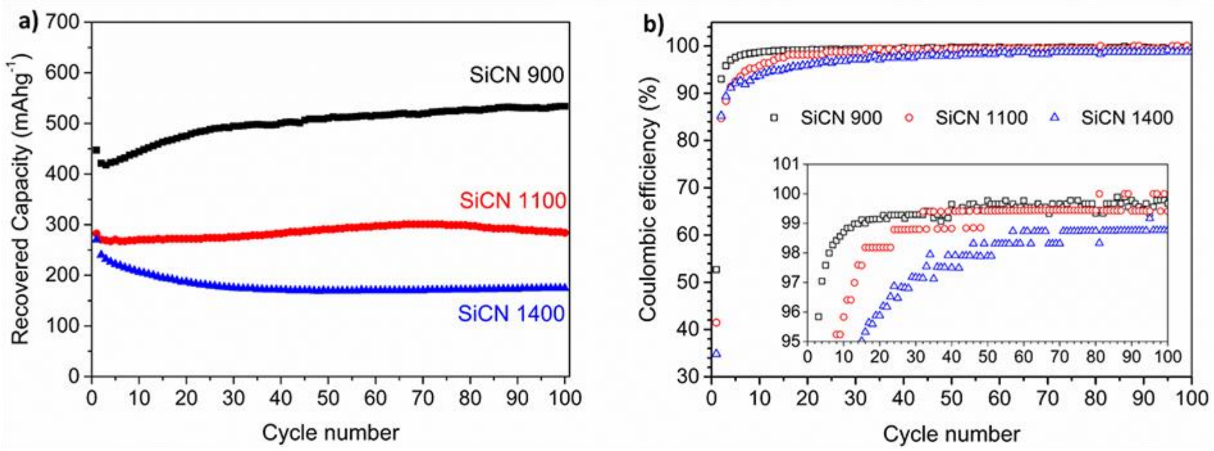

Figure 24: Extended cycling behaviour of the selected porous ceramics. (a) Constant current Li-ion insertion/extraction at 72 mA·g^{-1} of the samples pyrolyzed at 900, 1100 and 1400 °C. (b) Corresponding Coulombic efficiencies (CE). Reproduced from Ref. [6] with permission from the Solid State Ionics.

To evaluate the nature of the Li-ion uptake the first and the hundredth cycle voltage-profiles of investigated materials are presented in Figure 25. The first cycle lithiation capacity of 849 mAh·g^{-1}, the delithiation capacity of 477 mAh·g^{-1} and the corresponding Coulombic efficiency of 52.7% for SiCN 900 are in the range of the values reported for dense SiCN ceramics [250, 256, 257]. When the pyrolysis temperature is increased, the Coulombic efficiency decreases to 41.4% for the 1100 °C and to 30.9% for the 1400 °C sample. The low first cycle CE originate from SEI formation on the porous ceramic and the irreversible capture of lithium ions in the disordered carbon phase (compare Raman spectroscopy study) [161]. The decomposition of the electrolyte for all the samples starts during the first Li-ion uptake at the potential ~1.5 V, resulting in a sloping plateau below 1 V (Figure 25a). At voltages below 0.5 V mainly intercalation of Li-ions within the free carbon phase present in the SiCN microstructure takes place. The free carbon phase offers various Li-ion storage sites, namely intercalation between the carbon layers in the clusters, adsorption at the surface and the edges of carbon-crystallite and the lithiation of defect sites and pores [258, 259]. When the delithiation branch is considered, the first part (up to a potential of 1 V) is based on delithiation of the free carbon phase while the second part (1 to 3 V) corresponds to desorption of Li-ions from the surface and pores [260, 261]. A pronounced hysteresis for SiCN 900 is attributed to a high hydrogen content [262, 263]. However, increasing the pyrolysis temperature leads to lower hydrogen content but in the same time increases the organisation of the carbon phase resulting in lower specific capacity. Figure 25b shows voltage profiles of the 100th cycle where the lithiation branch has the typical sloping shape of porous disordered hydrogen-containing carbons [258, 261].

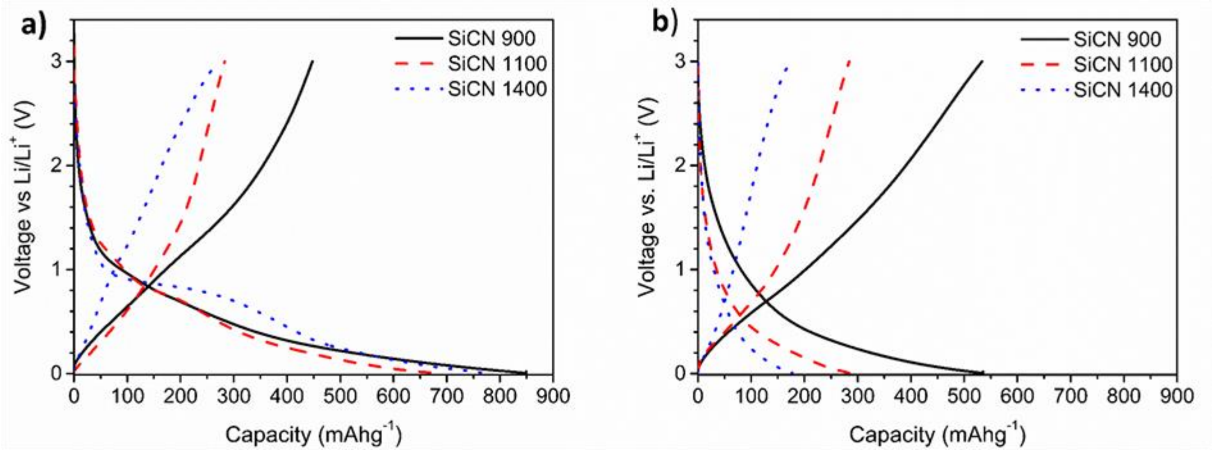

Figure 25: Insertion/extraction voltage-capacity transients. (a) Voltage profiles of the first cycles recorded for SiCN 900, 1100 and 1400. (b) The corresponding voltage profiles of the 100th cycle. Reproduced from Ref. [6] with permission from the Solid State Ionics.

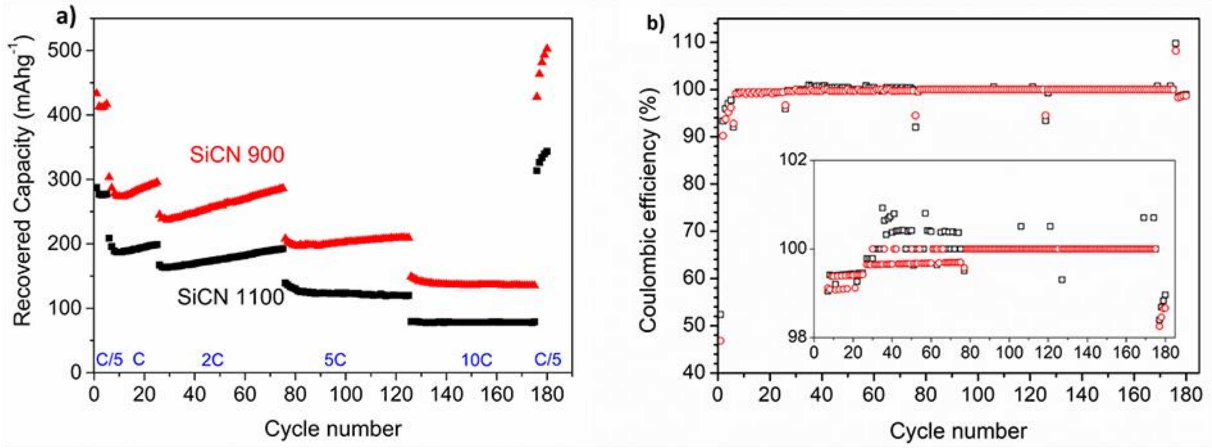

Figure 26: Electrochemical performance of the selected porous ceramics at various current densities. (a) The capacities recovered at different current densities by SiCN 900 and SiCN 1100. (b) The corresponding Coulombic efficiencies. Reproduced from Ref. [6] with permission from the Solid State Ionics.

In order to verify the storage stability of the porous ceramics rate capability tests were performed. Figure 26ab shows recovered capacities at different current densities and corresponding Coulombic efficiencies of SiCN 900 and SiCN 1100. At all current rates the ceramic obtained at 900 °C shows higher capacities than the 1100 °C sample. One should note that the stable retained capacity of 135 mAh·g^{-1} at the cycling rate of 10C (3720 mA·g^{-1}) is the highest ever reported in literature for any dense SiCN ceramic [264]. Such exceptional cycling stability and capacity at high current densities is rationalised by the introduction of the porosity and therefore shorter Li-ion diffusion path/faster ionic transport [265, 266].

Among the investigated samples, SiCN 900 demonstrated the best electrochemical performance. The lithium storage capacity tends to decrease significantly with the increasing pyrolysis temperature. This decrease is induced by the structural evolution of free carbon phase from highly disordered toward more organised configurations. Higher organisation of carbon supresses available Li-ion storing sites and, in consequence, leads to lower overall capacities. On another hand, higher T_{pyr} diminishes the hydrogen content and lowers the voltage hysteresis. At 1400 °C significant changes within the ceramic microstructure occur, the SiCN matrix undergoes solid state reaction with carbon forming electrochemically inactive SiC. Nevertheless, the porous samples SiCN 900 and SiCN 1100 show, in comparison to their dense analogues, improved high current-rate capabilities in terms of capacity and cycling stability. While the simple and facile synthesis route allows to produce large amounts of porous and carbon-rich SiCN ceramics rendering the investigated materials as a promising anode materials in LIBs.

3.2.6. Statement of personal contribution

[6] M. Storch, **D. Vrankovic**, M. Graczyk-Zajac, R. Riedel, The influence of pyrolysis temperature on the electrochemical behavior of porous carbon-rich SiCN polymer-derived ceramics, *Solid State Ionics* **315** (2018) 59.

The idea behind of this work was developed by myself. Most of the experimental work was carried out by M. Sc. Mathias Storch during his master thesis. M. Sc. Mathias Storch worked under my co-supervision during entire time. In particular, I supported N_2-physisorption measurements, XRD studies, Raman spectroscopy measurements, electrode processing, electrochemical measurements, as well as data evaluation and interpretation. The manuscript was written by M. Sc. Mathias Storch and revised by myself. Dr. Magdalena Graczyk-Zajac and Prof. Ralf Riedel revised and approved of the manuscript before publication.

4. Summary and Outlook

This PhD work has been focused on new materials with a tailored microstructure for the application in green energy technologies notably Li-ion battery- and CCS-technology. Polymer-derived SiCN/SiOC ceramics were employed to stabilize the silicon anode in Li-ion batteries during the lithiation/delithiation process. In particular, the influence of anode microstructure on the cycling behaviour of elemental silicon was investigated. Commercially available dense silicon nanoparticles coated with carbon and embedded in the SiCN matrix were electrochemically tested. The void space required for the accommodation of the silicon volume change during lithiation/delithiation was generated by out-burning of the carbon shell. Although this experiment resulted in only a minor improvement of the electrochemical performance, it provided critical guidelines for further experimental work.

Significant improvement has been achieved by tailoring silicon morphology. Magnesiothermic reduction of silica at 800 °C yielded silicon nanoparticles with highly open porosity and specific surface area in the range of 200 to 600 m^2g^{-1}. The carbon/SiOC protective layer, together with a void space located in the pores of Si, provided a dense stable shell around Si nanoparticles acting as a separation barrier for the electrolyte. This led to a stable SEI and resulted in constant capacities of 575 $mAh \cdot g^{-1}$ over 50 cycles and good Coulombic efficiencies.

A systematic screening of different compositions allowed us to identify the role of carbon and the ceramic contributing to the electrochemical performance. The carbon present in the pores and around Si particles enhanced the electrical conductivity and suppressed the agglomeration of primary silicon particles. The SiOC ceramic preserved the composite morphology and effectively separated Si from the electrolyte. The sole carbon shell did not provide sufficient protection of Si against the electrolyte, leading to low Coulombic efficiencies and the capacity fading with ongoing cycling.

Next, $AlCl_3$ assisted magnesiothermic/aluminothermic reduction of SiO_2 was applied at 220 °C, yielding highly porous Si. It simplified the synthesis of silicon significantly and made the overall procedure cost-effective and up-scalable. The highly porous silicon embedded in the C/SiOC matrix showed exceptionally high Coulombic efficiencies of 99.5%, and nearly 100% of capacity retention over more than 100 cycles. The rate capability tests confirmed remarkable stability despite the relatively high electrode mass loading of more than 2 $mg \cdot cm^{-2}$. Finally, the up-scaling potential has been demonstrated by using commercially available glass fibers as a precursor of porous Si. Extensive electrochemical tests revealed the outstanding performance of fiber-based composites with the Coulombic efficiency of 99.5%, and nearly 100% of capacity retention, see Figure 27. The excellent electrochemical performance was assessed by molecular dynamic (MD) simulations.

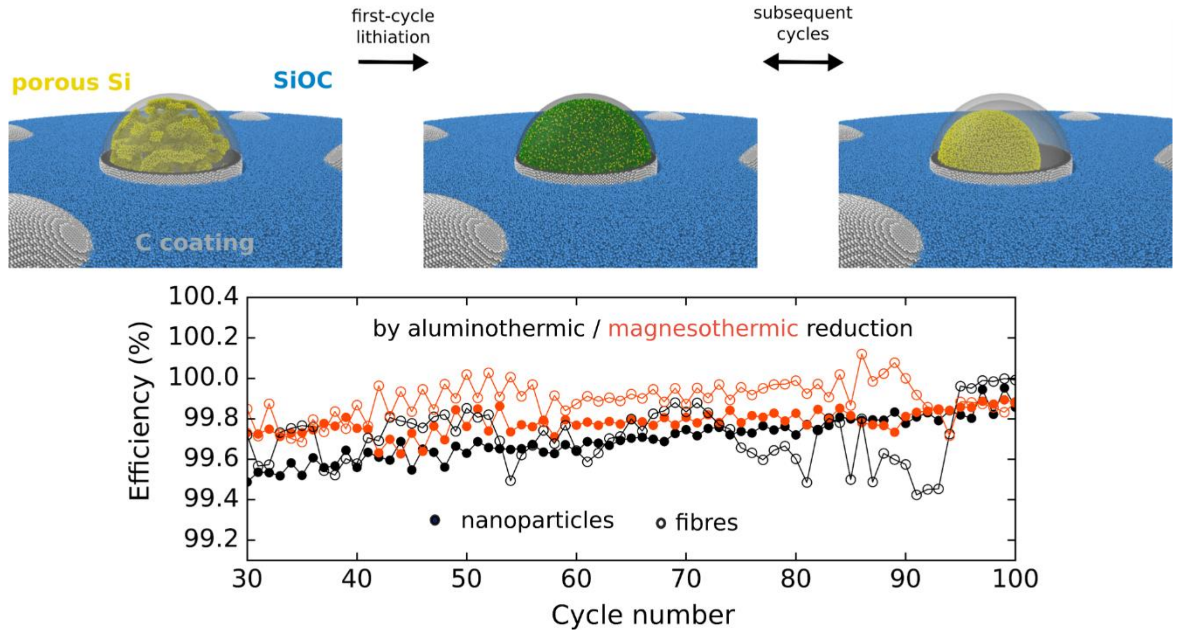

Figure 27: Schematic of the lithiation/delithiation of Si/C/SiOC and the electrochemical performance of the investigated composites. Electrochemical tests reveal the outstanding performance of nanoparticle-based and fiber-based composites with Coulombic efficiency of 99.5%, and nearly 100% of capacity retention over 100 cycles.

The MD studies showed that the macroscopic expansion of porous Si at the maximum Li content remains well below that of the dense silicon, namely 25% for the investigated system vs. 280% for dense Si. Upon delithiation no significant re-opening of the pores occurs. Instead, the system shrinks homogeneously and the free volume that was initially distributed over the pores reappears as free volume between the surface of the dense Si particle and the SiOC matrix (Figure 27). This feature explains the outstanding cycling stability and high Coulombic efficiency.

The significant irreversible loss of Li in SiOC and disordered carbon during the first lithiation remains a major challenge in the process. Decreasing the amount of SiOC ceramic, responsible for the irreversible trapping of Li-ions in the proximity of polar Si-O bonds, would significantly increase the first cycle efficiency. It should also boost overall composite capacities due to the higher Si content. Another approach would be to exchange Si-O containing ceramics against Si-N ceramics. The more covalent character of the Si-N bonds might help to decrease first cycle losses. Moreover, any other electrically conductive ceramic matrix providing a stable composite shell will solve the problem of the first cycle irreversibility.

The second part of this thesis discloses a *de novo* invented synthesis route allowing to tailor the porosity of Si-based ceramics using simple chemical tools. Perhydropolysilazane, divinylbenzene (DVB), and di-n-butyl ether (DBE) were used as the starting reaction mixture. Ceramics with different textural properties were obtained from a crosslinked precursor after thermal treatment at T > 700 °C. Increase of the pyrolysis temperature led to a decrease of the specific surface area (SSA) and the total pore volume (TPV). Pyrolysis at 1100 °C yielded stable pores located within the ceramic, emphasizing the uniqueness of the new synthesis procedure. The texture of the final ceramic was also affected by the pyrolysis atmosphere. Using argon, vacuum and switching from argon to vacuum at temperature of 500 °C enabled to tune the type and amount of pores. Mesoporous ceramics with SSA of 169 $m^2 \cdot g^{-1}$ and TPV 0.48 $cm^3 \cdot g^{-1}$ were obtained at 900 °C under argon atmosphere whereas the combination of argon and vacuum resulted in a slight decrease in SSA (125 $m^2 \cdot g^{-1}$) and TPV (0.47 $cm^3 \cdot g^{-1}$). When vacuum was applied during pyrolysis, the SSA and the TPV decreased to 72 $m^2 g^{-1}$ and 0.1 $cm^3 \cdot g^{-1}$, respectively. Moreover, some micropores appeared while large mesopores disappeared.

Varying the concentration of DBE in the starting mixture appeared to be a versatile tool in tailoring the ceramic microstructure. The gradual change of the DBE concentration enabled the tuning of the amount/type of pores, while in the absence of DBE only dense ceramics were obtained. With 2 – 4% of DBE a mixture of micro- and meso-pores occurred. At high dilution (more than 50% of DBE) meso- and macro-porosity was achieved.

Electrochemical properties of the porous carbon-rich SiCN ceramics pyrolyzed at 900, 1100 and 1400 °C were investigated with respect to the reversible storage of lithium ions. Samples pyrolyzed at 900 °C revealed the best performance with a stable capacity of 534 $mAh \cdot g^{-1}$ (at a current density of 74 $mA \cdot g^{-1}$). The Li storage capacities were found to decrease with increasing pyrolysis temperature. This decrease can be explained by the structural change of the free carbon phase from highly disordered towards more organized carbon. During pyrolysis at 1400 °C the amount of free carbon decreases due to the carbothermal reaction. Nevertheless, all porous carbon-rich SiCN ceramics showed an enhanced current capability in comparison to their dense analogues.

Use of hierarchically porous SiCN ceramics for the CCS technology

The CO_2 capture capacity is supposed to be enhanced by the presence of nitrogen-containing groups, together with hierarchical mesostructures, which include a high BET surface, a stable framework, and the presence of a large number of micropores and small mesopores. Thus the SiCN 800 ceramic has been examined with respect to the CO_2 capture. The first tests revealed 1.5 and 1.9 mmol of CO_2 (per gram of SiCN) adsorbed at 1 bar pressure at 25 and 0 °C, respectively. These values are comparable with storage capacities of commercial carbons and zeolites.

The preparation method described above allows to synthesize functionalized Si-based ceramics with tailored hierarchical porosity stable beyond 1000 °C. For example, replacing DVB by divinyltiophene (DVT) will provide S-containing porous ceramics, whereas divinylpyrrole as crosslinking agent introduces additional nitrogen. The functionalized porous ceramics can be considered to be applied as electrically conductive matrices for sulphur electrodes in Li-S batteries and as high-capacity, thermally and chemically stable CO_2 sorbents/selective membranes.

References

[1] D. Vrankovic, L.M. Reinold, R. Riedel, M. Graczyk-Zajac, *Journal of Materials Science* **51** (2016) (12) 6051.

[2] D. Vrankovic, K. Wissel, M. Graczyk-Zajac, R. Riedel, *Solid State Ionics* **302** (2017) 66.

[3] K. Wissel, D. Vrankovic, G. Trykowski, M. Graczyk-Zajac, *Solid State Ionics* **302** (2017) 180.

[4] J. Rohrer, D. Vrankovic, D. Cupid, R. Riedel, H.J. Seifert, K. Albe, M. Graczyk-Zajac, *International Journal of Materials Research* **108** (2017) (11) 920.

[5] D. Vrankovic, M. Graczyk-Zajac, C. Kalcher, J. Rohrer, M. Becker, C. Stabler, G. Trykowski, K. Albe, R. Riedel, *ACS Nano* **11** (2017) 11409.

[6] M. Storch, D. Vrankovic, M. Graczyk-Zajac, R. Riedel, *Solid State Ionics* **315** (2018) 59.

[7] D. Vrankovic, M. Storch, C. Schitco, M. Graczyk-Zajac, R. Riedel, Solvent assisted synthesis of micro/mesoporous ceramics from preceramic polymers, German Patent registration DE 10 2016 116 732 A1.

[8] J.M. Tour, C. Kittrell, V.L. Colvin, *Nature Materials* **9** (2010) 871.

[9] X.J. Yang, H. Hu, T. Tan, J. Li, *Environmental Development* **20** (2016) (Supplement C) 83.

[10] J. Ren, N.M. Musyoka, H.W. Langmi, M. Mathe, S. Liao, *International Journal of Hydrogen Energy* **42** (2017) (1) 289.

[11] J.W. Choi, D. Aurbach, *Nature Reviews Materials* **1** (2016) 16013.

[12] J.M. Tarascon, *Philosophical Transactions of the Royal Society A: Mathematical, Physical and Engineering Sciences* **368** (2010) (1923) 3227.

[13] J.M. Tarascon, M. Armand, *Nature* **414** (2001) (6861) 359.

[14] M. Armand, J.M. Tarascon, *Nature* **451** (2008) (7179) 652.

[15] H. Kawamoto, *Science and Technology Trends - Quarterly Review* **36** (2010) 34.

[16] G.L. Soloveichik, *Annual Review of Chemical and Biomolecular Engineering* **2** (2011) 503.

[17] J. Liu, *Advanced Functional Materials* **23** (2013) (8) 924.

[18] C.H. Hamann, A. Hamnett, W. Vielstich, *Electrochemistry*, Wiley (2007).

[19] J.-K. Park, *Principles and Applications of Lithium Secondary Batteries*, Wiley-VCH Verlag GmbH & Co. KGaA (2012).

[20] J. Wang, X. Sun, *Energy & Environmental Science* **5** (2012) (1) 5163.

[21] J. Chen, *Materials* **6** (2013) (1) 156.

[22] C.M. Hayner, X. Zhao, H.H. Kung, *Annual Review of Chemical and Biomolecular Engineering* **3** (2012) (1) 445.

[23] G.E. Blomgren, *Journal of The Electrochemical Society* **164** (2017) (1) A5019.

[24] P. Bruce, *Press, Cambridge* (1995).

[25] U. Kasavajjula, C. Wang, A.J. Appleby, *Journal of Power Sources* **163** (2007) (2) 1003.

[26] J.R. Szczech, S. Jin, *Energy & Environmental Science* **4** (2011) (1) 56.

[27] B. Liang, Y. Liu, Y. Xu, *Journal of Power Sources* **267** (2014) 469.

[28] S. Ohara, J. Suzuki, K. Sekine, T. Takamura, *Journal of Power Sources* **136** (2004) (2) 303.

[29] Y. Sun, N. Liu, Y. Cui, *Nature Energy* **1** (2016) 16071.

[30] M. Wachtler, J.O. Besenhard, M. Winter, *Journal of Power Sources* **94** (2001) (2) 189.

[31] M. Winter, W.K. Appel, B. Evers, T. Hodal, K.-C. Möller, I. Schneider, M. Wachtler, M.R. Wagner, G.H. Wrodnigg, J.O. Besenhard, *Monatshefte für Chemie* **132** (2001) (4) 473.

[32] X.H. Liu, L. Zhong, S. Huang, S.X. Mao, T. Zhu, J.Y. Huang, *Acs Nano* **6** (2012) (2) 1522.

[33] J. Saint, M. Morcrette, D. Larcher, L. Laffont, S. Beattie, J.P. Peres, D. Talaga, M. Couzi, J.M. Tarascon, *Advanced Functional Materials* **17** (2007) (11) 1765.

[34] W.R. Liu, J.H. Wang, H.C. Wu, D.T. Shieh, M.H. Yang, N.L. Wu, *Journal of the Eletrochemical Society* **152** (2005) (9) A1719.

[35] X.L. Yang, Z.Y. Wen, X.X. Xu, B. Lin, Z.X. Lin, *Journal of the Electrochemical Society* **153** (2006) (7) A1341.

[36] I.S. Kim, G.E. Blomgren, P.N. Kumta, *Journal of Power Sources* **130** (2004) 275.

[37] N. Dimov, S. Kugino, M. Yoshio, *Journal of Power Sources* **136** (2004) (1) 108.

[38] N. Dimov, S. Kugino, M. Yoshio, *Electrochimica Acta* **48** (2003) (11) 1579.

[39] I.-S. Kim, P.N. Kumta, *Journal of Power Sources* **136** (2004) (1) 145.

[40] W. Ren, Y. Wang, Q. Tan, Z. Zhong, F. Su, *Journal of Power Sources* **332** (2016) 88.

[41] Z. Yang, Y. Xia, J. Ji, B. Qiu, K. Zhang, Z. Liu, *RSC Advances* **6** (2016) 12107.

[42] D. Lin, Z. Lu, P.-C. Hsu, H.R. Lee, N. Liu, J. Zhao, H. Wang, C. Liu, Y. Cui, *Energy & Environmental Science* **8** (2015) 2371.

[43] H. Wu, G. Zheng, N. Liu, T.J. Carney, Y. Yang, Y. Cui, *Nano Letters* **12** (2012) (2) 904.

[44] L. Yue, W. Zhang, J. Yang, L. Zhang, *Electrochimica Acta* **125** (2014) 206.

[45] X. Zhou, J. Tang, J. Yang, J. Xie, L. Ma, *Electrochimica Acta* **87** (2013) 663.

[46] X. Li, P. Meduri, X. Chen, W. Qi, M.H. Engelhard, W. Xu, F. Ding, J. Xiao, W. Wang, C. Wang, J.-G. Zhang, J. Liu, *Journal of Materials Chemistry* **22** (2012) (22) 11014.

[47] D. Mazouzi, B. Lestriez, L. Roue, D. Guyomard, *Electrochemical and Solid State Letters* **12** (2009) (11) A215.

[48] C. Martin, M. Alias, F. Christien, O. Crosnier, D. Belanger, T. Brousse, *Advanced Materials* **21** (2009) (46) 4735.

[49] B. Chen, A.K. Flatt, H. Jian, J.L. Hudson, J.M. Tour, *Chemistry of Materials* **17** (2005) (19) 4832.

[50] Y.H. Xu, G.P. Yin, P.J. Zuo, *Electrochimica Acta* **54** (2008) (2) 341.

[51] C. Martin, O. Crosnier, R. Retoux, D. Belanger, D.M. Schleich, T. Brousse, *Advanced Functional Materials* **21** (2011) (18) 3524.

[52] S. Yang, G. Li, Q. Zhu, Q. Pan, *Journal of Materials Chemistry* **22** (2012) 3420.

[53] D. Chen, R. Yi, S. Chen, T. Xu, M.L. Gordin, D. Wang, *Solid State Ionics* **254** (2014) 65.

[54] C.K. Chan, H. Peng, G. Liu, K. McIlwrath, X.F. Zhang, R.A. Huggins, Y. Cui, *Nat Nano* **3** (2008) (1) 31.

[55] C.K. Chan, R. Ruffo, S.S. Hong, R.A. Huggins, Y. Cui, *Journal of Power Sources* **189** (2009) (1) 34.

[56] A. Vlad, A.L.M. Reddy, A. Ajayan, N. Singh, J.-F.o. Gohy, S. Melinte, P.M. Ajayan, *Proceedings of the National Academy of Sciences* **109** (2012) (38) 15168.

[57] S.W. Lee, H.-W. Lee, I. Ryu, W.D. Nix, H. Gao, Y. Cui, *Nature Communications* **6** (2015) 7533.

[58] Z. Bao, M.R. Weatherspoon, S. Shian, Y. Cai, P.D. Graham, S.M. Allan, G. Ahmad, M.B. Dickerson, B.C. Church, Z. Kang, H.W. Abernathy Iii, C.J. Summers, M. Liu, K.H. Sandhage, *Nature* **446** (2007) (7132) 172.

[59] Y. Yu, L. Gu, C. Zhu, S. Tsukimoto, P.A. van Aken, J. Maier, *Advanced Materials* **22** (2010) (20) 2247.

[60] H. Jia, P. Gao, J. Yang, J. Wang, Y. Nuli, Z. Yang, *Advanced Energy Materials* **1** (2011) (6) 1036.

[61] Z. Lu, J. Zhu, D. Sim, W. Zhou, W. Shi, H.H. Hng, Q. Yan, *Chemistry of Materials* **23** (2011) (24) 5293.

[62] J. Xie, G. Wang, Y. Huo, S. Zhang, G. Cao, X. Zhao, *Electrochimica Acta* **135** (2014) 94.

[63] W. Wang, Z. Favors, R. Ionescu, R. Ye, H.H. Bay, M. Ozkan, C.S. Ozkan, *Scientific Reports* **5** (2015) 8781.

[64] J. Ryu, D. Hong, M. Shin, S. Park, *ACS Nano* **10** (2016) (11) 10589.

[65] N. Lin, Y. Han, J. Zhou, K. Zhang, T. Xu, Y. Zhu, Y. Qian, *Energy & Environmental Science* **8** (2015) 3187.

[66] N. Lin, T. Xu, Y. Han, K. Shen, Y. Zhu, Y. Qian, *RSC Advances* **6** (2016) 79890.

[67] N. Lin, Y. Han, L. Wang, J. Zhou, J. Zhou, Y. Zhu, Y. Qian, *Angewandte Chemie International Edition* **54** (2015) (12) 3822.

[68] Z.-W. Zhou, Y.-T. Liu, X.-M. Xie, X.-Y. Ye, *Chemical Communications* **52** (2016) 8401.

[69] M. Zhang, T. Zhang, Y. Ma, Y. Chen, *Energy Storage Materials* **4** (2016) 1.

[70] P. Colombo, R. Riedel, G.D. Soraru, H.J. Kleebe, *Polymer Derived Ceramics, From Nano-Structure to Applications*, DEStech Publications, Inc. (2010).

[71] F.W. Ainger, J.M. Herbert, *Special Ceramics* (1960) 168.

[72] P.G. Chantrell, P. Popper, *Special Ceramics* (1965) 67.

[73] W. Verbeek, Ger. Pat. No. 2218960 (1973).

[74] W. Verbeek, G. Winter, Ger. Pat. No. 2236078 (1974).

[75] G. Winter, W. Verbeek, M. Mansmann, Ger. Pat. No. 2243527 (1974).

[76] S. Yajima, J. Hayashi, M. Omori, *Chemistry Letters* **4** (1975) (9) 931.

[77] S. Yajima, J. Hayashi, M. Omori, K. Okamura, *Nature* **261** (1976) (5562) 683.

[78] S. Yajima, K. Okamura, J. Hayashi, M. Omori, *Journal of the American Ceramic Society* **59** (1976) 324.

[79] R. West, L.D. David, P.I. Djurovich, Y.U. Hyuk, R. Sinclair, *American Ceramic Society bulletin* **62** (1983) (8) 899.

[80] D. Seyferth, G.H. Wiseman, C. Prud'homme, *Journal of the American Ceramic Society* **66** (1983) (1) C13.

[81] K.J. Wynne, R.W. Rice, *Annual Review of Materials Science* **14** (1984) (1) 297.

[82] G. Pouskouleli, *Ceramics International* **15** (1989) (4) 213.

[83] M. Peuckert, T. Vaahs, M. Brück, *Advanced Materials* **2** (1990) (9) 398.

[84] S. Dire, F. Babonneau, C. Sanchez, J. Livage, *Journal of Materials Chemistry* **2** (1992) (2) 239.

[85] G.D. Soraru, M. Mercadini, R.D. Maschio, F. Taulelle, F. Babonneau, *Journal of the American Ceramic Society* **76** (1993) (10) 2595.

[86] A.M. Wootton, M. Rappensberger, M.H. Lewis, S. Kitchin, A.P. Howes, R. Dupree, *Journal of Non-Crystalline Solids* **204** (1996) (3) 217.

[87] R. Riedel, A. Kienzle, W. Dressler, L. Ruwisch, J. Bill, F. Adlinger, *Nature* **382** (1996) (6594) 796.

[88] R. Riedel, L.M. Ruswisch, L. An, R. Raj, *Journal of the American Ceramic Society* **81** (1998) (12) 3341.

[89] S. Dire, R. Ceccato, S. Gialanella, F. Babonneau, *Journal of the European Ceramic Society* **19** (1999) (16) 2849.

[90] Z.-C. Wang, F. Aldinger, R. Riedel, *Journal of the American Ceramic Society* **84** (2001) (10) 2179.

[91] A. Zimmermann, A. Bauer, M. Christ, Y. Cai, F. Aldinger, *Acta Materialia* **50** (2002) (5) 1187.

[92] F. Hoenack, R. Riedel, *Advanced Engineering Materials* **5** (2003) (3) 122.

[93] R. Harshe, C. Balan, R. Riedel, *Journal of the European Ceramic Society* **24** (2004) (12) 3471.

[94] S. Bernard, K. Ayadi, M.-P. Berthet, F. Chassagneux, D. Cornu, J.-M. Letoffe, P. Miele, *Journal of Solid State Chemistry* **177** (2004) (6) 1803.

[95] S. Bernard, M. Weinmann, P. Gerstel, P. Miele, F. Aldinger, *Journal of Materials Chemistry* **15** (2005) (2) 289.

[96] M.A. Schiavon, C. Gervais, F. Babonneau, G.D. Soraru, *Journal of the American Ceramic Society* **87** (2004) (2) 203.

[97] E. Ionescu, B. Papendorf, H.-J. Kleebe, F. Poli, K. Müller, R. Riedel, *Journal of the American Ceramic Society* **93** (2010) (6) 1774.

[98] E. Ionescu, B. Papendorf, H.-J. Kleebe, R. Riedel, *Journal of the American Ceramic Society* **93** (2010) (6) 1783.

[99] E. Ionescu, C. Linck, C. Fasel, M. Müller, H.J. Kleebe, R. Riedel, *Journal of the American Ceramic Society* **93** (2010) (1) 241.

[100] B. Papendorf, K. Nonnenmacher, E. Ionescu, H.-J. Kleebe, R. Riedel, *Small* **7** (2011) (7) 970.

[101] E. Ionescu, B. Papendorf, H.-J. Kleebe, H. Breitzke, K. Nonnenmacher, G. Buntkowsky, R. Riedel, *Journal of the European Ceramic Society* **32** (2012) (9) 1873.

[102] E. Kroke, Y.-L. Li, C. Konetschny, E. Lecomte, C. Fasel, R. Riedel, *Materials Science and Engineering: R: Reports* **26** (2000) (4-6) 97.

[103] R.M. Laine, F. Babonneau, *Chemistry of Materials* **5** (1993) (3) 260.

[104] P. Colombo, G. Mera, R. Riedel, G.D. Soraru, *Journal of the American Ceramic Society* **93** (2010) (7) 1805.

[105] H. Zhang, C.G. Pantano, *Journal of the American Ceramic Society* **73** (1990) (4) 958.

[106] C.G. Pantano, A.K. Singh, H. Zhang, *Journal of Sol-Gel Science and Technology* **14** (1999) (1) 7.

[107] Y.D. Blum, D.B. MacQueen, H.-J. Kleebe, *Journal of the European Ceramic Society* **25** (2005) (2-3) 143.

[108] F. Babonneau, K. Thorne, J.D. Mackenzie, *Chemistry of Materials* **1** (1989) (5) 554.

[109] J. Livage, F. Babonneau, C. Sanchez, In: J. Harrod, R. Laine, Editors, *Inorganic and Organometallic Oligomers and Polymers*, Springer Netherlands (1991), 217-228.

[110] G.M. Renlund, S. Prochazka, R.H. Doremus, *Journal of Materials Research* **6** (1991) 2716.

[111] G.M. Renlund, S. Prochazka, R.H. Doremus, *Journal of Materials Research* **6** (1991) 2723.

[112] F. Babonneau, L. Bois, J. Livage, *Journal of Non-Crystalline Solids* **147** (1992) 280.

[113] F. Babonneau, L. Bois, C.Y. Yang, L.V. Interrante, *Chemistry of Materials* **6** (1994) (1) 51.

[114] L. Bois, J. Maquet, F. Babonneau, H. Mutin, D. Bahloul, *Chemistry of Materials* **6** (1994) (6) 796.

[115] L. Bois, J. Maquet, F. Babonneau, D. Bahloul, *Chemistry of Materials* **7** (1995) (5) 975.

[116] R.J.P. Corriu, D. Leclercq, P.H. Mutin, A. Vioux, *Journal of Materials Science* **30** (1995) (9) 2313.

[117] F. Babonneau, G.D. Soraru, G. D'Andrea, S. Dire, L. Bois, *Materials Research Society Symposium Proceedings* **271** (1992) 789.

[118] G.D. Soraru, D. Suttor, *Journal of Sol-Gel Science and Technology* **14** (1999) (1) 69.

[119] G.D. Soraru, G. D'Andrea, R. Campostrini, F. Babonneau, G. Mariotto, *Journal of the American Ceramic Society* **78** (1995) (2) 379.

[120] G.D. Soraru, *Journal of Sol-Gel Science and Technology* **2** (1994) (1) 843.

[121] G.D. Soraru, E. Dallapiccola, G. D'Andrea, *Journal of the American Ceramic Society* **79** (1996) (8) 2074.

[122] G.D. Soraru, R. Campostrini, S. Maurina, F. Babonneau, *Journal of the American Ceramic Society* **80** (1997) (4) 999.

[123] T. Rouxel, G. Massouras, G.-D. Soraru, *Journal of Sol-Gel Science and Technology* **14** (1999) (1) 87.

[124] T. Rouxel, J.-C. Sanglebf, J.-P. Guin, V. Keryvin, G.-D. Soraru, *Journal of the American Ceramic Society* **84** (2001) (10) 2220.

[125] C. Turquat, H.-J. Kleebe, G. Gregori, S. Walter, G.D. Soraru, *Journal of the American Ceramic Society* **84** (2001) (10) 2189.

[126] H.-J. Kleebe, C. Turquat, G.D. Soraru, *Journal of the American Ceramic Society* **84** (2001) (5) 1073.

[127] G.D. Soraru, S. Modena, E. Guadagnino, P. Colombo, J. Egan, C. Pantano, *Journal of the American Ceramic Society* **85** (2002) (6) 1529.

[128] G.D. Soraru, L. Pederiva, J. Latournerie, R. Raj, *Journal of the American Ceramic Society* **85** (2002) (9) 2181.

[129] G. Trimmel, R. Badheka, F. Babonneau, J. Latournerie, P. Dempsey, D. Bahloul-Houlier, J. Parmentier, G.D. Soraru, *Journal of Sol-Gel Science and Technology* **26** (2003) (1) 279.

[130] H. Brequel, J. Parmentier, S. Walter, R. Badheka, G. Trimmel, S. Masse, J. Latournerie, P. Dempsey, C. Turquat, A. Desmartin-Chomel, L. Le Neindre-Prum, U.A. Jayasooriya, D. Hourlier, H.J. Kleebe, G.D. Soraru, S. Enzo, F. Babonneau, *Chemistry of Materials* **16** (2004) (13) 2585.

[131] G. Mera, A. Navrotsky, S. Sen, H.-J. Kleebe, R. Riedel, *Journal of Materials Chemistry A* **1** (2013) (12) 3826.

[132] H.-J. Kleebe, G. Gregori, Y.D. Blum, F. Babonneau, *International Journal of Materials Research* **97** (2006) 699.

[133] G. Gregori, H.-J. Kleebe, Y.D. Blum, F. Babonneau, *International Journal of Materials Research* **97** (2006) 710.

[134] S.J. Widgeon, S. Sen, G. Mera, E. Ionescu, R. Riedel, A. Navrotsky, *Chemistry of Materials* **22** (2010) (23) 6221.

[135] J. Cordelair, P. Greil, *Journal of the European Ceramic Society* **20** (2000) (12) 1947.

[136] H.-J. Kleebe, Y.D. Blum, *Journal of the European Ceramic Society* **28** (2008) (5) 1037.

[137] S. Martínez-Crespiera, E. Ionescu, H.-J. Kleebe, R. Riedel, *Journal of the European Ceramic Society* **31** (2011) (5) 913.

[138] Y. Iwamoto, W. Völger, E. Kroke, R. Riedel, *Journal of the American Ceramic Society* **84** (2001) 2170.

[139] G. Mera, R. Riedel, F. Poli, K. Müller, *Journal of the European Ceramic Society* **29** (2009) (13) 2873.

[140] R. Morcos, G. Mera, A. Navrotsky, T. Varga, R. Riedel, F. Poli, K. Müller, *Journal of the American Ceramic Society* **91** (2008) (10) 3349.

[141] G. Mera, A. Tamayo, H. Nguyen, S. Sen, R. Riedel, *Journal of the American Ceramic Society* **93** (2010) (4) 1169.

[142] Y. Gao, G. Mera, H. Nguyen, K. Morita, H.-J. Kleebe, R. Riedel, *Journal of the European Ceramic Society* **32** (2012) (9) 1857.

[143] J.R. Dahn, A.M. Wilson, W. Xing, G.A. Zank, In: D.C. Corporation, Editor, *United States Patent* (1997).

[144] A.M. Wilson, J.N. Reimers, E.W. Fuller, J.R. Dahn, *Solid State Ionics* **74** (1994) (3-4) 249.

[145] W. Xing, A.M. Wilson, K. Eguchi, G. Zank, J.R. Dahn, *Journal of The Electrochemical Society* **144** (1997) (7) 2410.

[146] W. Xing, A.M. Wilson, G. Zank, J.R. Dahn, *Solid State Ionics* **93** (1997) (3-4) 239.

[147] A.M. Wilson, G. Zank, K. Eguchi, W. Xing, B. Yates, J.R. Dahn, *Chemistry of Materials* **9** (1997) (7) 1601.

[148] A.M. Wilson, G. Zank, K. Eguchi, W. Xing, J.R. Dahn, *Journal of Power Sources* **68** (1997) (2) 195.

[149] A.M. Wilson, W. Xing, G. Zank, B. Yates, J.R. Dahn, *Solid State Ionics* **100** (1997) (3-4) 259.

[150] H. Fukui, O. Hisashi, T. Hino, K. Kanamura, *Applied Materials and Interfaces* **4** (2010) 998.

[151] H. Fukui, H. Ohsuka, T. Hino, K. Kanamura, *Journal of Power Sources* **196** (2011) (1) 371.

[152] H. Fukui, H. Ohsuka, T. Hino, K. Kanamura, *Journal of The Electrochemical Society* **158** (2011) (5) A550.

[153] H. Fukui, K. Eguchi, H. Ohsuka, T. Hino, K. Kanamura, *Journal of Power Sources* **243** (2013) 152.

[154] P. Dibandjo, M. Graczyk-Zajac, R. Riedel, V.S. Pradeep, G.D.a. Soraru, *Journal of the European Ceramic Society* **32** (2012) (10) 2495.

[155] V.S. Pradeep, M. Graczyk-Zajac, M. Wilamowska, R. Riedel, G.D. Soraru, *Solid State Ionics* **262** (2014) 22.

[156] V.S. Pradeep, M. Graczyk-Zajac, R. Riedel, G.D. Soraru, *Electrochimica Acta* **119** (2014) 78.

[157] M. Graczyk-Zajac, L. Toma, C. Fasel, R. Riedel, *Solid State Ionics* **225** (2012) 522.

[158] J. Kaspar, M. Graczyk-Zajac, R. Riedel, *Solid State Ionics* **225** (2012) 527.

[159] J. Kaspar, M. Graczyk-Zajac, R. Riedel, *Journal of Power Sources* **244** (2013) 450.

[160] M. Wilamowska, V.S. Pradeep, M. Graczyk-Zajac, R. Riedel, G.D. Soraru, *Solid State Ionics* **260** (2014) 94.

[161] M. Graczyk-Zajac, L.M. Reinold, J. Kaspar, P.V.W. Sasikumar, G.-D. Soraru, R. Riedel, *Nanomaterials* **5** (2015) (1) 233.

[162] V.S. Pradeep, D.G. Ayana, M. Graczyk-Zajac, G.D. Soraru, R. Riedel, *Electrochimica Acta* **157** (2015) 41.

[163] J. Kaspar, M. Graczyk-Zajac, S. Choudhury, R. Riedel, *Electrochimica Acta* **216** (2016) 196.

[164] M. Wilamowska-Zawlocka, P. Puczkarski, Z. Grabowska, J. Kaspar, M. Graczyk-Zajac, R. Riedel, G.D. Soraru, *RSC Advances* (2016).

[165] H. Konno, T. Morishita, S. Sato, H. Habazaki, M. Inagaki, *Carbon* **43** (2005) (5) 1111.

[166] H. Fukui, H. Ohsuka, T. Hino, K. Kanamura, *Chemistry Letters* **38** (2009) (1) 86.

[167] D. Ahn, R. Raj, *Journal of Power Sources* **195** (2010) (12) 3900.

[168] M. Haaks, J. Kaspar, A. Franz, M. Graczyk-Zajac, R. Riedel, M. Vogel, *Solid State Ionics* **287** (2016) 28.

[169] H. Fukui, Y. Harimoto, M. Akasaka, K. Eguchi, *ACS Applied Materials & Interfaces* **6** (2014) (15) 12827.

[170] H. Fukui, H. Ohsuka, T. Hino, K. Kanamura, *Journal of The Electrochemical Society* **160** (2013) (8) A1276.

[171] P.E. Sanchez-Jimenez, R. Raj, *Journal of the American Ceramic Society* **93** (2010) (4) 1127.

[172] J. Kaspar, M. Graczyk-Zajac, R. Riedel, *Electrochimica Acta* **115** (2014) 665.

[173] P. Kroll, *MRS Online Proceedings Library* **1313** (2011) 1.

[174] N. Liao, B. Zheng, H. Zhou, W. Xue, *Journal of Power Sources* **334** (2016) 39.

[175] R. Kolb, C. Fasel, V. Liebau-Kunzmann, R. Riedel, *Journal of the European Ceramic Society* **26** (2006) (16) 3903.

[176] M. Graczyk-Zajac, M. Wimmer, C. Neumann, R. Riedel, *Journal of Solid State Electrochemistry* **19** (2015) 2763.

[177] M. Wilamowska, M. Graczyk-Zajac, R. Riedel, *Journal of Power Sources* **24** (2013) 80.

[178] M. Graczyk-Zajac, C. Fasel, R. Riedel, *Journal of Power Sources* **196** (2011) (15) 6412.

[179] Y. Feng, N.-N. Feng, G.-X. Du, *International Journal of Electrochemical Science* **7** (2012) 3135.

[180] M. Wilamowska, M. Graczyk-Zajac, R. Riedel, *Journal of Power Sources* **244** (2013) 80.

[181] Y. Chen, C. Li, Y. Wang, Q. Zhang, C. Xu, B. Wei, L. An, *Journal of Materials Chemistry* **21** (2011) 18186.

[182] Y. Feng, N. Feng, Y. Wei, Y. Bai, *Journal of Materials Chemistry A* **2** (2014) 4168.

[183] Y. Feng, G.-X. Du, X.-J. Zhao, E.-C. Yang, *Journal of Applied Electrochemistry* **41** (2011) (8) 999.

[184] M. Graczyk-Zajac, G. Mera, J. Kaspar, R. Riedel, *Journal of the European Ceramic Society* **30** (2010) (15) 3235.

[185] J. Kaspar, G. Mera, A.P. Nowak, M. Graczyk-Zajac, R. Riedel, *Electrochimica Acta* **56** (2010) (1) 174.

[186] D. Su, Y.-L. Li, Y. Feng, J. Jin, *Journal of the American Ceramic Society* **92** (2009) (12) 2962.

[187] Y. Feng, *Electrochimica Acta* **55** (2010) (20) 5860.

[188] L.M. Reinold, M. Graczyk-Zajac, Y. Gao, G. Mera, R. Riedel, *Journal of Power Sources* **236** (2013) 224.

[189] S.-H. Baek, L.M. Reinold, M. Graczyk-Zajac, R. Riedel, F. Hammerath, B. Buchner, H.-J. Grafe, *Journal of Power Sources* **253** (2014) 342.

[190] M. Haaks, J. Kaspar, A. Franz, M. Graczyk-Zajac, R. Riedel, M. Vogel, *Solid State Ionics* **287** (2016) 28.

[191] M. Graczyk-Zajac, M. Wimmer, Y. Xu, G. Buntkowsky, C. Neumann, R. Riedel, *Journal of Solid State Electrochemistry* **21** (2017) (1) 47.

[192] F. Ji, Y.-L. Li, J.-M. Feng, D. Su, Y.-Y. Wen, Y. Feng, F. Hou, *Journal of Materials Chemistry* **19** (2009) (47) 9063.

[193] R. Bhandavat, M. Cologna, G. Singh, *Nanomaterials and Energy* **1** (2012) 57.

[194] R. Bhandavat, G. Singh, *Journal of Physical Chemistry C* **117** (2013) (23) 11899.

[195] L. David, K.M. Shareef, M.A. Abass, G. Singh, *RSC Advances* **6** (2016) 53894.

[196] J. Kaspar, C. Terzioglu, E. Ionescu, M. Graczyk-Zajac, S. Hapis, H.-J. Kleebe, R. Riedel, *Advanced Functional Materials* **24** (2014) (26) 4097.

[197] L.M. Reinold, M. Graczyk-Zajac, C. Fasel, R. Riedel, *ECS Transactions* **35** (2011) 37.

[198] J. Kaspar, M. Graczyk-Zajac, S. Lauterbach, H.-J. Kleebe, R. Riedel, *Journal of Power Sources* **269** (2014) 164.

[199] X. Liu, K. Xie, J. Wang, C. Zheng, Y. Pan, *Journal of Materials Chemistry* **22** (2012) (37) 19621.

[200] A. Feinle, M.S. Elsaesser, N. Husing, *Chemical Society Reviews* **45** (2016) (12) 3377.

[201] B.-L. Su, C. Sanchez, X.-Y. Yang, *Hierarchically Structured Porous Materials*, Wiley-VCH Verlag GmbH & Co. KGaA (2011), 1-27.

[202] P. Colombo, C. Vakifahmetoglu, S. Costacurta, *Journal of Materials Science* **45** (2010) (20) 5425.

[203] K. Lu, *Materials Science and Engineering: R: Reports* **97** (2015) 23.

[204] J. Rouquerol, D. Avnir, C.W. Fairbridge, D.H. Everett, J.M. Haynes, N. Pernicone, J.D.F. Ramsay, K.S.W. Sing, K.K. Unger, Recommendations for the characterization of porous solids (Technical Report), *Pure and Applied Chemistry* (1994), 1739.

[205] W. Schwieger, A.G. Machoke, T. Weissenberger, A. Inayat, T. Selvam, M. Klumpp, A. Inayat, *Chemical Society Reviews* **45** (2016) (12) 3353.

[206] W. Li, D. Zhao, *Chemical Communications* **49** (2013) (10) 943.

[207] P. Colombo, *Science* **322** (2008) (5900) 381.

[208] A. Stein, Z. Wang, M.A. Fierke, *Advanced Materials* **21** (2009) (3) 265.

[209] Y. Shi, Y. Wan, D. Zhao, *Chemical Society Reviews* **40** (2011) (7) 3854.

[210] Y. Ren, Z. Ma, P.G. Bruce, *Chemical Society Reviews* **41** (2012) (14) 4909.

[211] Y. Wan, Zhao, *Chemical Reviews* **107** (2007) (7) 2821.

[212] D.M. D'Alessandro, B. Smit, J.R. Long, *Angewandte Chemie International Edition* **49** (2010) (35) 6058.

[213] M.Z. Jacobson, *Energy & Environmental Science* **2** (2009) (2) 148.

[214] McKinsey Climate Change Initiative, Carbon Capture & Storage: Assessing the Economics McKinsey & Company (2008).

[215] E. Kintisch, *Science* **317** (2007) (5835) 184.

[216] G.T. Rochelle, *Science* **325** (2009) (5948) 1652.

[217] P. Markewitz, W. Kuckshinrichs, W. Leitner, J. Linssen, P. Zapp, R. Bongartz, A. Schreiber, T.E. Müller, *Energy & Environmental Science* **5** (2012) (6) 7281.

[218] P.D. Vaidya, E.Y. Kenig, *Chemical Engineering & Technology* **30** (2007) (11) 1467.

[219] H. Yang, A.M. Khan, Y. Yuan, S.C. Tsang, *Chemistry – An Asian Journal* **7** (2012) (3) 498.

[220] K. Li, J.D. Kress, D.S. Mebane, *The Journal of Physical Chemistry C* **120** (2016) (41) 23683.

[221] P. Nugent, Y. Belmabkhout, S.D. Burd, A.J. Cairns, R. Luebke, K. Forrest, T. Pham, S. Ma, B. Space, L. Wojtas, M. Eddaoudi, M.J. Zaworotko, *Nature* **495** (2013) (7439) 80.

[222] J.D. Figueroa, T. Fout, S. Plasynski, H. McIlvried, R.D. Srivastava, *International Journal of Greenhouse Gas Control* **2** (2008) (1) 9.

[223] M.G. Plaza, S. García, F. Rubiera, J.J. Pis, C. Pevida, *Chemical Engineering Journal* **163** (2010) (1–2) 41.

[224] M.G. Plaza, C. Pevida, A. Arenillas, F. Rubiera, J.J. Pis, *Fuel* **86** (2007) (14) 2204.

[225] C.-H. Yu, C.-H. Huang, C.-S. Tan, *Aerosol and Air Quality Research* **12** (2012) 745.

[226] R.A. Khatri, S.S.C. Chuang, Y. Soong, M. Gray, *Energy & Fuels* **20** (2006) (4) 1514.

[227] M.D. Soutullo, C.I. Odom, B.F. Wicker, C.N. Henderson, A.C. Stenson, J.H. Davis, *Chemistry of Materials* **19** (2007) (15) 3581.

[228] A.S. Jalilov, G. Ruan, C.-C. Hwang, D.E. Schipper, J.J. Tour, Y. Li, H. Fei, E.L.G. Samuel, J.M. Tour, *ACS Applied Materials & Interfaces* **7** (2015) (2) 1376.

[229] C.-C. Hwang, J.J. Tour, C. Kittrell, L. Espinal, L.B. Alemany, J.M. Tour, *Nature Communications* **5** (2014) 3961.

[230] J. Marszewska, M. Jaroniec, *Journal of Colloid and Interface Science* **487** (2017) 162.

[231] K.J. Shah, T. Imae, *Biomacromolecules* **17** (2016) (5) 1653.

[232] D.P. Bezerra, R.S. Oliveira, R.S. Vieira, C.L. Cavalcante, D.C.S. Azevedo, *Adsorption* **17** (2011) (1) 235.

[233] Q. Li, J. Yang, D. Feng, Z. Wu, Q. Wu, S.S. Park, C.-S. Ha, D. Zhao, *Nano Research* **3** (2010) (9) 632.

[234] K.V. Kumar, K. Preuss, L. Lu, Z.X. Guo, M.M. Titirici, *The Journal of Physical Chemistry C* **119** (2015) (39) 22310.

[235] B. Adeniran, R. Mokaya, *Chemistry of Materials* **28** (2016) (3) 994.

[236] V.W.S. Pradeep, E. Zera, M. Graczyk-Zajac, R. Riedel, G.D. Soraru, *Journal of the American Ceramic Society* **99** (2016) (9) 2977.

[237] C. Schitco, M.S. Bazarjani, R. Riedel, A. Gurlo, *Journal of Materials Chemistry A* **3** (2015) 805.

[238] C. Schitco, M. Seifollahi Bazarjani, R. Riedel, A. Gurlo, *Journal of Materials Research* **30** (2015) (19) 2958.

[239] C. Schitco, PhD thesis: NH3-Assisted Synthesis of Silicon Oxycarbonitride Ceramics for Gas Capture and Separation, *Technische Universitat Darmstadt* (2015).

[240] K.S.W. Sing, D.H. Everett, R.A.W. Haul, L. Moscou, R.A. Pierotti, J. Rouquerol, T. Siemieniewska, *Pure and Applied Chemistry* **57** (1985) (4) 603.

[241] J.H. de Boer, B.G. Linsen, T. van der Plas, G.J. Zondervan, *Journal of Catalysis* **4** (1965) (6) 649.

[242] P. Dibandjo, S. Dirè, F. Babonneau, G. Soraru, *Journal of Non-Crystalline Solids* **356** (2010) (3) 132.

[243] V.L. Nguyen, E. Zera, A. Perolo, R. Campostrini, W. Li, G.D. Sorarù, *Journal of the European Ceramic Society* **35** (2015) (12) 3295.

[244] D. Pavia, G. Lampman, G. Kriz, J. Vyvyan, *Introduction to spectroscopy*, Cengage Learning (2008).

[245] N. Janakiraman, F. Aldinger, *Journal of the European Ceramic Society* **29** (2009) (1) 163.

[246] J. Lücke, J. Hacker, D. Suttor, G. Ziegler, *Applied Organometallic Chemistry* **11** (1997) (2) 181.

[247] J. Ludwinowicz, M. Jaroniec, *Carbon* **94** (2015) 673.

[248] B. Wang, A.P. Cote, H. Furukawa, M. O'Keeffe, O.M. Yaghi, *Nature* **453** (2008) (7192) 207.

[249] L.M. Reinold, Y. Yamada, M. Graczyk-Zajac, H. Munakata, K. Kanamura, R. Riedel, *Journal of Power Sources* **282** (2015) 409.

[250] S.-H. Baek, L.M. Reinold, M. Graczyk-Zajac, R. Riedel, F. Hammerath, B. Büchner, H.-J. Grafe, *Journal of Power Sources* **253** (2014) 342.

[251] A. Sadezky, H. Muckenhuber, H. Grothe, R. Niessner, U. Poeschl, *Carbon* **43** (2005) (8) 1731.

[252] J. Wagner, M. Ramsteiner, C. Wild, P. Koidl, *Physical Review B* **40** (1989) (3) 1817.

[253] T. Jawhari, A. Roid, J. Casado, *Carbon* **33** (1995) (11) 1561.

[254] H. Azuma, H. Imoto, S.i. Yamada, K. Sekai, *Journal of Power Sources* **81-82** (1999) 1.

[255] L. Qie, W.-M. Chen, Z.-H. Wang, Q.-G. Shao, X. Li, L.-X. Yuan, X.-L. Hu, W.-X. Zhang, Y.-H. Huang, *Advanced Materials* **24** (2012) (15) 2047.

[256] L.M. Reinold, M. Graczyk-Zajac, Y. Gao, G. Mera, R. Riedel, *Journal of Power Sources* **236** (2013) 224.

[257] G. Liu, J. Kaspar, L.M. Reinold, M. Graczyk-Zajac, R. Riedel, *Electrochimica Acta* **106** (2013) 101.

[258] F. Bonino, S. Brutti, P. Reale, B. Scrosati, L. Gherghel, J. Wu, K. Müllen, *Advanced Materials* **17** (2005) (6) 743.

[259] I. Mochida, C.-H. Ku, Y. Korai, *Carbon* **39** (2001) (3) 399.

[260] J.R. Dahn, T. Zheng, Y. Liu, J. Xue, *Science* **270** (1995) (5236) 590.

[261] K.T. Lee, J.C. Lytle, N.S. Ergang, S.M. Oh, A. Stein, *Advanced Functional Materials* **15** (2005) (4) 547.

[262] H. Fujimoto, A. Mabuchi, K. Tokumitsu, T. Kasuh, *Journal of Power Sources* **54** (1995) (2) 440.

[263] T. Zheng, J.S. Xue, J.R. Dahn, *Chemistry of Materials* **8** (1996) (2) 389.

[264] D. Ahn, R. Raj, *Journal of Power Sources* **196** (2011) (4) 2179.

[265] Y.S. Hu, P. Adelhelm, B.M. Smarsly, S. Hore, M. Antonietti, J. Maier, *Advanced Functional Materials* **17** (2007) (12) 1873.

[266] A.S. Arico, P. Bruce, B. Scrosati, J.-M. Tarascon, W. van Schalkwijk, *Nature Materials* **4** (2005) (5) 366.

List of Figures

List of Tables

Publications

[1] **D. Vrankovic**, L.M. Reinold, R. Riedel, M. Graczyk-Zajac, Void-shell silicon/carbon/SiCN nanostructures: toward stable silicon-based electrodes, *Journal of Materials Science* **51** (2016) (12) 6051.

[2] **D. Vrankovic**, K. Wissel, M. Graczyk-Zajac, R. Riedel, Novel 3D Si/C/SiOC nanocomposites: toward electrochemically stable lithium storage in silicon, *Solid State Ionics*, **302** (2017) 66.

[3] K. Wissel, **D. Vrankovic**, G. Trykowski, M. Graczyk-Zajac, Synthesis of 3D silicon with tailored nanostructure: Influence of morphology on the electrochemical properties, *Solid State Ionics*, **302** (2017) 180.

[4] J. Rohrer, **D. Vrankovic**, D. Cupid, R. Riedel, HJ. Seifert, K. Albe, M. Graczyk-Zajac, Novel Si- and Sn-containing SiOCN-based nanocomposites as anode materials for lithium ion batteries: synthesis, thermodynamic characterization and modelling, *International Journal of Materials Research*, **108** (2017) (11) 920.

[5] **D. Vrankovic**, M. Graczyk-Zajac, C. Kalcher, J. Rohrer, M. Becker, C. Stabler, G. Trykowski, K. Albe, R. Riedel, Highly Porous Silicon Embedded in a Ceramic Matrix: A Stable High-Capacity Electrode for Li-Ion Batteries, *ACS Nano,* **11** (2017) 11409.

[6] M. Storch, **D. Vrankovic**, M. Graczyk-Zajac, R. Riedel, The influence of pyrolysis temperature on the electrochemical behavior of porous carbon-rich SiCN polymer-derived ceramics, *Solid State Ionics* **315** (2018) 59.

Patent:
[7] **D. Vrankovic**, M. Storch, C. Schitco, M. Graczyk-Zajac, R. Riedel, Solvent assisted synthesis of micro/mesoporous ceramics from preceramic polymers, German Patent registration DE 10 2016 116 732 A1.

J Mater Sci (2016) 51:6051–6061

Void-shell silicon/carbon/SiCN nanostructures: toward stable silicon-based electrodes

Dragoljub Vrankovic[1], Lukas Mirko Reinold[1,2], Ralf Riedel[1], and Magdalena Graczyk-Zajac[1,*]

[1] Fachbereich Material- und Geowissenschaften, Technische Universität Darmstadt, Jovanka-Bontschits-Straße 2, 64287 Darmstadt, Germany
[2] Present address: Hüttenes-Albertus Chemische Werke GmbH, Hansastr. 1, 30419 Hannover, Germany

Received: 14 January 2016
Accepted: 17 March 2016

ABSTRACT

We present a systematic work to design a void-shell nanostructures for improving the stability of silicon electrodes while alloying with lithium. To enhance the electrical conductivity, silicon is coated with carbon by using a simple and non-hazard route prior to embedding the Si particles in silicon carbonitride (SiCN). An inactive matrix, namely a polymer-derived SiCN ceramic is used to stabilize the composite. Additionally, cavities around silicon to accommodate volume changes are introduced by partial carbon burning. Significant increase in porosity of more than one order of magnitude is found by means of BET measurements for the samples obtained after additional heat treatment in air. TGA coupled with FTIR spectrometry shows that the ceramic matrix is stable upon heating, while burned carbon originates from pyrolyzed fructose. TEM micrographs confirm the presence of carbon/void around silicon particles embedded in the ceramic matrix. Electrochemical investigations reveal an improved conductivity due to the presence of carbon coating. Contribution of silicon in lithium storage is identified, whereas voids introduced around the silicon particles are found to improve cycling stability of silicon.

Introduction

The outstanding specific and volumetric capacity of silicon, arising from its ability to reversibly alloy with lithium, raises interest in this material for application as anode material in lithium ion batteries.

Obrovac and Christensen [1] showed that crystalline silicon becomes amorphous during the first alloying process and crystallizes to $Li_{15}Si_4$ at potentials lower than 50 mV, which was further confirmed by in situ X-ray diffraction studies [2]. $Li_{15}Si_4$ corresponds to a specific capacity of 3579 mAh g^{-1} which is the highest electrochemically available capacity of silicon at room temperature. During dealloying, the crystalline $Li_{15}Si_4$ phase vanishes and amorphous Li_xSi is formed.

The application of silicon anode materials is limited due to a large volume increase of about 260 % during the alloying process. This large volume

---

Address correspondence to E-mail: graczyk@materials.tu-darmstadt.de

DOI 10.1007/s10853-016-9911-x

change causes stress followed by cracking and pulverization of the electrode and finally leads to the loss of electric contact between active material and current collector. This consequently brings a rapid fading of the capacity with ongoing cycling. Furthermore, the large volume expansion leads to cracking of the solid electrolyte interface (SEI) on the silicon surface followed by irreversible capacity losses with ongoing cycling [3].

Numerous approaches in order to improve the cycling stability of silicon anodes are proposed in the literature, namely: (i) diminishing the size of Si particles (threshold value of about 150 nm) [4], (ii) embedding nanosilicon into an active or inactive matrix [5–10], (iii) chemical bonding of silicon nanoparticles to the binder or conductive additive [11–17], (iv) utilization of nanowires [18–20], and (v) the synthesis of nanosilicon-carbon composites with cavities around the silicon particles [21–25].

Nanostructured silicon electrodes face some important challenges as well. High surface-to-volume ratios can facilitate efficient transfer of lithium from the solvent to the active material to achieve high rates, but poor volumetric storage capacity is an important issue that has to be addressed. Moreover, the potential for uncontrolled reaction and thermal runaway is greater for high surface area electrodes. Although this problem is only mentioned in the literature [26], high surface area of nanostructured silicon presents a serious problem, and morphological optimization to achieve a balance between high rates and safety is needed. Further, it is of importance that used materials are inexpensive and environmentally benign.

Embedding nanosized silicon in an inexpensive matrix, which is able to accommodate the stresses during alloying, achieving additional storage capacity and in parallel stability against thermal runaway could be a promising solution with respect to the above-mentioned problems with nanostructured silicon-based systems.

Recently, Kaspar et al. [27] have reported on composite materials based on silicon particles dispersed in a polymer-derived silicon oxycarbide (SiOC) matrix. The sample containing amorphous silicon showed an improved cycling stability (capacity retention of 88 % after 100 cycles), while the electrode with crystalline silicon demonstrated an initial capacity increase followed by continuous fading. It has been reported that carbon-rich silicon carbonitride (SiCN) recovers the capacities as high as 600 mAh g^{-1} [28], while storing lithium mostly in carbon phase [29, 30]. The composite materials consisting of graphite/carbon-poor SiCN [31] or precursor-derived Si(B)CN-coated multiwalled carbon nanotube (CNT) composite [32] exceed by far the sum of the capacities of the single components. Reinold et al. [33]. showed the advantage of using polymer-derived silicon carbonitride (SiCN) ceramic as an inactive matrix for crystalline silicon nanopowder (30–50 nm) and stated the protective character of the SiCN matrix in terms of SEI stabilization for samples prepared at 1100 °C. Further, promising efforts have been done by using SiCN as stabilizing matrix for MoS_2 [34] and boron nitride [35]. Authors report significant improvement in electrochemical performances when polymer-derived ceramics are used compared to pure materials. Moreover, it has been reported that embedding in SiCN ceramic matrix leads to significant enhancement in rate capability of the composites [32, 36]. Core–shell silicon oxycarbide–carbon nanotubes composites demonstrate extremely high capacities of ~800 mAh g^{-1} and good capacity recovering at high current [37]. Fabrication of porous electrode structures to accommodate the large volume changes of silicon also drew a lot of attention. Among them, core–shell structures with cavities around the silicon particles have been investigated in detail [22–25]. Porous silicon-carbon composites are obtained by the controlled formation of a silicon oxide layer on silicon particles followed by carbon coating. To form hollow spaces around the silicon particles, the silicon oxide layer is finally removed by a treatment with hydrofluoric acid. The produced active material shows capacity retention of 86 % after 100 cycles [25].

From the point of view of a possible application in LiBs, carbon derived from organic source is environmentally friendly and cheap; however, it fails when battery safety issues are addressed [38].

Within this work, we present a systematic design of core–shell structures around silicon for improving its cycling stability during lithium insertion/extraction. On the one hand, coating with environmentally friendly organic carbon is applied to increase the composite conductivity, whereas partial burning of carbon leads to the formation of voids around silicon, proved by BET and TEM measurements. In parallel, polymer-derived silicon carbonitride ceramic (SiCN) [39] with low carbon content is used to form stable shells and to maintain the porous structure. The presence of stable SiCN ceramics should also help to stabilize the high active surface structure against thermal runaway, while the void/shell microstructures around the silicon brings about enhanced cycling stability of the electrode.

Experimental part

A schematic representation of the different composite materials and their preparation routes are shown in Fig. 1 showing synthesied composites b, c, and d; Figure S2, which includes materials defined by a and a', and Table 1 containing the list of all investigated composites. Following the steps of composites, synthesis can be defined: (i) coating with carbon, (ii) embedding of silicon covered with carbon in a ceramic matrix, and (iii) the introduction of cavities around the silicon particles.

For the carbon coating step, D-(-)-Fructose (purity >99 %, Sigma-Aldrich) was dissolved in an ethanol/water mixture (ratio 9:1). The silicon nanopowder (nanocrystalline, 30–50 nm, Nanostructured & Amorphous Materials Inc., USA), the ceramic, or the composite was uniformly dispersed in the solution of fructose using an ultra-turrax (IKA T25 digital ultra-turrax). After the solvents were evaporated, carbonization was performed at elevated temperatures under argon atmosphere.

In the second step, coated nanocrystalline silicon was dispersed in the pre-ceramic organosilicon polymer (HTT1800, Clariant, Germany). The obtained mixture was pyrolyzed under a constant argon flow at 1100 °C using a quartz Schlenk tube and quartz crucible. The heating and cooling rates were set to 100 °C h^{-1} and the dwelling time was amounted for 3 h. An additional crosslinking step was applied at 250 °C with a holding time of 3 h.

To create free space around the silicon particles, the composite material comprised silicon nanopowder covered with carbon and embedded into a SiCN matrix derived from HTT1800 was heated in air in an alumina furnace at 500 °C for 2 h.

Besides the composite materials, pure fructose was also carbonized at temperatures ranging from 300 to 1100 °C to obtain reference materials with respect to yield, the electrical conductivity, and the electrochemical behavior. Pure crystalline silicon powder was also coated with pre-ceramic organosilicon polymer (procedure ii), pyrolyzed and coated with carbon according to the procedure i (compare S2, Supplementary information).

The obtained materials were ground by hand and sieved with a mesh size of 40 µm.

X-ray powder diffraction was performed on the as-prepared powders using a STOE STAD1 P equipped with monochromatic Mo-K_α radiation in flat-sample transmission geometry.

Thermogravimetric analysis (TGA) was employed to monitor the reaction of the free carbon phase with oxygen. TGA was performed with STA 449C Jupiter (Netzsch Gerätebau GmbH, Germany) coupled to a FTIR-spectrometer Bruker Tensor27 allowing the measurement of the mass change as well as the evolution of carbon oxides. The analysis was performed under a constant oxygen gas flow (Air Liquide, purity ≥99.5 %) of 30 mL min^{-1}. The temperature program was set according to the program used for the additional heat treatment of the composite materials (heating rate 100 °C h^{-1}, dwelling time 2 h at 500 °C).

Nitrogen (N_2) adsorption was performed at 77 K using an Autosorb-3B (Quantachrome Instruments,

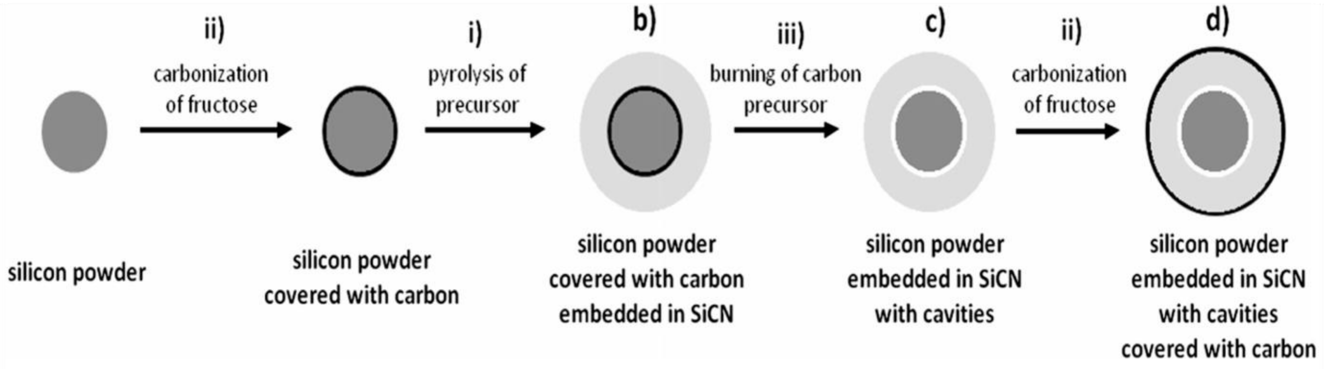

Figure 1 Synthesized composites and preparation route.

Table 1 Compositions and abbreviations of the investigated composites (a, a' see S2)

Composites	Sample name	Si:SiCN (wt%) after pyrolysis	Si:carbon (wt%) after carbonization[b]	$T^a_{Carbonization}$ (°C)	$T^b_{Carbonization}$ (°C)
a	Si:SiCN	1:4	–	–	–
a'	Si:SiCN:30F	1:4	7:3	–	900
b	Si:30F:SiCN	1:4	7:3	600	–
	Si:60F:SiCN	1:4	2:3	1100	–
c	Si:F:SiCN	1:4	7:3	600	–
	Si:F:SiCN(60)	1:4	2:3	1100	–
d	Si:F:SiCN:30F-900	1:4	7:3	600	900
	Si:F:SiCN(60):30F-900	1:4	2:3	1100	900

[a] Carbonization temperature for the coating of the silicon particles

[b] Carbonization temperature for the coating of the composite material after the additional heat treatment on air

USA). The samples were preheated at 150 °C for 24 h under vacuum before the measurements. The N_2 isotherm at 77 K was used to calculate the specific surface area (SSA) from the linear BET (Brunauer–Emmett–Teller) plots over the relative pressure range of $0.05 < p/p_o < 0.3$. The total pore volume (V_t) was determined from the amount of vapor adsorbed at a relative pressure $p/p_o \approx 1$ [40]. The micropore volume (V_m) was calculated using the de Boer's t-plot analysis [41]. The pore size distribution for mesoporous sample was estimated using BJH (Barrett–Joyner–Halenda) method for the desorption branch of the isotherm [40].

Transmission electron microscopy (TEM) studies on powder samples were performed with a FEI CM20 instrument equipped with an EDX Detector (TEM 250 with SDD Detector, Oxford Instruments), operated at 200 keV. Specimens were prepared by sectioning of epoxy resin-embedded (EPON 502) powder with a Reichert-Jung UltracutE Microtome equipped with a diamond knife. Obtained ultrathin sections (100 nm) were placed on a copper grid and introduced to the microscope chamber.

For electrochemical testing, prepared powders were mixed with 5 wt% of Carbon Black Super P® (Timcal Ltd., Switzerland) as conducting additive and 10 wt% of polyvinylidene fluoride (PVdF, SOLEF, Solvay, Germany) dissolved in N-methyl-2-pyrrolidone (NMP, BASF, Germany) as a binder. Additional NMP was added to adjust the viscosity of the mixture. The obtained slurry was printed on the rough side of a copper foil (10 µm, Copper SE-Cu58 (C103), Schlenk Metallfolien, Germany) by doctor blade technique and dried at 40 °C for 24 h. Electrodes of 10 mm diameter were cut out of the coated copper foil and dried at 80 °C under vacuum in a Buchi oven for 24 h. The dried electrodes were transferred without further contact with air to a glove box (MBraun, Germany) for cell assembly (Swagelok® type cell). The counter/reference electrode with a diameter of 10 mm was cut out of a metallic lithium foil (99.9 % purity, 0.75 mm thickness, Alfa Aesar, Germany). QMA (Whatmann™, UK) was used as a separator. For gravimetric capacity calculation, the mass of active material was used. The active electrode mass excludes that of the carbon black and PVDF fractions used in electrode preparation. The testing was performed with VMP multipotentiostat (BioLogic Science instruments) at charging/discharging rate of C/50 assuming a theoretical capacity C of 3579 mAh g^{-1} (C/50 being 72 mA g^{-1}).

Four-point measurements based on van der Pauw method have been employed in order to monitor the influence of the different preparation steps (Fig. 1, Table 1) on the electrical conductivity of obtained composites. Measurements were performed using a home-made setup, on pellets prepared by spreading part of the electrode slurry on a glass plate for drying at 40 °C for 24 h. After NMP was evaporated, the material was scratched from the glass plate and ground to a powder. To obtain uniform pellets, approximately, 100 mg of the as-prepared powder was pressed uniaxially with 30 kN for 5 min.

SEM pictures of pristine and cycled electrodes were taken at a Philips XL30 FEG (Philips, Netherlands). The cycled electrodes were disassembled from the Swagelok® cell and washed with dimethyl carbonate. The samples were coated with a thin layer of gold using a Quorum Q300T D (Quorum Technologies Ltd, United Kingdom) for 20 s at 30 mA. Imaging was performed at an acceleration voltage of 10 kV with a secondary electron detector.

Results and discussion

Formation of cavities

TGA in combination with FTIR spectrometry was performed on Si:30F:SiCN composite and pure SiCN ceramic in order to monitor the reaction of the free carbon phase with oxygen (Fig. 2). During the additional heat treatment of the composite materials ((step iii), Fig. 1) in air, carbon burning is expected, leading to outgassing and mass loss. In particular, the carbon coating on the silicon particles should react with oxygen forming outgassing carbon oxides and leaving behind cavities around the silicon particles. The goal of this measurement is to verify if the free carbon phase present in the SiCN ceramic remains intact during burning of carbon coating. Besides the mass loss of the sample, the temperature program and integrated FTIR signals for carbon monoxide and carbon dioxide are displayed in dependence of the measurement time.

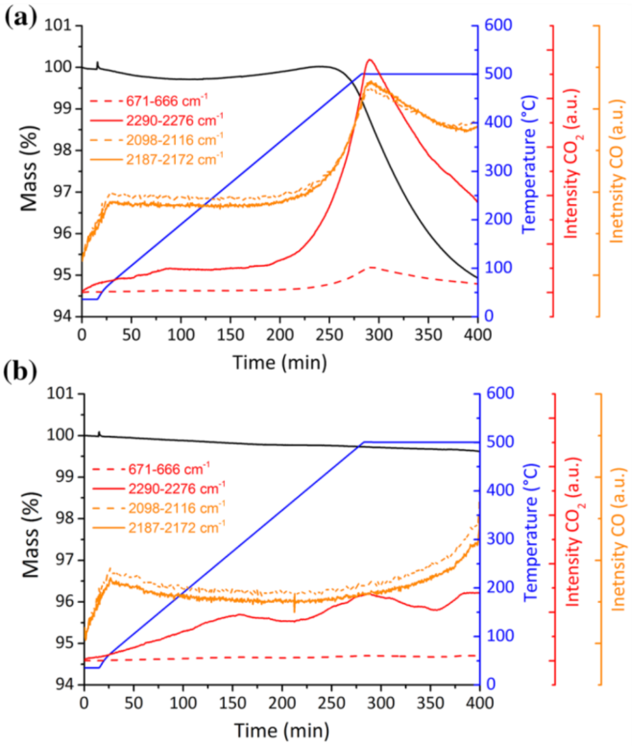

Figure 2 **a** TGA of Si:30F:SiCN. **b** TGA of pure SiCN derived from HTT1800 at pyrolysis temperature of 1100 °C. The *left y*-axis displays the change in sample mass. The *right-hand y*-axis show the temperature and the integrated intensity of CO and CO_2 band measured by FTIR spectroscopy.

At temperatures up to 210 °C, the mass of Si:30F:SiCN decreases slightly, probably due to the desorption of CO_2 and water. The mass gain between 210 °C (110 min) and 430 °C (240 min) might arise from an oxidation of the silicon. The measurement reveals the onset of the highest mass loss at approximately 450 °C (250 min). The mass loss is accompanied by an increase in the intensity of FTIR signals arising from carbon monoxide and carbon dioxide, clearly indicating that the carbon is reacting with oxygen. In contrary, pure SiCN ceramic (reference sample) derived from HTT1800 and pyrolyzed at 1100 °C does not show a major mass decrease at 450 °C (Fig. 2b). Namely, total mass loss of pure SiCN ceramic amounts to 0.5 wt%, compared to 5.5 wt% of Si:30F:SiCN, assigned mainly to the CO_2 desorption. This finding clearly indicates that only the carbon originating from the fructose precursor is reacting with oxygen and that SiCN ceramic stays unaffected, including the free carbon phase. This is explained by the fact that the free carbon phase originating from the pre-ceramic polymer is formed "in situ" during the pyrolysis process and is embedded in the form of nanodomains [39] in the ceramic matrix, which protects carbon from oxygen. Nevertheless, it should be noted that SiCN derived from HTT1800 is considered as a carbon-poor [42] polymer-derived silicon carbonitride ceramic containing approximately 18 wt% of carbon, corresponding to ca. 8 wt% of free carbon phase when pyrolyzed at 1100 °C in argon atmosphere [31].

In order to track changes in porosity due to additional heat treatment, nitrogen physisorption measurements were performed on non-treated (Si:60F:SiCN) and heat-treated [Si:F:SiCN(60)] composites. The Si:60F:SiCN exhibits a BET specific surface area of 12 m^2g^{-1} which is comparable to the results obtained for polymer-derived SiCN ceramic materials [30, 43]. The BET specific surface area of the sample

Table 2 Specific surface area (SSA), total pore volume (V_t), and micropore volume (V_m) obtained from nitrogen physisorption measurements

Sample name	SSA ($m^2 \cdot g^{-1}$)	V_t ($cm^3 \cdot g^{-1}$)	V_m ($cm^3 \cdot g^{-1}$)
Si:60F:SiCN	12	0.04	0
Si:F:SiCN(60)	167	0.12	0.06

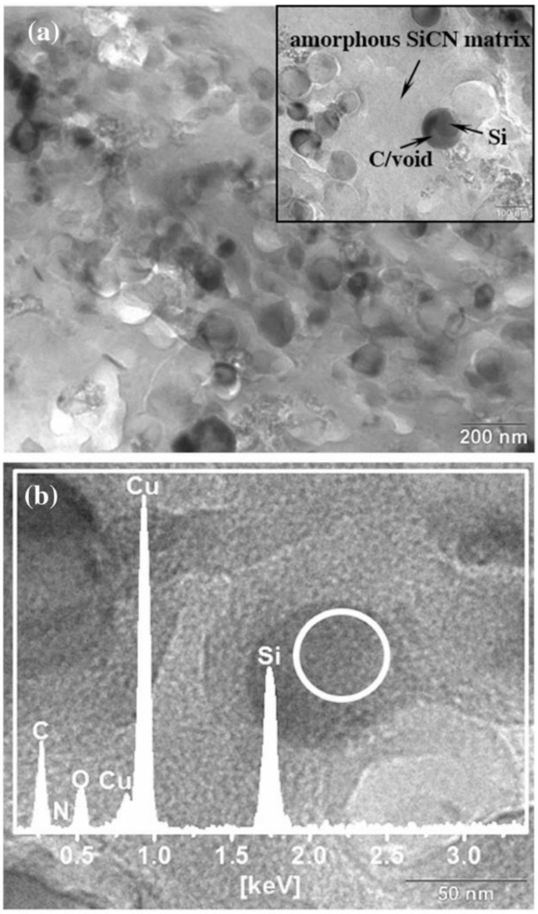

Figure 3 **a** TEM micrographs of Si:F:SiCN(60). **b** TEM micrograph of Si:F:SiCN(60) with EDS pattern of the selected area indicated by *circle*.

annealed in air increases significantly to 167 m^2g^{-1} for Si:F:SiCN(60). The effect of the heat treatment in air can also be seen in the sample porosity characteristics. For instance, total pore volume (V_t) and micropore volume (V_m) of the heat-treated sample are 0.12 and 0.06 cm^3g^{-1}, respectively. This, compared to a total pore volume of 0.04 cm^3g^{-1} and a micropore volume of 0 cm^3g^{-1} of the non-treated sample (Si:60F:SiCN, Table 2), clearly indicates that additional heat treatment in air introduces open porosity to the sample.

Annealing time of 2 h is not long enough to completely burn the carbon (mass loss of about 5.5 %). However, the existence of residual carbon is of advantage as a complete oxidation would cause problems with the electrical conductivity as observed for Si:SiCN composites (see Electrochemical results). TGA and BET measurements imply that a free volume was created; nevertheless, it is not clear, yet where porosity is located.

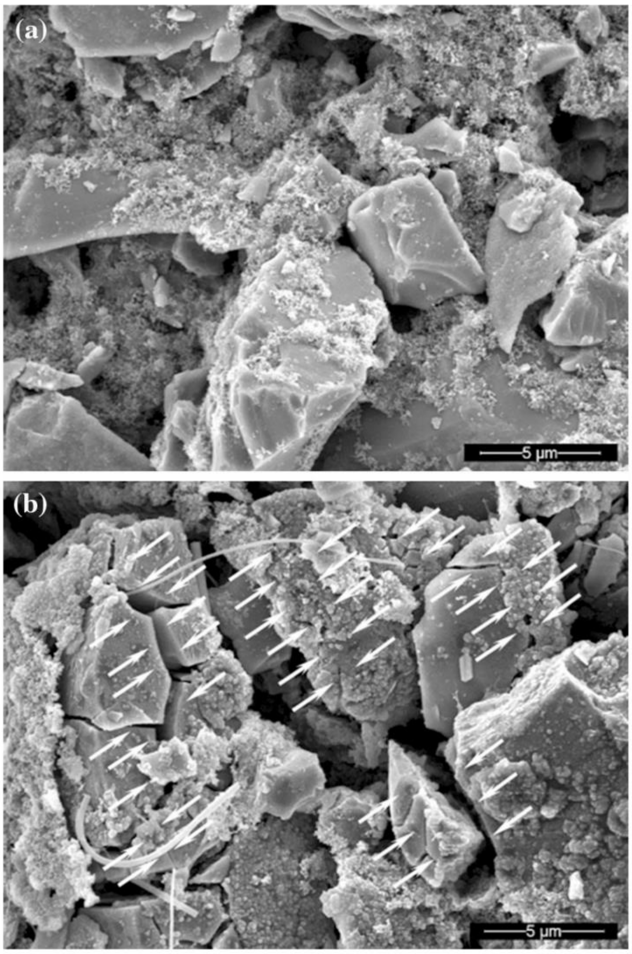

Figure 4 SEM micrographs of Si:30F:SiCN pristine (**a**) and cycled electrode (**b**) (magnification 5000×, observed cracks at cycled electrode are marked with *arrows*).

TEM measurements have been employed to clarify if the porosity is located around the silicon particles. Figure 3 presents TEM micrographs of the sample Si:F:SiCN(60). It demonstrates clearly that silicon particles were successfully coated with carbon prior to embedding. EDS pattern of the selected area (Fig. 3b) reveals that the silicon nanoparticle is present and covered with a SiO_2 layer. Silica scale present on the silicon was most probably created during the additional heat treatment in air which is in line with our TGA measurements (mass gain between 210 and 430 °C). Further, it is still difficult to distinguish whether carbon (or void) and in which amount is present around the silicon particles after the material was heat-treated in air. It should be noted that coating of silicon particles prior to embedding acts beneficially against agglomeration. It is of importance as the distribution of silicon nanopowder in ceramic

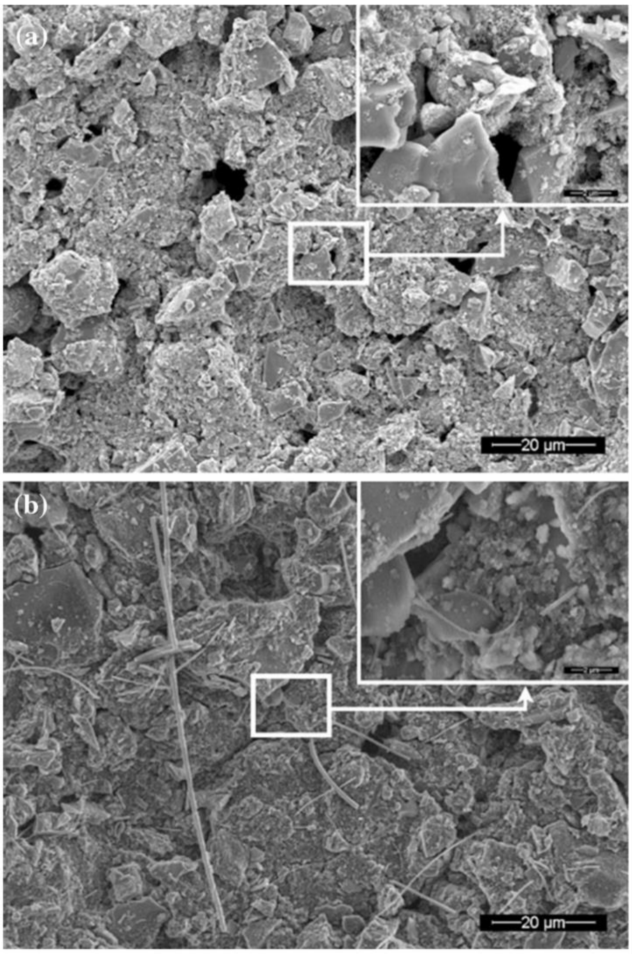

Figure 5 SEM micrographs of Si:F:SiCN(30) pristine (**a**) (magnification 1000× and insert picture at a magnification 10000×) and cycled electrode (**b**) (magnification 1000× and insert picture at a magnification 10000×).

matrixes is of importance for the cycling stability of the prepared composites [27].

Figures 4 and 5 show SEM micrographs of pristine (uncycled) and cycled electrodes of Si:30F:SiCN and Si:F:SiCN(30), respectively. The pristine electrodes show the ceramic particles embedded into a well-distributed, porous matrix of conducting additive and binder. Please note that the fibers on the cycled electrodes are due to the glass fiber separator used. The cycled electrodes of the Si:30F:SiCN reveal severe matrix rupture after cycling (Fig. 4, cracks indicated with arrows). It is concluded that the ceramic matrix is not able to withstand pressure developed by silicon volume increase during alloying with lithium. On the other hand, cycled electrodes of the Si:F:SiCN(30) display almost no cracks even though silicon activity was confirmed by electrochemical investigations.

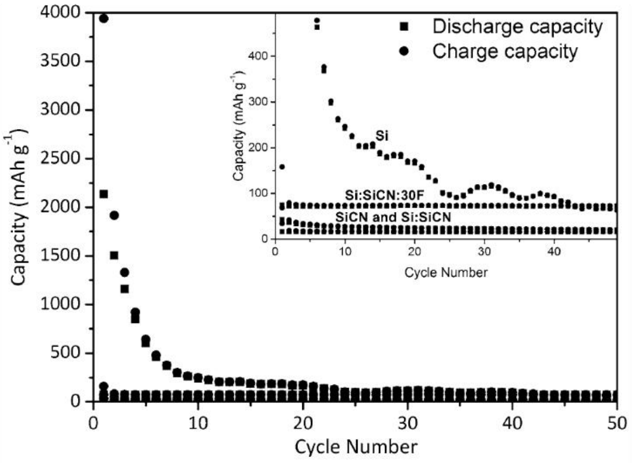

Figure 6 Alloying and dealloying capacities of a silicon reference electrode, SiCN, Si:SiCN, and Si:SiCN:30F cycled at C/50$_{Si}$.

Electrochemical performance

Figure 6 represents the alloying and dealloying capacities of the reference materials, namely the as-received nanosilicon and SiCN derived from HTT1800, Si:SiCN composite, and Si:SiCN covered with carbon (Si:SiCN:30F). The cell containing silicon nanopowder already reaches its end of life during the second cycle if 80 % of the initial capacity is taken as a basis [44]. The electrode made from pure SiCN ceramic derived from HTT1800 is almost inactive for lithium storage as discharge capacity is limited to 23 mAh g^{-1} [31, 45]. Further, charge and discharge capacities of the composite containing 20 wt% of the nanosilicon powder dispersed in the ceramic derived from HTT1800 (Si:SiCN) do not show an effect on the capacity in comparison to the pure ceramic. A first cycle lithiation capacity of about 715 mAh g^{-1} is expected if the silicon (3579 mAh g^{-1} for $Li_{15}Si_4$) present in the matrix would be active. The presence of silicon in the composite is confirmed by X-ray diffraction study (for details please see Supplementary information; S1), but it is obviously electrochemically inactive probably due to lack of electrical contact stemming from poor silicon conductivity and electrochemical inactivity of the SiCN matrix. The electrical conductivity obtained from 4-point measurements of selected composite materials is listed in Table 3. Please note that the values for the conductivity are not absolute values of the composites due to addition of Carbon Black Super P® and PVDF and can only be compared relatively among each other. However, Table 3 reveals that the conductivity of the

Table 3 Electrical conductivity obtained by 4-point measurement of selected composite powders mixed with carbon black and PVDF and pressed to pellets

Precursor	Conductivity (mS·cm^{-1})
SiCN	50
Si:SiCN	44
Si:30F:SiCN	122
Si:60F:SiCN	250
Si:F:SiCN	98
Si:F:SiCN(60)	159

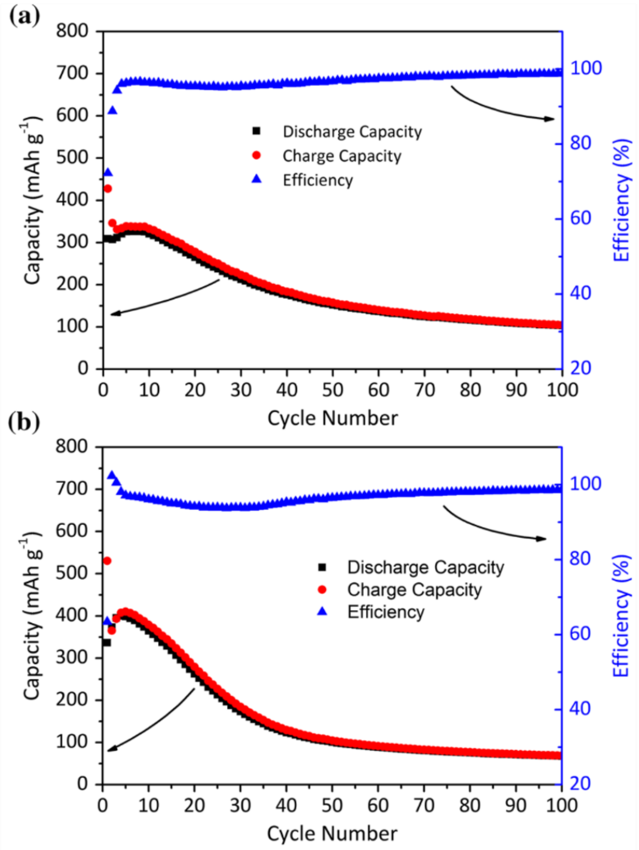

Figure 7 **a** Lithiation and delithiation capacities of Si:60F:SiCN at C/50$_{Si}$. **b** Lithiation and delithiation capacities of Si:F:SiCN(60) at C/50$_{Si}$.

pellets prepared from Si:F:SiCN decreased after the heat treatment but is still higher than that of the material prepared without a carbon covering.

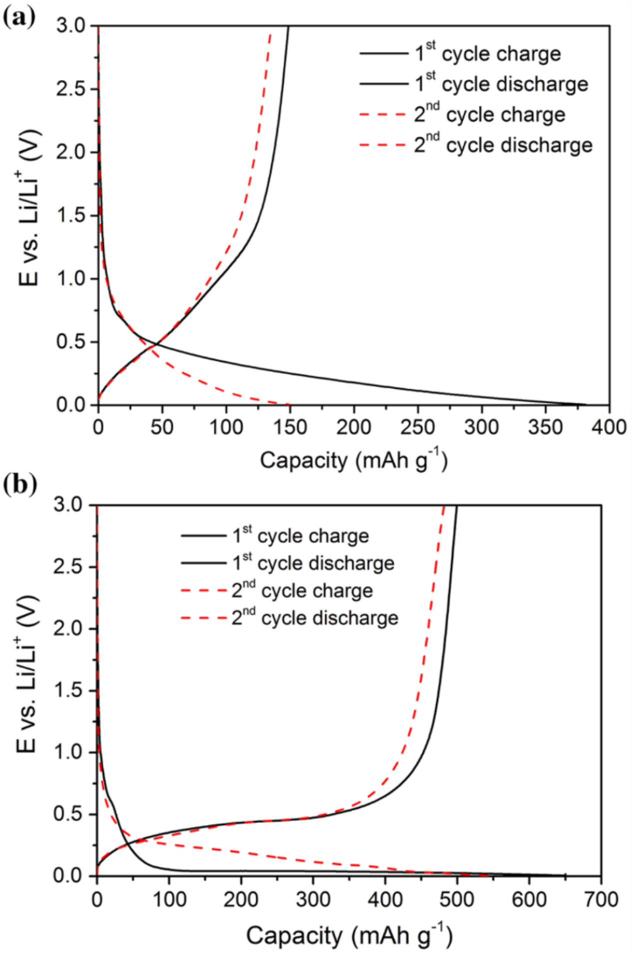

Figure 8 **a** 1st and 2nd cycle lithiation and delithiation curves of Si:SiCN:30F. **b** 1st and 2nd cycle lithiation and delithiation curves of Si:30F:SiCN.

In order to enhance the conductivity and electrochemically activate silicon, carbon coating was applied (Si:SiCN:30F). Unfortunately, simple carbon coating on the surface of the composite does not lead to significant improvement. As it is shown in Fig. 6, the overall capacity increases slightly, compared to that of pure SiCN ceramic and Si:SiCN composite, from 22 mAh g^{-1} to about 73 mAh g^{-1} for Si:SiCN:30F. The increase can be attributed to the additional storage sites provided by the carbon coating itself, but the amount of silicon of the composite is still inactive for lithium storage (Fig. 8a).

The lithiation and delithiation capacities of Si:60F:SiCN and Si:F:SiCN(60), which are obtained after the additional heat treatment in air, are given in Fig. 7. The electrochemical behavior of the corresponding composites with lower amount of carbon, namely Si:30F:SiCN and Si:F:SiCN(30), is presented in S3 (a) and (b), respectively. Both materials display an increase in the capacity and stability compared to Si:SiCN and Si:SiCN:30F low carbon composites. The carbon coating around silicon nanoparticles prior to embedding into the ceramic matrix makes silicon accessible to electrochemical alloying with lithium and brings silicon activity visible on the voltage vs.

capacity curves (plateau at 0.5 V, Fig. 8b) [1]. However, the accessibility of non-stabilized silicon leads to fading capacities. The fading is most pronounced for Si:30F:SiCN which reaches its end of life after six cycles. The higher amount of carbon in Si:60F:SiCN has a beneficial effect on the cycling stability of the composite, increasing the “life” of the cell to 24 cycles. SEM investigation of Si:30F:SiCN cycled electrodes reveals that the ceramic matrix is not able to withstand developed pressure due to Li–Si alloying leading to severe matrix rupture (see Fig. 4b). No improvement of the stability was achieved for Si:F:SiCN(60) in comparison with the untreated composites. However, SEM investigation of the cycled electrodes displays that the matrix did not break upon cycling (see Fig. 5). Pronounced capacity fading could be attributed to a loss of contact between the silicon nanoparticles and matrix (Table 3).

In order to enhance the electrical conductivity of the composite, an additional coating step was applied. It can be seen from Fig. 9 that the cycling stability of the obtained composites, i.e., Si:F:SiCN:30F(30) and Si:F:SiCN:30F(60), is significantly improved. The end of the life of the anode material is reached after 30 and 70 cycles, respectively. However, the consideration that 80 % of the initial delithiation capacity defines the end of the life may be misleading for Si:F:SiCN(60). The initial delithiation capacity is quite low, amounting only 199 mAh g^{-1}, and increases continuously up to the 17th cycle where it reaches a maximum of 297 mAh g^{-1}. Nevertheless, it should be kept in mind that the composites contain ∼16 wt% of silicon, so even with perfect efficiency the present silicon could deliver around 500 mAh g^{-1}.

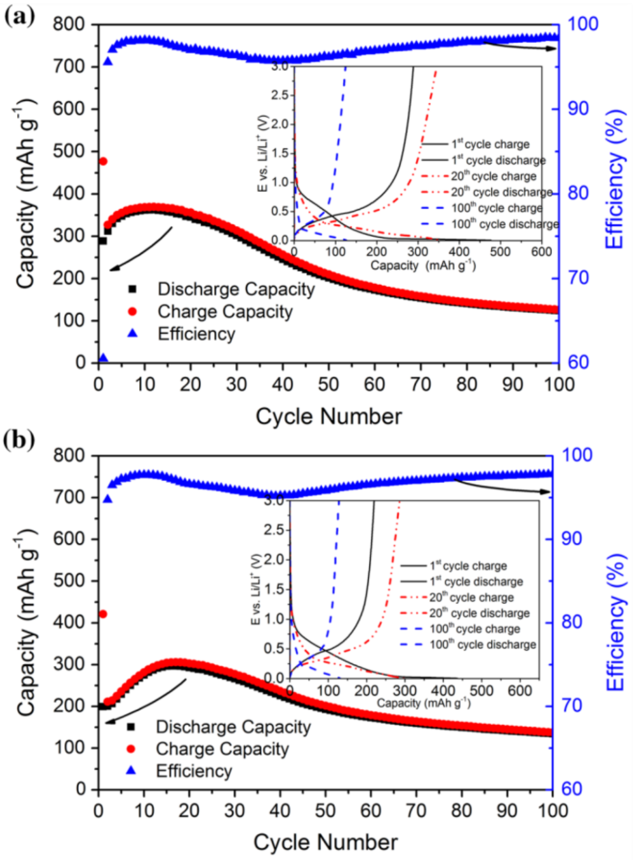

Figure 9 **a** Lithiation and delithiation capacities of Si:F:SiCN:30F(30) at C/50$_{Si}$. **b** Lithiation and delithiation capacities of Si:F:SiCN:30F(60) at C/50$_{Si}$.

Conclusions

Within this work, we describe an environmentally indifferent method to prepare silicon/carbon/silicon carbonitride core/void/shell nanostructures demonstrating enhanced electrochemical stability toward reversible lithium alloying compared to pure crystalline silicon. The multiple coating with fructose-derived carbon and SiCN ceramic accompanied by partial burning of carbon to form voids around silicon particles leads to significant increase in conductivity of composite electrode. Remaining (unburned) carbon allows also for electrochemical accessibility of silicon and its active participation in lithium storage. The formation of hollow space around silicon embedded into the SiCN matrix is demonstrated by a significant increase in the BET specific surface area. TEM imaging shows that the embedding protects silicon nanoparticles against agglomeration.

In conclusion, our TEM study confirms that the voids are located around the silicon particles; moreover, it is shown that carbon coating prevents silicon agglomeration. Significant improvement of the electrochemical stability of the composite is demonstrated as well. The electrodes prepared from composites with voids around silicon display almost no cracks even though silicon activity was confirmed by electrochemical investigations, as shown by SEM micrographs of pristine and cycled electrodes. Further tuning of this preparation method is in progress, as it enables tailoring the size of cavities and silicon content, possibly allowing for further improvements of cycling stability and capacity.

Acknowledgements

We gratefully acknowledge the financial support of the German Research Foundation (DFG) SPP1473/JP8. We thank Christina Schitco for fruitful discussions and attentive manuscript proof reading. Furthermore, we also thank Ulrike Kunz, Claudia Fasel, and Cristina Schitco for their help with material characterization.

Electronic supplementary material: The online version of this article (doi:10.1007/s10853-016-9911-x) contains supplementary material, which is available to authorized users.

References

[1] Obrovac MN, Christensen L (2004) Structural changes in silicon anodes during lithium insertion/extraction. Electrochem Solid-State Lett 7(5):A93–A96

[2] Li J, Dahn JR (2007) An in situ X-ray diffraction study of the reaction of Li with crystalline Si. J Electrochem Soc 154(3):A156–A161

[3] Wachtler M, Besenhard JO, Winter M (2001) Tin and tin-based intermetallics as new anode materials for lithium-ion cells. J Power Sources 94(2):189–193

[4] Liu XH, Zhong L, Huang S, Mao SX, Zhu T, Huang JY (2012) Size-dependent fracture of silicon nanoparticles during lithiation. ACS Nano 6(2):1522–1531

[5] Saint J, Morcrette M, Larcher D, Laffont L, Beattie S, Peres JP, Talaga D, Couzi M, Tarascon JM (2007) Towards a fundamental understanding of the improved electrochemical performance of silicon carbon composites. Adv Funct Mater 17(11):1765–1774

[6] Liu WR, Wang JH, Wu HC, Shieh DT, Yang MH, Wu NL (2005) Electrochemical characterizations on Si and C-coated Si particle electrodes for lithium-ion batteries. J Eletrochem Soc 152(9):A1719–A1725

[7] Yang XL, Wen ZY, Xu XX, Lin B, Lin ZX (2006) High-performance silicon/carbon/graphite composites as anode materials for lithium ion batteries. J Electrochem Soc 153(7):A1341–A1344

[8] Kim I-S, Kumta PN (2004) High capacity Si/C nanocomposite anodes for Li-ion batteries. J Power Sources 136(1):145–149

[9] Kim IS, Blomgren GE, Kumta PN (2004) Si-SiC nanocomposite anodes synthesized using high-energy mechanical milling. J Power Sources 130:275–280

[10] Dimov N, Kugino S, Yoshio M (2003) Carbon-coated silicon as anode material for lithium ion batteries: advantages and limitations. Electrochim Acta 48(11):1579–1587

[11] Mazouzi D, Lestriez B, Roue L, Guyomard D (2009) Silicon composite electrode with high capacity and long cycle life. Electrochem Solid State Lett 12(11):A215–A218

[12] Martin C, Alias M, Christien F, Crosnier O, Belanger D, Brousse T (2009) Graphite-grafted silicon nanocomposite as a negative electrode for lithium-ion batteries. Adv Mater 21(46):4735–4741

[13] Chen B, Flatt AK, Jian H, Hudson JL, Tour JM (2005) Molecular grafting to silicon surfaces in air using organic triazenes as stable diazonium sources and HF as a constant hydride-passivation source. Chem Mater 17(19):4832–4836

[14] Xu YH, Yin GP, Zuo PJ (2008) Geometric and electronic studies of Li15Si4 for silicon anode. Electrochim Acta 54(2):341–345

[15] Martin C, Crosnier O, Retoux R, Belanger D, Schleich DM, Brousse T (2011) Chemical coupling of carbon nanotubes and silicon nanoparticles for improved negative electrode performance in lithium-ion batteries. Adv Funct Mater 21(18):3524–3530

[16] Yang S, Li G, Zhu Q, Pan Q (2012) Covalent binding of Si nanoparticles to graphene sheets and its influence on lithium storage properties of Si negative electrode. J Mater Chem 22:3420–3425

[17] Chen D, Yi R, Chen S, Xu T, Gordin ML, Wang D (2014) Facile synthesis of graphene-silicon nanocomposites with an advanced binder for high-performance lithium-ion battery anodes. Solid State Ionics 254:65–71

[18] Chan CK, Peng H, Liu G, McIlwrath K, Zhang XF, Huggins RA, Cui Y (2008) High-performance lithium battery anodes using silicon nanowires. Nat Nano 3(1):31–35

[19] Chan CK, Ruffo R, Hong SS, Huggins RA, Cui Y (2009) Structural and electrochemical study of the reaction of lithium with silicon nanowires. J Power Sources 189(1):34–39

[20] Vlad A, Reddy ALM, Ajayan A, Singh N, Gohy J-Fo, Melinte S, Ajayan PM (2012) Roll up nanowire battery from silicon chips. Proc Natl Acad Sci 109(38):15168–15173

[21] Kasavajjula U, Wang C, Appleby AJ (2007) Nano- and bulk-silicon-based insertion anodes for lithium-ion secondary cells. J Power Sources 163(2):1003–1039

[22] Wu H, Zheng G, Liu N, Carney TJ, Yang Y, Cui Y (2012) Engineering empty space between Si nanoparticles for lithium-ion battery anodes. Nano Lett 12(2):904–909

[23] Yue L, Zhang W, Yang J, Zhang L (2014) Designing Si/porous-C composite with buffering voids as high capacity anode for lithium-ion batteries. Electrochim Acta 125:206–217

[24] Zhou X, Tang J, Yang J, Xie J, Lulu M (2013) Silicon@-carbon hollow core-shell heterostructures novel anode materials for lithium ion batteries. Electrochim Acta 87:663–668

[25] Li X, Meduri P, Chen X, Qi W, Engelhard MH, Xu W, Ding F, Xiao J, Wang W, Wang C, Zhang J-G, Liu J (2012) Hollow core–shell structured porous Si–C nanocomposites for Li-ion battery anodes. J Mater Chem 22(22):11014–11017

[26] Szczech JR, Jin S (2011) Nanostructured silicon for high capacity lithium battery anodes. Energy Environ Sci 4(1):56–72

[27] Kaspar J, Graczyk-Zajac M, Lauterbach S, Kleebe H-J, Riedel R (2014) Silicon oxycarbide/nano-silicon composite anodes for Li-ion batteries: considerable influence of nano-crystalline vs. nano-amorphous silicon embedment on the electrochemical properties. J Power Sources 269:164–172

[28] Reinold LM, Graczyk-Zajac M, Gao Y, Mera G, Riedel R (2013) Carbon-rich SiCN ceramics as high capacity/high stability anode material for lithium-ion batteries. J Power Sources 236:224–229

[29] Reinold LM, Yamada Y, Graczyk-Zajac M, Munakata H, Kanamura K, Riedel R (2015) The influence of the pyrolysis temperature on the electrochemical behavior of carbon-rich SiCN polymer-derived ceramics as anode materials in lithium-ion batteries. J Power Sources 282:409–415

[30] Baek S-H, Reinold LM, Graczyk-Zajac M, Riedel R, Hammerath F, Buchner B, Grafe H-J (2014) Lithium dynamics in carbon-rich polymer-derived SiCN ceramics probed by nuclear magnetic resonance. J Power Sources 253:342–348

[31] Graczyk-Zajac M, Fasel C, Riedel R (2011) Polymer-derived-SiCN ceramic/graphite composite as anode material with enhanced rate capability for lithium ion batteries. J Power Sources 196(15):6412–6418

[32] Bhandavat R, Singh G (2012) Improved electrochemical capacity of precursor-derived Si(B)CN-carbon nanotube composite as Li-Ion battery anode. ACS Appl Mater Inter 4(10):5092–5097. doi:10.1021/am3015795

[33] Reinold LM, Graczyk-Zajac M, Fasel C, Riedel R (2011) Prevention of solid electrolyte interphase damaging on silicon by using polymer derived SiCN ceramics. ECS Trans 35:37–44

[34] David L, Bhandavat R, Barrera U, Singh G (2015) Polymer-derived ceramic functionalized MoS2 composite paper as a stable lithium-ion battery electrode. Scientific Rep 5(9792):1–7

[35] David L, Bernard S, Gervais C, Miele P, Singh G (2015) Facile synthesis and high rate capability of silicon carbonitride/boron nitride composite with a sheet-like morphology. J Phys Chem C 119(5):2783–2791

[36] David L, Asok D, Singh G (2014) Synthesis and extreme rate capability of SiAlCN functionalized carbon nanotube spray-on coatings as Li-Ion battery electrode. ACS Appl Mater Inter 6(18):16056–16064

[37] Bhandavat R, Singh G (2013) Stable and efficient Li-Ion battery anodes prepared from polymer-derived silicon oxycarbide carbon nanotube shell/core composites. J Phys Chem C 117(23):11899–11905. doi:10.1021/jp310733b

[38] Joho F, Novak P, Spahr ME (2002) Safety aspects of graphite negative electrode materials for lithium-ion batteries. J Electrochem Soc 149(8):A1020–A1024

[39] Mera G, Navrotsky A, Sen S, Kleebe H-J, Riedel R (2013) Polymer-derived SiCN and SiOC ceramics—structure and energetics at the nanoscale. J Mater Chem A 1(12):3826–3836

[40] Sing KSW, Everett DH, Haul RAW, Moscou L, Pierotti RA, Rouquerol J, Siemieniewska T (1985) Reporting physisorption data for gas/solid systems with special reference to the determination of surface area and porosity. Pure Appl Chem 57(4):603–619

[41] de Boer JH, Linsen BG, van der Plas T, Zondervan GJ (1965) Studies on pore systems in catalysts: VII. description of the pore dimensions of carbon blacks by the t method. J Catal 4(6):649–653

[42] Colombo P, Riedel R, Soraru GD, Kleebe H-J (2010) Polymer derived ceramics: from nano-structure to applications. DEStech Publications Inc, Lancaster

[43] Schitco C, Bazarjani MS, Riedel R, Gurlo A (2015) NH3-assisted synthesis of microporous silicon oxycarbonitride ceramics from preceramic polymers: a combined N2 and CO2 adsorption and small angle X-ray scattering study. J Mater Chem A 3:805–818

[44] Park J-K (2012) Principles and applications of lithium secondary batteries. Wiley-VCH Verlag GmbH & Co, KGaA

[45] Graczyk-Zajac M, Wimmer M, Neumann C, Riedel R (2015) Lithium intercalation into SiCN/disordered carbon composite. Part 1: influence of initial carbon porosity on cycling performance/capacitygraczyk2015. J Solid State Electrochem 19:2763–2769

Solid State Ionics 302 (2017) 66–71

Contents lists available at ScienceDirect

Solid State Ionics

journal homepage: www.elsevier.com/locate/ssi

Novel 3D Si/C/SiOC nanocomposites: Toward electrochemically stable lithium storage in silicon

D. Vrankovic *, K. Wissel, M. Graczyk-Zajac, R. Riedel

Department of Materials and Earth Sciences, Technical University Darmstadt, Germany

ARTICLE INFO

Article history:
Received 1 August 2016
Received in revised form 13 October 2016
Accepted 4 November 2016
Available online 12 November 2016

ABSTRACT

In this work, we present an easy and environmentally friendly approach to stabilize nanostructured, porous crystalline (Si_{tc}) and amorphous (Si_{sa}) silicon synthesized via magnesiothermic reduction. As matrix, fructose-derived carbon, polymer-derived SiOC ceramic or both, carbon and SiOC, are used. By means of X-ray diffraction and Raman spectroscopy it is found that the crystallinity of Si_{tc} as well as the amorphous character of Si_{sa} is preserved in the final composites. Embedding of crystalline silicon into carbon leads to high initial capacities of ~600–650 $mAh \cdot g^{-1}$, but only the matrix consisting of carbon and SiOC results in a stable cycling behaviour over 50 cycles with a final capacity of 575 $mAh \cdot g^{-1}$. All composites derived from amorphous Si_{sa} show a stable cycling behaviour; the highest, stable capacity of ~500 $mAh \cdot g^{-1}$ is observed when silicon is covered with carbon and SiOC.

1. Introduction

In order to meet the ever increasing power requirements, current lithium battery technology needs improvement. Significant effort has already been made in developing high gravimetric and volumetric capacity batteries through improving all aspects of battery materials: cathode, anode, electrolyte, and separators [1,2]. Looking more closely to the anode materials, silicon based electrodes seem to meet most of the requirements proposed for new generation of Li-ion batteries. Availability, and outstanding specific and volumetric capacity imposes silicon as promising high capacity alternative to commercially used graphite anodes [3–5].

Compared to graphite with a stoichiometric limit of one Li-ion per six carbon atoms resulting in 372 $mAh \cdot g^{-1}$, the Si-Li alloy ($Li_{15}Si_4$) with specific capacity of 3579 $mAh \cdot g^{-1}$ [6] brings about ten times higher capacity.

Despite these advantages, large volume changes (about 260%) during alloying/dealloying with lithium remain a drawback for a commercial use of silicon-based electrodes. Stress generated by volume change causes cracking and pulverization of the electrode and finally leads to the loss of electric contact between the active material and the current collector. This consequently brings a rapid fading of the capacity with ongoing cycling. Furthermore, the large volume expansion leads to an unstable solid electrolyte interface (SEI) on the silicon surface. This brings the unprotected active material into contact with the electrolyte causing SEI thickening followed by irreversible capacity losses with ongoing cycling [7,8].

In order to overcome this fundamental issue and to improve the cycling stability of silicon anodes, numerous approaches are proposed in the literature: (i) keeping the size of Si particles below a threshold value (about 150 nm) [9], (ii) synthesis of nano-silicon-carbon composites with cavities around the silicon particles [3,10–14], (iii) embedding of nanosilicon particles into an active or inactive matrix [15–20], (iv) chemical bonding of silicon nanoparticles to a binder or conductive additive [21–27], (v) utilization of nanotubes, nanowires, nanostructured particles, etc. [28–30].

The aforementioned porous silicon nanostructures mostly require very expensive starting materials or high processing costs, limiting their practical application. As a promising alternative, Bao et al. [31] reported that SiO_2 can be reduced to Si in the presence of magnesium, following the reaction (1).

$$SiO_{2(s)} + 2Mg_g \rightarrow Si_{(s)} + 2MgO_{(s)} \tag{1}$$

Ever since, significant amount of work has been done in order to optimize this approach to provide a facile, feasible and environmental friendly approach to synthesize nanostructured porous silicon materials for battery application [32–36]. The porosity offers a large surface area accessible to the electrolyte, short Li-ion diffusion path, and void spaces necessary for volume expansion. This leads to an effective release and/or homogeneous strain-stress distribution within the structure.

However, nanostructured silicon electrodes face some important challenges as well. Although high surface-to-volume ratios can boost the transfer of lithium from the solvent to the active material achieving high rates, but at the same time electrodes suffer from poor volumetric storage capacity. Embedding nanostructured silicon in an inexpensive matrix, able to provide sufficient ion and charge transfer, achieving

---

* Corresponding author.
E-mail address: vrankovic@materials.tu-darmstadt.de (D. Vrankovic).

http://dx.doi.org/10.1016/j.ssi.2016.11.009
0167-2738/

additional storage capacity and stability against thermal runaway could be a promising solution to the above-mentioned problems with nanostructured silicon-based systems.

The electrochemical properties of silicon oxycarbide (SiOC) ceramics with respect to a reversible storage of lithium ions have been studied in the middle of the 1990′s for the first time [37–42]. SiOC materials are typically prepared by the thermal conversion of polyorganosiloxanes under inert atmosphere, by a so-called polymer-derived ceramic (PDC) process [43,44], or alternatively by the sol-gel method [45–47]. The microstructure of SiOC ceramics is typically composed of an amorphous Si-O-C network, which is interpenetrated by an amorphous free carbon phase. The amorphous Si-O-C network is built of tetrahedrally coordinated $SiO_{4-x}C_x$ ($x = 1–4$) structural units, including SiO_2 and C-enriched regions [48–52]. Among the various chemical compositions of SiOC, stoichiometries with an exceptionally high content of carbon are considered as perspective anode materials in terms of high gravimetric capacity, good rate capability and reliable cycling stability [53–68].

In our former works, we demonstrated that polymer-derived ceramics provide also a stable and inexpensive matrix to stabilize commercial silicon powders. Reinold et al. [69] showed the advantage of using polymer-derived silicon carbonitride (SiCN) ceramic as an inactive matrix for crystalline silicon nanopowder (30–50 nm) and stated a protective character of polymer-derived ceramics as matrix in terms of SEI stabilization for samples prepared at 1100 °C. Kaspar et al. [70] reported on composite materials based on commercially available silicon particles dispersed in a polymer-derived silicon oxycarbide (SiOC) matrix.

Fabrication of porous electrode structures to accommodate the large volume changes of silicon has also drawn a lot of attention. Among all, core-shell structures with cavities around the silicon particles have been investigated in detail [10–14].

Within this work, mesoporous nanostructured 3D amorphous/crystalline silicon obtained via magnesiothermic reduction [71] (this issue of SSI) is stabilized in a conductive matrix. As matrix, environmentally friendly organic carbon and polymer-derived SiOC ceramic are used. It is found, that the morphology and crystallinity of the starting silicon significantly influences the composites electrochemical performance.

2. Experimental part

Crystalline and amorphous mesoporous silicon nanopowders were prepared from monodisperse silica using magnesiothermic reduction as described in [71] (this issue of SSI). Two silicon nanopowders, synthesized through two-chamber (tc) and NaCl assisted (sa) routes were used for preparation of four different composites, as listed in Table 1.

In order to synthesize monodisperse SiO_2 nanoparticles, modified Stöber method was used [71] (this issue of SSI). Further optimisation and precise tailoring of used reaction conditions (pH, concentration, processing conditions) were performed to obtain silica particles of desired size and shape. Received silica was further used as starting material for magnesiothermic reduction reaction via two different routes. Namely, two-chamber method adopted and further optimized from reference [35] and NaCl assisted route adopted and optimized according to reference [36]. The obtained silicon using two-chamber route exhibited BET specific surface area (SSA) of 198 $m^2\ g^{-1}$ and average particle size of 56 nm (see Table 1). Additionally, an X-ray diffraction study shows crystalline nature of as prepared silicon. The silicon prepared using NaCl assisted route shows SSA of 623 $m^2\ g^{-1}$, average particle size of 35 nm and completely amorphous nature.

The particle size distribution of prepared silica and derived silicon was measured by dynamic laser light scattering (DLS) using a Zetasizer Nano ZS (Malvern). The powder was dispersed in water using an ultrasonic processor UP 200S (Hielscher-Ultrasound Technology). The particle size distribution and the cumulative numbers were used to determine the D_{50} value of the samples.

A carbon coating procedure was elaborated by us and is described elsewhere [14]. D-(−)-Fructose (purity >99%, Sigma-Aldrich) was dissolved in an ethanol/water mixture (ratio 9:1). The silicon nanopowders were uniformly dispersed in the solution of fructose using an IKA dispersing device (T25 digital ULTRA TURRAX®, IKA). Following, the solvents were evaporated and the carbonization was performed under a constant argon flow at 1100 °C in tubular furnace.

For SiOC coating, either nanostructured silicon (crystalline or amorphous), or nanostructured silicon coated with carbon were dispersed in the preceramic organosilicon polymer (RD-684a, Starfire Systems Inc.) with acetone (purity > 99.9%, Sigma-Aldrich) to adjust the viscosity. Solvents were evaporated and the obtained mixture was pyrolyzed under a constant argon flow at 1100 °C using a quartz Schlenk tube and quartz crucible. The heating and cooling rates were set to 100 $°C \cdot h^{-1}$ and the dwelling time was amounted for 3 h. An additional crosslinking step was applied at 250 °C with dwelling time of 3 h.

The as obtained composite materials were ground by hand and sieved with mesh size of 40 μm.

X-ray powder diffraction was performed on the as prepared powders using a STOE STADI P (STOE, Germany) equipped with monochromatic Mo-K_α radiation in flat-sample transmission geometry.

Micro-Raman spectra were recorded with a confocal micro-Raman spectrometer Horiba HR 800 (Horiba, Japan), using an Ar-Ion laser with a wavelength of 514.5 nm. Spectra were recorded in a Raman shift range from 0 to 4000 cm^{-1}.

For electrochemical testing, the prepared powders were mixed with 5 wt% of Carbon Black Super P® (Timcal Ltd., Switzerland) as conducting additive and 10 wt% of polyvinylidene fluoride (SOLEF®PVDF, Solvay, Germany) dissolved in *N*-methyl-2-pyrrolidone (NMP, BASF, Germany) as a binder. Additional NMP was added to adjust the viscosity of the mixture. The obtained slurry was printed on the rough side of a copper foil (10 μm, Copper SE-Cu58 (C103), Schlenk Metallfolien, Germany) by doctor blade technique and dried at 40 °C for 24 h. Electrodes of 10 mm diameter were cut out of the coated copper foil and dried at 80 °C under vacuum in a Buchi oven for 24 h. The dried electrodes were transferred without further contact with air to a glove box (MBraun, Germany) for cell assembly (Swagelok® type cell). The counter/reference electrode with a diameter of 10 mm was cut out of a metallic lithium foil (99.9%

Table 1
Overview of prepared composites including the corresponding properties of used silicon: specific surface area (SSA), total pore volume (V_t), D_{50} value and weight ratios of silicon to carbon and SiOC coating.

Composite name	Sample name	Si synthesis route	SSA [$m^2\ g^{-1}$]	Total pore volume [$cm^3\ g^{-1}$]	D_{50} [nm]	Si:carbon (wt%) after carbonization	Si:SiOC (wt%) after pyrolysis
Si_{tc}:30C	Si_{tc}	Two chamber	198	0.75	56	7:3	–
Si_{tc}:60C	Si_{tc}	Two chamber	198	0.75	56	2:3	–
Si_{tc}:SiOC	Si_{tc}	Two chamber	198	0.75	56	–	1:4
Si_{tc}:30C:SiOC	Si_{tc}	Two chamber	198	0.75	56	7:3	1:4
Si_{sa}:30C	Si_{sa}	NaCl assisted	623	1.13	35	7:3	–
Si_{sa}:60C	Si_{sa}	NaCl assisted	623	1.13	35	2:3	–
Si_{sa}:SiOC	Si_{sa}	NaCl assisted	623	1.13	35	–	1:4
Si_{sa}:30C:SiOC	Si_{sa}	NaCl assisted	623	1.13	35	7:3	1:4

purity, 0.75 mm thickness, Alfa Aesar, Germany). QMA (Whatmann TM, UK) was used as a separator. As electrolyte 180 μl of 1 M LiPF6 dissolved in EC:DMC-1:1 (Solvionic, France) was used. For gravimetric capacity calculation, the mass of active material was used. The active electrode mass excludes the mass of the carbon black and PVDF used in electrode preparation. The testing was performed with VMP multipotentiostat (BioLogic Science instruments, France) at charging/discharging rate of 72 mA·g^{-1} between 0.005 and 3 V.

3. Results and discussion

3.1. X-ray diffraction study

Fig. 1a and b present the X-ray diffraction patterns of nanostructured silicon obtained via two-chamber route and NaCl assisted route with the corresponding composites, respectively. The diffractograms shown in Fig. 1a reveal explicitly the crystalline nature of as prepared silicon, with crystallinity remaining unaffected by embedding. The intensity of reflexes corresponding to crystalline silicon decreases significantly when the amount of amorphous matrix increases.

Fig. 1b shows no sharp reflexes confirming the amorphous nature of the silicon derived by the NaCl assisted route. Furthermore, Si remains amorphous after exposition to 1100 °C during the composite preparation. This finding indicates the highly disordered nature of silicon derived by the NaCl route, since the crystallization of commercial amorphous silicon is usually observed at ~900 °C [70,72].

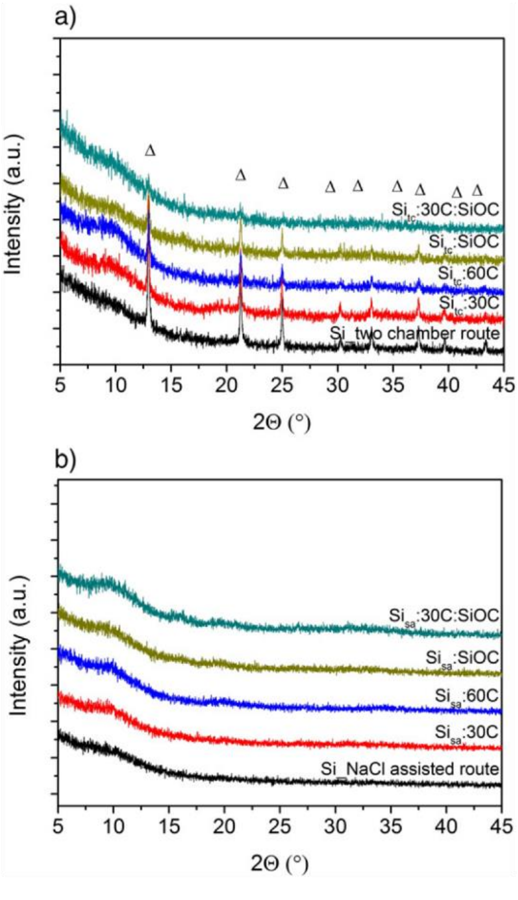

Fig. 1. X-ray diffraction patterns of the investigated composites compared to pure silicon obtained by: a) two-chamber route; b) NaCl assisted route. Silicon reflexes according to the powder diffraction file [27–1402] are marked with Δ.

3.2. Raman spectroscopy measurements

The Raman spectra of the composites, compared to the starting silicon powders, are given in Fig. 2a and b for two-chamber and salt-assisted route, respectively. For both routes, spectra obtained on pure starting material show the same features attributed to the characteristic vibrations of silicon. The most prominent band is located at about 510 cm^{-1} being the first-order optical phonon mode (TO) of crystalline silicon. This band is shifted toward a smaller wave number compared to monocrystalline Si (521 cm^{-1}) due to the nanoscale of the silicon powder. This finding confirms the results of the X-ray diffraction study, namely a pronounced broadening of silicon reflexes attributed to the nanosized crystallites [71] (this issue of SSI). The second-order transverse phonon mode (2TA) at around 300 cm^{-1} and the second-order optical phonon mode (2TO) at around 950 cm^{-1} are also visible whereby the intensities of these bands are depending on the intensity of the first-order optical phonon mode. The Raman spectrum of Si$_{sa}$ in Fig. 2b shows bands related to crystalline Si, although no sharp reflexes are identified by XRD (Fig. 1b). It indicates that the amorphous Si undergoes recrystallization under the laser irradiation [73]. For the composites prepared with amorphous Si from the salt-assisted route, no bands associated with crystalline Si are found (Fig. 2b). A recrystallization of the amorphous Si under the laser irradiation, as observed for pure silicon, is hindered since Si is embedded into a matrix consisting of C and/or SiOC, which acts as a shield.

In all composites containing crystalline Si$_{tc}$ (Fig. 2a), a sharp band between about 500 cm^{-1} and 510 cm^{-1} corresponding to the first-order optical phonon mode (TO) of crystalline Si is visible.

In all spectra of the composite materials, strong bands characteristic for carbonaceous materials appear. The D mode present at around

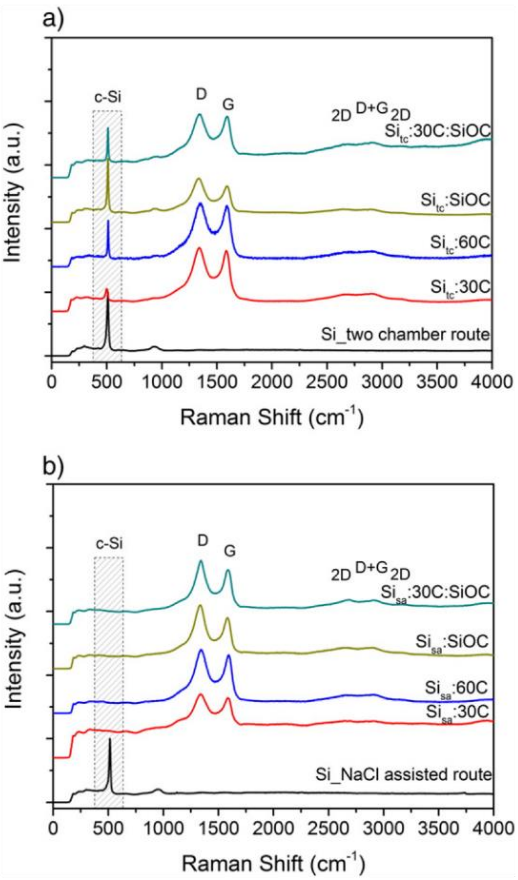

Fig. 2. Raman spectra of the investigated composites compared to pure silicon obtained by: a) two-chamber route and b) salt-assisted route.

1335 cm^{-1} is caused by disorder-induced breathing motions of six-fold aromatic rings. The G mode at around 1580 cm^{-1} is induced by in-plane bond stretching of sp^2 hybridized C atoms. The 2D bands at about 2700 cm^{-1} and 3200 cm^{-1} are attributed to second-order vibration modes of the D band. The band at about 2950 cm^{-1} is the D + G combination mode induced by carbon disorder. The higher intensity of the D band in comparison to the G band suggests that the carbon phase is amorphous and predominantly disordered which is in accordance with absence of graphitic reflexes in the XRD patterns [74–77].

3.3. Electrochemical characterization

Fig. 3 presents an example of the 1st cycle voltage vs. capacity curves of the composites containing silicon synthesized via two-chamber route. The profiles of Si_{sa} and related composites are similar and can be found in Supplementary information (Fig. S1). Presented profiles reveal pronounced silicon activity for all materials independently of used matrix [78]. During the first lithiation, the plateau at ~0.75 V corresponding to the formation of solid electrolyte interface (SEI) is visible. This plateau vanishes completely after the first cycle indicating that stable SEI is formed (see Fig. S2). Taking the large specific surface area of starting silicon into account, particularly in the case of salt-assisted route, the protective character of employed matrix materials should be emphasized. The losses related to SEI formation are significantly suppressed, when compared to pure Si_{tc} or Si_{sa} [71] (this issue of SSI), nevertheless Si_{tc}:30C still shows significant losses, indicating incomplete coverage of silicon. When the amount of carbon around silicon is increased, e.g. Si_{tc}:60C, losses attributed to SEI are further suppressed.

The lithiation and delithiation capacities of all composites are presented in Fig. 4a and 5a, for two-chamber and salt-assisted route, respectively. Fig. 4b and 5b present analogous graphs with capacities recalculated with respect to the amount of silicon, namely considering exclusively silicon as an active material. Carbon coated composites, Si_{tc}:30C and Si_{sa}:30C exhibit low initial capacities of 758 and 967 $mAh \cdot g^{-1}$ vs. amount of silicon, respectively (see Tables 2 and 3) indicating partial inactivity of embedded silicon. Nevertheless, the cycling stability is significantly improved with respect to pure silicon nanopowder and stable SEI is formed. Increasing the carbon amount further, enhances the cycling stability as well as silicon accessibility. The Si_{tc}:60C shows about 660 $mAh \cdot g^{-1}$ (1657 $mAh \cdot g^{-1}$ when calculated versus active silicon) for the first cycle discharge capacity with 73% of coulombic efficiency indicating that almost 50% of silicon contributed to the first cycle discharge capacity. When amorphous silicon (Si_{sa}:60C) is used, its electrochemical activity is significantly lower (29%) but the cycling stability and coulombic efficiency (>99.8% after 9th cycle and 100% after the 14th cycle) are significantly enhanced. Further, retained capacity after 50 cycles is 93% of the initial delithiation capacity. Please note that the calculations of capacity versus active silicon (Table 2, Fig. 4b and 5b) should be treated cautiously, because neither contribution of low-capacity amorphous carbon (~50 $mAh \cdot g^{-1}$ for 60 wt% of C around Si) nor SiOC was taken into account.

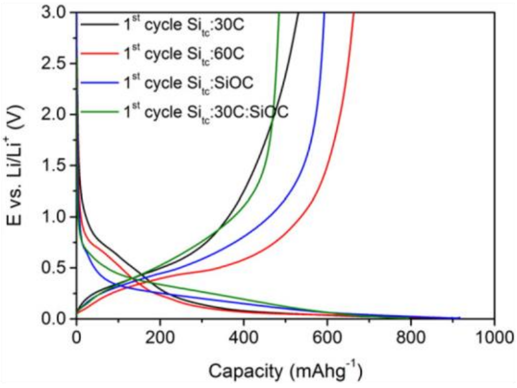

Fig. 3. 1st cycle lithiation and delithiation curves of composites containing silicon synthesized via two-chamber route.

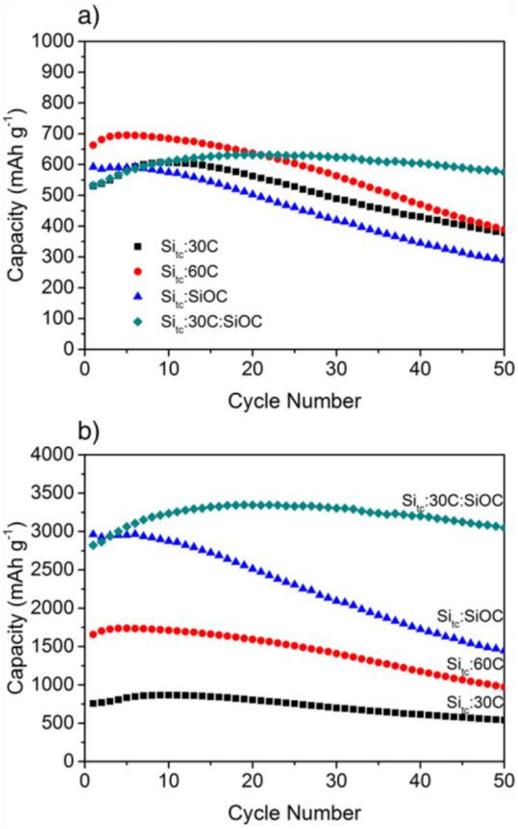

Fig. 4. a) Delithiation capacities of composites prepared by using silicon prepared via two-chamber route; b) Delithiation capacities normalized to amount of silicon present in composites.

Furthermore, HF etching of electrochemically inactive silica possibly remaining after magnesiothermic reduction and/or formed during processing of synthesized silicon has not been performed. HF treatment was omitted by purpose, since the native silica acts as protection barrier against carbothermal reduction of silicon leading to formation of electrochemically inactive SiC on silicon surface [70]. However, this remaining silica should also be considered as dead weight when the electrochemical performance of the composites is evaluated. Resuming to the arguments listed above, one should consider capacities calculated with respect to the silicon mass as relative values to be compared among others and not considered as absolute values.

Figs. 4 and 5 also show electrochemical performances of silicon stabilized by SiOC or a combination of carbon and SiOC. Si_{tc}:SiOC shows enhanced Si accessibility in first cycles leading to higher initial capacities (83% of Si contributing to first discharge capacity; 2963 $mAh \cdot g^{-1}$ vs. Si) but it is followed by continuous capacity fading with ongoing cycling. The system shows a retained capacity after 50 cycles of just 49%. However, when coating silicon with carbon prior to embedding into the ceramic matrix, the cycling stability of the Si_{tc} is significantly improved. Si_{tc}:30C:SiOC shows continuous increase in delithiation capacity until the 17th cycle (from 533 to 631 $mAh \cdot g^{-1}$; 2862 to 3343 $mAh \cdot g^{-1}$ vs Si) indicating that the embedded silicon still gets activated upon cycling. A combination of carbon and ceramic brings thus a superior stability. It is believed that carbon provides sufficient conductivity, improves buffering and delivers coffining effect while the SiOC ceramic brings necessary support and preserves electrode integrity. Instead of 108% of retained delithiation capacity after 50 cycles (marked with "*" in Table 2), a more realistic value of 91% with respect to the delithiation

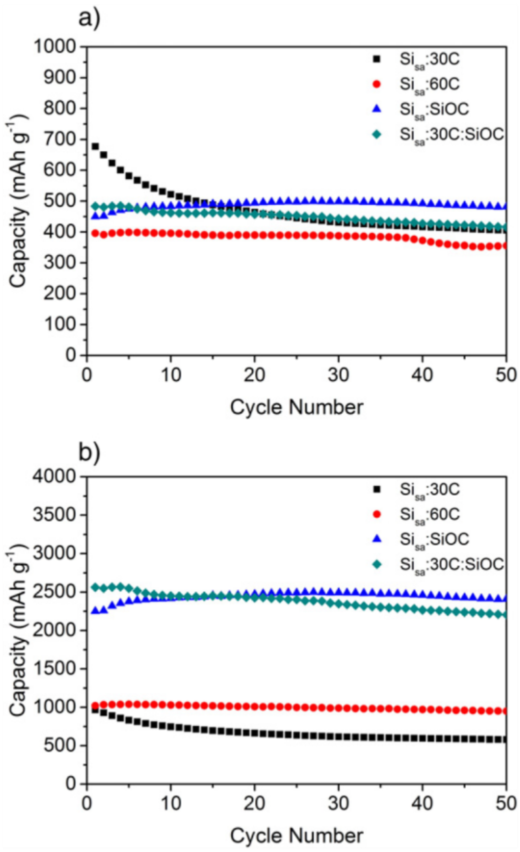

Fig. 5. a) Delithiation capacities of composites prepared by using silicon prepared via salt-assisted route; b) Delithiation capacities normalized to amount of silicon present in composites.

capacity of the 17th cycle should be considered. Nevertheless, the composite Si$_{tc}$:30C:SiOC shows much better cycling stability than reported for commercial crystalline silicon [35,36,70].

Amorphous silicon derived via salt-assisted route, exhibits a significantly larger surface area of 623 m^2 g^{-1} compared to 198 m^2 g^{-1} measured for two-chamber silicon. Additionally, fine tuning of the silica preparation route (SiO$_2$ particles of 35 nm in diameter) coupled with optimized magnesiothermic reduction lead to significantly higher SSA, compared to 214 m^2 g^{-1} obtained by Wang et al. using similar approach [36]. The SiOC and C/SiOC composites derived from amorphous silicon demonstrate extremely stable cycling behaviours and high coulombic efficiencies. This indicates that due to the developed porosity silicon is able to maintain its structure during lithiation/delithiation with relatively low amount of developed internal stresses. Si$_{sa}$:SiOC exhibits 98% of retained delithiation capacity after 50 cycles (considering delithiation capacity of the 17th cycle) and a coulombic efficiency of >99.9% after the 10th cycle. However, obtained discharge capacities with respect to silicon mass barely exceeded 2500 mAh·g^{-1} for Si$_{sa}$:SiOC and Si$_{sa}$:30C:SiOC indicating partial inactivity of embedded silicon. This could be associated with highly porous and small silicon particles prone to agglomerate leaving some parts without electrical contact. Moreover, due to high SSA more SiO$_2$ is formed on the surface resulting in much higher dead weight leading to lower capacity.

Table 2
Amount of silicon in composite, 1st cycle lithiation and delithiation capacity normalized to amount of silicon in composite and coulombic efficiency of the GCPL measurements displayed in Figs. 4 and 5.

Composite name	Si amount in composite [%]	C_{lith} 1st $_{cycle}$ vs Si [mAh·g^{-1}]	C_{delith} 1st $_{cycle}$ vs Si [mAh·g^{-1}]	η [%]
Si$_{tc}$:30C	70	1283	758	59
Si$_{tc}$:60C	40	2282	1657	73
Si$_{tc}$:SiOC	20	4580	2963	65
Si$_{tc}$:30C:SiOC	18.87	4604	2862	61
Si$_s$:30C	70	1542	967	63
Si$_s$:60C	40	1660	1020	61
Si$_s$:SiOC	20	3746	2251	60
Si$_s$:30C:SiOC	18.87	4542	2563	56

Table 3
1st and 50th cycle lithiation and delithiation capacity, coulombic efficiency and cycling stability of the GCPL measurements displayed in Figs. 4 and 5.

Composite name	C_{lith} 1st $_{cycle}$ [mAh·g^{-1}]	C_{delith} 1st $_{cycle}$ [mAh·g^{-1}]	η [%]	C_{lith} 50th $_{cycle}$ [mAh·g^{-1}]	C_{delith} 50th $_{cycle}$ [mAh·g^{-1}]	Cycling stability [%]
Si$_{tc}$:30C	898	530	59	387	379	72
Si$_{tc}$:60C	913	663	73	402	389	59
Si$_{tc}$:SiOC	916	593	65	292	289	49
Si$_{tc}$:30C:SiOC*	869	533	61	579	575	108
Si$_s$:30C	1079	677	63	404	405	60
Si$_s$:60C	664	408	61	379	379	93
Si$_s$:SiOC*	749	450	60	482	482	107
Si$_s$:30C:SiOC	857	484	56	416	416	86

4. Conclusions

Within this work, we demonstrate simple, environmentally indifferent and feasible approach to prepare nanostructured silicon based composite anodes with fair capacities and high cycling stability. Advanced tailoring of magnesiothermic reduction reaction allows for preparation of 3D nanostructured silicon with defined porosity. Enhanced nanostructuring of the silicon of monodisperse and spherical nanoparticles provides sufficient void spaces allowing volume expansion. Synthesized silicon is embedded into carbon and/or silicon oxycarbide matrix in order to provide sufficient electrical conductivity, protect the large silicon surface from electrolyte and preserve the electrode integrity. The coating with electronically conductive carbon/SiOC leads to stable electrochemical performance of the composites and extraction capacities of ~500 mAh·g^{-1} and 575 mAh·g^{-1} for the composites containing amorphous and crystalline silicon, respectively.

Supplementary data to this article can be found online at http://dx.doi.org/10.1016/j.ssi.2016.11.009.

Acknowledgments

We gratefully acknowledge the financial support of the German Research Foundation (DFG) SPP1473/JP8.

References

[1] S.D. Beattie, D. Larcher, M. Morcrette, B. Simon, J.M. Tarascon, J. Electrochem. Soc. 155 (2) (2008) A158.
[2] J.B. Goodenough, Y. Kim, Chem. Mater. 22 (3) (2010) 587.
[3] U. Kasavajjula, C. Wang, A.J. Appleby, J. Power Sources 163 (2) (2007) 1003.
[4] J.R. Szczech, S. Jin, Energy Environ. Sci. 4 (1) (2011) 56.
[5] B. Liang, Y. Liu, Y. Xu, J. Power Sources 267 (2014) 469.
[6] S. Ohara, J. Suzuki, K. Sekine, T. Takamura, J. Power Sources 136 (2) (2004) 303.
[7] M. Wachtler, J.O. Besenhard, M. Winter, J. Power Sources 94 (2) (2001) 189.
[8] M. Winter, W.K. Appel, B. Evers, T. Hodal, K.-C. Möller, I. Schneider, M. Wachtler, M.R. Wagner, G.H. Wrodnigg, J.O. Besenhard, Monatsh. Chem. 132 (4) (2001) 473.
[9] X.H. Liu, L. Zhong, S. Huang, S.X. Mao, T. Zhu, J.Y. Huang, ACS Nano 6 (2) (2012) 1522.
[10] H. Wu, G. Zheng, N. Liu, T.J. Carney, Y. Yang, Y. Cui, Nano Lett. 12 (2) (2012) 904.
[11] L. Yue, W. Zhang, J. Yang, L. Zhang, Electrochim. Acta 125 (0) (2014) 206.
[12] X. Zhou, J. Tang, J. Yang, J. Xie, L. Ma, Electrochim. Acta 87 (0) (2013) 663.
[13] X. Li, P. Meduri, X. Chen, W. Qi, M.H. Engelhard, W. Xu, F. Ding, J. Xiao, W. Wang, C. Wang, J.-G. Zhang, J. Liu, J. Mater. Chem. 22 (22) (2012) 11014.
[14] D. Vrankovic, L.M. Reinold, R. Riedel, M. Graczyk-Zajac, J. Mater. Sci. 51 (12) (2016) 6051.

[15] J. Saint, M. Morcrette, D. Larcher, L. Laffont, S. Beattie, J.P. Peres, D. Talaga, M. Couzi, J.M. Tarascon, Adv. Funct. Mater. 17 (11) (2007) 1765.
[16] W.R. Liu, J.H. Wang, H.C. Wu, D.T. Shieh, M.H. Yang, N.L. Wu, J. Electrochem. Soc. 152 (9) (2005) A1719.
[17] X.L. Yang, Z.Y. Wen, X.X. Xu, B. Lin, Z.X. Lin, J. Electrochem. Soc. 153 (7) (2006) A1341.
[18] I.S. Kim, G.E. Blomgren, P.N. Kumta, J. Power Sources 130 (2004) 275.
[19] N. Dimov, S. Kugino, M. Yoshio, Electrochim. Acta 48 (11) (2003) 1579.
[20] I.-S. Kim, P.N. Kumta, J. Power Sources 136 (1) (2004) 145.
[21] D. Mazouzi, B. Lestriez, L. Roue, D. Guyomard, Electrochem. Solid-State Lett. 12 (11) (2009) A215.
[22] C. Martin, M. Alias, F. Christien, O. Crosnier, D. Belanger, T. Brousse, Adv. Mater. 21 (46) (2009) 4735.
[23] B. Chen, A.K. Flatt, H. Jian, J.L. Hudson, J.M. Tour, Chem. Mater. 17 (19) (2005) 4832.
[24] Y.H. Xu, G.P. Yin, P.J. Zuo, Electrochim. Acta 54 (2) (2008) 341.
[25] C. Martin, O. Crosnier, R. Retoux, D. Belanger, D.M. Schleich, T. Brousse, Adv. Funct. Mater. 21 (18) (2011) 3524.
[26] S. Yang, G. Li, Q. Zhu, Q. Pan, J. Mater. Chem. 22 (2012) 3420.
[27] D. Chen, R. Yi, S. Chen, T. Xu, M.L. Gordin, D. Wang, Solid State Ionics 254 (0) (2014) 65.
[28] C.K. Chan, H. Peng, G. Liu, K. McIlwrath, X.F. Zhang, R.A. Huggins, Y. Cui, Nat. Nanotechnol. 3 (1) (2008) 31.
[29] C.K. Chan, R. Ruffo, S.S. Hong, R.A. Huggins, Y. Cui, J. Power Sources 189 (1) (2009) 34.
[30] A. Vlad, A.L.M. Reddy, A. Ajayan, N. Singh, J.-F.o. Gohy, S. Melinte, P.M. Ajayan, Proc. Natl. Acad. Sci. 109 (38) (2012) 15168.
[31] Z. Bao, M.R. Weatherspoon, S. Shian, Y. Cai, P.D. Graham, S.M. Allan, G. Ahmad, M.B. Dickerson, B.C. Church, Z. Kang, H.W. Abernathy Iii, C.J. Summers, M. Liu, K.H. Sandhage, Nature 446 (7132) (2007) 172.
[32] Y. Yu, L. Gu, C. Zhu, S. Tsukimoto, P.A. van Aken, J. Maier, Adv. Mater. 22 (20) (2010) 2247.
[33] H. Jia, P. Gao, J. Yang, J. Wang, Y. Nuli, Z. Yang, Adv. Energy Mater. 1 (6) (2011) 1036.
[34] Z. Lu, J. Zhu, D. Sim, W. Zhou, W. Shi, H.H. Hng, Q. Yan, Chem. Mater. 23 (24) (2011) 5293.
[35] J. Xie, G. Wang, Y. Huo, S. Zhang, G. Cao, X. Zhao, Electrochim. Acta 135 (2014) 94.
[36] W. Wang, Z. Favors, R. Ionescu, R. Ye, H.H. Bay, M. Ozkan, C.S. Ozkan, Sci. Rep. 5 (2015) 8781.
[37] A.M. Wilson, J.N. Reimers, E.W. Fuller, J.R. Dahn, Solid State Ionics 74 (3–4) (1994) 249.
[38] A.M. Wilson, W. Xing, G. Zank, B. Yates, J.R. Dahn, Solid State Ionics 100 (3–4) (1997) 259.
[39] A.M. Wilson, G. Zank, K. Eguchi, W. Xing, J.R. Dahn, J. Power Sources 68 (2) (1997) 195.
[40] A.M. Wilson, G. Zank, K. Eguchi, W. Xing, B. Yates, J.R. Dahn, Chem. Mater. 9 (7) (1997) 1601.
[41] W. Xing, A.M. Wilson, K. Eguchi, G. Zank, J.R. Dahn, J. Electrochem. Soc. 144 (7) (1997) 2410.
[42] W. Xing, A.M. Wilson, G. Zank, J.R. Dahn, Solid State Ionics 93 (3–4) (1997) 239.
[43] P. Colombo, R. Riedel, G.D. Sorarù, H.J. Kleebe, Polymer Derived Ceramics, From Nano-Structure to Applications, DEStech Publications, Inc., 2010
[44] P. Colombo, G. Mera, R. Riedel, G.D. Soraru, J. Am. Ceram. Soc. 93 (7) (2010) 1805.
[45] C.G. Pantano, A.K. Singh, H. Zhang, J. Sol-Gel Sci. Technol. 14 (1) (1999) 7.
[46] H. Zhang, C.G. Pantano, J. Am. Ceram. Soc. 73 (4) (1990) 958.
[47] G.D. Soraru, S. Modena, E. Guadagnino, P. Colombo, J. Egan, C. Pantano, J. Am. Ceram. Soc. 85 (6) (2002) 1529.
[48] Y.D. Blum, D.B. MacQueen, H.-J. Kleebe, J. Eur. Ceram. Soc. 25 (2–3) (2005) 143.
[49] G. Gregori, H.-J. Kleebe, Y.D. Blum, F. Babonneau, Int. J. Mater. Res. 97 (2006) 710.
[50] S.J. Widgeon, S. Sen, G. Mera, E. Ionescu, R. Riedel, A. Navrotsky, Chem. Mater. 22 (23) (2010) 6221.
[51] S. Martínez-Crespiera, E. Ionescu, H.-J. Kleebe, R. Riedel, J. Eur. Ceram. Soc. 31 (5) (2011) 913.
[52] G. Mera, A. Navrotsky, S. Sen, H.-J. Kleebe, R. Riedel, J. Mater. Chem. A 1 (12) (2013) 3826.
[53] H. Fukui, O. Hisashi, T. Hino, K. Kanamura, Appl. Mater. Interfaces 4 (2010) 998.
[54] H. Fukui, H. Ohsuka, T. Hino, K. Kanamura, J. Power Sources 196 (1) (2011) 371.
[55] H. Fukui, H. Ohsuka, T. Hino, K. Kanamura, J. Electrochem. Soc. 158 (5) (2011) A550.
[56] H. Fukui, K. Eguchi, H. Ohsuka, T. Hino, K. Kanamura, J. Power Sources 243 (2013) 152.
[57] P. Dibandjo, M. Graczyk-Zajac, R. Riedel, V.S. Pradeep, G.D.a. Soraru, J. Eur. Ceram. Soc. 32 (10) (2012) 2495.
[58] V.S. Pradeep, M. Graczyk-Zajac, M. Wilamowska, R. Riedel, G.D. Soraru, Solid State Ionics 262 (0) (2014) 22.
[59] V.S. Pradeep, M. Graczyk-Zajac, R. Riedel, G.D. Soraru, Electrochim. Acta 119 (0) (2014) 78.
[60] M. Graczyk-Zajac, L. Toma, C. Fasel, R. Riedel, Solid State Ionics 225 (0) (2012) 522.
[61] J. Kaspar, M. Graczyk-Zajac, R. Riedel, Solid State Ionics 225 (0) (2012) 527.
[62] J. Kaspar, M. Graczyk-Zajac, R. Riedel, J. Power Sources 244 (0) (2013) 450.
[63] M. Wilamowska, V.S. Pradeep, M. Graczyk-Zajac, R. Riedel, G.D. Soraru, Solid State Ionics 260 (0) (2014) 94.
[64] M. Graczyk-Zajac, L.M. Reinold, J. Kaspar, P.V.W. Sasikumar, G.-D. Soraru, R. Riedel, Nanomaterials 5 (1) (2015) 233.
[65] V.S. Pradeep, D.G. Ayana, M. Graczyk-Zajac, G.D. Soraru, R. Riedel, Electrochim. Acta 157 (2015) 41.
[66] M. Haaks, J. Kaspar, A. Franz, M. Graczyk-Zajac, R. Riedel, M. Vogel, Solid State Ionics 287 (2016) 28.
[67] J. Kaspar, M. Graczyk-Zajac, S. Choudhury, R. Riedel, Electrochim. Acta 216 (2016) 196.
[68] J. Kaspar, M. Graczyk-Zajac, R. Riedel, Electrochim. Acta 115 (0) (2014) 665.
[69] L.M. Reinold, M. Graczyk-Zajac, C. Fasel, R. Riedel, ECS Trans. 35 (2011) 37.
[70] J. Kaspar, M. Graczyk-Zajac, S. Lauterbach, H.-J. Kleebe, R. Riedel, J. Power Sources 269 (0) (2014) 164.
[71] D.V.M.G.-Z.K. Wissel, Solid State Ionics, 2016 (in this issue).
[72] G. Schierning, R. Theissmann, H. Wiggers, D. Sudfeld, A. Ebbers, D. Franke, V.T. Witusiewicz, M. Apel, J. Appl. Phys. 103 (8) (2008) 084305.
[73] P. Novak, J. Ocenasek, L. Prusakova, V. Vavrunkova, J. Savkova, J. Rezek, Appl. Surf. Sci. 364 (2016) 302.
[74] A.C. Ferrari, Solid State Commun. 143 (1–2) (2007) 47.
[75] A.C. Ferrari, J. Robertson, Phys. Rev. B 61 (20) (2000) 14095.
[76] M.A. Pimenta, G. Dresselhaus, M.S. Dresselhaus, L.G. Cancado, A. Jorio, R. Saito, Phys. Chem. Chem. Phys. 9 (11) (2007) 1276.
[77] A. Sadezky, H. Muckenhuber, H. Grothe, R. Niessner, U. Poeschl, Carbon 43 (8) (2005) 1731.
[78] M.N. Obrovac, L. Christensen, D.B. Le, J.R. Dahn, J. Electrochem. Soc. 154 (9) (2007) A849.

Solid State Ionics 302 (2017) 180–185

Contents lists available at ScienceDirect

Solid State Ionics

journal homepage: www.elsevier.com/locate/ssi

Synthesis of 3D silicon with tailored nanostructure: Influence of morphology on the electrochemical properties

K. Wissel [a], D. Vrankovic [a], G. Trykowski [b], M. Graczyk-Zajac [a,*]

[a] Department of Materials and Earth Sciences, Technical University Darmstadt, Germany
[b] Faculty of Chemistry, Nicolaus Copernicus University in Torun, Poland

ARTICLE INFO

Article history:
Received 29 July 2016
Received in revised form 5 December 2016
Accepted 7 December 2016
Available online 23 December 2016

ABSTRACT

Within this work, monodisperse porous silicon nanospheres have been derived from monodisperse silica nanospheres via two different magnesiothermic reduction routes, namely (i) magnesiothermic reduction using a two-chamber set-up, and (ii) magnesiothermic reduction using NaCl as heat scavenger. Both methods allow a size- and shape-preserving preparation of mesoporous silicon. Crystalline silicon with a particle size of 56 nm and a specific surface area of 198 $m^2 g^{-1}$ and amorphous silicon with a particle size of 35 nm and a specific surface area of 623 $m^2 g^{-1}$ are synthesized using the two chamber and salt assisted routes, respectively. TEM micrographs confirm enhanced porous character of silicon from NaCl assisted route. An unstable electrochemical performance of the crystalline silicon is found, whereas the amorphous Si presents a stable electrochemical behavior.

1. Introduction

Silicon is considered to be a promising material for the application as anode for next generation Li-ion batteries due to its high theoretical capacity of 3579 $mAh \cdot g^{-1}$ obtained through reversible alloying with lithium [1]. However, a general disadvantage of alloy electrodes is a large volume change (for Si about 260%) during cycling, causing electrode failure and resulting in low cycling stabilities. Repetitive cracking and reformation of the solid electrolyte interface (SEI) upon volume expansion lead to high irreversible capacity losses [2–4]. Promising approaches to prevent material degradation and to improve the cycling stability of silicon anodes proposed in literature are: (i) reduction of the particle size to nanosize as this reduces overall volume expansion and hence mitigates arising mechanical stresses, and (ii) use of nanostructured morphologies such as silicon thin films, nanowires, nanotubes or porous materials [4–8]. Combining the advantageous properties of nanosized silicon with the introduction of porosity within the silicon particles might open new possibilities to stabilize silicon with respect to continuous lithiation and delithiation.

The production of aforementioned porous silicon nanostructures, however, mostly demands expensive starting materials or high processing costs. Thus there is a need to develop a low-cost method, which can easily be up scaled. Bao et al. [9] reported a promising alternative where silica was reduced to silicon in the presence of magnesium (1):

$$SiO_{2(S)} + 2Mg_{(g)} \rightarrow Si_{(s)} + 2MgO_{(s)} \quad (1)$$

Strongly depending on the reaction conditions, magnesium silicide and magnesium orthosilicate are prone to be generated following reactions (2) and (3). These by-products significantly influence the final silicon yield and in order to increase the yield of reaction (1), reactions (2) and (3) must be suppressed. To accomplish this challenging task, where on one hand silica needs to be reduced as efficiently as possible, and on the other hand excess of magnesium causes formation of unwanted by-products, fine control of the reaction stoichiometry is needed. Furthermore, inhomogeneity in obtained product caused by an uneven distribution of reactants [10,11], or overheating caused by the highly exothermic reduction reaction, leading to melting of produced silicon and subsequent loss of nanostructured morphology [12] must be controlled as well.

$$2Mg_{(g)} + Si_{(s)} \rightarrow Mg_2Si_{(s)} \quad (2)$$

$$SiO_{2(S)} + 2MgO_{(g)} \rightarrow Mg_2SiO_{4\,(s)} \quad (3)$$

Till now, the development of controllable magnesiothermic reduction with high silicon yield, while the original shape of the silica precursor is preserved and easily removable by-products are formed remains a great challenge.

In this work, we report on the synthesis of monodisperse mesoporous silicon nanospheres via shape-preserving magnesiothermic

---

* Corresponding author.
E-mail address: graczyk@materials.tu-darmstadt.de (M. Graczyk-Zajac).

http://dx.doi.org/10.1016/j.ssi.2016.12.008
0167-2738/

reduction from monodisperse silica nanospheres using self-made reactors. Nanosized silica is synthesized by sol-gel processing and subsequently reduced via two magnesiothermic reduction routes. Both applied routes have been reported to allow a size- and shape-preserving preparation of mesoporous silicon [13,14]. Additionally, the influence of a heat-treatment of the silica precursor is discussed. Furthermore, the obtained silicon powders are investigated with respect to their potential application as negative electrode for Li-ion batteries.

2. Experimental part

2.1. Preparation of monodisperse SiO_2 nanospheres

Monodisperse SiO_2 nanospheres were prepared via a modified Stöber method [15,16]. It allows for the synthesis of nanosized spherical particles with a narrow size distribution due to the precise control of reaction conditions (pH, concentration, processing conditions).

For the modified Stöber method, tetraethyl orthosilicate (TEOS, Sigma Aldrich, purity 99.0%, USA) was added to a mixture of water and ethanol (Sol 1). A pH value of 1.8 was adjusted by adding citric acid (Sigma-Aldrich, purity 99%, USA). The mixture was stirred for 1 h. For Sol 2, water and ammonia (VWR Internationals, 28% water solution, USA) were mixed till a pH value of 11.0 was obtained. When Sol 1 was dropped under vigorous stirring to Sol 2, the pH value of the solution was kept around 11.0. The reaction was continued for 24 h. The molar ratios of the used compound are listed in Table 1. The suspension was separated by centrifugation, repeatedly washed with ethanol and deionized (DI) water and dried at 80 °C for 72 h in air. For calcination, the samples were heated to 400 °C under air. The heating rate was 30 °C/h, the dwelling time 24 h and the cooling rate 100 °C/h. Subsequently, a part of the SiO_2 powder was annealed (heating/cooling rate of 100 °C/h) to 1200 °C for 12 h under air.

2.2. Magnesiothermic reduction of monodisperse SiO_2 nanospheres to monodisperse mesoporous Si nanospheres

For the magnesiothermic reduction of synthesized SiO_2 precursors to porous Si, two different routes were pursued: (i) magnesiothermic reduction using a two-chamber set-up adapted from reference [13], and (ii) magnesiothermic reduction using NaCl as heat scavenger adapted from reference [14]. In order to assess the best reaction conditions and to insure a final product with desired nanostructure, porosity and yield, two weight ratios of SiO_2:Mg (1:1 and 1:1.25) and various reaction temperatures (ranking from 700 to 800 °C) were employed. It was found by means of XRD, FTIR and nitrogen adsorption measurements that the product with the best properties is obtained with a SiO_2:Mg ratio of 1:1 and a reaction temperature of 800 °C. Obtained results and material properties of non-optimized samples will not be shown here and are not further discussed due to space limitations.

In the route using a two-chamber set-up, the reduction was performed using a self-made reactor consisting of stainless steel (SS 316) as shown in Fig. 1. The reactor is divided into two chambers by a moveable, perforated steel plate (SS 313). The loading and sealing of the reactor was performed in an argon-filled glove box (MBraun UNIlab 2000, Germany). SiO_2 was placed in the middle of the steel plate and Mg powder (abcr GmbH, −325 mesh, purity 99.8%) was loaded below the SiO_2. In an alumina tube furnace operated under argon atmosphere, the reactor was heated to 800 °C with heating/cooling rates of 100 °C/h and a dwelling time of 12 h.

Table 1
Molar ratios of compounds for used modified Stöber method.

TEOS Sol1	H_2O Sol1	EtOH Sol1	Citric acid Sol1	H_2O Sol2	NH_4OH Sol2
1	93	28	0.17	1100	>1.5

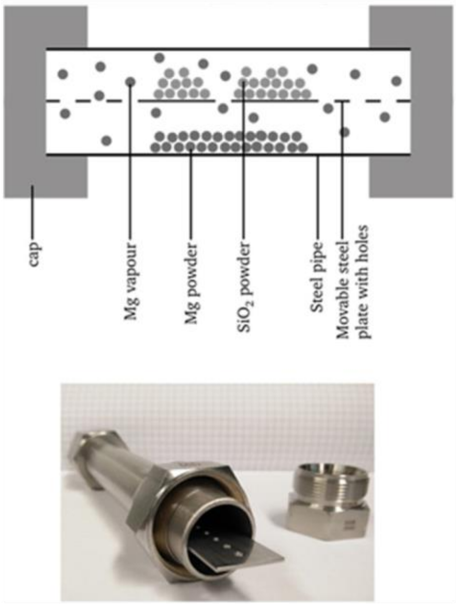

Fig. 1. Schematic illustration of reactor and species involved in magnesiothermic reduction using two-chamber set-up (a), and picture of self-made reactor (b).
(adapted from [13])

The obtained reaction product was etched overnight with 1 M HCl to remove unwanted by-products (MgO and Mg_2Si). The HCl was removed using centrifugation. The obtained powders were washed repeatedly with DI water and dried at 120 °C in air overnight.

For the route using NaCl as heat scavenger (Fig. 2), the synthesized SiO_2 precursors were mixed with NaCl (VWR Internationals, purity 99.8%, USA) in a weight ratio of SiO_2:NaCl of 1:10 and ground with a mortar and pestle. The powder mixture was immersed in water and

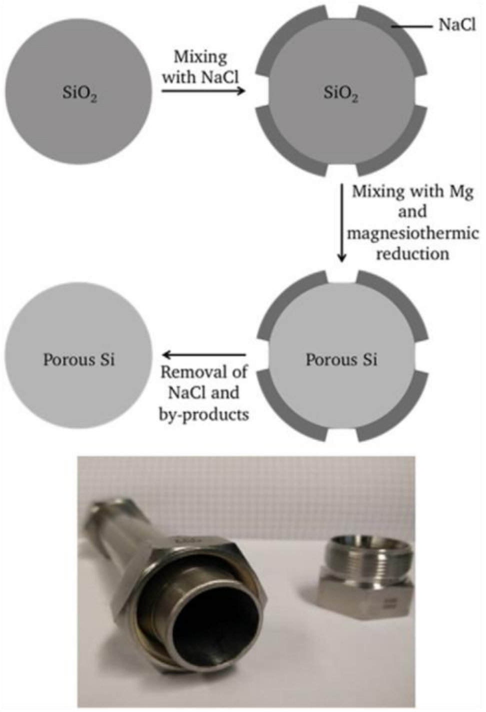

Fig. 2. Preparation steps of magnesiothermic reduction process using NaCl as heat scavenger (a), and picture of self-made reactor (b).
(adapted from [14])

ultra-sonicated for 1 h. Afterwards, it was stirred for 3 h at 50 °C. Vacuum drying was applied for 3 h to remove the water. The obtained SiO_2:NaCl powder was introduced into a glove box, where the assembly of the reactor was performed. The powder was mixed with magnesium and placed in the middle of the reactor. The reduction reaction was carried out with the same temperature program used for the reduction using the two-chamber set-up. The resulting powders were washed with DI water to remove NaCl. Centrifugation was used to remove the water. Etching, washing and drying was conducted as described above.

2.3. Material characterization

Powder X-ray diffraction (XRD) measurements were performed using a STOE STADI P X-ray diffractometer (Stoe & Cie GmbH, Germany) equipped with Mo Kα-radiation in flat-sample transmission geometry. Raman spectra were recorded with a confocal micro-Raman spectrometer Horiba HR 800 (Horiba, Japan) using an argon laser with wavelength 514.5 nm.

Nitrogen (N_2) adsorption was performed at 77 K using an Autosorb-3B (Quantachrome Instruments, USA). Before the measurements, the samples were preheated at 150 °C for 24 h under vacuum. Using the obtained N_2 adsorption isotherms, the specific surface area was determined from the linear Brunauer-Emmett-Teller (BET) plots; the relative pressure p/p_0 was between 0.05 and 0.3. The amount of vapour adsorbed at a relative pressure of $p/p_0 \approx 1$ was used to determine the total pore volume [17]. The micropore volume was determined using the de Boer's t-plot analysis [18]. The Barrett-Joyner-Halenda (BJH) method was applied to access the pore size distribution [17]. The particle size distribution was measured by dynamic laser light scattering (DLS) using a Zetasizer Nano ZS (Malvern, Germany).

Transmission electron microscopy (TEM) studies were performed with a FEI CM20 instrument equipped with an EDX Detector (TEM 250 with SDD Detector, Oxford Instruments), operated at 200 keV and with a FEI Tecnai F20 X-Twin equipped with an EDX spectrometer (SDD detector, EDAX Inc.).

2.4. Electrode preparation and electrochemical testing

For electrode preparation, homogeneous slurries consisting of 70 wt.% Si powder, 20 wt.% Carbon Black Super P® (TIMCAL Ltd., Switzerland) as conducting additive, and 10 wt.% polyvinylidene fluoride (Solef® PVDF, Solvay, Germany) as binder were prepared and tape casted onto the rough side of 10 μm thin copper foil (SE-Cu58, Schlenk Metallfolien, Germany). The binder solution consisted of 10 wt.% PVDF in *N*-methyl-2-pyrolidone (NMP, BASF, Germany). After tape casting, the printed electrodes were dried at 80 °C for 24 h. Subsequently, circles with a diameter of 10 mm were stamped out of the foil and the weight of these electrodes was measured. The electrodes were dried under vacuum in a Büchi oven (Büchi glass oven B-585, Germany) at 80 °C for 24 h before being transferred into an argon-filled glove box (MBraun UNIlab 2000, Germany).

For testing of the obtained electrode materials, measuring cells of two-electrode Swagelok® type set up were assembled. Reference/counter electrodes with a diameter of 10 mm were stamped out of Li foil (purity 99.9%, thickness 0.75 mm, Alfa Aesar, Germany). A porous glass fiber membrane (QMA, Whatman™, UK) was used as a separator, which was soaked in 180 μl electrolyte. The electrolyte was a solution of 1 M $LiPF_6$ in EC:DMC, ratio 1:1 (LP30, Merck KGaA, Germany).

The testing of hermetically closed cells was performed with a VMP multipotentiostat (BioLogic Science Instruments, France) at charging/discharging rates of 72 $mA \cdot g^{-1}$ between 0.005 and 3 V. Capacities were calculated with regards to the mass of the active material excluding the mass of carbon black and PVDF used in the electrode preparation.

3. Results and discussion

3.1. X-ray diffraction

Fig. 3 presents the X-ray diffraction patterns of Si powders derived via magnesiothermic reduction using the two-chamber set-up route and the NaCl-assisted route, as well as the diffractograms of the SiO_2 used as precursor.

The SiO_2 powder has an amorphous character. Magnesiothermic reduction applying the two-chamber set-up results in the formation of crystalline Si visible due to corresponding Bragg reflections. Broadening of observed reflexes indicates the presence of very small Si crystallites in the sample. Reduction reaction following the salt-assisted route leads to an amorphous Si. This is an indication for the ability of NaCl to effectively scavenge heat evolving during the exothermic reaction and to control temperatures inside the reactor. An amorphous state of Si after magnesiothermic reduction has, to our knowledge, not been reported in literature until now.

The XRD patterns of SiO_2 heat-treated at 1200 °C and the Si powders derived from it are shown in Fig. 4. The SiO_2 precursor experienced a structural ordering visible due to the broad reflection at a 2Θ position of about 10°. A complete crystallization is not achieved. However, it influences the crystallinity of the obtained Si powders since both reduction routes lead to the formation of crystalline Si. Therefore, it can be concluded, that the enhanced order of the heat-treated SiO_2 precursor accelerates the crystallization of the resulting Si.

3.2. Raman spectroscopy

The Raman spectra of the derived Si powders are given in Fig. 5. For both applied routes, regardless which SiO_2 precursor was used, characteristic Si vibrations are visible. The most prominent band is located at about 510 cm^{-1} corresponding to the first-order optical phonon mode (TO) of crystalline Si. The band is shifted towards a smaller Raman shift compared to monocrystalline Si (521 cm^{-1}) due to the nanometer size of the Si powder. The second-order transverse phonon mode (2TA) and the second-order optical phonon mode (2TO) appear at around 300 cm^{-1} and 950 cm^{-1}, respectively [7]. The presence of the bands associated with crystalline Si in the spectrum of Si derived using the NaCl-assisted route from the amorphous SiO_2 indicates that the amorphous Si (as overserved in XRD measurements (Fig. 3)) undergoes recrystallization due to the laser irradiation [19].

Additional bands are not visible. Hence, all residuals are successfully removed.

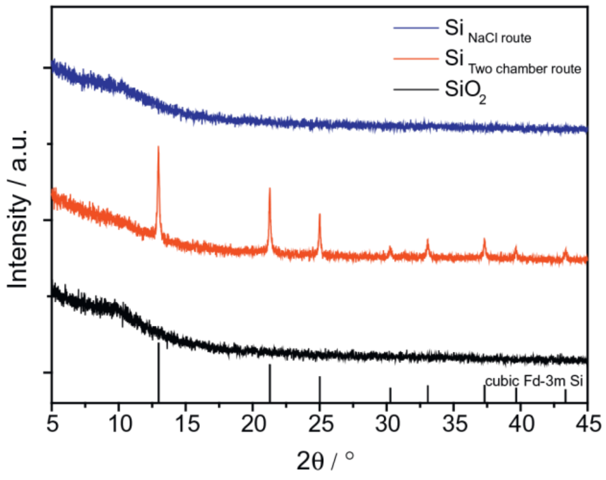

Fig. 3. XRD patterns of SiO_2 precursor and of Si derived via magnesiothermic reduction from SiO_2 using the two-chamber set-up route and the NaCl-assisted route.

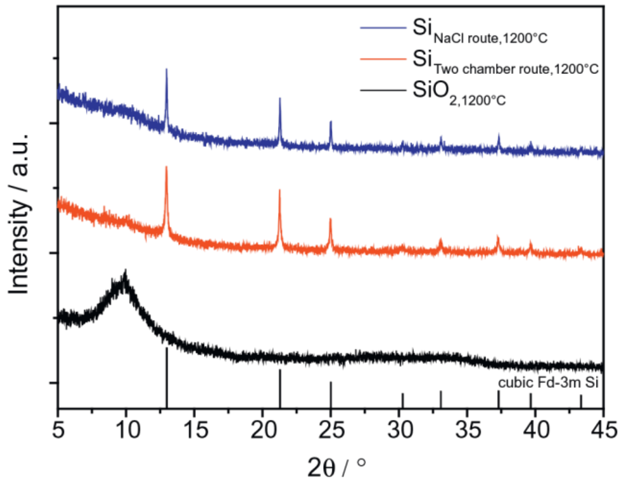

Fig. 4. XRD patterns of at 1200 °C heat-treated SiO_2 precursor and of Si derived via magnesiothermic using the two-chamber set-up route and the NaCl-assisted route.

3.3. Nitrogen adsorption and particle size measurements

Evolution of porosity starting from dense SiO_2 powder to the mesoporous Si was followed by means of nitrogen physisorption measurements. Characteristic features are summarized in Table 2 with corresponding isotherms presented in Fig. 6. Fig. 6 a) shows isotherms of the SiO_2 precursor and of the Si powders derived via two chamber and salt assisted route. The SiO_2 precursor exhibits a BET specific surface area of 68 $m^2\,g^{-1}$ and an entirely dense character (isotherm type II). The total pore volume of almost 0.5 cm^3/g generated from pores having sizes greater than the particle size of the investigated SiO_2 powder is attributed to strongly agglomerated nanoparticles. A significant increase in BET specific surface area to 198 and 623 $m^2\,g^{-1}$ was observed for Si derived via two chamber and NaCl-assisted route, respectively. This increase in specific surface area together with the increase in total pore volume (Table 2) clearly indicates that magnesiothermic reduction introduces open porosity to the sample. Moreover, the sample derived via salt-assisted route displays an one order of magnitude higher BET specific surface area than the SiO_2 precursor with presence of microporosity (Table 2) indicating superior heat-scavenging abilities of NaCl.

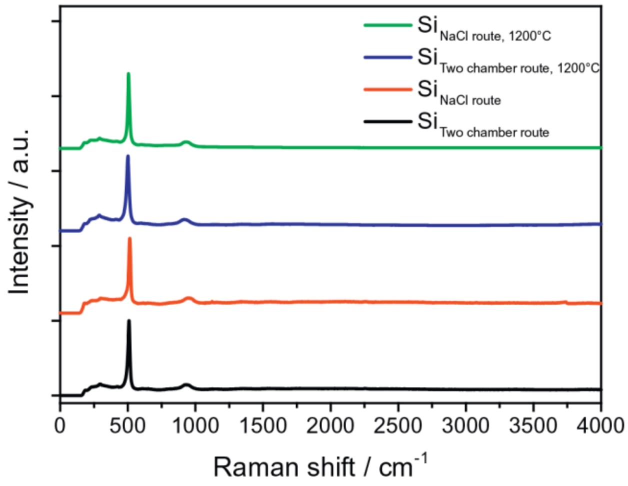

Fig. 5. Raman spectra of Si derived via magnesiothermic reduction from SiO_2 using the two-chamber set-up route and the NaCl-assisted route.

Table 2
Specific surface area (SSA), total pore volume (V_t), micropore volume (V_m), pore diameter and D_{50} value of SiO_2 precursors and Si derived via magnesiothermic reduction using the two-chamber set-up route and the NaCl-assisted route.

	SSA [$m^2\,g^{-1}$]	V_t [cm^3/g]	V_m [cm^3/g]	Pore diameter [nm]	D_{50} [nm]
SiO_2	68	0.49	0	N/A	72
$Si_{\text{Two chamber route}}$	198	0.75	0	3.9	56
$Si_{\text{NaCl-assisted route}}$	623	1.13	0.04	3.9	35
$SiO_{2,1200\ °C}$	13	0.02	0	N/A	73
$Si_{\text{Two chamber route,1200 °C}}$	110	0.35	0	3.9	49
$Si_{\text{NaCl route,1200 °C}}$	100	0.33	0	3.9	50

Fig. 6 b) presents isotherms of the SiO_2 precursor additionally annealed at 1200 °C and of the Si powders derived via two chamber and salt-assisted route. The additionally annealed SiO_2 exhibits a very low BET specific surface area of 13 $m^2\,g^{-1}$ despite the fact that the powder is still nanosized. This phenomenon is attributed to "sintering" of soft agglomerates and the inability of N_2 physisorption to address strongly agglomerated nanopowders. Furthermore, an increase in BET specific surface area and total pore volume is also observed after magnesiothermic reduction reaction. However, there is no significant

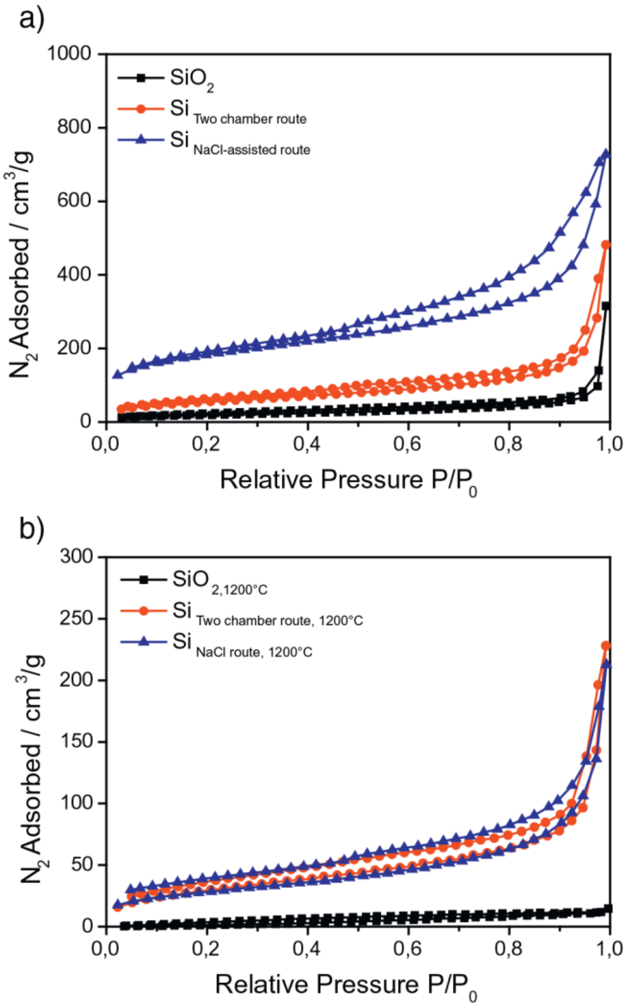

Fig. 6. Adsorption/desorption isotherms of SiO_2 precursor and of Si derived via magnesiothermic reduction from SiO_2 using the two-chamber set-up route and the NaCl-assisted route (a), and of at 1200 °C heat-treated SiO_2 precursor and of Si derived via magnesiothermic using the two-chamber set-up route and the NaCl-assisted route (b).

difference among Si derived via two chamber or salt-assisted route (Table 2).

The particle size measurements reveal narrow particle size distributions displaying the monodispersity of the particles.

3.4. Transmission electron microscopy

Fig. 7 a) and b) show TEM micrographs of the Si powders prepared from the SiO_2 precursor by magnesiothermic reduction using the two-chamber set-up route and the salt-assisted route, respectively. The particles appear to be monodisperse and spherical. The particle size corresponds to the values obtained from the particle size measurement. For Si obtained using the two-chamber set-up the outer lines of the spherical particles are visible. There is no sharp outer line of the Si particles derived via the NaCl-assisted route. The material is more textured suggesting a high porosity. Hence, TEM micrographs confirm the results of the nitrogen adsorption measurements.

3.5. Electrochemical measurements

The galvanostatic charge-discharge profiles of the electrodes containing derived Si powders are shown in Fig. 8. The profiles of the electrodes containing crystalline Si (independently on the preparation approach) are very similar and show characteristic voltage plateaus at ~0.18 V and ~0.45 V corresponding to lithiation and delithiation of Si, respectively [2,3,20]. Therefore, only the example of Si derived from SiO_2 using the two-chamber set-up route is (Fig. 8 a)), shown exemplarily. During the first lithiation, the sloping plateau between 2 and 0.75 V corresponding to the formation of SEI is visible. This plateau vanishes completely after the first cycle indicating that stable SEI is formed. The first insertion capacities of the investigated samples range 1010 and 1070 $mAh\cdot g^{-1}$, for crystalline and amorphous material, respectively. Furthermore, a rapid capacity fading is observable indicating electrode degradation and loss of electric contact.

For the electrode containing Si derived from the SiO_2 precursor using the salt-assisted route, none of the typical plateaus associated to alloying and dealloying of Si with Li are present. The losses for SEI formation are much higher due to extraordinarily high active surface of the material, namely 623 $m^2\,g^{-1}$ (Table 2). The shape of the delithiation curve with capacity recovered over the entire range of the potential up to 3 V, is suggesting that ad- and desorption processes of Li on the surface of the highly porous Si particles play an important role in the electrochemical Li storage properties of this material. Similar phenomena have been found for porous carbon materials [21]. Therefore, even though alloying and dealloying of Si with Li cannot be completely ruled out, the stable cycling performance over prolonged cycling with recovered stable capacities of ~400 $mAh\cdot g^{-1}$ is attributed to predominantly occurring ad- and desorption processes.

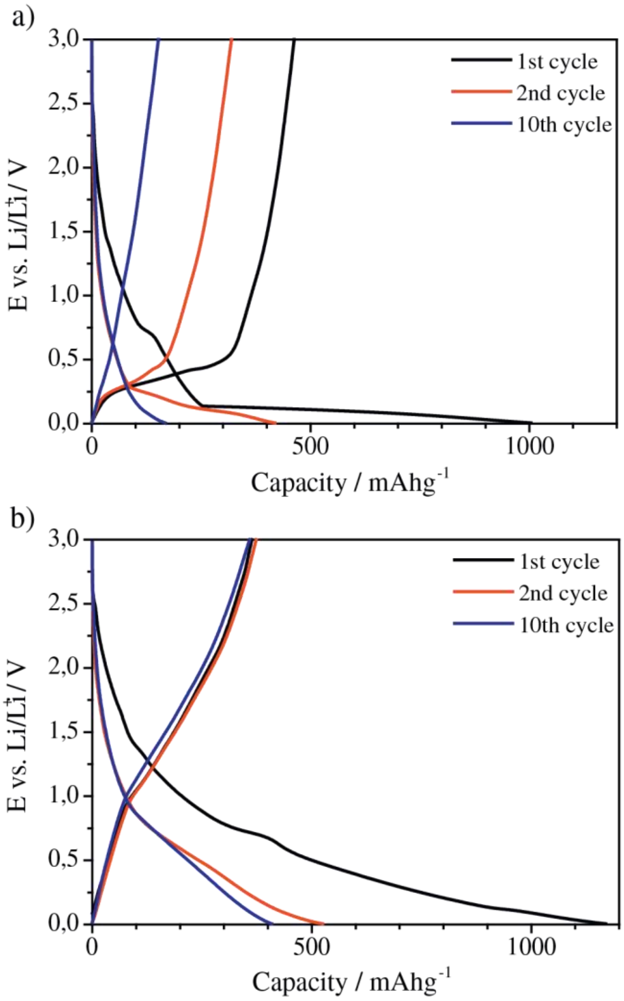

Fig. 8. Galvanostatic charge-discharge profiles of the 1st, 2nd and 10th cycle of the crystalline (a) and amorphous (b) Si electrodes.

Overall recovered capacities of the prepared Si electrodes are lower than the theoretical value (3579 $mAh\cdot g^{-1}$). One should however note, that 20 wt.% of conductive additives present in the electrode composition is obviously not enough to provide sufficient electronic conductivity. Moreover, the material tends strongly to agglomerate

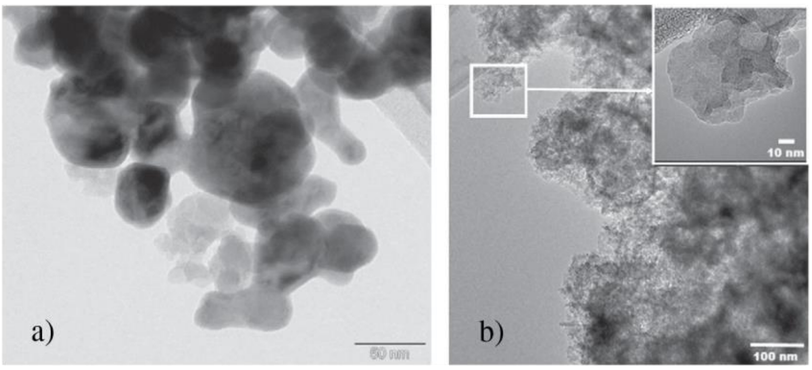

Fig. 7. TEM images of Si derived via magnesiothermic reduction from SiO_2 using the two-chamber set-up route (a), and of Si derived via magnesiothermic reduction from SiO_2 using the NaCl-assisted route (b).

what further hinders uniform distribution of conductive additives. Thus, it is possible that the part of the Si is unavailable for Li ions, what leads to a capacity much lower than theoretically expected. Furthermore, it has to be kept in mind, that HF etching of electrochemically inactive SiO_2 possibly remaining after magesiothermic reduction and/or formed during processing of synthetized Si has not been performed. Thus, the remaining SiO_2 should be considered as dead weight when the electrochemical performance is evaluated.

4. Conclusion

This study demonstrates that by tailoring the known magnesiothermic reduction reaction of silica, it is possible to design the porosity and morphology of the final silicon. Further, the silicon morphology and crystallinity influence the mechanism of lithium storage and the electrochemical stability of the material. Crystalline nano-silicon reacts with lithium predominantly through alloying mechanism presenting unstable cycling behavior. Amorphous silicon with an extraordinary high specific surface area of 623 $m^2\ g^{-1}$ demonstrates, however, a stable electrochemical performance with storing lithium mainly through adsorption/desorption mechanism.

Acknowledgments

We gratefully acknowledge the financial support of the German Research Foundation (DFG) SPP1473/JP8. We thank Dr. Christina Schitco and Ulrike Kunz for their help with material characterization.

References

[1] R.A. Huggins, J. Power Sources 81–82 (1999) 13.
[2] M.N. Obrovac, L. Christensen, Electrochem. Solid-State Lett. 7 (5) (2004) A93.
[3] M.N. Obrovac, L.J. Krause, J. Electrochem. Soc. 154 (2) (2007) A103.
[4] U. Kasavajjula, C. Wang, A.J. Appleby, J. Power Sources 163 (2) (2007) 1003.
[5] X.H. Liu, L. Zhong, S. Huang, S.X. Mao, T. Zhu, J.Y. Huang, ACS Nano 6 (2) (2012) 1522.
[6] J. Graetz, C.C. Ahn, R. Yazami, B. Fultz, Electrochem. Solid-State Lett. 6 (9) (2003) A194.
[7] M. Holzapfel, H. Buqa, L.J. Hardwick, M. Hahn, A. Wursig, W. Scheifele, P. Novak, R. Kotz, C. Veit, F.M. Petrat, Electrochim. Acta 52 (3) (2006) 973.
[8] J.R. Szczech, S. Jin, Energ. Environ. Sci. 4 (1) (2011) 56.
[9] Z. Bao, M.R. Weatherspoon, S. Shian, Y. Cai, P.D. Graham, S.M. Allan, G. Ahmad, M.B. Dickerson, B.C. Church, Z. Kang, H.W. Abernathy Iii, C.J. Summers, M. Liu, K.H. Sandhage, Nature 446 (7132) (2007) 172.
[10] Z. Favors, W. Wang, H.H. Bay, Z. Mutlu, K. Ahmed, C. Liu, M. Ozkan, C.S. Ozkan, Sci. Rep. 4 (2014) 5623.
[11] E.K. Richman, C.B. Kang, T. Brezesinski, S.H. Tolbert, Nano Lett. 8 (9) (2008) 3075.
[12] Y. Yu, L. Gu, C. Zhu, S. Tsukimoto, P.A. van Aken, J. Maier, Adv. Mater. 22 (20) (2010) 2247.
[13] J. Xie, G. Wang, Y. Huo, S. Zhang, G. Cao, X. Zhao, Electrochim. Acta 135 (2014) 94.
[14] W. Wang, Z. Favors, R. Ionescu, R. Ye, H.H. Bay, M. Ozkan, C.S. Ozkan, Sci. Rep. 5 (2015) 8781.
[15] W. Stöber, A. Fink, E. Bohn, J. Colloid Interface Sci. 26 (1) (1968) 62.
[16] A. Lukowiak, J. Lao, J. Lacroix, J.-M. Nedelec, Chem. Commun. 49 (59) (2013) 6620.
[17] K.S.W. Sing, Reporting physisorption data for gas/solid systems with special reference to the determination of surface area and porosity (recommendations 1984), Pure Appl. Chem. (1985) 603.
[18] J.H. de Boer, B.G. Linsen, T. van der Plas, G.J. Zondervan, J. Catal. 4 (6) (1965) 649.
[19] P. Novák, J. Očenášek, L. Prušáková, V. Vavruňková, J. Savková, J. Rezek, Appl. Surf. Sci. 364 (2016) 302.
[20] J. Li, J.R. Dahn, J. Electrochem. Soc. 154 (3) (2007) A156.
[21] S. Flandrois, B. Simon, Carbon 37 (2) (1999) 165.

Jochen Rohrer[a], Dragoljub Vrankovic[b], Damian Cupid[c], Ralf Riedel[b], Hans J. Seifert[c], Karsten Albe[a], Magdalena Graczyk-Zajac[b]
[a] Materialmodellierung, Technische Universität Darmstadt, Darmstadt, Germany
[b] Disperse Feststoffe, Technische Universität Darmstadt, Darmstadt, Germany
[c] IAM – Angewandte Werkstoffphysik, Karlsruher Institut für Technologie, Eggenstein-Leopoldshafen, Germany

Si- and Sn-containing SiOCN-based nanocomposites as anode materials for lithium ion batteries: synthesis, thermodynamic characterization and modeling

Novel nanocomposites consisting of silicon/tin nanoparticles (n-Si/n-Sn) embedded in silicon carbonitride (SiCN) or silicon oxycarbide (SiOC) ceramic matrices are investigated as possible anode materials for Li-ion batteries. The goal of our study is to exploit the large mass specific capacity of Si/Sn (3579 mAh g^{-1}/994 mAh g^{-1}), while avoiding rapid capacity fading due to the large volume changes of Si/Sn during Li insertion. We show that a large amount ($\sim$30–40 wt.%) of disordered carbon phase is dispersed within the SiOC/SiCN matrix and stabilizes the Si/Sn nanoparticles with respect to extended reversible lithium ion storage. Silicon nanocomposites are prepared by mixing of a polymeric precursor with commercial and "home-synthesized" crystalline and amorphous silicon. Tin nanocomposites, in contrast, are prepared using a single precursor approach, which allows the in-situ generation of Sn nanoparticles homogeneously dispersed within the SiOC host. The best electrochemical stability along with capacities of 600–700 mAh g^{-1} is obtained when amorphous/porous silicon is used. Mechanisms contributing to the increase of storage capacity and the cycle stability are clarified by analyzing elemental composition, local solid-state structures, intercalation hosts and Li-ion mobility. Our work is supplemented by first-principles based atomistic modeling and thermochemical measurements.

Keywords: Silicon-tin/SiOCN nanocomposite; Li-ion battery; DFT; Atomistic modeling; Calorimetry

1. Introduction

A material class which is considered as a replacement for carbon-based anodes in Li-ion battery technology [1, 2] is alloying electrodes (e. g. silicon or tin), which are able to reversibly form Li$_x$M intermetallic compounds (Eq. (1)) when polarized to sufficiently low voltage levels. As the potential decreases, intermetallic phases with fixed stoichiometry form:

$$x\mathrm{Li}^+ + x\mathrm{e}^- + M \rightleftarrows \mathrm{Li}_xM \qquad (1)$$

Because of their outstanding specific and volumetric capacity, and also availability, these materials are promising high capacity alternatives to commercially used graphite anodes [3–5]. Large volume changes during alloying/dealloying with lithium, lead to electrode degradation and prevent the commercial use of silicon- and tin-based electrode materials [6, 7]. Stress generated by volume change causes cracking and pulverization of the electrode and finally leads to the loss of electrical contact between the active material and the current collector. This consequently results in a rapid fading of the capacity with ongoing cycling. Furthermore, the large volume expansion leads to an unstable solid electrolyte interface (SEI) on the silicon surface. This brings the unprotected active material in contact with the electrolyte, causing SEI thickening followed by irreversible capacity losses with ongoing cycling [8, 9].

In order to improve the cycling stability of silicon anodes, numerous approaches have been proposed in the literature, including: (i) limiting the size of Si particles to less than 150 nm in diameter [10], (ii) synthesis of nano-silicon–carbon composites with cavities around the silicon particles [3, 11–14], (iii) embedding of nanosilicon particles into an active or inactive matrix [15–20], (iv) chemical bonding of silicon nanoparticles to a binder or conductive additive [21–27], (v) utilization of nanotubes, nanowires, nanostructured particles [28–30], etc.

Also for tin, there have been intense efforts in order to suppress the degradation of the electrode during repeated cycling by adopting nanostructured Sn-based architectures [31–33]. Sn-coated Cu-nanopillars for example, provide sufficient space to accommodate volume changes during the alloying/dealloying process, while demonstrating an enhanced cycle life [34]. However, such type of nano-architectures exhibit low energy densities due to a rather low active mass-to-volume ratio. Embedding tin nanoparticles into a carbonaceous matrix appeared to be a promising approach. Derrien et al. demonstrated improved cycle stability of Sn/C nanocomposites prepared by embedding Sn nanoparticles into a carbon matrix [33, 35]. Since the Sn particles are well distributed throughout the matrix, the initial microstructure remains stable during long term cycling. Additionally, the carbon matrix increases the electrical conductivity and ensures electrical wiring, even when cracking and pulverization occur.

Within this article, we present our work on nanocomposites as anode materials for Li-ion batteries consisting of silicon/tin nanoparticles (n-Si/n-Sn) embedded in silicon carbonitride (SiCN) or silicon oxycarbide (SiOC) ceramic matrices. Experimental measurements are supported and guided by calculations within density-functional theory, classical molecular-dynamics simulations and experimental thermochemistry.

2. Ceramic amorphous SiOC/SiCN matrices

2.1. Synthesis and characterization

The electrochemical properties of silicon oxycarbide (SiOC) ceramics with respect to a reversible storage of lithium ions were first studied in the middle of the 1990s [36–41]. SiOC materials are typically prepared by thermal conversion of polyorganosiloxanes under inert atmosphere, by a so-called polymer-derived ceramic (PDC) process [42, 43], or alternatively by the sol–gel method [44–46]. Among the various chemical compositions of SiOC, stoichiometries with an exceptionally high carbon content were considered as anode materials because of the high gravimetric capacity, good rate capability and reliable cycling stability [47–61]. The microstructure of SiOC ceramics is typically composed of an amorphous Si–O–C network, which is interpenetrated by an amorphous free carbon phase. The amorphous Si–O–C network is composed of tetrahedrally coordinated $SiO_{4-x}C_x$ ($x = 1-4$) structural units, including SiO_2 and C-enriched regions [62–66]. Depending on the amount of free carbon, either isolated carbon nanodomains (lower amount of free C) or a carbon percolation network (higher amount of free C) exist, as demonstrated by electrical conductivity measurements and TEM analysis [65, 67, 68]. The prefix "carbon-rich" typically classifies SiOC ceramics in which the content of free carbon exceeds 20 wt.% [43]. Three electrochemically active sites for Li-ion storage have been identified within carbon-rich SiOC by ^{7}Li-MAS-NMR measurements [47, 48, 50, 69]. Major Li-ion host sites are interstitial spaces and edges of graphene and carbon layers within the free carbon phase. Minor storage contribution is assigned to less ionic Li-species that are stored in micropores. Finally, some diamagnetic Li-species are directly or indirectly stored in the amorphous Si–O–C network. The comparison of the voltage profiles of carbon-rich SiOC and amorphous carbon confirms the Li-ion insertion and extraction within the free carbon phase in the ceramic microstructure [47, 55, 58, 70].

Even though in 1997 Dahn et al. filed a patent for the use of silazane-derived SiCN ceramics, where reversible discharge capacities up to 560 $mAh \cdot g^{-1}$ were reported [71], little research has been done since that time on the application of these materials in lithium ion batteries in comparison to SiOC. Electrochemical results on lithium insertion into SiCN derived electrode materials were first reported in 2006 by Kolb et al. [72]. In these early studies, a stable electrochemical behavior of carbon-rich polysilylcarbodiimides was reported [73, 74]. Similarly, Reinold et al. [75], demonstrated the excellent performance of carbon-rich SiCN materials and discussed the influence of the molecular polymer structure on the resulting ceramic microstructure and eventually on the electrochemical performance of the material. Later, nanocomposites of carbon and polymer derived silicon carbonitride (SiCN) ceramics were studied as anodes for lithium ion batteries [58, 72, 76–78], which showed a much better rate capability than pure carbon. Solid state NMR studies on carbon-rich SiCN ceramics clearly identify carbon as the main lithium storage site [79, 80]

In order to accommodate volume changes during lithiation of silicon/tin, the ceramic matrix has to withstand the corresponding internal stresses. Scarmi et al. [81] have proposed model structures of carbon-poor and carbon-rich SiOC amorphous ceramics. According to their model, carbon-poor SiOC materials are represented as nanodomains of sp^2 carbon which are discontinuously dispersed in silica. Carbon rich SiOC consists of a cellular network of graphene sheets of sp^2 carbon, where the nanodomains of silica are sequestered within the cells created by the graphene sheets. Accordingly, structures in which silica is encapsulated by a graphene network can show viscoelastic behavior while no viscosity reduction is expected for carbon-poor systems. Creep deformation in the silica phase leads to load transfer from the silica to the graphene network which eventually causes the deformation to saturate; when the applied stress is removed, the graphene network springs back to its original form. By combining the results of our studies [47–61] we have identified the critical material properties influencing the electrochemical performance of the SiCN/SiOC ceramics [58]. For carbon-rich SiOC-based ceramics, the amount of free carbon phase has no significant impact on the first cycle lithiation and delithiation capacities of SiOC. However, for SiCN, the capacity increases with the amount of carbon until a threshold value is reached at about 50% of the carbon phase. The cycling stability of carbon-poor ceramics is very low for SiCN and SiOC. For carbon-poor SiOC, a clear linear dependence of the insertion capacity on the amount of the silicon oxycarbide phase is shown, while for silicon carbonitride there is no dependence between first cycle insertion capacity and SiCN matrix amount. In contrast to the tendency observed for SiOC, the SiCN lithiation capacity is very low for high (>70%) amounts of the SiCN matrix.

By combining experimental observations with theoretical calculations we suggest that replacing oxygen with nitrogen renders the mixed bond Si-tetrahedra unable to sequester lithium. Lithium is more attracted by oxygen in the SiOC network due to the more ionic character of Si–O bonds, leading to a high electron density on oxygen. This brings about very high initial lithiation capacities, even at low carbon content. With continuing cycling, lithium is irreversibly captured within the SiOC network resulting in a low cycling stability. If oxygen is replaced by nitrogen, the ceramic network becomes much less attractive for lithium ions due to the more covalent character of Si-N bonds and lower electron density on the nitrogen atom. This explains why a significant difference in electrochemical behavior of carbon-poor SiCN and SiOC materials is observed. For carbon-rich ceramics, the free carbon phase leads to high cycling stability and high reversible capacity [58, 60, 61, 69, 76, 79].

2.2. Atomistic modeling

One of the main challenges in understanding the electrochemical properties of SiOC ceramics is correctly assessing the influence of their amorphous character. Therefore, we used atomistic modeling and simulation techniques to be able to clarify the nature of the amorphous SiOC structures. A popular computational approach for generating amorphous model structures is the cook-and-quench method, where a crystalline system is heated well above the melting point, equilibrated and quenched down to a desired temperature. For SiOC, however, there is no corresponding crystalline phase that can be used as a starting point. Therefore, previous studies have considered an SiO_2 network and added carbon. In a pioneering work, Kroll [82–84] constructed SiOC where C is bonded exclusively to four Si neighbors (CSi_4 bonding) as in crystalline SiC. More recently [85, 86], C was considered to substitute O, with (CH_2Si_2 bonding) or without (CSi_2 bonding) additional saturation of dangling bonds by H. However, a consistent comparison of energetics of differently bonded C in SiOC is still lacking. Furthermore, to our knowledge, structure models that would substantiate negative formation enthalpies relative to cristobalite, SiC and graphite as reported in various studies based on calorimetric measurements [87, 88], have not been identified so far either.

In our work, we followed two strategies for designing SiOC structure models. In the first strategy (see top panel of Fig. 1), we tried to mimic the synthesis procedure of SiOC by pyrolysis of complex precursor molecules. First, the precursor backbone (without H groups) is divided into smaller SiOC, $SiOC_2$ and $SiOC_{12}$ substructures. These substructures are then used as building blocks to construct continuous networks that are accommodated in cubic periodic simulation cells. The networks consist of 50 Si, 46 O and 173 C atoms ($Si_{0.186}O_{0.171}C_{0.643}$ being close to experimentally relevant C-rich compositions), do not contain C-O bonds and the volume of the supercells is initially set to the experimental density ($1.6\ g\ cm^{-3}$). The network structures are then subjected to cook-and-quench simulations and subsequent structure optimizations at zero K. Calculations were performed using the projector augmented-plane-wave code vasp [89, 90] in conjunction with the generalized gradient–gradient approximation of Perdew, Wang and Ernzerhof [91]. An energy cutoff of 400 eV and a $2 \times 2 \times 2$ Monkhorst–Pack [92] k-point mesh were used. Electronic self-consistency was considered to be achieved as energy changes in subsequent cycles were below 10^{-6} eV and forces were relaxed below $0.01\ eV\ Å^{-1}$. In the cook-and-quench simulations, an annealing temperature of 2000 K, a timestep of 1 fs and overall simulation times of 10 ps were used. Formation energies were calculated relative to diamond (diamond and graphite are energetically almost degenerate but the former does not require use of specific van der Waals functionals [93]), 3c-SiC and cristobalite (with k-point meshes adjusted accordingly), (Eq. (2))

$$E_f = (E_{SiOC} - n_{Si}\ \varepsilon_{Si} - n_O\ \varepsilon_O - n_C\ \varepsilon_C)/n_{SiOC} \qquad (2)$$

Here E_{SiOC} is the total energy of the SiOC model, E_{SiO2} is the total energy of cristobalite, n_x is the number of species x in the SiOC model, ε_x is the reference energy of species

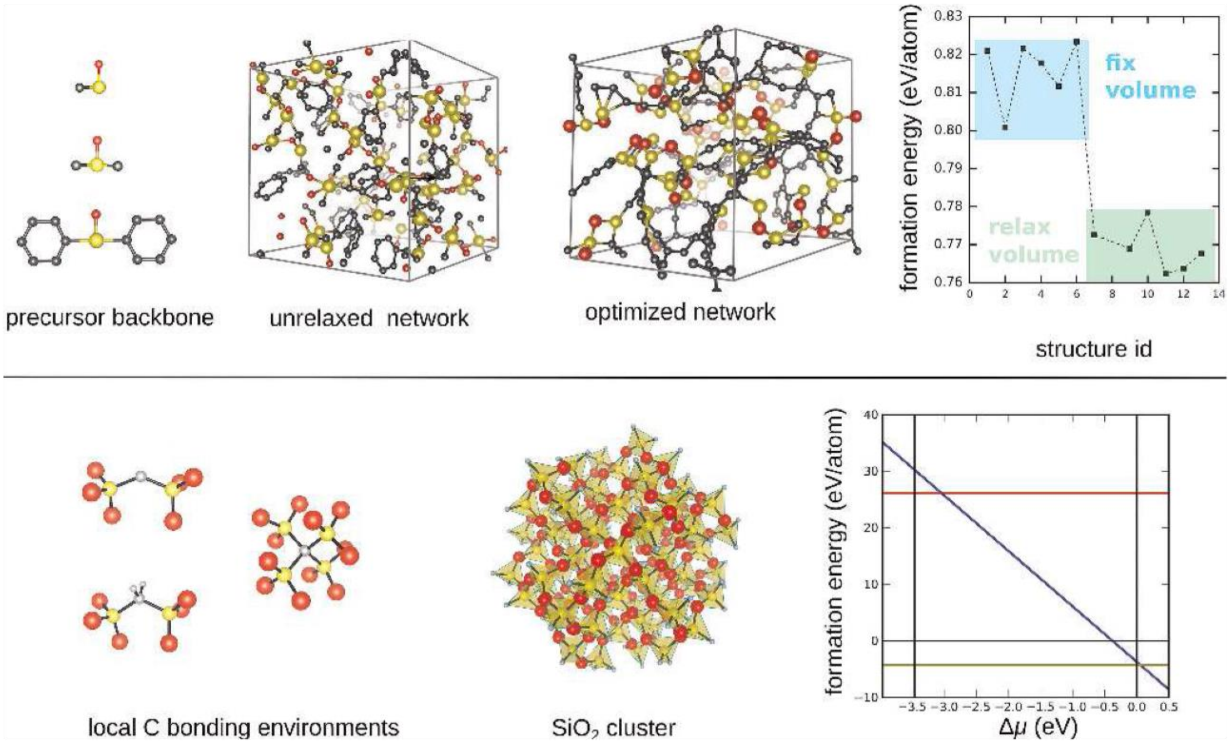

Fig. 1. Atomistic modeling of structure and thermodynamics of SiOC. The top panel illustrates our approach to mimic experimental synthesis by constructing networks based on a precursor backbone. The bottom panel shows different potential local bonding geometries of C in SiOC that are realized in an SiO_2 cluster host to study ideal formation energies. Color coding: Si = yellow, O = red, C = gray.

x [$\varepsilon_C = \varepsilon_{diamond}$, $\varepsilon_{Si} = \varepsilon_{SiC} - \varepsilon_C$, and $\varepsilon_O = (\varepsilon_{SiO2} - \varepsilon_{Si})/2$] and n_{SiOC} is the total number of SiOC atoms.

The calculated formation energies are shown in the top panel of Fig. 1 in two sets of data points. The first set corresponds to structure models where the cell volume was fixed to reproduce the experimental density. In the second set of data points we also relax the volume yielding a considerable increase in the density to 2.1 g cm^{-3} and a gain in formation energy. However, the calculated formation energies of $E_f > +760$ meV atom^{-1} (+73 kJ mol^{-1}) differ considerably from those of other structure models [82], and in particular from the negative values indicated by calorimetric measurements [87, 88].

A potential origin of this disagreement is the fact that our models contain a large portion of disordered carbon rings and strings instead of a free-carbon phase and essentially no continuous region of SiO_2 as expected from experimental structure analysis [64, 94]. Thus, despite the conceptual appeal of generating structure models by mimicking experimental synthesis, reaching necessary simulation times to follow relevant structural transformation is challenging. In order to overcome this time-limitation issue, better initial guesses for the resulting local structure of SiOC are necessary.

Therefore, we also studied various possibilities of local bonding of C in SiOC, fully neglecting the details of the synthesis process and assuming that the SiO_2 structure is characteristic for Si-O bonding in SiOC [64, 94]. The bottom panel of Fig. 1 details three different bonding environments. We consider C bonded to two Si neighbors (CSi_2), C bonded to two Si neighbors and two additional H neighbors (CSi_2H_2) and C bonded to four Si neighbors (CSi_4). In order to evaluate the formation energies of C in theses bonding environments, the three configurations were embedded in a SiO_2 cluster model also shown in Fig. 1. Calculations are performed using the GPAW code [95], linear combinations of atomic orbitals (LCAO) as basis functions and the local density approximation (LDA) [96]. The SiO_2 reference cluster consists of 87 Si, 136 O and 76 H atoms within a cubic cell of side length 32 Å (corresponding to 68 SiO_2 units plus additional surface atoms). A grid spacing of 0.167 Å and a Γ-point sampling of the Brillouin zone was used. Structural optimization was performed until forces on individual atoms were smaller than 0.01 eV Å^{-1}. The formation energies are defined as:

$$Ef = (E_{SiOC} - E_{SiO2} - \Delta n_{Si}\,\varepsilon_C - \Delta n_O\,\varepsilon_O) \\ -\Delta n_C\,\varepsilon_C - \Delta n_H\,\mu_H)/n_{SiOC} \qquad (3)$$

where E_{SiOC} is the total energy of the SiOC model, E_{SiO2} is the total energy of the SiO_2 cluster, Δn_x is the difference in the number of species x between the SiOC and the SiO2 cluster, ε_x is the reference energy of species x as before, $\mu_H = 0.5\ \varepsilon_{H2} + \Delta\mu_H$ is the chemical potential of hydrogen (measured relative to H_2) and n_{SiOC} is the total number of relevant SiOC atoms (excluding Si and H atoms at the surface of the cluster).

We find that the CSi_4 configuration is energetically preferred over the entire range of the H chemical potential (the minimum allowed value is set by $\varepsilon_{C6H6} - \varepsilon_{C6H5}$). The formation energy of this configuration is considerably lower than the formation energies of our precursor-derived model structures. Most strikingly, it is slightly negative which agrees with calorimetric measurements (see below and Refs. [87, 88]). We note that the CH_2Si_2 configuration may become important as a defect structure at high H chemical potential or, since it is less susceptible to stresses, as the C concentration raises.

2.3. High-temperature oxide melt solution calorimetry

The enthalpies of formation of SiOC-based materials prepared by pyrolysis of the precursor derived ceramics were determined by high temperature oxide melt solution calorimetry using a Setaram AlexSys-1000 calorimeter (Setaram Instrumentation, Caluire, France). The AlexSys-1000 is a commercial Tian-Calvet calorimeter constructed according to the specifications of the custom-built calorimeters as detailed by Navrotsky [97, 98]. In this calorimeter, two, symmetric measurement chambers are each surrounded by 64 thermocouple junctions arranged in series to form the thermopiles. These thermopiles offer a heat conduction path with a defined thermal resistance from the calorimeter chambers to the surrounding block. The calorimeter is operated in isoperibolic conditions by maintaining the surrounding block at a temperature 701 °C by the use of electric resistors. The calibration factor associated with the heat flow rate through the thermopiles was determined by dropping sapphire spheres of known mass from room temperature into the individual calorimeter chambers at the operating temperature. For the solution calorimetry experiments, the precursor derived ceramic samples were dropped from room temperature into approximately 28 g of self-prepared $3Na_2O \cdot 4MoO_3$ which was located in platinum crucibles in the measurement chambers. The samples for solution calorimetry were made by homogeneously mixing the SiOC powders with sodium-molybdate solvent in a 1 : 4 ratio and pressing them into pellets with a diameter of 3 mm and a mass of 3–5 mg. The pellets were dropped from room temperature directly into the sodium molybdate solution in the platinum crucibles located inside the calorimeter at 701 °C. To ensure complete oxidation and improve the dissolution process, oxygen was used for both, the flushing and stirring gases.

Since there is residual hydrogen in the SiOC samples after synthesis, the reaction associated with the enthalpy of drop solution of the ceramics can be written as:

$$Si_xO_yC_zH_{p(\mathrm{amorph,298\,K})} + (x+z+p/(4-y)/2)O_{2(\mathrm{gas,973\,K})} \\ \rightarrow xSiO_{2(\mathrm{crist.,974\,K})} + zCO_{2(\mathrm{gas,974\,K})} + p/4H_2O_{(\mathrm{gas,974\,K})}$$

The reaction associated with standard enthalpy formation of the SiOC compounds from cristobalite, SiC, C, and H_2 is:

$$y/2SiO_{2(\mathrm{crist})} + (x-y/2)SiC_{(s)} + (z-x+y/2)C_{(s)} \\ + y/2H_{2(g)} \rightarrow Si_xO_yC_zH_{p(\mathrm{amorph})}$$

whereas the reaction showing the standard enthalpy of formation of the SiOC compounds from the elements can be expressed as:

$$xSi_{(\mathrm{crist})} + y/2O_{2(s)} + zC_{(s)} + p/2H_{2(g)} \rightarrow Si_xO_yC_zH_{p(\mathrm{amorph})}$$

The enthalpies of formation of the SiOC precursor derived ceramics from cristobalite, SiC, C, and H_2 are shown in

Fig. 2a, whereas the data for the enthalpies of formation from the elements are shown in Fig. 2b. Our values are in good agreement with those of Morcos et al. [88], except for the sample with composition $Si_{0.343}O_{0.530}C_{0.090}H_{0.04}$, which has the lowest C-content. Interestingly, there is no obvious trend in the standard enthalpy of formation data from cristobalite, SiC, C, and H_2 (Fig. 2a), whereas as the amount of C increases, the enthalpy of formation of the SiOC matrix from the elements becomes less exothermic. This trend is linear, as indicated by the red dashed line in Fig. 2b. For the sample with lowest C-content, however, there seems to be insufficient C to react exothermically with O_2 to produce CO_2 during calorimetry. However, this highly exothermic reaction is important since it supplies the required activation energy to drive the formation of cristobalite from the Si–O component of the amorphous SiOC matrix. Therefore, one can assume that the SiO_2 regions remain partially amorphous on the time scale of the reaction (1 hour) for the sample with lowest C-content. Interestingly, since the enthalpy data for this low C content sample is positively displaced from the enthalpy data for all other samples as schematically indicated by the arrows in Fig. 1a and b, one would expect that the formation of crystalline SiO_2 from the amorphous Si-O regions is an exothermic process. This suggests that the amorphous Si-O matrix is indeed less thermodynamically stable than cristobalite.

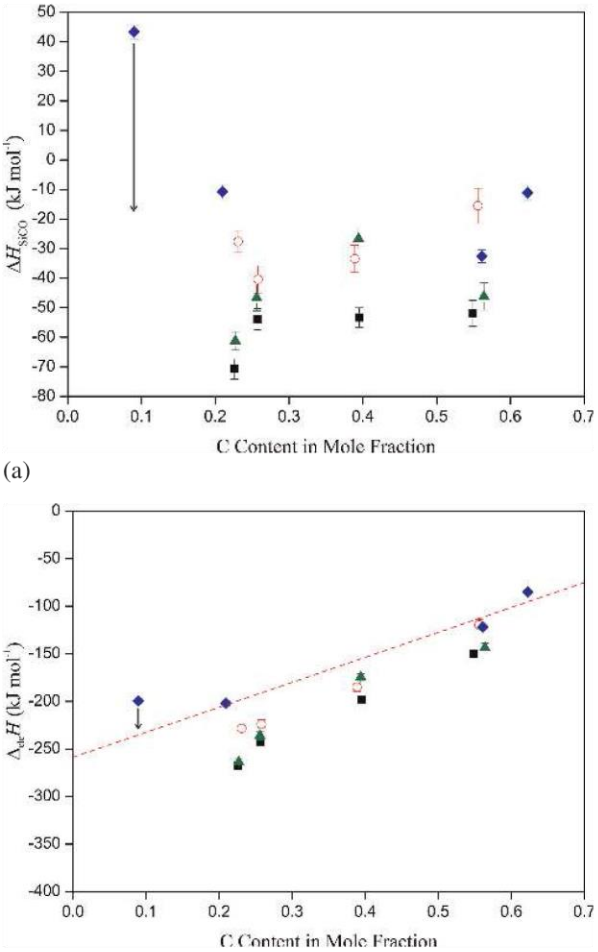

(a)

(b)

Fig. 2. Standard enthalpy of formation of the SiOC compounds from (a) SiO_2 and SiC and (b) from the elements. The blue symbols are the values determined in this work, whereas the black, red, and green symbols represent data from Morcos et al. [88] following heat treatment of the SiOC samples at 1000, 1200, and 1400 °C respectively. The dashed line in (b) is a linear fit of the enthalpy of formation data from our work excluding the sample with lowest C-content. The arrows indicate expected exothermic enthalpy change, which would be associated with the transformation of an amorphous Si-O matrix to cristobalite.

3. Silicon and tin

3.1. Electrochemical properties

Silicon/tin undergo massive volume changes during lithium alloying/dealloying, causing fracture and loss of the electrical contact between grains, ultimately leading to capacity fading on cycling. By using nanoparticles of Si/Sn, this effect can be reduced [3]. In our study [99] of silicon-based negative electrodes for lithium ion batteries, we demonstrated that the initial morphology and crystallinity of silicon influences the electrochemical performance of the nanocomposite material. In order to be able to design the required porosity and morphology of the silicon, we have successfully tailored and controlled the known magnesiothermic reaction of silica reduction. We found that the crystalline porous nanoslicon reacts with lithium through an alloying mechanism which presents an unstable cycling behavior. Amorphous nanosilicon (Fig. 3a) of an extraordinary high active surface of 623 $m^2 g^{-1}$ demonstrates stable electrochemical performance (Fig. 3b) with storing lithium through adsorption/desorption mechanism [100].

3.2. Atomistic modeling

Amorphous Li-Si systems have been widely studied using atomistic methods. However, model structures based on cook-and-quench simulations [101, 102] are limited to relatively few compositions where intermetallic phases exist. For obtaining deeper insights, thermodynamic information for systems with arbitrary composition is required. Thus, we have generated such model structures using an iterative insertion algorithm, inspired by the work of Chevrier et al. [103], and extended to include a replica scheme and intermediate cook-and-quench simulations. For details, we refer to Ref. [104].

Figure 4 (left panel) shows calculated formation energies and selected structure models. For a detailed discussion we refer to Ref. [104]. Here we point out two main findings and their connection to experiment. (i) Li insertion in crystalline Si (c-Si) results in two-phase lithiation where amorphous Li_xSi (a-Li_xSi) with $x = 2$ coexists with Si. Li insertion in amorphous Si (a-Si) leads to homogeneous single-phase lithiation. This accounts for the better cyclability of a-Si anodes as compared to c-Si [105]. The two-phase lithiation leads to large stresses due to the mismatch in specific volume of the coexisting phases. The two-phase system is therefore much more prone to degradation due to disintegration. (ii) Although our calculations do not hint at a potential origin of experimentally observed sudden recrystallization of $Li_{15}Si_4$ phase [6], our calculations show that the presence of this phase leads to two-phase delithiation where again the a-Li_2Si phase coexists. Cycling Si electrodes with limited capacity can avoid this two-phase delithiation and thus again prolong lifetime [106].

We emphasize that the two-phase lithiation also accounts for anisotropic swelling observed in first-cycle Li insertion in Si nanowires [107]. As pointed out in Ref. [108], this anisotropic swelling can be understood as a result of anisotropic interface mobilites. We have investigated a-Li_2Si/c-Si (*hkl*) interfaces where (*hkl*) is one of (111), (110), (001). Structure models, interface energies and barriers for Li hopping are also shown in Fig. 4 (right panel). The Li hopping

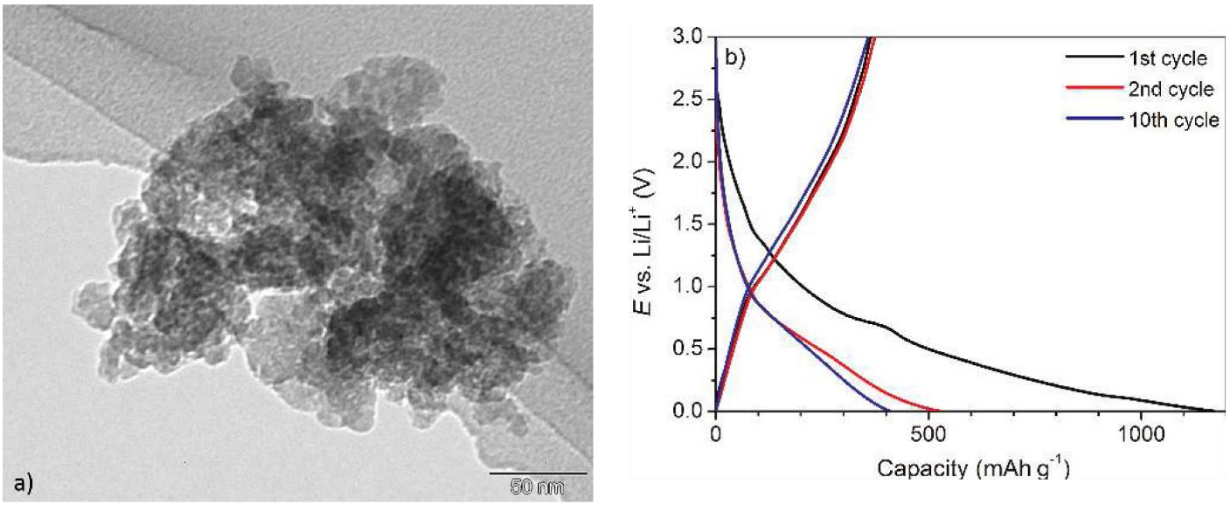

Fig. 3. (a) The morphology the amorphous silicon synthesized in magnesiothermic reaction and (b) the electrochemical cycling of this material, from [97].

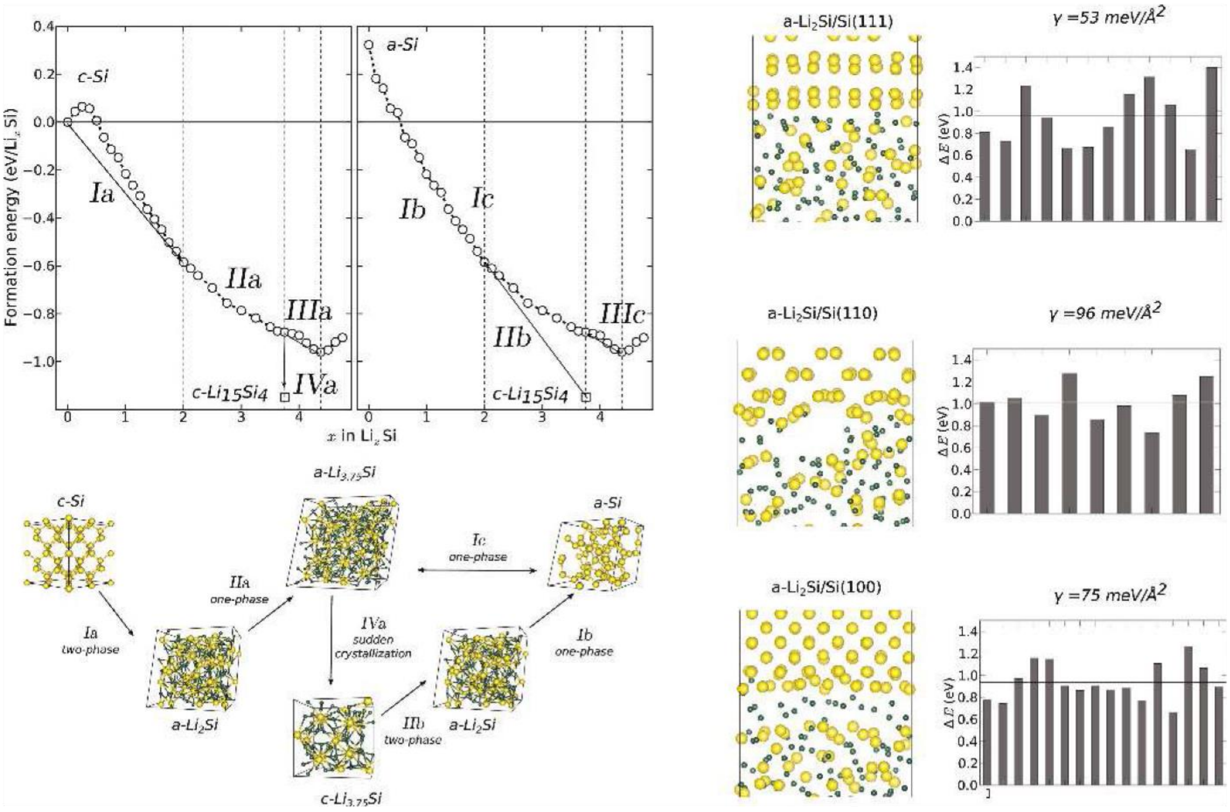

Fig. 4. Structure, thermodynamics and kinetics of amorphous Li-Si systems. The left shows formation energies and an illustration of the corresponding phase evolution. Structure models are not drawn to scale. The right panel shows differently oriented interfaces between lithiated and pristine Si, corresponding interface energies and barriers for Li hopping across the interface (different Li-ion/paths are represented by different bars). Color coding: Si = yellow, Li = green.

barriers are not very sensitive to interface orientation. The variation of barriers for different paths at fixed orientation is larger than the variation of average barriers for different orientations. Therefore, the interface mobility is largely governed by the nucleus formation energy for propagation, E_{nucl}. This nucleus formation energy depends on the excess energy of interfaces that are formed between the nucleus and the pristine Si. Our calculations show a hierarchy of interface energies that imply $E_{\mathrm{nucl}}^{(111)} > E_{\mathrm{nucl}}^{(100)} > E_{\mathrm{nucl}}^{(110)}$ when assuming that interfaces between the nucleus and the pristine Si have an orientation that is perpendicular to the propagation direction. This hierarchy is in accordance with mobilities that can explain the observed swelling behavior [107, 108]. A detailed analysis and discussion is given in Ref. [109].

Despite the fact that Sn (or Sn-based) electrodes do not transform into amorphous alloys but remain crystalline upon electrochemical lithiation [7, 110], we also apply our iterative structure-generation scheme to Li_xSn systems. The results and comparison to Li_xSi help understanding why chemically similar Si and Sn behave so differently upon Li insertion. Calculations have been performed using the projector augmented-plane wave code vasp [89, 90] in conjunction with the generalized gradient–gradient approximation of Perdew, Wang and Ernzerhof [91]. An energy cutoff of 400 eV and a $3 \times 3 \times 2$ Monkhorst–Pack [92] k-point mesh were used. Electronic self-consistency was considered to be achieved as energy changes in subsequent cycles were below 10^{-6} eV and forces were relaxed below 0.01 eV $\mathrm{Å}^{-1}$. In the cook-and-quench simulations, and annealing temperature of 1 000 K, a timestep of 1 fs and overall simulation times of 10 ps were used. As the unlithiated starting point, a β-Sn structure (consisting of 12 atoms) was used, as this is the stable polymorph at room temperature or even below as the particle size reaches the nanoscale [111].

Figure 5 shows the calculated formation energies of hypothetical amorphous Li_xSn alloys. We find exclusively two-phase regions. Most importantly, although initial Li insertion favors the formation of an amorphous phase with composition Li_1Sn_1, a corresponding (crystalline) intermetallic phase with that composition exists, which has a lower energy [110]. This system is therefore prone to crystallize on lithiation. In Si, however, although initial Li insertion stabilizes an amorphous Li_2Si phase, this amorphous phase has no crystalline counterpart. Crystallization of a nearby intermetallic phase would require activation of diffusion processes over unrealistically large distances. In Sn, the amount of atomic rearrangements to form a crystalline nucleus is manageable and has much lower kinetic-energy barriers (due to the localized nature of the rearrangements). Experimental observation of crystalline Li–Sn phases during electrochemical cycling [7, 110] is therefore traceable on a theoretical basis.

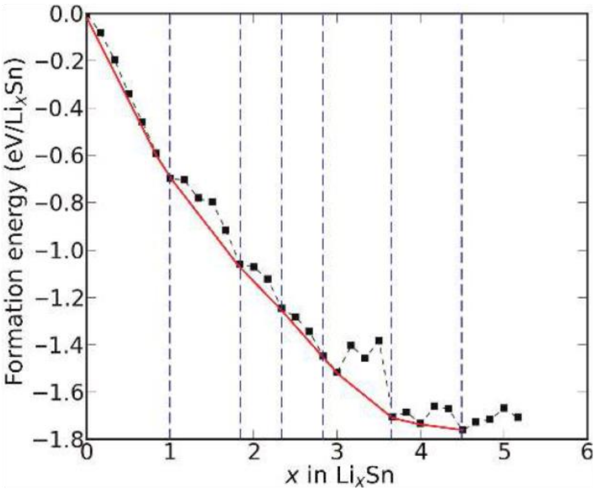

Fig. 5. Formation energies of hypothetic amorphous Li-Sn systems. On initial Li insertion an Sn/LiSn two-phase region is predicted. Since a crystalline phase with the very same composition exists, the amorphous system is prone to crystallize. A similar argument holds at high Sn concentrations.

4. Nanocomposites

The SiOC and SiCN ceramics, optimized with respect to their capability to withstand volume changes during silicon/tin alloying process were investigated as a stabilizing matrix. Various synthetic routes are proposed to ensure good electrical contact between the nanoparticles and matrix and homogeneous particle dispersion. Commercial and “home-synthesized” crystalline and amorphous silicon are used, while a uniform distribution of tin was ensured by using a single precursor approach.

4.1. Nanocomposites with silicon

By using polymer-derived silicon carbonitride (SiCN) ceramic as an inactive matrix for the crystalline silicon nanopowder (30 – 50 nm) we have obtained [112] a protective character of polymer-derived ceramics as matrix in terms of SEI stabilization for samples prepared at 1100 °C. Carbon-rich SiOC matrix has been used to stabilize commercial crystalline (30 – 50 nm) and amorphous (30 nm) silicon [99]. Nanocomposites were prepared by mixing silicon nanopowder with ceramic precursor followed by pyrolysis. The nanocomposites demonstrate a high gravimetric capa-

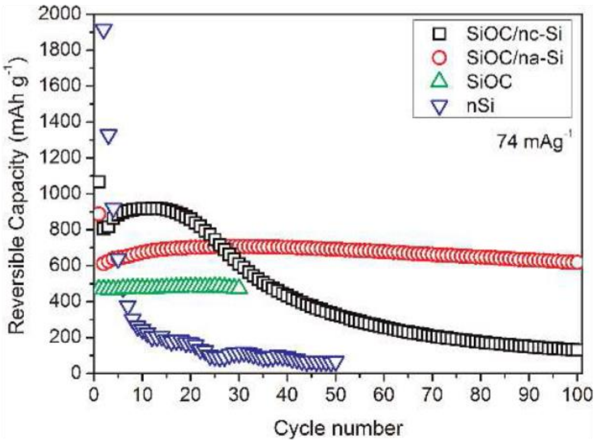

Fig. 6. Comparison of the reversible capacity depending on cycle number for SiOC/nc-Si, SiOC/na-Si, pure SiOC and pure nSi, from [98].

city of 905 mAh g^{-1} and 704 mAh g^{-1} for SiOC/nc-Si and SiOC/na-Si, respectively (Fig. 6). A strong capacity fading is found for the SiOC/nc-Si material, whereas the incorporation of amorphous Si into the SiOC matrix provides a stable cycling performance up to 100 cycles. Fundamental microstructural differences have been identified as the main reason for the difference in the electrochemical behavior. In the case of SiOC/nc-Si, crystalline silicon grains/agglomerates up to 100 nm in diameter are present within the matrix, while in the case of SiOC/na-Si silicon and silicon carbide crystallites of ~10 nm in size are found. Due to the smaller size of the Si precipitates, the absolute volume expansion of the formed Li–Si alloy in SiOC/na-Si is less critical, leading to minor mechanical load locally applied to the matrix. The arising stresses can be well accommodated by the SiOC host without degradation. In the case of SiOC/nc-Si, the expansion of the larger Si grains causes a severe matrix failure and, as a consequence, fading of the capacity is well pronounced. Moreover, nano-sized SiC grains present in SiOC/na-Si, increase the electrical conductivity and contribute to the superior electrochemical behavior of the composite. Finally, we explain the deviation between the theoretically estimated capacity of SiOC/na-Si (651 mAh g^{-1}) and SiOC/nc-Si (1 097 mAh g^{-1}) and the registered ones of 704 mAh g^{-1} and 905 mAh g^{-1}, respectively. For the sample based on amorphous silicon, it is suggested that the initially amorphous silicon crystallized only partially, leaving the electrochemically amorphous phase unconsidered in the estimation, while for SiOC/nc-Si a slow activation of the available crystalline silicon is assumed to be responsible for registered lower capacity values.

In order to stabilize nanosilicon within the SiCN matrix, we have systematically designed core-shell structures around silicon for improving its cycling stability during lithium insertion/extraction (Fig. 7) [113]. On the one hand, coating with environmentally friendly organic carbon is applied to increase the composite conductivity whereas partial burning of carbon leads to the formation of voids around silicon, proved by nitrogen physisorption (BET) and transmission electron microscopy (TEM) measurements. In parallel, polymer-derived silicon carbonitride ceramic (SiCN) with low carbon content is used to form stable shells and to maintain the porous structure. The presence of stable SiCN ceramic also helps to stabilize the high active surface structure against thermal runaway while the void/shell microstructures around the silicon lead to the enhanced cycling stability of the electrode.

Figure 8 presents TEM micrographs of the sample of Si/C/void/SiCN/C. It demonstrates clearly that silicon particles are successfully coated with carbon prior to embedding. The EDS pattern of the selected area (Fig. 8b) reveals that the silicon nanoparticle is present and covered with an SiO_2 layer. It is however still difficult to distinguish whether carbon (or void) and in which amount is present around the silicon particles after the material was heat-treated in air. It should be noted that coating of silicon particles prior to embedding also acts beneficially against agglomeration. This is important as the distribution of silicon nanopowder in ceramic matrices significantly influences the cycling stability of the prepared composites [99]. The TEM study confirms as well that the voids are located around the silicon particles. Significant improvement of the electrochemical stability of the composite is demonstrated as well. The electrodes prepared from composites with voids around silicon display almost no cracks even though silicon activity is confirmed by electrochemical investigations.

In order to further improve the cycling stability and capacity of composite materials, we further tailored the above described synthesis. Thus, nanostructured, porous crystalline (Si_{tc}) and amorphous (Si_{sa}) silicon synthesized via magnesiothermic reduction [100] have been stabilized within the ceramic matrix [114]. For electronic conductivity and silicon stabilization, fructose-derived carbon, polymer-derived SiOC ceramic or both carbon and SiOC, are used. By means of X-ray diffraction and Raman spectroscopy it is found that the crystallinity of Si_{tc} as well as the amorphous character of Si_{sa} are preserved in the final composites. Embedding of crystalline silicon into carbon leads to high initial capacities of ~600–650 mAh · g^{-1}, but only the matrix consisting of carbon and SiOC results in a stable cycling behavior over 50 cycles with a final capacity of 575 mAh · g^{-1} (Fig. 9a). All composites derived from amorphous Si_{sa} show a stable cycling behavior; the highest, stable capacity of ~500 mAh g^{-1} is observed when silicon is covered with carbon and SiOC. Figure 9b presents material capacities recalculated with respect to the amount of silicon, namely

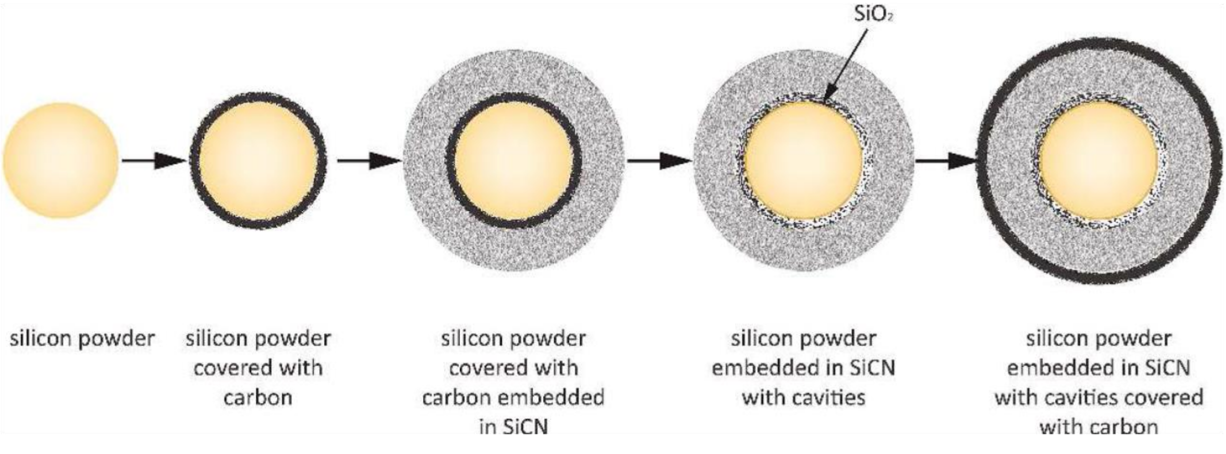

Fig. 7. Synthesized composites and a preparation route.

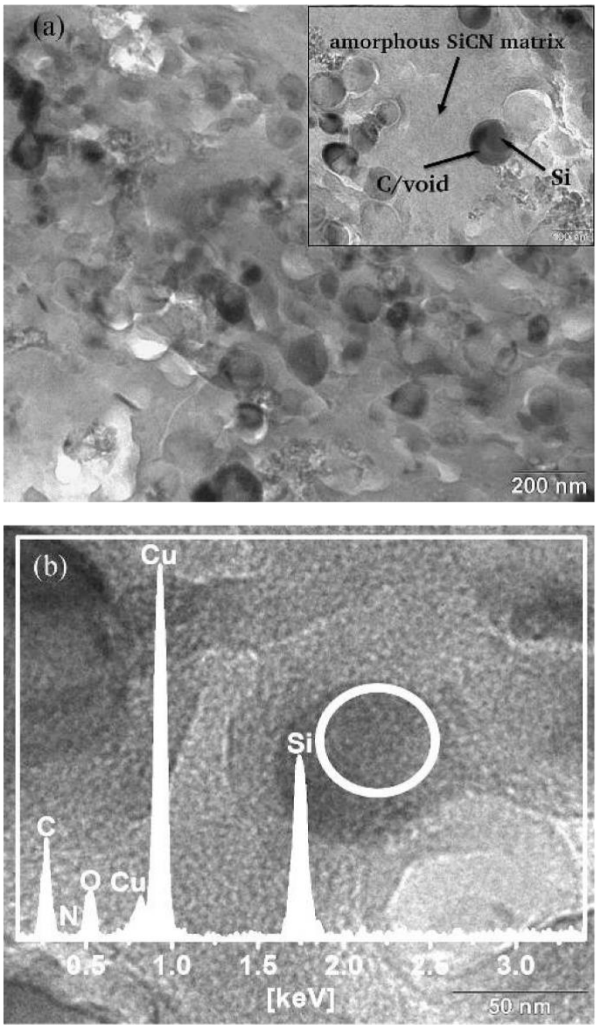

Fig. 8. (a) TEM micrographs of Si/C/void/SiCN/C nanocomposites; (b) TEM micrograph of same material with EDS analysis overlayed.

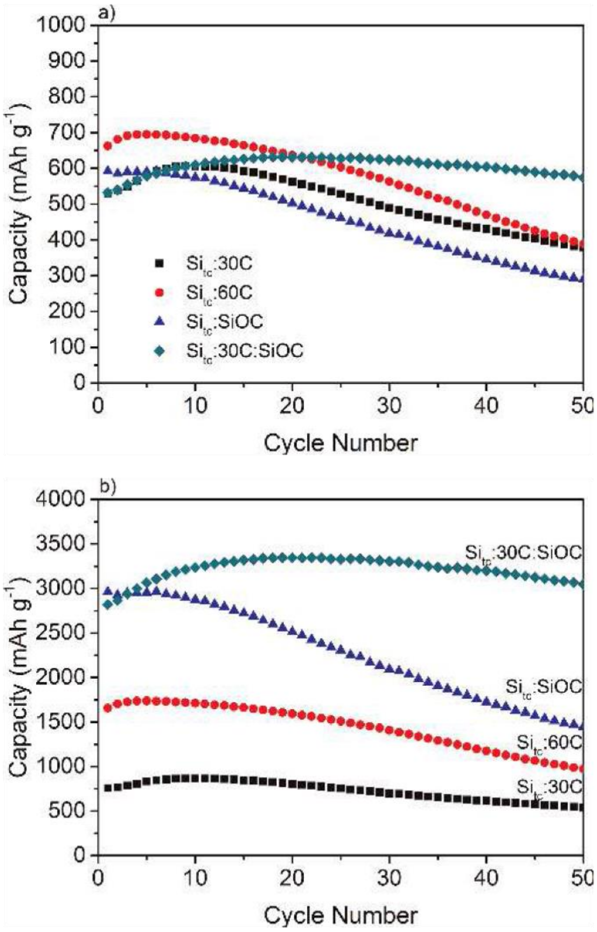

Fig. 9. (a) Delithiation capacities of composites prepared with porous silicon from magnesothermic route; (b) Delithiation capacities normalized to amount of silicon present in composites.

considering exclusively silicon as an active material. It shows that silicon within C/SiOC matrix demonstrates a stable electrochemical behavior with capacities close to the theoretical.

4.2. Nanocomposites with tin

A direct synthesis of novel ceramic/tin nanocomposites is achieved by an innovative single-source precursor approach [115]. Accordingly, polyorganosiloxanes modified with tin(II)acetate are prepared and thermally converted into SiOC/Sn nanocomposites at 1 000 °C. Two different commercially available polysiloxanes are used for the modification, namely i) polysilsesquioxane Wacker-Belsil PMS MK, which transforms into a silicon oxycarbide matrix ($SiOC_{MK}$) with moderate free carbon content (~6 wt.%) and a Young's modulus of ca. 85–96 GPa and ii) polysiloxane Polyramic RD-684a, which converts into a carbon-rich (~41 wt.% free carbon) silicon oxycarbide matrix ($SiOC_{RD}$) with a consequently lower value of the Young's modus of 66 GPa [54–56, 65, 116]. Interestingly, the electrochemical performance of the SiOC/Sn-based nanocomposites correlates with the phase composition and the stiffness of the silicon oxycarbide matrices. The carbon-poor and stiff matrix (as for $SiOC_{MK}$) is found to be unable to withstand volume changes related to Li–Sn alloying, since serious damage of the electrodes accompanied by a strong capacity fading is found. If the matrix is carbon-rich and soft (as for $SiOC_{RD}$), it is able to accommodate the high volume expansion upon alloy formation and thus prevents the electrode failure.

Galvanostatic cycling of both composites demonstrates a first cycle reversible capacity of 566 mAh g^{-1} for $SiOC_{MK}$/Sn and 651 mAh g^{-1} for $SiOC_{RD}$/Sn (Fig. 10). We attribute the superior cycling stability and rate capability of $SiOC_{RD}$/Sn as compared to $SiOC_{MK}$/Sn to the soft, carbon-rich SiOC matrix derived from the RD-684a polymer, which accommodates the Sn-related volume changes during Li-uptake and release. The poor cycling stability found for $SiOC_{MK}$/Sn is related to mechanical failure of the rather stiff and fragile, carbon-poor matrix produced from PMS MK. Incremental capacity measurements outline different final Li–Sn alloy stages, depending on the matrix. For $SiOC_{RD}$/Sn, alloying up to Li_7Sn_2 is registered, whereas for $SiOC_{MK}/Sn$ $Li_{22}Sn_5$ stoichiometry is reached. The suppression of $Li_{22}Sn_5$ phase in $SiOC_{RD}/Sn$ is rationalized by an expansion restriction of the matrix and thus prevention of a higher Li content in the alloy. For $SiOC_{MK}/Sn$ in contrast, the matrix severely ruptures, providing an unlimited free volume for expansion and thus formation of $Li_{22}Sn_5$ phase.

5. Conclusions

Our work on stabilization of electrochemical lithiation/delithiation of nano-Si/Sn shows that carbon-rich silicon oxycarbide and silicon carbonitride are appropriate matrix materials to ensure extended cycling stability and high capacity of the composite materials. Thermochemical measurements demonstrate negative enthalpies of formation (energetic stabilities) for carbon rich SiOC ceramics. DFT

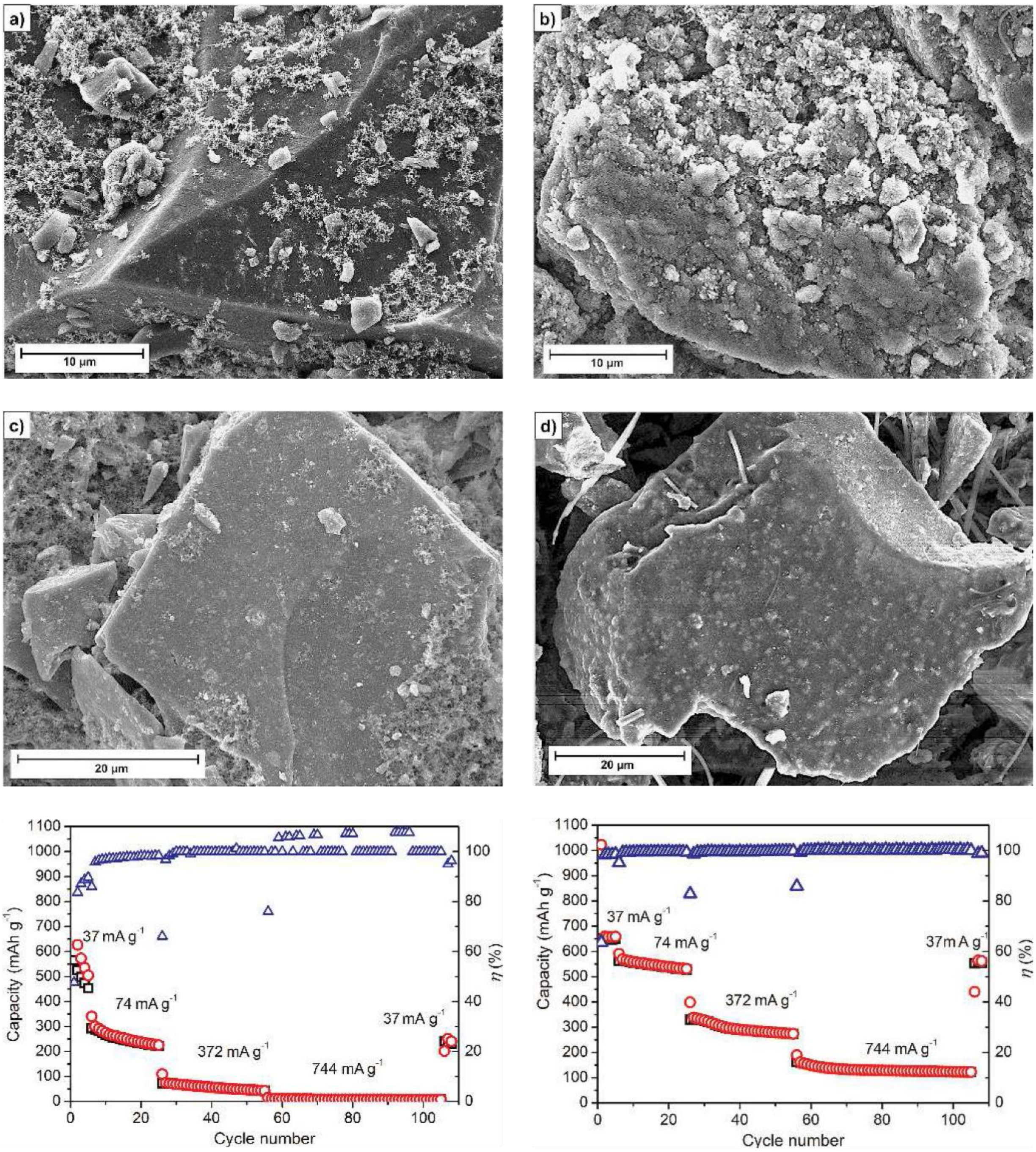

Fig. 10. SEM image of (a) $SiOC_{MK}/Sn$ electrode before cycling, (b) after 108 cycles; (c) $SiOC_{RD}/Sn$ electrode before cycling, (d) after 108 cycles (the fibers represent remaining rests of separator) with (e, f) corresponding electrochemical extended cycling behavior.

calculations substantiate this finding, at least for low carbon concentration when using carefully designed atomistic models. As the amount of C increases, the enthalpy of formation of the matrix becomes less negative, which is in good agreement with the observations showing a less stiff nature of the matrix with increasing C contents. The thermodynamics of the Li–Si system show a transition into an amorphous phase and the existence of two-phase regions. We propose simple synthetic routes of nanocomposite preparation that ensure good electrical contact between the nanoparticles and matrix, and homogeneous particle dispersion. Nanoamorphous/porous silicon is advantageous over crystalline nanoparticles, since two-phase regions are avoided during lithiation/delithiation. A single-source precursor approach provides a uniform distribution of tin nanoparticles within SiOC matrices and leads to high capacities and stable electrochemical lithiation and delithiation of tin.

Authors acknowledge the financial support by the Deutsche Forschungsgemeinschaft (DFG), Bonn, Germany within SPP1473/JP8.

References

[1] N. Nitta, F. Wu, J.T. Lee, G. Yushin: Mater. Today 18 (2015) 252. DOI:10.1016/j.mattod.2014.10.040
[2] N. Nitta, G. Yushin: Part. Part. Syst. Char. 31 (2014) 317. DOI:10.1002/ppsc.201300231
[3] U. Kasavajjula, C. Wang, A.J. Appleby: J. Power Sources 163 (2007) 1003. DOI:10.1016/j.jpowsour.2006.09.084
[4] J.R. Szczech, S. Jin: Energy Environ. Sci. 4 (2011) 56. DOI:10.1039/C0EE00281J
[5] B. Liang, Y. Liu, Y. Xu: J. Power Sources 267 (2014) 469. DOI:10.1016/j.jpowsour.2014.05.096
[6] M.N. Obrovac, L. Christensen: Electrochem. Solid-State Lett. 7 (2004) A93. DOI:10.1149/1.1652421
[7] M. Winter, J.O. Besenhard: Electrochim. Acta 45 (1999) 31. DOI:10.1016/S0013-4686(99)00191-7
[8] M. Wachtler, J.O. Besenhard, M. Winter: J. Power Sources 94 (2001) 189. DOI:10.1016/S0378-7753(00)00585-1
[9] M. Winter, W.K. Appel, B. Evers, T. Hodal, K.-C. Möller, I. Schneider, M. Wachtler, M.R. Wagner, G.H. Wrodnigg, J.O. Besenhard: Monatsh. Chem. 132 (2001) 473. DOI:10.1007/s007060170110
[10] X.H. Liu, L. Zhong, S. Huang, S.X. Mao, T. Zhu, J.Y. Huang: ACS Nano 6 (2012) 1522. DOI:10.1021/nn202452c
[11] H. Wu, G. Zheng, N. Liu, T.J. Carney, Y. Yang, Y. Cui: Nano Lett. 12 (2012) 904. DOI:10.1021/nl203967r
[12] L. Yue, W. Zhang, J. Yang, L. Zhang: Electrochim. Acta 125 (2014) 206. DOI:10.1016/j.electacta.2014.01.094
[13] X. Zhou, J. Tang, J. Yang, J. Xie, L. Ma: Electrochim. Acta 87 (2013) 663. DOI:10.1016/j.electacta.2012.10.008
[14] X. Li, P. Meduri, X. Chen, W. Qi, M.H. Engelhard, W. Xu, F. Ding, J. Xiao, W. Wang, C. Wang, J.-G. Zhang, J. Liu: J. Mater. Chem. 22 (2012) 11014. DOI:10.1039/c2jm31286g
[15] J. Saint, M. Morcrette, D. Larcher, L. Laffont, S. Beattie, J.P. Peres, D. Talaga, M. Couzi, J.M. Tarascon: Adv. Funct. Mater. 17 (2007) 1765. DOI:10.1002/adfm.200600937
[16] W.R. Liu, J.H. Wang, H.C. Wu, D.T. Shieh, M.H. Yang, N.L. Wu: J. Electrochem. Soc. 152 (2005) A1719. DOI:10.1149/1.1954967
[17] X.L. Yang, Z.Y. Wen, X.X. Xu, B. Lin, Z.X. Lin: J. Electrochem. Soc. 153 (2006) A1341. DOI:10.1149/1.2199435
[18] I.S. Kim, G.E. Blomgren, P.N. Kumta: J. Power Sources 130 (2004) 275. DOI:10.1016/j.jpowsour.2003.12.014
[19] N. Dimov, S. Kugino, M. Yoshio: Electrochim. Acta 48 (2003) 1579. DOI:10.1016/S0013-4686(03)00030-6
[20] I.-S. Kim, P.N. Kumta: J. Power Sources 136 (2004) 145. DOI:10.1016/j.jpowsour.2004.05.016
[21] D. Mazouzi, B. Lestriez, L. Roue, D. Guyomard: Electrochem. Solid State Lett. 12 (2009) A215. DOI:10.1149/1.3212894
[22] C. Martin, M. Alias, F. Christien, O. Crosnier, D. Belanger, T. Brousse: Adv. Mater. 21 (2009) 4735. DOI:10.1002/adma.200900235
[23] B. Chen, A.K. Flatt, H. Jian, J.L. Hudson, J.M. Tour: Chem. Mater. 17 (2005) 4832. DOI:10.1021/cm051104 h
[24] Y.H. Xu, G.P. Yin, P.J. Zuo: Electrochim. Acta 54 (2008) 341. DOI:10.1016/j.electacta.2008.07.083
[25] C. Martin, O. Crosnier, R. Retoux, D. Belanger, D.M. Schleich, T. Brousse: Adv. Funct. Mater. 21 (2011) 3524. DOI:10.1002/adfm.201002100
[26] S. Yang, G. Li, Q. Zhu, Q. Pan: J. Mater. Chem. 22 (2012) 3420. DOI:10.1039/C2JM15232 K
[27] D. Chen, R. Yi, S. Chen, T. Xu, M.L. Gordin, D. Wang: Solid State Ionics 254 (2014) 65. DOI:10.1016/j.ssi.2013.11.020
[28] C.K. Chan, H. Peng, G. Liu, K. McIlwrath, X.F. Zhang, R.A. Huggins, Y. Cui: Nat. Nano 3 (2008) 31. PMid:18654447; DOI:10.1038/nnano.2007.411
[29] C.K. Chan, R. Ruffo, S.S. Hong, R.A. Huggins, Y. Cui: J. Power Sources 189 (2009) 34. DOI:10.1016/j.jpowsour.2008.12.047
[30] A. Vlad, A.L.M. Reddy, A. Ajayan, N. Singh, J.-F. Gohy, S. Melinte, P.M. Ajayan: Proc. Nat. Acad. Sci. 109 (2012) 15168. PMid:22949696; DOI:10.1073/pnas.1208638109
[31] J. Hassoun, K.-S. Lee, Y.-K. Sun, B. Scrosati: J. Am. Chem. Soc. 133 (2011) 3139. PMid:21291261; DOI:10.1021/ja110522x
[32] J. Hassoun, S. Panero, B. Scrosati: Fuel Cells 9 (2009) 277. DOI:10.1002/fuce.200800070
[33] G. Derrien, J. Hassoun, S. Panero, B. Scrosati: Adv. Mater. 19 (2007) 2336. DOI:10.1002/adma.200700748
[34] L. Bazin, S. Mitra, P.L. Taberna, P. Poizot, M. Gressier, M.J. Menu, A. Barnabe, P. Simon, J.M. Tarascon: J. Power Sources 188 (2009) 578. DOI:10.1016/j.jpowsour.2008.12.025
[35] N. Zhang, Q. Zhao, X. Han, J. Yang, J. Chen: Nanoscale 6 (2014) 2827. DOI:10.1039/C3NR05523J
[36] A.M. Wilson, J.N. Reimers, E.W. Fuller, J.R. Dahn: Solid State Ionics 74 (1994) 249. DOI:10.1016/0167-2738(94)90217-8
[37] A.M. Wilson, W. Xing, G. Zank, B. Yates, J.R. Dahn: Solid State Ionics 100 (1997) 259. DOI:10.1016/S0167-2738(97)00409-8
[38] A.M. Wilson, G. Zank, K. Eguchi, W. Xing, J.R. Dahn: J. Power Sources 68 (1997) 195. DOI:10.1016/S0378-7753(96)02551-7
[39] A.M. Wilson, G. Zank, K. Eguchi, W. Xing, B. Yates, J.R. Dahn: Chem. Mater. 9 (1997) 1601. DOI:10.1021/cm970002r
[40] W. Xing, A.M. Wilson, K. Eguchi, G. Zank, J.R. Dahn: J. Electrochem. Soc. 144 (1997) 2410. DOI:10.1149/1.1837828
[41] W. Xing, A.M. Wilson, G. Zank, J.R. Dahn: Solid State Ionics 93 (1997) 239. DOI:10.1016/S0167-2738(96)00512-7
[42] P. Colombo, R. Riedel, G.D. Sorarù, H.J. Kleebe, Polymer Derived Ceramics, From Nano-Structure to Applications, DEStech Publications, Inc., Lancaster, PA, USA (2010).
[43] P. Colombo, G. Mera, R. Riedel, G.D. Soraru: J. Am. Ceram. Soc. 93 (2010) 1805. DOI:10.1111/j.1551-2916.2010.03876.x
[44] C.G. Pantano, A.K. Singh, H. Zhang: J. Sol-Gel Sci. Technol. 14 (1999) 7. DOI:10.1023/A:1008765829012
[45] H. Zhang, C.G. Pantano: J. Am. Ceram. Soc. 73 (1990) 958. DOI:10.1111/j.1151-2916.1990.tb05091.x
[46] G.D. Soraru, S. Modena, E. Guadagnino, P. Colombo, J. Egan, C. Pantano: J. Am. Ceram. Soc. 85 (2002) 1529. DOI:10.1111/j.1151-2916.2002.tb00308.x
[47] H. Fukui, O. Hisashi, T. Hino, K. Kanamura: ACS Appl. Mater. Interfaces 4 (2010) 998. PMid:20423119; DOI:10.1021/am100030f
[48] H. Fukui, H. Ohsuka, T. Hino, K. Kanamura: J. Power Sources 196 (2011) 371. DOI:10.1016/j.jpowsour.2010.06.077
[49] H. Fukui, H. Ohsuka, T. Hino, K. Kanamura: J. Electrochem. Soc. 158 (2011) A550. DOI:10.1149/1.3567956
[50] H. Fukui, K. Eguchi, H. Ohsuka, T. Hino, K. Kanamura: J. Power Sources 243 (2013) 152. DOI:10.1016/j.jpowsour.2013.05.124

[51] P. Dibandjo, M. Graczyk-Zajac, R. Riedel, V.S. Pradeep, G.D. Soraru: J. Eur. Ceram. Soc. 32 (2012) 2495. DOI:10.1016/j.jeurceramsoc.2012.03.010

[52] V.S. Pradeep, M. Graczyk-Zajac, M. Wilamowska, R. Riedel, G.D. Soraru: Solid State Ionics 262 (2014) 22. DOI:10.1016/j.ssi.2013.08.043

[53] V.S. Pradeep, M. Graczyk-Zajac, R. Riedel, G.D. Soraru: Electrochim. Acta 119 (2014) 78. DOI:10.1016/j.electacta.2013.12.037

[54] M. Graczyk-Zajac, L. Toma, C. Fasel, R. Riedel: Solid State Ionics 225 (2012) 522. DOI:10.1016/j.ssi.2011.12.007

[55] J. Kaspar, M. Graczyk-Zajac, R. Riedel: Solid State Ionics 225 (2012) 527. DOI:10.1016/j.ssi.2012.01.026

[56] J. Kaspar, M. Graczyk-Zajac, R. Riedel: J. Power Sources 244 (2013) 450. DOI:10.1016/j.jpowsour.2012.11.086

[57] M. Wilamowska, V.S. Pradeep, M. Graczyk-Zajac, R. Riedel, G.D. Soraru: Solid State Ionics 260 (2014) 94. DOI:10.1016/j.ssi.2014.03.021

[58] M. Graczyk-Zajac, L.M. Reinold, J. Kaspar, P.V.W. Sasikumar, G.-D. Soraru, R. Riedel: Nanomaterials 5 (2015) 233. PMid:28347008; DOI:10.3390/nano5010233

[59] V.S. Pradeep, D.G. Ayana, M. Graczyk-Zajac, G.D. Soraru, R. Riedel: Electrochim. Acta 157 (2015) 41. DOI:10.1016/j.electacta.2015.01.088

[60] J. Kaspar, M. Graczyk-Zajac, S. Choudhury, R. Riedel: Electrochim. Acta 216 (2016) 196. DOI:10.1016/j.electacta.2016.08.121

[61] M. Wilamowska-Zawlocka, P. Puczkarski, Z. Grabowska, J. Kaspar, M. Graczyk-Zajac, R. Riedel, G.D. Soraru: RSC Advances (2016). DOI:10.1039/C6RA24539 K

[62] Y.D. Blum, D.B. MacQueen, H.-J. Kleebe: J. Eur. Ceram. Soc. 25 (2005) 143. DOI:10.1016/j.jeurceramsoc.2004.07.019

[63] G. Gregori, H.-J. Kleebe, Y.D. Blum, F. Babonneau: Int. J. Mater. Res. 97 (2006) 710.

[64] S.J. Widgeon, S. Sen, G. Mera, E. Ionescu, R. Riedel, A. Navrotsky: Chem. Mater. 22 (2010) 6221. DOI:10.1021/cm1021432

[65] S. Martínez-Crespiera, E. Ionescu, H.-J. Kleebe, R. Riedel: J. Eur. Ceram. Soc. 31 (2011) 913. DOI:10.1016/j.jeurceramsoc.2010.11.019

[66] G. Mera, A. Navrotsky, S. Sen, H.-J. Kleebe, R. Riedel: J. Mater. Chem. A 1 (2013) 3826. DOI:10.1039/C2TA00727D

[67] J. Cordelair, P. Greil: J. Eur. Ceram. Soc. 20 (2000) 1947. DOI:10.1016/S0955-2219(00)00068-6

[68] H.-J. Kleebe, Y.D. Blum: J. Eur. Ceram. Soc. 28 (2008) 1037. DOI:10.1016/j.jeurceramsoc.2007.09.024

[69] M. Haaks, J. Kaspar, A. Franz, M. Graczyk-Zajac, R. Riedel, M. Vogel: Solid State Ionics 287 (2016) 28. DOI:10.1016/j.ssi.2016.01.041

[70] J. Kaspar, M. Graczyk-Zajac, R. Riedel: Electrochim. Acta 115 (2014) 665. DOI:10.1016/j.electacta.2013.10.184

[71] J.R. Dahn, A.M. Wilson, W. Xing, G.A. Zank: US Patent Nr. 5631106 (1997).

[72] R. Kolb, C. Fasel, V. Liebau-Kunzmann, R. Riedel: J. Eur. Ceram. Soc. 26 (2006) 3903. DOI:10.1016/j.jeurceramsoc.2006.01.009

[73] M. Graczyk-Zajac, G. Mera, J. Kaspar, R. Riedel: J. Eur. Ceram. Soc. 30 (2010) 3235. DOI:10.1016/j.jeurceramsoc.2010.07.010

[74] J. Kaspar, G. Mera, A.P. Nowak, M. Graczyk-Zajac, R. Riedel: Electrochim. Acta 56 (2010) 174. DOI:10.1016/j.electacta.2010.08.103

[75] L.M. Reinold, M. Graczyk-Zajac, Y. Gao, G. Mera, R. Riedel: J. Power Sources 236 (2013) 224. DOI:10.1016/j.jpowsour.2013.02.046

[76] M. Graczyk-Zajac, M. Wimmer, C. Neumann, R. Riedel: J. Solid State Electrochem. 19 (2015) 2763. DOI:10.1007/s10008-015-2814-y

[77] M. Wilamowska, M. Graczyk-Zajac, R. Riedel: J. Power Sources 24 (2013) 80. DOI:10.1016/j.jpowsour.2013.03.137

[78] M. Graczyk-Zajac, C. Fasel, R. Riedel: J. Power Sources 196 (2011) 6412. DOI:10.1016/j.jpowsour.2011.03.076

[79] S.-H. Baek, L.M. Reinold, M. Graczyk-Zajac, R. Riedel, F. Hammerath, B. Buchner, H.-J. Grafe: J. Power Sources 253 (2014) 342. DOI:10.1016/j.jpowsour.2013.12.065

[80] M. Graczyk-Zajac, M. Wimmer, Y. Xu, G. Buntkowsky, C. Neumann, R. Riedel: J. Solid State Electrochem. 21 (2017) 47. DOI:10.1007/s10008-016-3337-x

[81] A. Scarmi, G.D. Soraru, R. Raj: J. Non-Cryst. Solids 351 (2005) 2238. DOI:10.1016/j.jnoncrysol.2005.06.008

[82] P. Kroll: J. Mater. Chem. 13 (2003) 1657. DOI:10.1039/B301389H

[83] P. Kroll, in: R. Riedel, I.-W. Chen (Eds.), Ceramics Science and Technology, Wiley-VCH & Weinheim, Germany (2008) 39.

[84] P. Kroll: J Mater. Chem. 20 (2010) 10528. DOI:10.1039/C0JM01583K

[85] H. Ding, M.J. Demkowicz: Sci. Rep. 5 (2015) 13051. DOI:10.1038/srep13051

[86] N. Liao, B. Zheng, H. Zhou, W. Xue: Electrochim. Acta 156 (2015) 115. DOI:10.1016/j.electacta.2015.01.053

[87] T. Varga, A. Navrotsky, J.L. Moats, R.M. Morcos, F. Poli, K. Müller, A. Saha, R. Raj: J. Am. Ceram. Soc. 90 (2007) 3213. DOI:10.1111/j.1551 – 2916.2007.01874.x

[88] R.M. Morcos, A. Navrotsky, T. Varga, Y. Blum, D. Ahn, F. Poli, K. Müller, R. Raj: J. Am. Ceram. Soc. 91 (2008) 2969. DOI:10.1111/j.1551-2916.2008.02543.x

[89] P.E. Blöchl: Phys. Rev. B 50 (1994) 17953. DOI:10.1103/PhysRevB.50.17953

[90] G. Kresse, J. Furthmüller: Phys. Rev. B 54 (1996) 11169. DOI:10.1103/PhysRevB.54.11169

[91] J.P. Perdew, K. Burke, M. Ernzerhof: Phys. Rev. Let 77 (1996) 3865. PMid:10062328; DOI:10.1103/PhysRevLett.77.3865

[92] H.J. Monkhorst, J.D. Pack: Phys. Rev. B 13 (1976) 5188. DOI:10.1103/PhysRevB.13.5188

[93] M. Dion, H. Rydberg, E. Schröder, D.C. Langreth, B.I. Lundqvist: Phys. Rev. Lett. 92 (2004) 246401. PMid:15245113; DOI:10.1103/PhysRevLett.92.246401

[94] A. Saha, R. Raj, D.L. Williamson: J. Am. Ceram. Soc. 89 (2006) 2188. DOI:10.1111/j.1551-2916.2006.00920.x

[95] J. Enkovaara, C. Rostgaard, J.J. Mortensen, J. Chen, M. Dulak, L. Ferrighi, J. Gavnholt, C. Glinsvad, V. Haikola, H.A. Hansen, H.H. Kristoffersen, M. Kuisma, A.H. Larsen, L. Lehtovaara, M. Ljungberg, O. Lopez-Acevedo, P.G. Moses, J. Ojanen, T. Olsen, V. Petzold, N.A. Romero, J. Stausholm-Moller, M. Strange, G.A. Tritsaris, M. Vanin, M. Walter, B. Hammer, H. Hakkinen, G.K. Madsen, R.M. Nieminen, J.K. Norskov, M. Puska, T.T. Rantala, J. Schiotz, K.S. Thygesen, K.W. Jacobsen: J. Phys. Condens. Matter 22 (2010) 253202. PMid:21393795; DOI:10.1088/0953-8984/22/25/253202

[96] J.P. Perdew, Y. Wang: Phys. Rev. B 45 (1992) 13244. DOI:10.1103/PhysRevB.45.13244

[97] A. Navrotsky: Phys. Chem. Miner. 24 (1997) 222. DOI:10.1007/s002690050035

[98] A. Navrotsky: Phys. Chem. Miner. 2 (1977) 89. DOI:10.1007/bf00307526

[99] J. Kaspar, M. Graczyk-Zajac, S. Lauterbach, H.-J. Kleebe, R. Riedel: J. Power Sources 269 (2014) 164. DOI:10.1016/j.jpowsour.2014.06.089

[100] K. Wissel, D. Vrankovic, G. Trykowski, M. Graczyk-Zajac: Solid State Ionics 302 (2017) 180. DOI:10.1016/j.ssi.2016.12.008

[101] H. Kim, C.-Y. Chou, J.G. Ekerdt, G.S. Hwang: J. Phys. Chem. C 115 (2011) 2514. DOI:10.1021/jp1083899

[102] V.B. Shenoy, P. Johari, Y. Qi: J. Power Sources 195 (2010) 6825. DOI:10.1016/j.jpowsour.2010.04.044

[103] V.L. Chevrier, J.R. Dahn: J. Electrochem. Soc. 156 (2009) A454. DOI:10.1149/1.3111037

[104] J. Rohrer, K. Albe: J. Phys. Chem. C 117 (2013) 18796. DOI:10.1021/jp401379d

[105] T.D. Hatchard, J.R. Dahn: J. Electrochem. Soc. 151 (2004) A838. DOI:10.1149/1.1739217

[106] Y. Oumellal, N. Delpuech, D. Mazouzi, N. Dupre, J. Gaubicher, P. Moreau, P. Soudan, B. Lestriez, D. Guyomard: J. Mater. Chem. 21 (2011) 6201. DOI:10.1039/C1JM10213C

[107] X.H. Liu, H. Zheng, L. Zhong, S. Huang, K. Karki, L.Q. Zhang, Y. Liu, A. Kushima, W.T. Liang, J.W. Wang, J.-H. Cho, E. Epstein, S.A. Dayeh, S.T. Picraux, T. Zhu, J. Li, J.P. Sullivan,

J. Cumings, C. Wang, S.X. Mao, Z.Z. Ye, S. Zhang, J.Y. Huang: Nano Lett. 11 (2011) 3312. DOI:10.1021/nl201684d
[108] H. Yang, S. Huang, X. Huang, F. Fan, W. Liang, X.H. Liu, L.-Q. Chen, J.Y. Huang, J. Li, T. Zhu, S. Zhang: Nano Lett. 12 (2012) 1953. DOI:10.1021/nl204437t
[109] J. Rohrer, A. Moradabadi, K. Albe, P. Kaghazchi: J. Power Sources 293 (2015) 221. DOI:10.1016/j.jpowsour.2015.05.057
[110] I.A. Courtney, J.S. Tse, O. Mao, J. Hafner, J.R. Dahn: Phys. Rev. B 58 (1998) 15583. DOI:10.1103/PhysRevB.58.15583
[111] N.G. Hörmann, A. Gross, J. Rohrer, P. Kaghazchi: Appl. Phys. Lett. 107 (2015) 123101. DOI:10.1063/1.4931353
[112] L.M. Reinold, M. Graczyk-Zajac, C. Fasel, R. Riedel: ECS Trans. 35 (2011) 37. DOI:10.1149/1.3654200
[113] D. Vrankovic, L.M. Reinold, R. Riedel, M. Graczyk-Zajac: J. Mater. Sci. 51 (2016) 6051. DOI:10.1007/s10853-016-9911-x
[114] D. Vrankovic, K. Wissel, M. Graczyk-Zajac, R. Riedel: Solid State Ionics 302 (2017) 66. DOI:10.1016/j.ssi.2016.11.009
[115] J. Kaspar, C. Terzioglu, E. Ionescu, M. Graczyk-Zajac, S. Hapis, H.-J. Kleebe, R. Riedel: Adv. Funct. Mater. 24 (2014) 4097. DOI:10.1002/adfm.201303828
[116] C. Moysan, R. Riedel, R. Harshe, T. Rouxel, F. Augereau: J. Eur. Ceram. Soc. 27 (2007) 397. DOI:10.1016/j.jeurceramsoc.2006.01.016

(Received November 18, 2016; accepted April 24, 2017; online since July 17, 2017)

Correspondence address

Dr.-Ing. Magdalena Graczyk-Zajac
Technische Universität Darmstadt
Jovanka-Bontschits-Straße 2
D-64287 Darmstadt
Germany
Tel.: +49 6151 16-21621
Fax: +49 6151 16-21623
E-mail: graczyk@materials.tu-darmstadt.de

Bibliography
DOI 10.3139/146.111517
Int. J. Mater. Res. (formerly Z. Metallkd.)
108 (2017) 11; page 920 – 932

ISSN 1862-5282

ACSNANO
Cite This: ACS Nano 2017, 11, 11409-11416
www.acsnano.org

Highly Porous Silicon Embedded in a Ceramic Matrix: A Stable High-Capacity Electrode for Li-Ion Batteries

Dragoljub Vrankovic,[†] Magdalena Graczyk-Zajac,[*,†] Constanze Kalcher,[‡] Jochen Rohrer,[*,‡] Malin Becker,[†] Christina Stabler,[†] Grzegorz Trykowski,[§] Karsten Albe,[‡] and Ralf Riedel[†]

[†]Disperse Feststoffe and [‡]Materialmodellierung, Technische Universität Darmstadt, 64289 Darmstadt, Germany
[§]Faculty of Chemistry, Nicolaus Copernicus University in Torun, 87-100 Torun, Poland

Supporting Information

ABSTRACT: We demonstrate a cost-effective synthesis route that provides Si-based anode materials with capacities between 2000 and 3000 mAh·g_{Si}^{-1} (400 and 600 mAh·$g_{composite}^{-1}$), Coulombic efficiencies above 99.5%, and almost 100% capacity retention over more than 100 cycles. The Si-based composite is prepared from highly porous silicon (obtained by reduction of silica) by encapsulation in an organic carbon and polymer-derived silicon oxycarbide (C/SiOC) matrix. Molecular dynamics simulations show that the highly porous silicon morphology delivers free volume for the accommodation of strain leading to no macroscopic changes during initial Li–Si alloying. In addition, a carbon layer provides an electrical contact, whereas the SiOC matrix significantly diminishes the interface between the electrolyte and the electrode material and thus suppresses the formation of a solid–electrolyte interphase on Si. Electrochemical tests of the micrometer-sized, glass-fiber-derived silicon demonstrate the up-scaling potential of the presented approach.

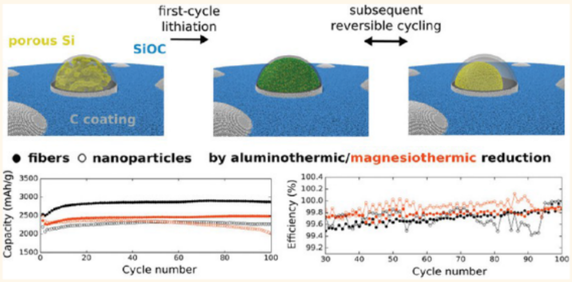

KEYWORDS: *Li-ion battery, porous silicon, molecular dynamics simulations, silicon oxycarbide, nanocomposite anode material*

Silicon and silicon oxide (SiO_x)-based systems have long been considered as desirable anode materials for the next generation of Li-ion batteries, which is attributed to the abundance of Si, the low working potential (<0.5 V *versus* Li/Li^+) and the high mass-specific capacity (3579 mAh·g^{-1} for $Li_{15}Si_4$).[1−4] Nevertheless, cycling instabilities and capacity fading still plague the development toward commercially utilizable Si-based electrodes. The key challenge is the large volume change (>280%) during alloying/dealloying with lithium that can lead to disintegration of the electrode particle itself and to rupture and repetitive growth and thickening of a solid–electrolyte interphase (SEI). In consequence, this leads to low Coulombic efficiencies (CE) and capacity fading.[5]

Numerous advanced nanomaterial design strategies have been developed in the past to mitigate volume expansion and to stabilize SEI on the silicon electrodes. A few examples include (but are not limited to) (i) nanosizing (keeping the size of silicon nanoparticles (NPs) below a threshold value of about 150 nm),[6] (ii) embedding of nanosilicon particles into active or inactive matrix materials,[7−15] (iii) synthesis of nanosilicon–carbon composites with free volume around the silicon particles,[1,16−21] (iv) chemical bonding of silicon NPs to a binder or conductive additive,[22−27] and (v) preparation of nanowires, nanotubes, and nanostructured particles.[28−32] These approaches indeed lead to a significant improvement of cycle life and specific capacities. However, complex preparation procedures and expensive raw materials together with a relatively low areal mass loading still limit their practical application.

In the present work, we propose a cost-effective and easy to implement preparation technique that provides Si-based anode materials with capacities between 2000 and 3000 mAh·g_{Si}^{-1}, high CE above 99.5%, and almost 100% capacity retention over 100 cycles and more. The materials consist of porous, carbon-coated Si that is embedded in a ceramic SiOC matrix (Si/C/SiOC). Key to the stable electrochemical behavior is (i) the synthesis of highly porous Si (50 to 70% of the relative porosity) by alumino- or magnesiothermic reduction of silica in molten $AlCl_3$ described by Lin *et al.*[33] to supply sufficient free volume for accommodation of lithium ions, (ii) carbon

Received: August 24, 2017
Accepted: October 23, 2017
Published: October 23, 2017

DOI: 10.1021/acsnano.7b06031
ACS Nano 2017, 11, 11409−11416

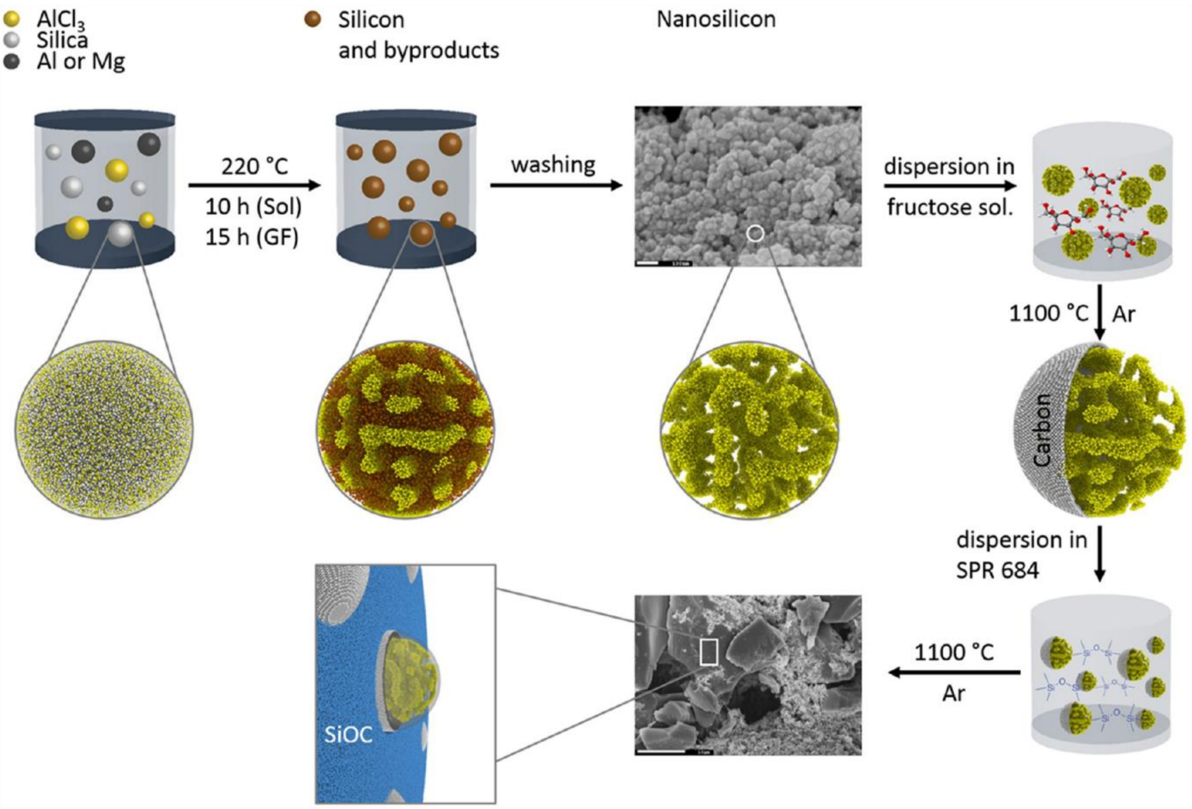

Figure 1. Schematics of composite preparation. Silica is first reduced by alumino/magnesiothermic reduction and then washed to obtain clean porous Si. The porous Si is further dispersed in a solution of fructose which forms a carbon coating after carbonization at 1100 °C. Finally, the C-coated porous Si (Si/C) is mixed with the preceramic commercial polymer SPR 684a (Starfire Systems) and pyrolyzed at 1100 °C, leading to embedding of Si/C particles in a silicon oxycarbide (SiOC) matrix.

coating[17] of porous Si to ensure good electrical contact, and (iii) encapsulation of coated Si in carbon-rich SiOC matrix[17,31,32,34–36] to minimize SEI formation at Si surfaces.

In the following we give a brief description of the preparation route of Si/C/SiOC, including structural and microstructural analyses of intermediate and final products, thereby focusing on Si in the form of NPs. We then present the results of electrochemical testing and elucidate the highly reversible and stable performance with the aid of atomistic simulations. After this proof-of-principle, we demonstrate the upscaling potential of the preparation technique by replacing the Si NPs by micron-sized fibers that can easily be obtained from commercially available silica glass fibers (GFs) and whose electrochemical performance is only marginally below that of the NPs.

RESULTS AND DISCUSSION

Preparation and Structural/Microstructural Characterization. Figure 1 presents a schematic picture of the preparation of Si/C/SiOC composites, consisting of three steps. In the first step, highly porous silicon is synthesized by $AlCl_3$ assisted aluminothermic (Al) or magnesiothermic (Mg) reduction of silica. Subsequently, byproducts are removed by washing. As raw materials, we first use in-house synthesized silica NPs and later commercially available silica GFs. Depending on the raw material and the reduction route, the resulting Si samples are denoted as Si_{NP-Al}, Si_{NP-Mg}, Si_{GF-Al}, and Si_{GF-Mg}. Our X-ray diffraction (XRD) and Raman Spectroscopy measurements confirm that the prepared Si_{NP} samples consist of phase-pure silicon (Figure 2c,d). Rietveld refinement shows that the samples are mainly amorphous with <10% of crystallinity (Table 1). The average particle size is 50−60 nm, which can be deduced from transmission electron microscopy (TEM, Figure 2a,b). The TEM imaging also confirms the high porosity of the samples which is further quantified by N_2-adsorption measurements and subsequent analysis of total pore volume and of specific surface area on the basis of the Brunauer−Emmett−Teller formalism[10] (BET SSA, Table 1). We note that the significantly increased average value of the particle size distribution (measured by DLS, Figure S3, Supporting Information) for Si_{NP-Mg} (D_{50} value in Table 1) is due to a higher reaction temperature leading to more pronounced coalescence (see also SEM micrographs in Figure 2a,b). In the second preparation step, carbon-coated porous Si (Si_X/C) is obtained *via* dispersion of Si_X in fructose and subsequent carbonization at 1100 °C under argon. A detailed description is given in ref 31 and in the Supporting Information (SI). Raman spectroscopy confirms the presence of carbon on the silicon (Figure 2e). In the third and final preparation step, Si_X/C embedded in SiOC ($Si_X/C/SiOC$) is obtained *via* mixing of Si_X/C with the preceramic polymer SPR 684a in acetone and, after evaporation of the solvent, pyrolysis under argon at

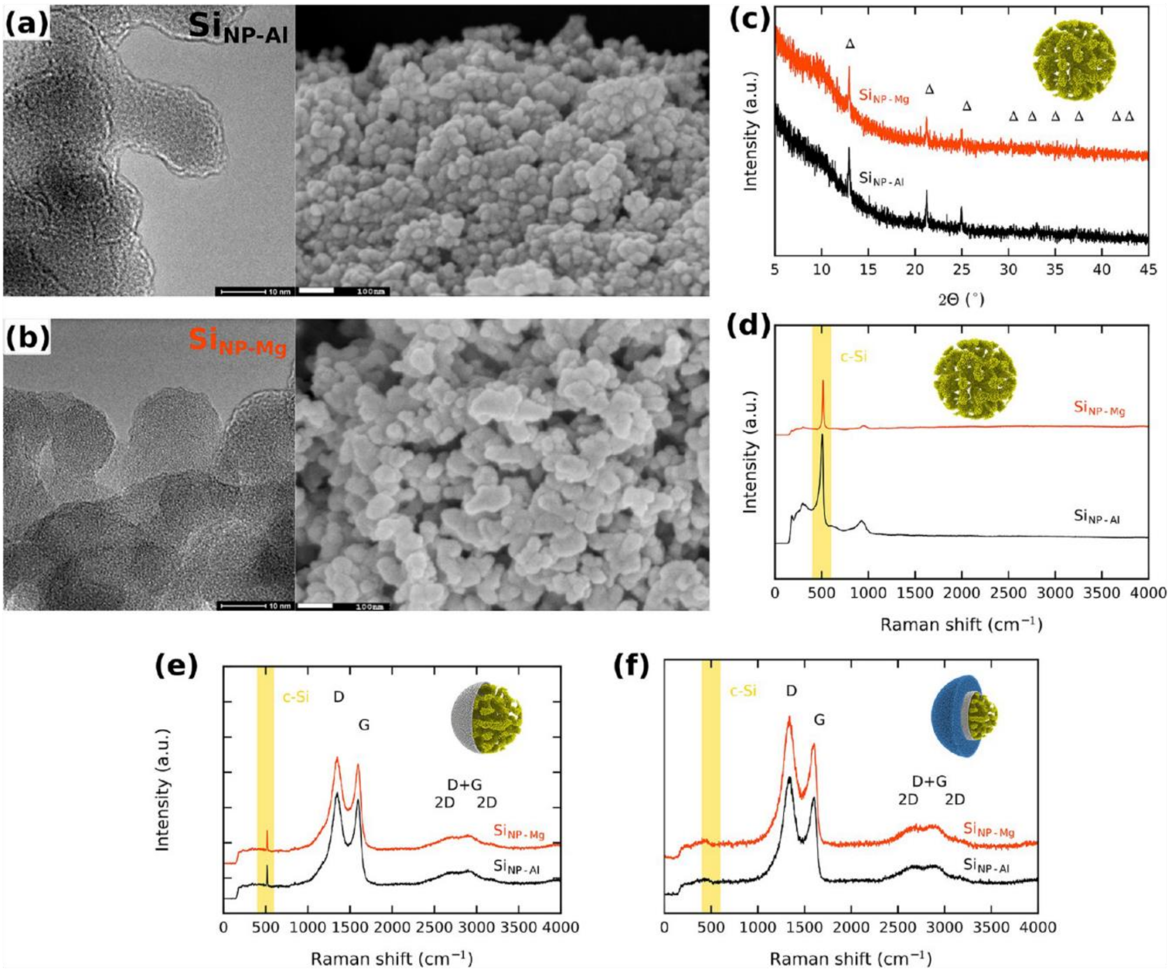

Figure 2. Microstructural characterization. (a,b) TEM and SEM micrographs of porous Si$_{NP}$ highlighting the mesoporous texture and the particle size of 50−60 nm as well as partial coalescence. (c,d) Corresponding XRD and Raman spectra showing phase purity and partial crystallization. (e,f) Raman spectra of Si$_{NP}$/C and Si$_{NP}$/C/SiOC showing partial and complete coverage of Si with C and SiOC.

Table 1. Overview of the Synthesized Silicon and Prepared Composites Including the Corresponding Properties of Used Raw Materials[a]

sample	a-Si fraction [%]	c-Si fraction [%]	crystallite size [nm]	SSA [m^{2}g^{-1}]	total pore volume [cm^{3}g^{-1}]	D$_{50}$ [nm]	Si content in composite [wt %]
Si$_{NP-Al}$/C/SiOC	91.7	8.3	41.6	150	1.37	63	18
Si$_{NP-Mg}$/C/SiOC	93.3	6.7	44.7	140	1.31	132	18

[a] Relative amounts of crystalline and amorphous silicon as well as crystallite size obtained from quantitative Rietveld refinement, specific surface area (SSA), total pore volume (V_t), D$_{50}$ value, and relative Si content in the composites.

1100 °C. Raman spectroscopy confirms full coverage of Si$_X$/C in SiOC (Figure 2f) which is important to avoid contact between Si and the electrolyte during the electrochemical reaction. For further details on the preparation method and structure analysis, we refer to the Methods and SI sections.

Electrochemical Performance. Figure 3 documents the electrochemical performance of the Si$_X$/C/SiOC composites with Si NPs (glass-fiber-derived samples are discussed later). After the first cycle, the samples achieve delithiation capacities as high as ~2900 mAh·g$_{Si}^{-1}$, high areal capacities, high capacity retention, and CE efficiencies above 99.5% during extended cycling at C/5 (Figure 3a−c, C = 372 mA·g^{-1}). The only fly in the ointment is the low CE in the first cycle which is associated with irreversible loss of Li in SiOC and disordered carbon (Figure 3c).

Rate capability tests were performed by stepwise increasing the charge/discharge rate from C/20 to 1 C and from C/10 to 5 C and back to the initial values (Figure S10). While the capacities (averaged over at least 20 cycles) are sensitive to the C rate (Figure 3d), the CE remains stable above 99%, independent of the cycling rate (Figure 3e). After the rate capability tests, both composites reach 94% (88%) of their initial capacity when returning to the initial C/10 (C/20) rate (Figure S9c). This signals that the high current tests did not

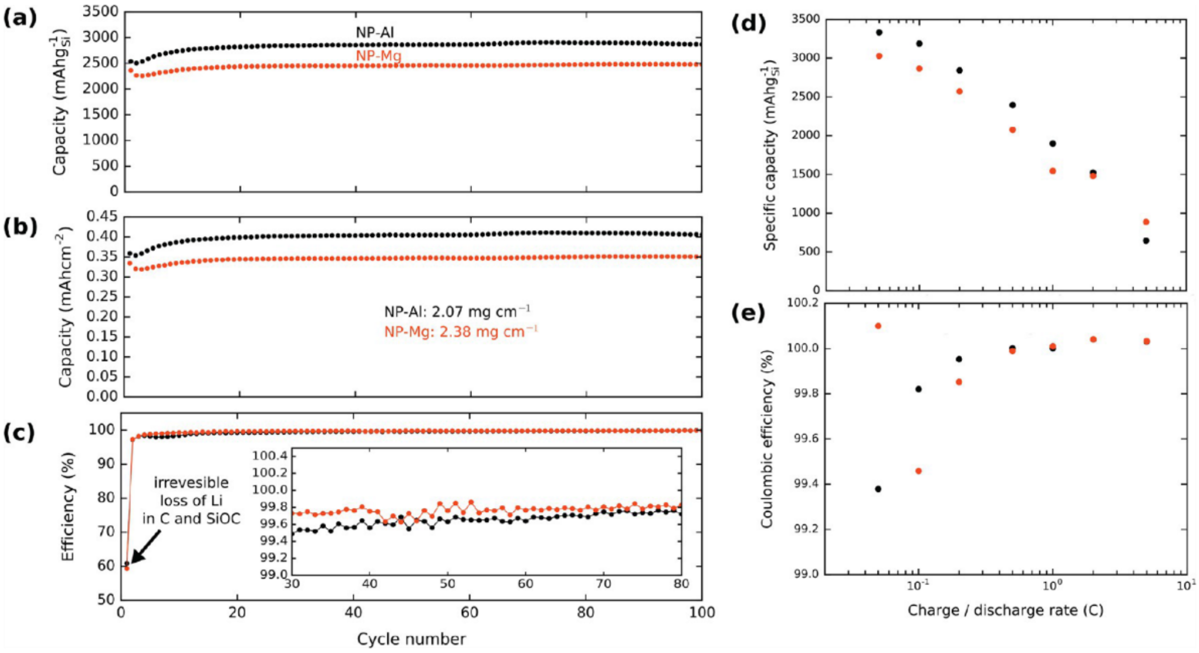

Figure 3. Electrochemical performance. (a) Delithiation capacities of Si_{NP} composites at 72 $mA \cdot g^{-1}$ current density. (b) Delithiation capacities normalized to electrode surface area with corresponding areal mass loadings. (c) Corresponding Coulombic efficiencies. Irreversible loss of Li-ions in the SiOC matrix occurs during the first cycle. Thereafter, the system stabilizes, and Coulombic efficiencies of 99.4−100% are achieved. (d) Mean values of discharge capacities obtained at different cycling rates. (e) Corresponding mean cycling efficiencies (excluding few initial cycles); the inset displays the ratio between the initial capacity and the capacity recovered after rate capability tests.

cause appreciable permanent damage neither to the material nor to the electrode. We emphasize the relatively high areal mass loading of more than 2 $mg \cdot cm^{-2}$. For practical use in a battery material, a high areal mass loading is required, although a low areal mass loading helps to achieve better performance. Finally, we note that $Si_{NP\text{-}Mg}$/C/SiOC shows slightly lower capacities. We suggest that this originates from the more pronounced coalescence of NPs leading to reduced electronic conductivity upon C coating.

Origin of the Stable Electrochemical Performance. In order to elucidate the stable cycling behavior of the Si_X/C/SiOC composites, we next performed molecular dynamics simulations of the lithiation and delithiation process of porous bulk Si. Various initial configurations corresponding to different porosities and ligaments thicknesses were investigated and show conceptually similar behavior (Figure S13 and corresponding discussion). In the following, we therefore focus on a system that contains an initial porosity of 80% and additional impurity atoms that are located inside the pores. The role of these impurity atoms is to mimic the presence of potential oxide, carbide, carbon, or SiOC overlayers at the pore surfaces. Such overlayers may form during individual preparation steps and are expected to eventually prevent a full closure of the pores. Results of our simulations are summarized in Figure 4; for clarity reasons, the impurity atoms are not shown.

Our simulations show that initial lithiation does not affect the macroscopic volume of the Si particles (Figure 4a, top panel). Only as a critical Li content is reached, a macroscopic expansion sets in. For the chosen porosity this critical Li content is $x = 1.75$, x in Li_xSi, but it generally scales with the porosity (Figure S13). At the maximum Li content, the macroscopic expansion remains well below that of dense Si. For the presented sample we have a maximum volume change of 25% (*versus* 280% for a dense sample); again, the detailed value relates to the initial porosity (Figure S13). The macroscopic integrity is a consequence of the porous internal structure. Instead of a macroscopic expansion, swelling of the ligaments occurs (Figure 4b, Movie S1) until individual pores become very small and the impurity atoms start to repel the Li and Si atoms at internal surfaces. Without impurity atoms, the pores fully close (Figure S13). The system strives for a macroscopic expansion only when the pores are (almost) closed.

We emphasize that Si undergoes a significant elastic softening during Li insertion and that at intermediate Li contents the moduli have dropped to roughly half of their initial values.[37,38] In the experiment, the embedding SiOC matrix is therefore capable to counteract the inherent expansion to a large extent. Structural characterization of virgin and cycled samples support this assumption. Neither damage nor cracking of the SiOC matrix is found by SEM imaging of the cycled $Si_{NP\text{-}Al}$/C/SiOC electrode (Figure 5a,b).

Upon delithiation, no significant reopening of the pores could be observed (Figure 4b, Movie S2), instead the system shrinks homogeneously (Figure 4a). We emphasize that this is rather unproblematic for a reversible functioning of the Si_X/C/SiOC electrode. In fact, since the SiOC matrix cannot compensate the volume decrease of Si, the free volume that initially was distributed over the pores is regained after full delithiation but will reappear as free volume between the surface of the contracted dense Si particles and the SiOC matrix (Figure 4c, right panel). This free volume can again accommodate the volume changes in subsequent lithiation cycles. Effectively, the composite therefore behaves as if the Si still were porous, yielding stable cycling behavior. Figure 4c

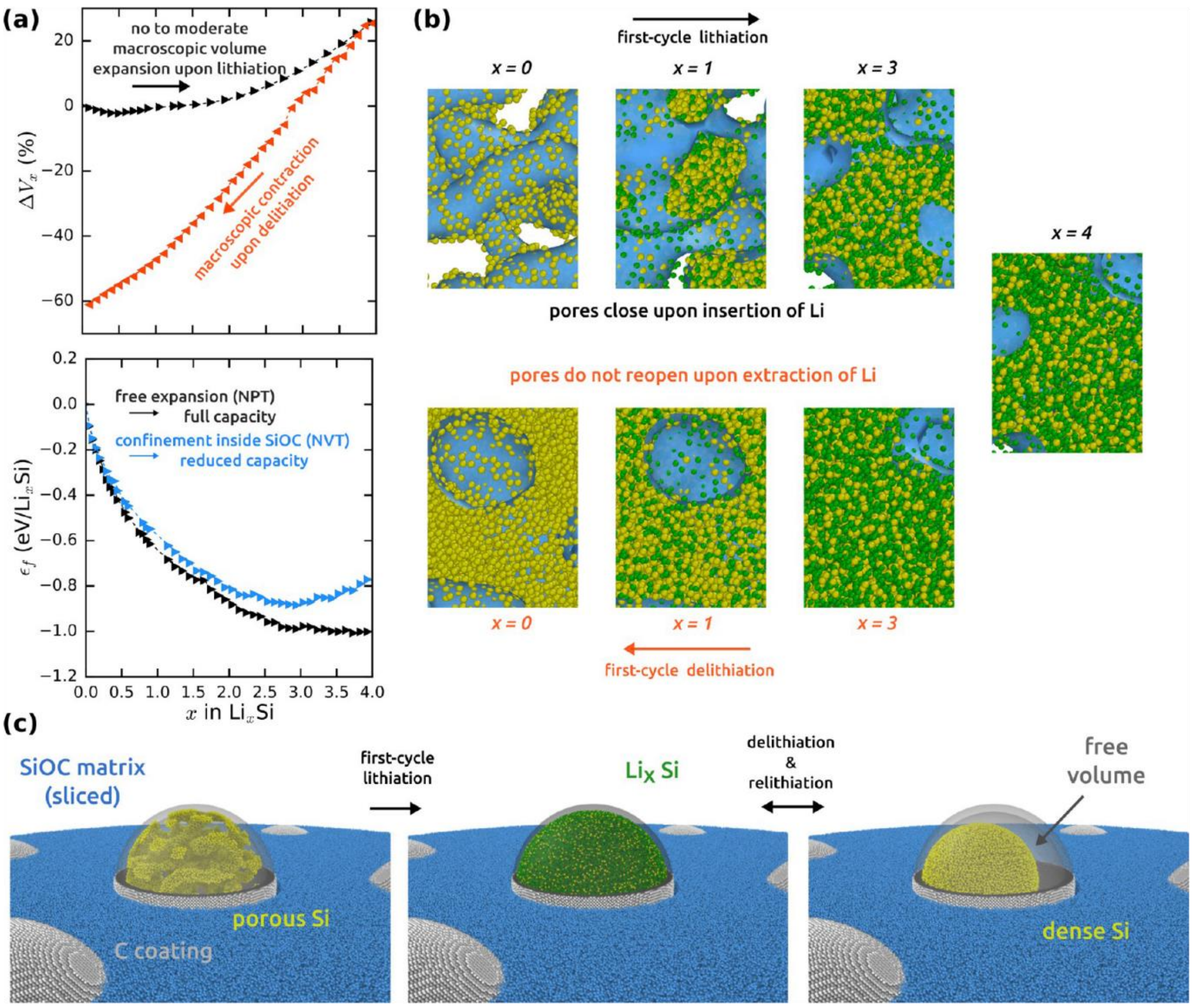

Figure 4. Atomistic modeling and suggested cycling mechanism. (a, top) Porous Si undergoes no significant macroscopic volume change upon initial Li insertion. At maximum Li content, the overall volume change is below 30% of dense (nonporous) Si. Upon extraction of Li, significant volume shrinkage occurs. (a, bottom) At fixed volume (NVT), the maximum amount of Li that can be stored in Si (associated with the minimum in the formation energy) is shifted to lower values compared to an unconstrained expansion (NPT); effectively, embedding of Si in SiOC therefore leads to a reduced mass-specific capacity. (b) Snapshots of the atomic structure highlighting the thickening of ligaments in porous Si upon Li insertion, eventually leading to closure of (most of) the pores. Upon extraction of Li, no significant reopening of pores is observed and residual pores do not grow in diameter. (c) Suggested mechanism of lithiation/delithiation of Si/C/SiOC composites. During first-cycle lithiation, porous Si is transformed into (essentially) dense Li$_x$Si with $x \sim 3$. Upon delithiation, a (essentially) dense Si particle emerges. The free volume that initially was distributed over the pores reappears as an empty shell between the dense Si and the C coating/SiOC and is available for accommodation of volume changes in subsequent cycles.

schematically summarizes the suggested mechanism that leads to the outstanding cycling properties of Si$_X$/C/SiOC electrodes.

Finally, our simulations also suggest that the experimentally observed reduction of the capacity of embedded Si (<3000 mAh·g^{-1} *versus* 3579 mAh·g^{-1} for pure Si) is a direct consequence of the constrained volume expansion due to the SiOC matrix. A comparison of the variation of the formation energy between a freely expanding (NPT) and a volume-confined system (NVT) shows that the minimum, which corresponds to the maximum possible Li uptake, is shifted to lower concentrations when no expansion is allowed, *i.e.*, assuming a completely rigid matrix (Figure 4a, bottom panel). This shows that embedding of Si generally reduces the capacity and that a higher porosity implies a higher mass-specific capacity.

Upscaling Opportunities. We now turn our focus toward large-scale fabrication of Si/C/SiOC composites. The silica precursor of Si$_{NP}$ is synthesized by applying a modified Stöber process (commonly denoted as sol−gel method).[32] It is an excellent procedure to prepare nanosized silica on the laboratory scale. However, apart from various advantages, the sol−gel route faces many limitations such as being expensive, time-consuming, requiring moisture-sensitive precursors, and shrinkage and cracking during drying.[39] Hence, this method is considered as nonapplicable for large-scale production. For

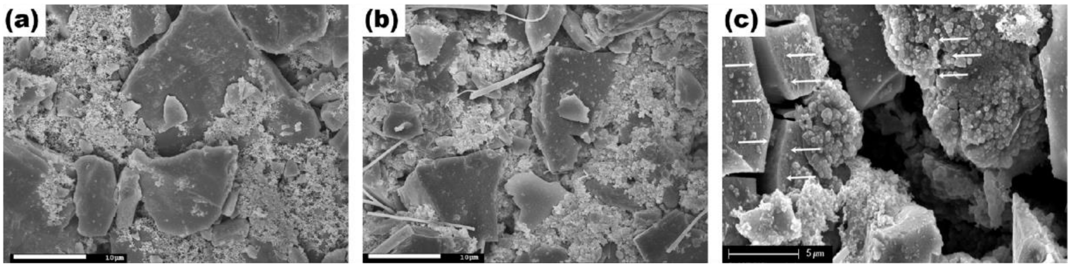

Figure 5. Morphological integrity upon cycling. SEM micrographs of $Si_{NP\text{-}Al}$/C/SiOC (a) before cycling and (b) after 270 cycles reveal neither cracks in the particles nor electrode delamination. (c) An exemplary micrograph of a cracked and partially delaminated Si/SiOC composite electrode (for comparison). The cracks in the ceramic matrix are marked with arrows. The morphological integrity of all investigated composites is presented in Figure S7.

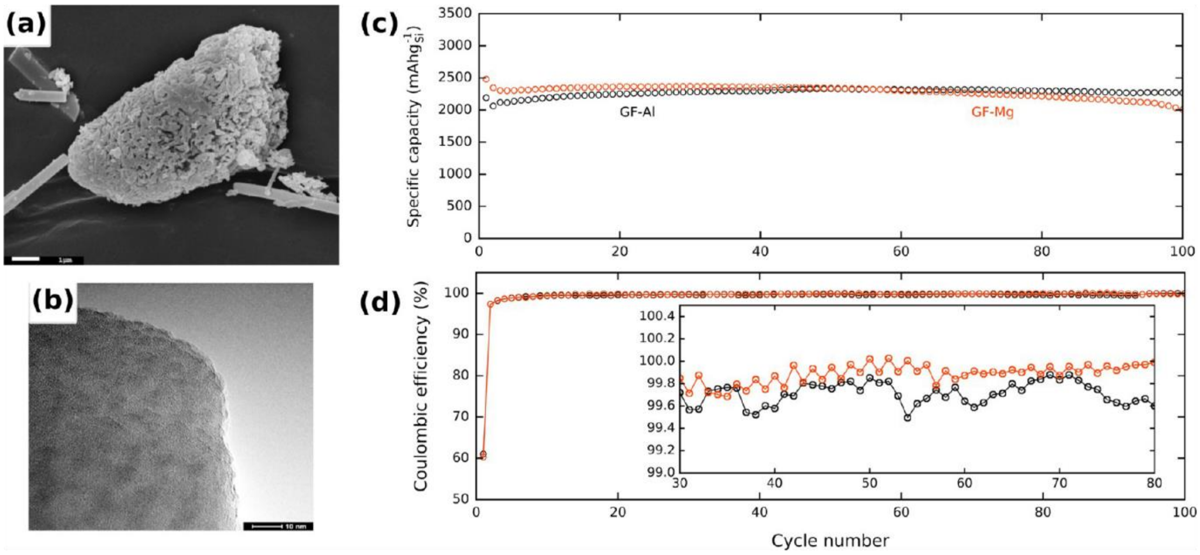

Figure 6. Microsized silicon fibers: microstructure and electrochemical performance. (a) SEM and (b) TEM micrographs demonstrate the macroporous texture of $Si_{GF\text{-}Mg}$ (lack of the mesopores). (c) Delithiation capacities of Si_{GF} composites at 72 mA·g^{-1} current density. (d) Corresponding Coulombic efficiencies. Irreversible loss of Li-ions in the SiOC matrix occurs during the first cycle. Thereafter, the system stabilizes and Coulombic efficiencies of 99.4−100% are achieved.

preparing porous silicon for use as an electrode in commercial batteries, a commercially available silicon precursor is desirable. Thus, we apply the same reduction procedure as for silica NPs to commercially available GFs.

Figure 6a,b shows our microstructural characterization of Si_{GF}. The visible pores in the silicon fiber are larger than 50 nm, no pores smaller than 20 nm are present. Thus, the porosity cannot be quantified using N_2 adsorption due to the limitations of the BET method, delivering only a semiquantitative description of the macroporosity.[40] We have confirmed full coverage with C and SiOC by Raman spectroscopy (Figure S1). Figure 6c,d documents the electrochemical performance tests of Si_{GF}/C/SiOC composites. Again the composite samples achieve high delithiation capacities, high areal capacities, and CE efficiencies above 99.5% during extended cycling at C/5. The upscaling of Si does neither influence the rate capability nor the corresponding capacity retention (Figure S9). The irreversible loss of Li in SiOC remains a challenge, though (Figure 6d).

We emphasize that, despite the slightly reduced capacities of the Si_{GF}/C/SiOC samples as compared to the Si_{NP}/C/SiOC materials, the results for the GF-derived composites are highly encouraging for commercial application. The GF systems allow for simple up-scaling from nano- to micron-sized primary Si particles. Micron-sized particles ensure easier handling during powder processing and composite preparation, cheaper raw materials, and a lower required reaction volume since the fibers present negligible specific surface area.

CONCLUSIONS

In this work, we realized Si/C/SiOC composite electrodes with high capacities of above 2000 mAh·g_{Si}^{-1}, Coulombic efficiencies of more than 99.5% and high capacity retentions of almost 100% over more than 100 cycles. The material is prepared in three steps: aluminothermic or magnesiothermic reduction of silica, followed by carbon coating, and eventual embedding in SiOC. The excellent electrochemical performance is rationalized by (i) accommodation of the volume changes during Si lithiation in the open porosity, (ii) effective ionic and electronic transport ensured by conductive carbon present in the pores, and (iii) encapsulation in the SiOC ceramic stabilizing the volume expansion and minimizing the SEI formation.

Molecular dynamics simulations confirm the accommodation of volume changes inside pores and explain the reduced capacities of Si relative to the nominal capacity of pristine, dense Si as an effect of encapsulation. We emphasize the opportunity for a large-scale production of the composite by use of commercially available silica GFs as a source for porous Si, demonstrating the potential for commercial use.

METHODS

Synthesis of Si. The schematic of the preparation procedure is shown in Figure 1 with detailed description in the SI. In short, commercial GF silica microparticles (Whatman) and sol–gel-derived NPs were used as raw materials for aluminothermic and magnesiothermic reduction reactions. The reaction was carried out in steel reactors at 220 °C for 10 h under the presence of $AlCl_3$ as the reaction medium. After washing with deionized water and etching with HCl, the resulting Si powders were further dispersed in fructose dissolved in an ethanol/water mixture. After the solvents were evaporated, carbonization was performed under a constant argon flow at 1100 °C in a tubular furnace. Finally, carbon-coated silicon was dispersed in preceramic organosilicon polymer (SPR 684a, Starfire Systems, USA) in acetone and pyrolyzed under constant argon flow at 1100 °C in a quartz glass Schlenk tube.

Characterization. The particle size distribution of nanopowders was measured by dynamic light scattering (DLS) using a Zetasizer Nano ZS (Malvern). The evolution of the porosity starting from dense silica to porous silicon was followed by means of nitrogen physisorption measurements at 77 K using an Autosorb-3B (Quantachrome Instruments, USA). SEM and TEM images of the original silica, the derived silicon, and the final composites were taken using a JEOL JSM-7600F field emission SEM (acceleration voltage 10 kV) and with a FEI Tecnai F20 X-Twin equipped with an EDX spectrometer (SDD detector, EDAX Inc.), respectively. Further characterization was carried out by using monochromatic Mo–K_α radiation X-ray diffractometry (STOE STADI P, STOE, Germany) in transmission geometry using capillaries and flat-sample configuration and by using Raman spectroscopy (514.5 nm excitation laser, Horiba HR 800, Horiba, Japan) in a Raman shift range from 0 to 4000 cm^{-1}.

Modeling. Atomistic simulations were performed using the molecular dynamics code LAMMPS.[41,42] We generally used a time step of 0.5 fs for the integration of the equations of motion and a Nose-Hoover thermostat[43,44] with a target temperature of $T = 300$ K. For constant pressure simulations, a Parinello–Rahman barostat[45,46] at ambient pressure was used. Porous bulk Si models with different porosities and ligament thicknesses were prepared following the recipe of refs 47 and 48. The system presented in the main text (which is qualitatively representative for all considered systems) has a cubic box length of ∼21 nm, contains ∼127,000 Si atoms, a porosity of 80%, and an average ligament thickness of 1.5 nm. Lithiation/delithiation was modeled by successive addition/removal of Li atoms and intermediate equilibration and optimization steps, similar to ref 49. The Li–Si interactions were modeled using the MEAM potential of Cui *et al.*[38] In order to prevent full closure of pores (which in reality could be due to oxide, carbide, carbon, or SiOC overlayers at pore surfaces forming during individual preparation steps), impurity atoms were added inside the pores of selected systems. Interactions among impurity atoms and between impurity atoms and Li/Si atoms were modeled using Lennard-Jones potentials that are only weakly attractive. Visualization and analysis of the pores were performed using the OVITO software.[50] Further details may be retrieved from the SI.

Electrochemical Measurement. To prepare working electrodes, Si-based composites were mixed with carbon black (Super P) and polyvinylidene fluoride binder (85:5:10 by weight) in *N*-methyl-2-pyrrolidone to form a slurry. This slurry was coated onto a copper foil using a doctor blade and dried at 40 °C for 24 h. Electrodes of 10 mm diameter were cut out of the coated copper foil and dried at 80 °C under vacuum in a Buchi oven for 24 h. Without further contact to air, the dried electrodes were transferred to an argon-filled glovebox for cell assembly (Swagelok-type cell) using lithium foil as the counter electrode and QMA (Whatmann, UK) as a separator. As an electrolyte, 180 μL of 1 M $LiPF_6$ dissolved in EC:DMC-1:1 (Solvionic, France) was used. All cells were cycled at charging/discharging rates from 18 $mA\cdot g^{-1}$ to about 2 $A\cdot g^{-1}$ between 0.005 and 3 V *versus* Li/Li^+. Specific capacity values were calculated based on the mass of the active material and total mass of the $Si_X/C/SiOC$ composite.

ASSOCIATED CONTENT

Ⓢ Supporting Information

The Supporting Information is available free of charge on the ACS Publications website at DOI: 10.1021/acsnano.7b06031.

Movie 1: Lithiation of porous Si. The left panel shows the detailed evolution of the atomic structure. The right panel shows internal surfaces. During the process, pores successively shrink while the overall cell volume remains almost constant. Color coding: Li (green), Si (yellow), pore surfaces light yellow. (AVI)

Movie 2: As Movie 1 but for delithiation of lithiated Si. Remnant pores do not reopen but the overall cell volume decreases. (AVI)

Detailed description of the synthesis procedures, complementary SEM and TEM images, N_2-physisorption isotherms, Raman spectra with the corresponding discussion, X-ray diffraction studies and the atomistic modeling procedure. (PDF)

AUTHOR INFORMATION

Corresponding Authors

*E-mail: graczyk@materials.tu-darmstadt.de.
*E-mail: rohrer@mm.tu-darmstadt.de.

ORCID

Magdalena Graczyk-Zajac: 0000-0002-4283-6549

Notes

The authors declare no competing financial interest.

ACKNOWLEDGMENTS

We gratefully acknowledge the financial support of the German Research Foundation (DFG) within SPP 1473/JP8, RO 4542/2-1 and IO 64/7-1.

REFERENCES

(1) Kasavajjula, U.; Wang, C.; Appleby, A. J. Nano- and Bulk Silicon-Based Insertion Anodes for Lithium-Ion Secondary Cells. *J. Power Sources* **2007**, *163*, 1003–1039.

(2) Szczech, J. R.; Jin, S. Nanostructured Silicon for High Capacity Lithium Battery Anodes. *Energy Environ. Sci.* **2011**, *4*, 56–72.

(3) Liang, B.; Liu, Y.; Xu, Y. Silicon-Based Materials as High Capacity Anodes for Next Generation Lithium Ion Batteries. *J. Power Sources* **2014**, *267*, 469–490.

(4) Sun, Y.; Liu, N.; Cui, Y. Promises and Challenges of Nanomaterials for Lithium-Based Rechargeable Batteries. *Nat. Energy* **2016**, *1*, 16071.

(5) Wachtler, M.; Besenhard, J. O.; Winter, M. Tin and Tin-Based Intermetallics as New Anode Materials for Lithium-Ion Cells. *J. Power Sources* **2001**, *94*, 189–193.

(6) Liu, X. H.; Zhong, L.; Huang, S.; Mao, S. X.; Zhu, T.; Huang, J. Y. Size-Dependent Fracture of Silicon Nanoparticles During Lithiation. *ACS Nano* **2012**, *6*, 1522–1531.

(7) Saint, J.; Morcrette, M.; Larcher, D.; Laffont, L.; Beattie, S.; Peres, J. P.; Talaga, D.; Couzi, M.; Tarascon, J. M. Towards a Fundamental Understanding of the Improved Electrochemical Performance of Silicon Carbon Composites. *Adv. Funct. Mater.* **2007**, *17*, 1765–1774.

(8) Liu, W. R.; Wang, J. H.; Wu, H. C.; Shieh, D. T.; Yang, M. H.; Wu, N. L. Electrochemical Characterizations on Si and C-Coated Si

Particle Electrodes for Lithium-Ion Batteries. *J. Electrochem. Soc.* **2005**, *152*, A1719−A1725.

(9) Kim, I. S.; Blomgren, G. E.; Kumta, P. N. Si-SiC Nanocomposite Anodes Synthesized Using High-Energy Mechanical Milling. *J. Power Sources* **2004**, *130*, 275−280.

(10) Dimov, N.; Kugino, S.; Yoshio, M. Mixed Silicon Graphite Composites as Anode Material for Lithium Ion Batteries: Influence of Preparation Conditions on the Properties of the Material. *J. Power Sources* **2004**, *136*, 108−114.

(11) Dimov, N.; Kugino, S.; Yoshio, M. Carbon-Coated Silicon as Anode Material for Lithium Ion Batteries: Advantages and Limitations. *Electrochim. Acta* **2003**, *48*, 1579−1587.

(12) Kim, I.-S.; Kumta, P. N. High Capacity Si/C Nanocomposite Anodes for Li-Ion Batteries. *J. Power Sources* **2004**, *136*, 145−149.

(13) Ren, W.; Wang, Y.; Tan, Q.; Zhong, Z.; Su, F. Novel Silicon/Carbon Nano-Branches Synthesized by Reacting Silicon with Methyl Chloride: A High Performing Anode Material in Lithium Battery. *J. Power Sources* **2016**, *332*, 88−95.

(14) Yang, Z.; Xia, Y.; Ji, J.; Qiu, B.; Zhang, K.; Liu, Z. Superior Cycling Performance of a Sandwich Structure Si/C Anode for Lithium Ion Batteries. *RSC Adv.* **2016**, *6*, 12107−12113.

(15) Choi, S.; Jung, D. S.; Choi, J. W. Scalable Fracture-Free SiOC Glass Coating for Robust Silicon Nanoparticle Anodes in Lithium Secondary Batteries. *Nano Lett.* **2014**, *14*, 7120−7125.

(16) Lin, D.; Lu, Z.; Hsu, P.-C.; Lee, H. R.; Liu, N.; Zhao, J.; Wang, H.; Liu, C.; Cui, Y. A High Tap Density Secondary Silicon Particle Anode Fabricated by Scalable Mechanical Pressing for Lithium-Ion Batteries. *Energy Environ. Sci.* **2015**, *8*, 2371−2376.

(17) Vrankovic, D.; Reinold, L. M.; Riedel, R.; Graczyk-Zajac, M. Void-Shell Silicon/Carbon/SiCN Nanostructures: Toward Stable Silicon-Based Electrodes. *J. Mater. Sci.* **2016**, *51*, 6051−6061.

(18) Wu, H.; Zheng, G.; Liu, N.; Carney, T. J.; Yang, Y.; Cui, Y. Engineering Empty Space Between Si Nanoparticles for Lithium-Ion Battery Anodes. *Nano Lett.* **2012**, *12*, 904−909.

(19) Yue, L.; Zhang, W.; Yang, J.; Zhang, L. Designing Si/Porous-C Composite with Buffering Voids as High Capacity Anode for Lithium-Ion Batteries. *Electrochim. Acta* **2014**, *125*, 206−217.

(20) Zhou, X.; Tang, J.; Yang, J.; Xie, J.; Ma, L. Silicon@Carbon Hollow Core-Shell Heterostructures Novel Anode Materials for Lithium-Ion Batteries. *Electrochim. Acta* **2013**, *87*, 663−668.

(21) Li, X.; Meduri, P.; Chen, X.; Qi, W.; Engelhard, M. H.; Xu, W.; Ding, F.; Xiao, J.; Wang, W.; Wang, C.; Zhang, J.-G.; Liu, J. Hollow Core-Shell Structured Porous Si-C Nanocomposites for Li-Ion Battery Anodes. *J. Mater. Chem.* **2012**, *22*, 11014−11017.

(22) Martin, C.; Alias, M.; Christien, F.; Crosnier, O.; Belanger, D.; Brousse, T. Graphite-Grafted Silicon Nanocomposite as a Negative Electrode for Lithium-Ion Batteries. *Adv. Mater.* **2009**, *21* (46), 4735−4741.

(23) Chen, B.; Flatt, A. K.; Jian, H.; Hudson, J. L.; Tour, J. M. Molecular Grafting to Silicon Surfaces in Air Using Organic Triazenes as Stable Diazonium Sources and HF as a Constant Hydride-Passivation Source. *Chem. Mater.* **2005**, *17*, 4832−4836.

(24) Xu, Y. H.; Yin, G. P.; Zuo, P. J. Geometric and Electronic Studies of Li15Si4 for Silicon Anode. *Electrochim. Acta* **2008**, *54*, 341−345.

(25) Martin, C.; Crosnier, O.; Retoux, R.; Belanger, D.; Schleich, D. M.; Brousse, T. Chemical Coupling of Carbon Nanotubes and Silicon Nanoparticles for Improved Negative Electrode Performance in Lithium-Ion Batteries. *Adv. Funct. Mater.* **2011**, *21*, 3524−3530.

(26) Yang, S.; Li, G.; Zhu, Q.; Pan, Q. Covalent Binding of Si Nanoparticles to Graphene Sheets and its Influence on Lithium Storage Properties of Si Negative Electrode. *J. Mater. Chem.* **2012**, *22*, 3420−3425.

(27) Chen, D.; Yi, R.; Chen, S.; Xu, T.; Gordin, M. L.; Wang, D. Facile Synthesis of Graphene-Silicon Nanocomposites with an Advanced Binder for High-Performance Lithium-Ion Battery Anodes. *Solid State Ionics* **2014**, *254*, 65−71.

(28) Chan, C. K.; Peng, H.; Liu, G.; McIlwrath, K.; Zhang, X. F.; Huggins, R. A.; Cui, Y. High-Performance Lithium Battery Anodes Using Silicon Nanowires. *Nat. Nanotechnol.* **2008**, *3*, 31−35.

(29) Chan, C. K.; Ruffo, R.; Hong, S. S.; Huggins, R. A.; Cui, Y. Structural and Electrochemical Study of the Reaction of Lithium with Silicon Nanowires. *J. Power Sources* **2009**, *189*, 34−39.

(30) Lee, S. W.; Lee, H.-W.; Ryu, I.; Nix, W. D.; Gao, H.; Cui, Y. Kinetics and Fracture Resistance of Lithiated Silicon Nanostructure Pairs Controlled by their Mechanical Interaction. *Nat. Commun.* **2015**, *6*, 7533−7533.

(31) Vrankovic, D.; Wissel, K.; Graczyk-Zajac, M.; Riedel, R. Novel 3D Si/C/SiOC Nanocomposites: Toward Electrochemically Stable Lithium Storage in Silicon. *Solid State Ionics* **2017**, *302*, 66−71.

(32) Wissel, K.; Vrankovic, D.; Trykowski, G.; Graczyk-Zajac, M. Synthesis of 3D Silicon with Tailored Nanostructure: Influence of Morphology on the Electrochemical Properties. *Solid State Ionics* **2017**, *302*, 180−185.

(33) Lin, N.; Han, Y.; Zhou, J.; Zhang, K.; Xu, T.; Zhu, Y.; Qian, Y. A Low Temperature Molten Salt Process for Aluminothermic Reduction of Silicon Oxides to Crystalline Si for Li-Ion Batteries. *Energy Environ. Sci.* **2015**, *8*, 3187−3191.

(34) Reinold, L. M.; Graczyk-Zajac, M.; Fasel, C.; Riedel, R. Prevention of Solid Electrolyte Interphase Damaging on Silicon by Using Polymer Derived SiCN Ceramics. *ECS Trans.* **2011**, *35*, 37−44.

(35) Kaspar, J.; Graczyk-Zajac, M.; Lauterbach, S.; Kleebe, H.-J.; Riedel, R. Silicon Oxycarbide/Nano-Silicon Composite Anodes for Li-Ion Batteries: Considerable Influence of Nano-Crystalline *vs* Nano-Amorphous Silicon Embedment on the Electrochemical Properties. *J. Power Sources* **2014**, *269*, 164−172.

(36) David, L.; Bhandavat, R.; Barrera, U.; Singh, G. Silicon Oxycarbide Glass-Graphene Composite Paper Electrode for Long-Cycle Lithium-Ion Batteries. *Nat. Commun.* **2016**, *7*, 10998.

(37) Shenoy, V. B.; Johari, P.; Qi, Y. Elastic Softening of Amorphous and Crystalline LiSi Phases with Increasing Li Concentration: A First-Principles Study. *J. Power Sources* **2010**, *195* (19), 6825−6830.

(38) Cui, Z.; Gao, F.; Cui, Z.; Qu, J. A Second Nearest-Neighbor Embedded Atom Method Interatomic Potential for Li−Si Alloys. *J. Power Sources* **2012**, *207*, 150−159.

(39) Wright, J. D.; Sommerdijk, N. A. *Sol−Gel Materials: Chemistry and Applications*; CRC press: Boca Raton, FL, 2000; Vol. *4*.

(40) Sing, K. The Use of Nitrogen Adsorption for the Characterisation of Porous Materials. *Colloids Surf., A* **2001**, *187−188*, 3−9.

(41) *Large-scale Atomic/Molecular Massively Parallel Simulator (LAMMPS)*; Sandia National Laboratories: Albuquerque, NM; http://lammps.sandia.gov.

(42) Plimpton, S. Fast Parallel Algorithms for Short-Range Molecular Dynamics. *J. Comput. Phys.* **1995**, *117*, 1−19.

(43) Nosé, S. A Unified Formulation of the Constant Temperature Molecular Dynamics Methods. *J. Chem. Phys.* **1984**, *81*, 511−519.

(44) Hoover, W. G. Canonical Dynamics: Equilibrium Phase-Space Distributions. *Phys. Rev. A: At., Mol., Opt. Phys.* **1985**, *31*, 1695−1697.

(45) Parrinello, M.; Rahman, A. Crystal Structure and Pair Potentials: A Molecular-Dynamics Study. *Phys. Rev. Lett.* **1980**, *45*, 1196−1199.

(46) Parrinello, M.; Rahman, A. Polymorphic Transitions in Single Crystals: A New Molecular Dynamics Method. *J. Appl. Phys.* **1981**, *52*, 7182−7190.

(47) Kalcher, C.; Brink, T.; Rohrer, J.; Stukowski, A.; Albe, K. Interface-Controlled Creep in Metallic Glass Composites. *Acta Mater.* **2017**, DOI: 10.1016/j.actamat.2017.08.058.

(48) Ngô, B.-N. D.; Stukowski, A.; Mameka, N.; Markmann, J.; Albe, K.; Weissmüller, J. Anomalous Compliance and Early Yielding of Nanoporous Gold. *Acta Mater.* **2015**, *93*, 144−155.

(49) Rohrer, J.; Albe, K. Insights into Degradation of Si Anodes from First-Principle Calculation. *J. Phys. Chem. C* **2013**, *117*, 18796−18803.

(50) Stukowski, A. Visualization and Analysis of Atomistic Simulation Data with OVITO−the Open Visualization Tool. *Modell. Simul. Mater. Sci. Eng.* **2010**, *18*, 015012.

Solid State Ionics 315 (2018) 59–64

Contents lists available at ScienceDirect

Solid State Ionics

journal homepage: www.elsevier.com/locate/ssi

The influence of pyrolysis temperature on the electrochemical behavior of porous carbon-rich SiCN polymer-derived ceramics

Mathias Storch, Dragoljub Vrankovic*, Magdalena Graczyk-Zajac, Ralf Riedel

Department of Materials and Earth Sciences, Technical University Darmstadt, Germany

ARTICLE INFO

Keywords:
Porous
Silicon carbonitride
Polymer-derived ceramic
Carbon organization
Lithium-ion battery

ABSTRACT

Within this study we report on the impact of the pyrolysis temperature on the structural and electrochemical properties of porous carbon-rich polymer-derived silicon carbonitride (SiCN) ceramics. Microstructural features of the synthesized materials were characterized in detail and discussed with respect to the lithium storage properties. X-ray diffraction study reveals the amorphous nature of the pyrolysed ceramics up to 1100 °C, while a crystalline SiC-phase is formed at 1400 °C. Micro-Raman spectroscopy shows that pyrolysed samples contain a free disordered carbon phase which tends to order with increasing pyrolysis temperature. Galvanostatic cycling with potential limitation enables to monitor the lithiation and delithiation performance. High irreversible losses are identified during the first cycle lithiation due to formation of SEI. Nevertheless the highest electrode capacities are recorded for the sample pyrolysed at 900 °C reaching a first cycle reversible capacity of 447 mAh·g^{-1} and a 100th cycle reversible capacity of 534 mAh·g^{-1} at a current of 72 mA·g^{-1}. Further it is found that the prepared materials offer improved high current lithium storage ability compared to dense SiCN ceramics reported in literature so far.

1. Introduction

The Lithium-ion battery is one of the most common energy storage devices used in consumer electronics, also successfully implemented into electric vehicles. Therefore high energy and power densities as well as long lifetime are required and need to be improved. One possible way to improve the lithium-ion battery can be the exchange of active materials. It has been already shown that polymer-derived ceramics (PDCs), in particular carbon-rich SiOC and SiCN represent an interesting group of potential negative electrode materials [1–4]. Promising results on the polysilazane derived ceramic materials pyrolysed at 1000 °C possessing high reversible capacities (520 to 540 mAh·g^{-1}) were reported by Dahn et al. in 1997 [1]. Additionally, blending the preceramic polymer with different amounts of pitch resulted in 450 mAh·g^{-1} for a high content of pitch (75%) and 560 mAh·g^{-1} for a low pitch content (25%). In 2006 Kolb et al. have observed a capacity increase when blending graphite with a commercially available polysilazane (VL20®). These investigations have revealed that the ceramic SiCN phase prevents the graphite from exfoliating and thus stabilizes electrode material during cycling. The measured capacity was 474 mAh·g^{-1} without any fading up to 50th cycle [5].

In the following years several SiCN ceramics and SiCN composites have been investigated regarding to their lithium storage ability. Studies of Graczyk-Zajac et al. revealed good rate capability for SiCN/graphite composites derived from commercially available polysilazane HTT1800. It was shown that the ceramic matrix enhances the electrode performance at high current rates [6]. Chen et al. and Wilamowska et al. started to focus on producing SiCN composites containing highly disordered carbon derived from divinyl benzene and starch. Introduction of disordered carbon into the composites leads to further increase of reversible capacities to 484 mAh·g^{-1} and 570 mAh·g^{-1}, respectively [7,8]. Furthermore, significant improvements in electrochemical performances of functionalized PDCs have been reported in literature [9–15] emphasizing benefits of Si-based ceramics. Reinold et al. published results on carbon-rich SiCN ceramics derived from in-house synthesized preceramic polymers reaching reversible capacities of ~640 mAh·g^{-1} and outstanding cycling stability [4]. The dependence of electrochemical performance on the pyrolysis temperature of non-porous SiCN ceramics has also been addressed [16].

Within this work, we focus on the influence of the pyrolysis temperature on the lithium storage properties of highly porous carbon-rich SiCN ceramics synthesized at 900 °C, 1100 °C and 1400 °C. The differences in the electrochemical performance of the studied ceramics are rationalized by the increasing organization of the free carbon phase within the SiCN matrix. Hence, the ceramic powders are characterized by means of N_2-adsorption, X-ray diffraction, Scanning Electron

---

* Corresponding author.
E-mail address: vrankovic@materials.tu-darmstadt.de (D. Vrankovic).

https://doi.org/10.1016/j.ssi.2017.11.032
Received 15 September 2017; Received in revised form 22 November 2017; Accepted 29 November 2017

Microscopy (SEM) and by Raman spectroscopy. Electrochemical studies reveal the excellent electrochemical performance of 900 °C samples with stable delithiation capacities up to ~550 mAh·g^{-1} at 72 mA·g^{-1} current density over > 100 cycles and > 200 mAh·g^{-1} at 1890 mA·g^{-1}.

2. Experimental part

The details of the synthesis of porous carbon-rich SiCN are reported elsewhere [17]. This method allows for producing mesoporous ceramics with total carbon content of ~50 wt%, whereas the carbon content does not change significantly with increase of pyrolysis temperature [18]. The samples were produced by setting the pyrolysis temperature (T_{pyr}) to 900 °C, 1100 °C and 1400 °C.

The carbon content in prepared SiCN samples was analyzed by hot-gas extraction using a Leco-200 carbon analyzer. It amounts 49–50 wt% in 900 and 1100 °C samples, respectively and increases slightly to 54 wt% for 1400 °C due to the carbothermal reduction leading to the loss of nitrogen, $Si_3N_4 + 3C \rightarrow 3SiC + 2\,N_2$. The increase of carbon content is however not significant due to the low reaction extent at 1400 °C.

X-ray powder diffraction was performed on the as prepared powders using a STOE STADI P (STOE, Germany) equipped with monochromatic Mo-K_α radiation in flat-sample transmission geometry in the 2θ range of 5° to 45°.

Micro-Raman spectra of the powder samples were recorded by using a micro-Raman spectrometer Horiba HR800 (Horiba, Japan) using an Ar-Ion laser of wavelength 514.5 nm and a Raman shift range of 0 cm^{-1} to 4000 cm^{-1}. For all samples the filters and measuring parameters were kept constant.

Nitrogen (N_2) adsorption was performed at 77 K using an Autosorb-3B (Quantachrome Instruments, USA). The samples were preheated at 150 °C for 24 h under vacuum before the measurements. The N_2 isotherm at 77 K was used to calculate the specific surface area (SSA) from the linear BET (Brunauer–Emmett–Teller) plots over the relative pressure range of $0.05 < p/p_o < 0.3$. The total pore volume (V_t) was determined from the amount of vapor adsorbed at a relative pressure $p/p_o \approx 1$ [19].

SEM pictures of pristine and cycled electrodes were taken at a JEOL JSM-7600F Field Emission electron microscope (JEOL, Japan). The cycled electrodes were disassembled from the Swagelok® cell and washed with dimethyl carbonate. The samples were coated with a thin layer of gold using a Quorum Q300T D (Quorum Technologies Ltd., United Kingdom) for 20 s at 30 mA. Imaging was performed at an acceleration voltage of 10 kV with a secondary electron detector.

For electrochemical testing, electrodes were produced by dispersing 85 wt% active material, 5 wt% Carbon Black Super P® (Timcal Ltd., Switzerland) as conduction additive and 10 wt% polyvinylidenflouride (PVDF, SOLEF Solvay, Germany) as binder, in N-Methyl-2-pyrrolidone (NMP, BASF, Germany). The slurry was printed on a copper foil (10 µm, Copper SE-Cu58 (C103), Schlenk Metallfolien, Germany) with a coating thickness of 100 µm. After drying round electrodes 10 mm in diameter and an average loading of approximately 2.50 mg·cm^{-2} were cut out and dried in glass oven B-585 Drying (Büchi Labortechnik AG, Germany) for 24 h at 80 °C under vacuum.

Electrochemical study was done using Swagelok® type cells with lithium foil (99.9% purity, 0.75 mm thickness, Alfa Aesar, Germany) of 10 mm in diameter as counter electrode, 180 µL of 1 M $LiPF_6$ in EC:DMC-1:1 electrolyte (Solvionic, France) and QMA glass fiber filters (Whatman™, United Kingdom) as separator. Measurements were done using VMP-multipotentiostat (Biologic Science Instruments, France) and controlled constant temperature of 25 °C. Cells were cycled by galvanostatic cycling with potential limitation (GCPL) in a potential range of 0.005 V–3 V with a current of 72 mA·g^{-1} for 100 cycles and high current cycling with stepwise increasing currents (rates) of 74.4 mA·g^{-1}(C/5), 372 mA·g^{-1} (C), 744 mA·g^{-1} (2C), 1860 mA·g^{-1} (5C), 3720 mA·g^{-1} (10C).

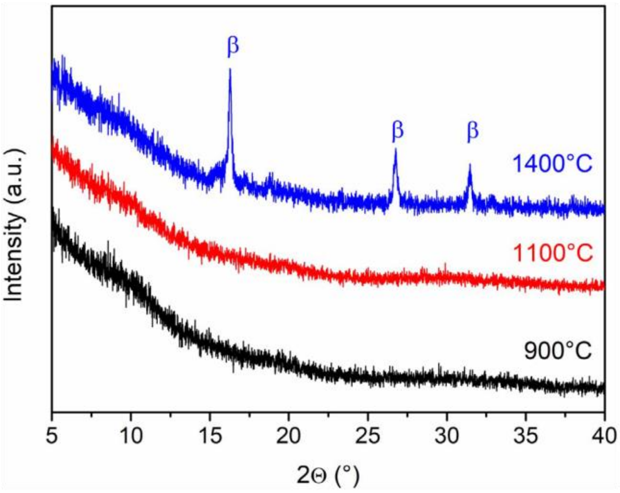

Fig. 1. X-ray diffraction pattern of 900 °C, 1100 °C and 1400 °C samples measured with Mo-K_α source.

3. Results and discussion

3.1. X-ray diffraction study

The recorded X-ray diffraction patterns depicted in Fig. 1 indicate the highly amorphous nature of the samples pyrolysed at 900 °C and 1100 °C [20]. With increasing the pyrolysis temperature to 1400 °C, three reflexes (β marker) arise at 2θ angles of 16.3°, 26.7° and 31.4°. These reflexes are attributed to a SiC-phase formed during carbothermal reduction [21]. Furthermore this onset of crystallization at 1400 °C is in good accordance with the work of Mera et al. who reported crystallization of SiC from poly(phenylvinylsilylcarbodiimide) at around 1400 °C [22].

3.2. Nitrogen adsorption

Porosity analysis via N_2-adsorption has shown that the specific surface area (SSA) and the total pore volume (V_t) decrease with increasing pyrolysis temperature from 900 °C to 1100 °C (Table 1). The steady decrease of SSA and V_t with increase of pyrolysis temperature is attributed to sintering of small mesopores. In the temperature range of 1100 °C to 1400 °C an additional pore formation is found implying the increase of SSA and V_t. This increase is related to the reaction of the free carbon phase with the *Si*-network to the formation of SiC [23].

3.3. Electrochemical characterization

Fig. 2a presents the extended cycling performance of porous SiCN ceramics pyrolysed at 900 °C, 1100 °C and 1400 °C, whereas the corresponding coulombic efficiencies are presented in Fig. 2b. The decrease of performance in the first few cycles is attributed to irreversible loss originating from the ongoing decomposition of the electrolyte known as solid electrolyte interface (SEI) and irreversible trapping of Li-ions in the porous structure. Subsequently the sample pyrolysed at 900 °C shows steady increase of capacity up to 534 mAh·g^{-1} due to

Table 1
Specific surface area and total pore volume measured via N_2-adsorption.

Sample	SSA (m^2·g^{-1})	V_t (cm^3·g^{-1})
900 °C	169	0.48
1100 °C	104	0.46
1400 °C	446	0.72

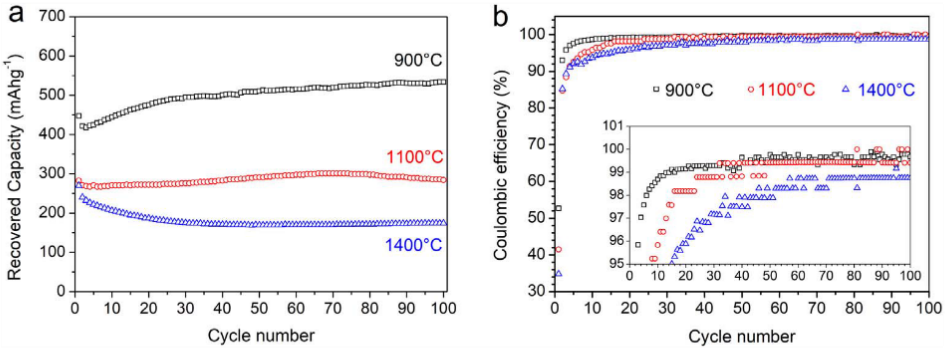

Fig. 2. a) Delithiation capacities of porous ceramics pyrolysed at 900, 1100 and 1400 °C, b) Corresponding coulombic efficiencies.

activation processes of the porous structure [24]. The 1100 °C sample shows constant discharge capacities of ~280 mAh·g^{-1} over hundred cycles while the 1400 °C sample presents continuous decrease in capacity until cycle number 40, followed by stable capacity of 168 mAh·g^{-1}.

In order to verify the stability of the porous ceramics with respect to the fast charging/discharging rates, the electrodes were tested under high currents following the procedure: 5 cycles at 74.4 mA·g^{-1}, 20 cycles at 372 mA·g^{-1}, 50 cycles at 744 mA·g^{-1}, 50 cycles at 1860 mA·g^{-1}, 50 cycles at 3720 mA·g^{-1} and 5 cycles at 372 mA·g^{-1}. The corresponding insertion/extraction voltage profiles of the 1100 °C sample are presented in Fig. 3. At all rates the majority (~75%) of lithium ions is extracted at the potential below 1.5 V. The shape of the voltage profiles below 1.5 V resembles the one of the dense SiCN ceramics. It has been attributed to the lithium storage in the disordered free carbon phase (also in the edges/voids formed by small graphitic clusters) as identified by means of electrochemical and solid state NMR techniques [25,26]. The sloping shape of the extraction curve beyond 1.5 V is characteristic for the porous material and related to the adsorption of lithium ions at the surface through an adsorption-like mechanism.

Fig. 4a shows corresponding capacity values recovered by 900 °C and 1100 °C samples with the corresponding coulombic efficiencies depicted in Fig. 4b. The delithiation capacities of the last cycles for each current step are listed in Table 2. The 900 °C ceramic recovers higher capacities than the 1100 °C sample at all current rates. In particular, at the highest current rate of 3720 mA·g^{-1} the stable recovered capacity of 135 mAh·g^{-1} is higher than ever reported in literature for any dense SiCN [3]. The significantly improved cycling stability compared to nonporous SiCN ceramics [4,27] is rationalized by the introduction of the porosity and therefore shorter Li-ion diffusion path/faster ionic transport [28,29].

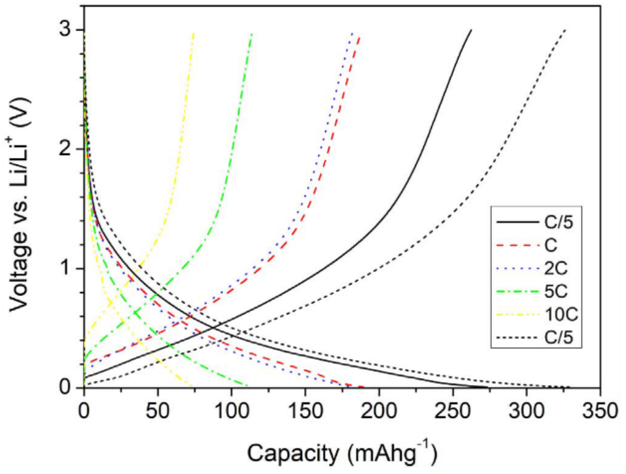

Fig. 3. Voltage profiles of lithium insertion/extraction into SiCN 1100 at various current rates (compare the data in Fig. 4a,b).

Fig. 5a,b present voltage vs. capacity curves for the 1st and 100th cycle. Coulombic efficiency η_1 (Eq. (1)) and cycling stability η_{1-100} (Eq. (2)) are introduced in order to further evaluate the electrochemical performance of the investigated materials. Table 3 summarizes the results.

$$\eta_1 = \frac{C_{\text{recovered}}\,1^{\text{st}}}{C_{\text{lit}}\,1^{\text{st}}} * 100\% \tag{1}$$

$$\eta_{1-100} = \frac{C_{\text{recovered}}\,100^{\text{th}}}{C_{\text{recovered}}\,1^{\text{st}}} * 100\% \tag{2}$$

The 1st cycle lithiation capacity of 849 mAh·g^{-1}, the recovered capacity of 447 mAh·g^{-1} and the coulombic efficiency of 52.7% found for the 900 °C SiCN sample are in the range of the values reported for dense carbon-rich SiCN ceramics [4,27]. With increasing pyrolysis temperature the efficiency η_1 decreases to 41.4% / 30.9% for the 1100 and 1400 °C samples, respectively. In particular for 1400 °C material the SEI losses are significant due to the high active surface of 446 m^2·g^{-1}. The first cycle losses are related to the SEI formation and the irreversible capture of lithium ions in the disordered carbon phase [30,31]. The decomposition of electrolyte starts at the potential ~1.5 V, resulting in a sloping plateau below 1 V (Fig. 5a). Additionally the insertion of Li-ions into carbon structures, containing high amounts of hydrogen, contributes to this plateau [32,33]. Significant hysteresis, namely the notable difference in the insertion/extraction potential is also attributed to higher hydrogen content in SiCN 900 sample [16]. The reduced amount of hydrogen in SiCN 1100 leads to lower hysteresis in voltage vs. capacity transients. In parallel, the increase of free carbon organization brings about lower specific capacity due to a higher ordering of the free carbon phase. Thus there is always a trade-off between the choice of pyrolysis temperature and its influence on the hysteresis, rate capability, charge transfer resistance and stability/capacity. At voltages below 0.5 V mainly intercalation of lithium-ions between the carbon layers in the clusters, the adsorption of lithium at the surface and the edges and the lithiation of defect sites and pores in the free carbon phase takes place [34,35]. The delithiation branch of the voltage profile can be separated into two parts. The first part up to a potential of ~1 V is based on the extraction of Li-ions from the free carbon phase. The second part in the potential range of 1 V to 3 V shows desorption of Li-ions from the surface and pores [36,37].

Considering the 100th cycle voltage profiles (Fig. 5b) the lithiation branch has the typical sloping shape of porous disordered carbons [34,37]. In case of 900 °C sample it is conspicuous that the 100th cycle delithiation capacity increases to 534 mAh·g^{-1}, resulting in η_{1-100} of 119.5% (Table 3). This feature is explained by an activation process of the porous structure with continuous cycling, similar to reported by Qie et al. for porous carbon nanofibers [24].

The amount of lithium stored reversibly over 100 cycles in the materials decreases with pyrolysis temperature, namely 534 mAh·g^{-1},

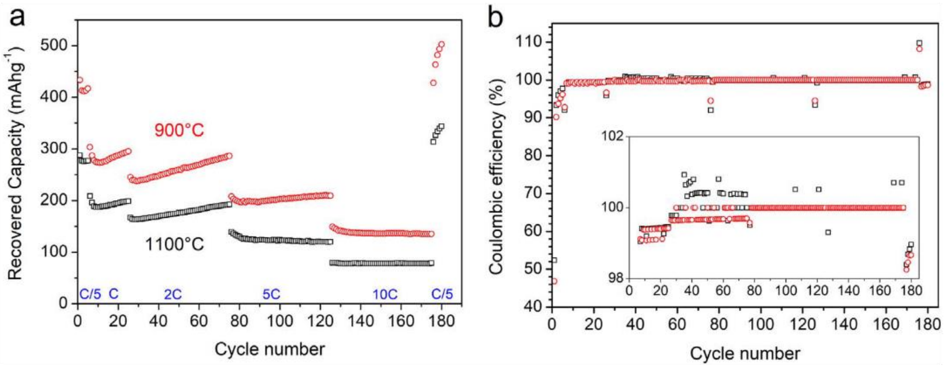

Fig. 4. a) High current cycling: 5 cycles at 74.4 mA·g^{-1}, 20 cycles at 372 mA·g^{-1}, 50 cycles at 744 mA·g^{-1}, 50 cycles at 1860 mA·g^{-1}, 50 cycles at 3720 mA·g^{-1} and 5 cycles at 372 mA·g^{-1}. b) Corresponding Coulombic efficiencies at different current densities.

Table 2
High current cycling: capacity of last cycle at each current step (in mAh·g^{-1}).

Sample	$C_{recovered}$ 74.4 mA·g^{-1}	$C_{recovered}$ 372 mA·g^{-1}	$C_{recovered}$ 744 mA·g^{-1}	$C_{recovered}$ 1860 mA·g^{-1}	$C_{recovered}$ 3720 mA·g^{-1}	$C_{recovered}$ 74.4 mA·g^{-1}
900 °C	417	295	286	209	135	503
1100 °C	277	199	192	120	79	344

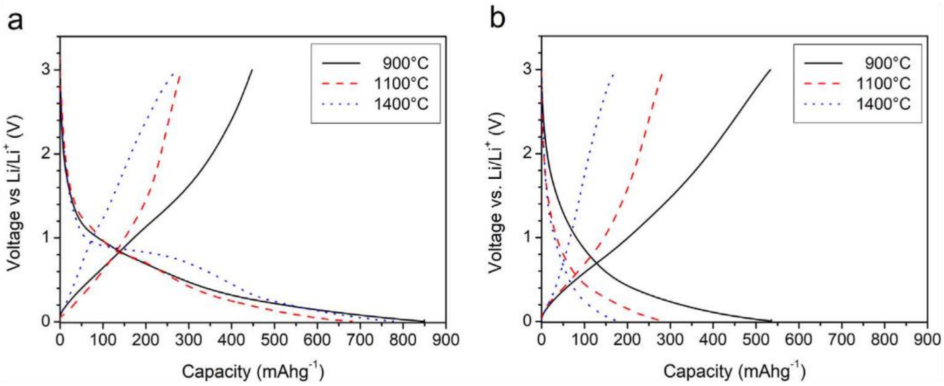

Fig. 5. Voltage profiles of lithium insertion/extraction for a) 1st cycle b) 100th cycle.

Table 3
Summary of the 1st- and 100th-cycle capacity and corresponding efficiencies.

sample	C_{lit} 1st cycle (mAh·g^{-1})	$C_{recovered}$ 1st cycle (mAh·g^{-1})	η_1 (%)	$C_{recovered}$ 100th cycle (mAh·g^{-1})	η_{1-100} (%)
900 °C	849	447	52.7	534	119.5
1100 °C	681	282	41.4	284	100.7
1400 °C	776	240	30.9	175	72.9

284 mAh·g^{-1} and 175 mAh·g^{-1} for 900 °C, 1100 °C and 1400 °C, respectively [38]. The same trend has been observed for the dense SiCN sample with almost twice higher capacities recovered by materials pyrolysed at 800 °C in comparison to 1300 °C [16]. Similarly, the porous SiOC ceramics revealing the best high-rate performance have been synthesized at 900–1000 °C [39,40]. The drastic decrease of SiCN 1400 capacity partly originates from the reduced amount of the free carbon phase. Namely, at 1400 °C the electrochemically inactive SiC-phase arises as a result of the ongoing carbothermal reduction. It leads to decrease in the free carbon content (compare Fig. 1). Due to the newly formed large amount of pores and the high specific surface area,

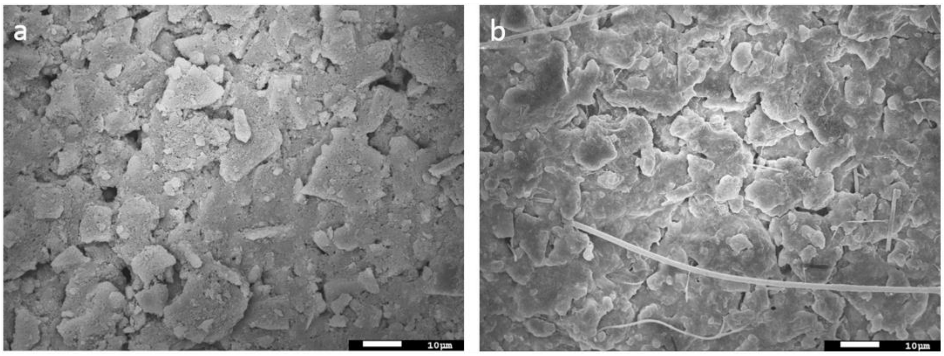

Fig. 6. SEM micrographs of the 900 °C samples pristine a) and after 100 cycles b).

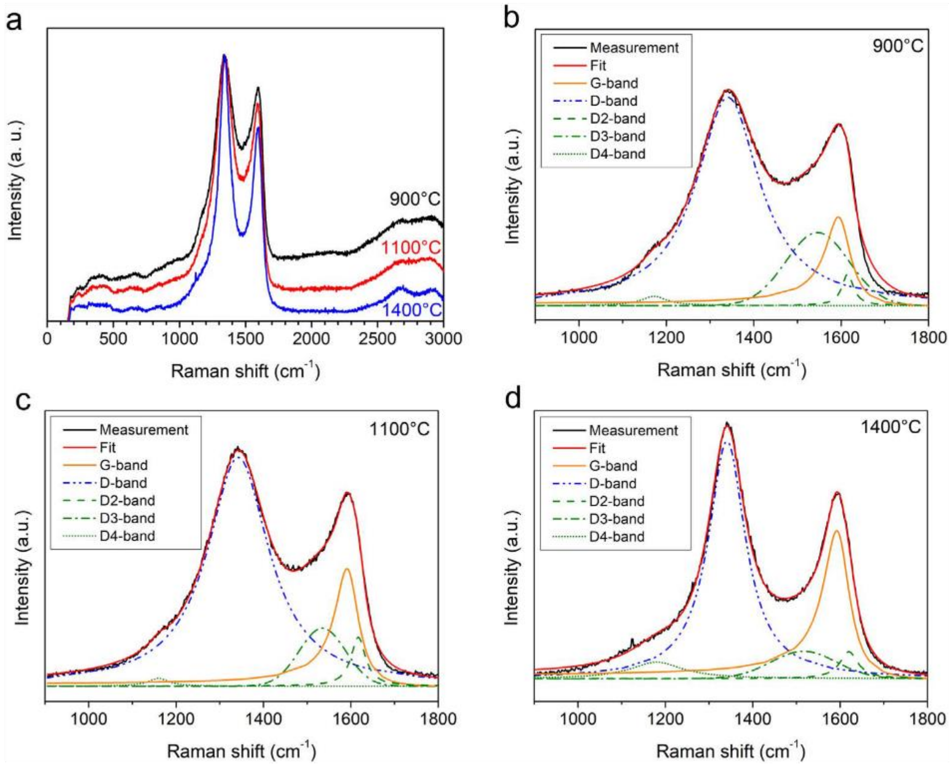

Fig. 7. Micro-Raman spectra a) comparison of increasing temperature b) excerpt of 900 °C curve fitting c) excerpt of 1100 °C curve fitting d) excerpt of 1400 °C curve fitting.

Table 4
I(D)/I(G) ratio, I(D)/I(D3) ratio and L_a of the samples pyrolysed at 900 °C, 1100 °C and 1400 °C.

Sample	900 °C	1100 °C	1400 °C
I(D)/I(G) ratio	2.35	1.95	1.60
I(D)/I(D3) ratio	2.85	3.95	8.68
L_a (nm)	1.87	2.26	2.74

a strongly pronounced plateau of SEI formation can be seen in the potential range of 1 V to 0.8 V.

SEM micrographs of the pristine and cycled 900 °C electrode are shown in Fig. 6. The pristine electrode shows the ceramic particles homogenously embedded in a conducting additive and binder. No cracks of particles or electrode delamination are found in the micrograph of the cycled electrode despite high electrode mass loading (2.55 mg·cm^{-1}). Comparing to the pristine one, the micrograph of the cycled electrode reveals only a continuous layer attributed to SEI formed during initial cycles. Note that the fibers detected on the cycled electrodes originate from the glass fiber separator used.

3.4. Raman spectroscopy measurements

Free carbon phase has been identified as a major lithium storage site within the SiCN ceramic [16,25,30,31,41]. The microstructure of carbon in the SiCN matrix was analyzed by Micro-Raman spectroscopy in order to understand the difference in the capacities recovered by the 900, 1100 and 1400 °C samples. The overall measurement data is shown in Fig. 7a. In order to deconvolute the Raman-spectra into G-band and four D-bands (D, D2, D3, D4) a fitting procedure was applied. The curve types were adopted from extensive studies of Sadezky et al. and Ferrari et al. [42,43] and set as G = BWF, D3 = Gaussian and D, D2, D4 = Lorentzian. Resulting curve fitting data is listed in Table 4 and the fitted graphs are shown in Fig. 7b–d. For all samples the D-band is the strongest band revealing the presence of a disordered graphitic lattice. The G-band is comparably less pronounced than the D-Band due to low degree of order in the carbon phase. D3-band indicating amorphous carbon is unlikely very strong pointing out the highly amorphous nature of the material (compare X-ray diffraction pattern in Fig. 1). Additionally large specific surface area related to the high fraction of pores can result in enhanced D3-band [44]. The shift of the D3-band from ~1500 cm^{-1} to 1545 cm^{-1} permits the specific classification of the carbon phase into a mixture of sp^2 and sp^3 bonded carbon as well as carbon bonded to silicon atoms [45]. The D3-band decreases with increasing pyrolysis temperature, what is demonstrated by an increase of the I(D)/I(D3) ratio from 2.85 for the 900 °C sample to 3.95 for the 1100 °C and to 8.68 for the 1400 °C sample. In parallel, the increase of the pyrolysis temperature leads to an increase of the G-band revealed in the decrease of the I(D)/I(G) ratio from 2.35 for the 900 °C sample to 1.95 for the 1100 °C and to 1.60 for the 1400 °C sample (see Table 4). The intensity ratio of D-mode to G-mode can be used to calculate the in-plane crystallite size L_a by Eq. (3) which was determined by Tunistra et al. [46]. The carbon cluster size L_a increases from 1.87 nm for the 900 °C sample to 2.74 nm for the 1400 °C sample. The D-band overtone and the D + G-Band combination mode are more pronounced for the material pyrolysed at 1400 °C.

$$\frac{I(D)}{I(G)} = \frac{C(\lambda_L)}{L_a} \qquad (3)$$

Summarizing, the D3-band intensity decreases whereas the G-band intensity and the carbon cluster size increase with increasing pyrolysis temperature. These findings can be interpreted as a beginning of an ongoing graphitization process resulting in a higher degree of organization as well as a loss of hydrogen [47,48]. It leads to the diminution in charge storage due to a decrease in available Li-ion storing sites within the free carbon phase. As found by Raman spectroscopy, the organization of the free carbon phase increases with temperature of pyrolysis. According to our previous reports [49] and findings of Azuma et al. [50], higher ordered carbons can host less Li-ions than order-less configurations, meaning that at lower T_{pyr} the corresponding capacities must be higher than at higher T_{pyr}. This in turn leads to the decrease in the recovered capacity at a higher pyrolysis temperature.

4. Conclusion

We demonstrated that the temperature of pyrolysis (T_{pyr}) has a significant impact on the electrochemical properties of the porous carbon-rich SiCN ceramics. The best electrochemical performance has been shown for the sample pyrolysed at 900 °C. The analyzed capacities are found to decrease with the increasing pyrolysis temperature due to the structural evolution of the free carbon phase from highly disordered towards more organized configurations. It leads to the lower storage capacity because highly ordered carbons intercalate less Li-ions in comparison to disordered ones. Moreover, at 1400 °C the SiCN matrix breaks due to a solid state reaction of Si—N bonds with carbon resulting in SiC formation. Thus, the amount of free carbon decreases leading to lower capacities. Nevertheless, in comparison to so far synthesized SiCN ceramics, the produced porous carbon-rich SiCN ceramics show an improved high current-rate capability in terms of capacity and cycling stability.

Acknowledgements

We gratefully acknowledge the financial support of the German Research Foundation (DFG) SPP1473/JP8.

References

[1] J.R. Dahn, A.M. Wilson, W. Xing, G.A. Zank, Electrodes for Lithium Ion Batteries Using Polysilazanes Ceramic with Lithium, US5631106A, (1997).
[2] H. Fukui, H. Ohsuka, T. Hino, K. Kanamura, ACS Appl. Mater. Interfaces 2 (4) (2010) (998).
[3] D. Ahn, R. Raj, J. Power Sources 196 (4) (2011) (2179).
[4] L.M. Reinold, M. Graczyk-Zajac, Y. Gao, G. Mera, R. Riedel, J. Power Sources 236 (2013) (224).
[5] R. Kolb, C. Fasel, V. Liebau-Kunzmann, R. Riedel, J. Eur. Ceram. Soc. 26 (16) (2006) (3903).
[6] M. Graczyk-Zajac, C. Fasel, R. Riedel, J. Power Sources 196 (15) (2011) (6412).
[7] Y. Chen, C. Li, Y. Wang, Q. Zhang, C. Xu, B. Wei, L. An, J. Mater. Chem. 21 (45) (2011) (18186).
[8] M. Wilamowska, M. Graczyk-Zajac, R. Riedel, J. Power Sources 244 (80) (2013).
[9] R. Bhandavat, G. Singh, ACS Appl. Mater. Interfaces 4 (10) (2012) (5092).
[10] R. Bhandavat, G. Singh, ACS Appl. Mater. Interfaces 5 (1) (2012) (222).
[11] L. David, D. Asok, G. Singh, ACS Appl. Mater. Interfaces 6 (18) (2014) (16056).
[12] L. David, S. Bernard, C. Gervais, P. Miele, G. Singh, J. Phys. Chem. C 119 (5) (2015) (2783).
[13] L. David, R. Bhandavat, U. Barrera, G. Singh, Sci. Rep. 5 (9792) (2015) (1).
[14] L. David, R. Bhandavat, U. Barrera, G. Singh, Nat. Commun. 7 (2016).
[15] L. David, K.M. Shareef, M.A. Abass, G. Singh, RSC Adv. 6 (59) (2016) (53894).
[16] L.M. Reinold, Y. Yamada, M. Graczyk-Zajac, H. Munakata, K. Kanamura, R. Riedel, J. Power Sources 282 (0) (2015) (409).
[17] D. Vrankovic, M. Storch, C. Schicto, M. Graczyk-Zajac, R. Riedel, Method for producing porous ceramics and a porous ceramic product, German Patent Registration 10 2016 116 732.0, Technische Universitat Darmstadt, 2016.
[18] V.L. Nguyen, E. Zera, A. Perolo, R. Campostrini, W. Li, G.D. Sorarù, J. Eur. Ceram. Soc. 35 (12) (2015) (3295).
[19] K.S.W. Sing, D.H. Everett, R.A.W. Haul, L. Moscou, R.A. Pierotti, J. Rouquerol, T. Siemieniewska, Pure Appl. Chem. 57 (4) (1985) (603).
[20] F. Bonino, S. Brutti, M. Piana, S. Natale, B. Scrosati, L. Gherghel, K. Müllen, Electrochim. Acta 51 (17) (2006) (3407).
[21] X. Li, L. Liu, Y. Zhang, S.D. Shen, S. Ge, L.C. Ling, Carbon 39 (2) (2001) (159).
[22] G. Mera, R. Riedel, F. Poli, K. Müller, J. Eur. Ceram. Soc. 29 (13) (2009) (2873).
[23] Y.L. Li, E. Kroke, R. Riedel, C. Fasel, C. Gervais, F. Babonneau, Appl. Organomet. Chem. 15 (10) (2001) (820).
[24] L. Qie, W.-M. Chen, Z.-H. Wang, Q.-G. Shao, X. Li, L.-X. Yuan, X.-L. Hu, W.-X. Zhang, Y.-H. Huang, Adv. Mater. 24 (15) (2012) (2047).
[25] M. Graczyk-Zajac, M. Wimmer, Y. Xu, G. Buntkowsky, C. Neumann, R. Riedel, J. Solid State Electrochem. 21 (1) (2017) (47).
[26] S.-H. Baek, L.M. Reinold, M. Graczyk-Zajac, R. Riedel, F. Hammerath, B. Buechner, H.-J. Grafe, J. Power Sources 253 (0) (2014) (342).
[27] G. Liu, J. Kaspar, L.M. Reinold, M. Graczyk-Zajac, R. Riedel, Electrochim. Acta 106 (2013) (101).
[28] Y.S. Hu, P. Adelhelm, B.M. Smarsly, S. Hore, M. Antonietti, J. Maier, Adv. Funct. Mater. 17 (12) (2007) (1873).
[29] A.S. Arico, P. Bruce, B. Scrosati, J.-M. Tarascon, W. van Schalkwijk, Nat. Mater. 4 (5) (2005) (366).
[30] M. Graczyk-Zajac, D. Vrankovic, P. Waleska, C. Hess, P. Vallachira Sasikumar, S. Lauterbach, H.-J. Kleebe, G.D. Soraru, J. Mater. Chem. A (2017), http://dx.doi.org/10.1039/C7TA09236A.
[31] M. Graczyk-Zajac, L.M. Reinold, J. Kaspar, P.V.W. Sasikumar, G.-D. Soraru, R. Riedel, Nano 5 (1) (2015) (233).
[32] H. Fujimoto, A. Mabuchi, K. Tokumitsu, T. Kasuh, J. Power Sources 54 (2) (1995) (440).
[33] T. Zheng, J.S. Xue, J.R. Dahn, Chem. Mater. 8 (2) (1996) (389).
[34] F. Bonino, S. Brutti, P. Reale, B. Scrosati, L. Gherghel, J. Wu, K. Müllen, Adv. Mater. 17 (6) (2005) (743).
[35] I. Mochida, C.-H. Ku, Y. Korai, Carbon 39 (3) (2001) (399).
[36] J.R. Dahn, T. Zheng, Y. Liu, J. Xue, Science 270 (5236) (1995) (590).
[37] K.T. Lee, J.C. Lytle, N.S. Ergang, S.M. Oh, A. Stein, Adv. Funct. Mater. 15 (4) (2005) (547).
[38] M. Graczyk-Zajac, L. Toma, C. Fasel, R. Riedel, Solid State Ionics 225 (2012) (522).
[39] V.S. Pradeep, D.G. Ayana, M. Graczyk-Zajac, G.D. Soraru, R. Riedel, Electrochim. Acta 157 (2015) (41).
[40] P. Vallachira Warriam Sasikumar, E. Zera, M. Graczyk-Zajac, R. Riedel, G.D. Soraru, J. Am. Ceram. Soc. 99 (9) (2016) 2977.
[41] M. Graczyk-Zajac, M. Wimmer, C. Neumann, R. Riedel, J. Solid State Electrochem. 19 (2015) (2763).
[42] A. Sadezky, H. Muckenhuber, H. Grothe, R. Niessner, U. Pöschl, Carbon 43 (8) (2005) (1731).
[43] A.C. Ferrari, J. Robertson, Phys. Rev. B 61 (20) (2000) (14095).
[44] G. Mera, A. Navrotsky, S. Sen, H.-J. Kleebe, R. Riedel, J. Mater. Chem. A 1 (12) (2013) (3826).
[45] J. Wagner, M. Ramsteiner, C. Wild, P. Koidl, Phys. Rev. B 40 (3) (1989) (1817).
[46] F. Tuinstra, J.L. Koenig, J. Chem. Phys. 53 (3) (1970) (1126).
[47] N. Janakiraman, F. Aldinger, J. Eur. Ceram. Soc. 29 (1) (2009) (163).
[48] T. Jawhari, A. Roid, J. Casado, Carbon 33 (11) (1995) (1561).
[49] J. Kaspar, M. Graczyk-Zajac, R. Riedel, J. Power Sources 244 (0) (2013) (450).
[50] H. Azuma, H. Imoto, S.i. Yamada, K. Sekai, J. Power Sources 1 (1999) 81–82.

Deutsches
Patent- und Markenamt

Erfinderbenennung

Die Erfinderbenennung muss auch erfolgen, wenn der Anmelder selbst der Erfinder ist. Ist der Anmelder Miterfinder, so ist er auch mitzubenennen.

Amtliches Aktenzeichen*(wenn bereits bekannt)*

Platz für **Zeichen des Anmelders/Vertreters**
123-0015

Bezeichnung der Erfindung *(bitte vollständig)*

Method for producing porous ceramics and a porous ceramic product

Erfinder (1)

Vor- und Zuname
Dragoljub Vrankovic

Straße, Hausnummer
Kiesstrasse 79

Postleitzahl: 64287
Ort: Darmstadt, DE

☐ Erfinder stellt Antrag auf Nichtnennung *(§ 63 Abs.1 S. 3 PatG)*

Erfinder (2)

Vor- und Zuname
Mathias Storch

Straße, Hausnummer
Jovanka-Bontschits-Straße 2

Postleitzahl: 64287
Ort: Darmstadt, DE

☐ Erfinder stellt Antrag auf Nichtnennung *(§ 63 Abs.1 S. 3 PatG)*

Erfinder (3)

Vor- und Zuname
Cristina Schitco

Straße, Hausnummer
Elisabethenstr. 46

Postleitzahl: 64283
Ort: Darmstadt, DE

☐ Erfinder stellt Antrag auf Nichtnennung *(§ 63 Abs.1 S. 3 PatG)*

Erfinder (4)

Vor- und Zuname

Magdalena Graczyk-Zajac

Straße, Hausnummer
Sickingenstr. 57

Postleitzahl 69126
Ort Heidelberg, DE

☐ Erfinder stellt Antrag auf Nichtnennung *(§ 63 Abs.1 S. 3 PatG)*

Erfinder (5)

Vor- und Zuname
Ralf Riedel

Straße, Hausnummer
Bahnhofstr. 19

Postleitzahl 64832
Ort Babenhausen, DE

☐ Erfinder stellt Antrag auf Nichtnennung *(§ 63 Abs.1 S. 3 PatG)*

Das Recht auf das Patent ist **auf den Anmelder übergegangen durch:**

(z.B. Erfinder ist/sind d. Anmelder, Inanspruchnahme aufgrd. §§ 6 u. 7 ArbnErfG, Kaufvertrag mit Angabe des Datums, Erbschaft usw.)

zu 1: Inanspruchnahme nach ArbnErfG
zu 2: Vertrag
zu 3: Inanspruchnahme nach ArbnErfG
zu 4: Inanspruchnahme nach ArbnErfG
zu 5: Inanspruchnahme nach ArbnErfG

Es wird versichert, dass nach Wissen der signierenden Person (Anmelder bzw. dessen Vertreter) weitere Personen an der Erfindung nicht beteiligt sind.

Anmerkung zum Antrag auf Nichtnennung als Erfinder

Nur der Unterzeichner der Erfinderbenennung kann, sofern gleichzeitig Anmelder und Erfinder, einen Antrag auf Nichtnennung als Erfinder stellen. Falls der Erfinder nicht gleichzeitig der Anmelder ist oder mehrere Erfinder nicht genannt werden sollen, so ist der Antrag auf Nichtnennung als Erfinder mit dem Formular P2792 zu stellen (§ 63 Abs. 1 S. 3 PatG).

Der Antrag kann jederzeit widerrufen werden. Ein Verzicht des Erfinders auf Nennung ist ohne rechtl. Wirksamkeit (§ 63 Abs. 1 S. 4 u. 5 PatG).

Method for producing porous ceramics and a porous ceramic product

Field of the Invention

The present invention relates a method for producing porous ceramics and a porous ceramic product and, in particular, to a no-fillers synthesis of mesoporous oxide and nonoxide ceramic from preceramic polymers via solvent assisted route.

Background

Microporous and mesoporous materials exist as oxide and non-oxide ceramics and are of high interest for a number of important energy related technological applications such as gas adsorption, gas separation membranes or catalyst supports. In addition, micro/mesoporous ceramic materials can be used as dielectric materials, for gas sensing applications or as electrode materials for energy storage and conversion devices. Micro/mesoporous oxide ceramics have been successfully applied for a number of industrial applications such as catalysts, gas adsorption and separation. However, the synthesis of the micro/mesoporous nonoxide ceramics remains a compelling goal and are of particular interest, since nonoxide ceramic is known to exhibit superior properties, e.g. better shock resistance in reducing atmospheres, hydrothermal stability, than their oxidic counterparts. The well-established sol-gel synthesis is typically employed to prepare porous oxide ceramic, but it is not suitable for the synthesis of nonoxide ceramics.

An effective method to produce nonoxide ceramic is the so-called Polymer-Derived Ceramics (PDC) route. Using ceramic precursors such as chemical compounds, oligomers and polymers undergo a cleavage of chemicals bonds upon thermal treatment (pyrolysis) at temperatures of more than 500 °C, which is used to produce ceramics. In these methods, during the bond cleavage, a gaseous species such as hydrogen, organic compound etc. will be formed and might lead to the porous character of the ceramic.

A further known method is disclosed in US 5,059,267, wherein porous ceramic materials are produced using templates (e.g. pipes or other objects filled with polysilane) to produce the material. Another method is disclosed in US 6,624,228, wherein the porous ceramic material is produced using finely divided particles (so-called fillers), whose pyrolysis product gives rise to the porous structure. Yet another conventional method (see WO 2011/007001 A2) for producing porous ceramic materials is based on sacrificial agent which is thermally decomposed yielding the porous structure. Further conventional methods use a supercritical drying (see Pradeep VS, Ayana DG, Graczyk-Zajac M, Soraru GD, Riedel R “High Rate Capability of SiOC Ceramic Aerogels with Tailored Porosity as Anode Materials for Li-ion Batteries. Electrochimica Acta 157:41-45, 2015).

So-created materials are still insufficient for various reasons. For example, the porosity is stable only up to temperature of 900-1000 °C. Furthermore, there is not yet any synthesis of low/high carbon content ceramics (e.g. SiCN, SiOC, SiC) available, wherein the micro/meso-porosity is controllable and stable at pyrolysis temperatures from 500 up to 1400 °C and which does not involve fillers or supercritical drying.

Therefore, there is a demand for alternative methods for producing porous materials that can overcome at least some of these problems.

Summary

At least some of the above mentioned problems are solved by a method for producing porous ceramics according to claim 1 and a porous ceramic product according to claim 12. The dependent claims relate to further advantageous realizations of the subject matter of the independent claims.

The present invention relates to a method for producing porous ceramics. The method comprises forming a mixture comprising ceramic precursors, a solvent, and a crosslinking procedure, heating the mixture with a predetermined temperature profile and cooling the heated mixture. Crosslinking procedure includes at least one or all of the following reactions: a reaction of the polymer with a crosslinking agent, a thermal treatment of the mixture with a predetermined temperature profile, irradiation of the mixture with e.g. UV, Vis, and Synchrotron radiation. Crosslinking procedure takes place with or without the catalyst and leads to the formation of a solid body in a presence of the above mentioned solvent.

According to further embodiments the ceramic precursors comprise oligomers or polymers from greater than 5 up to about 99 parts by weight of a ceramic precursor and from about 1 to less than 95 parts by weight of solvent, wherein the solvent comprises compounds selected from the group including ethers and from about 0 to less than 1 parts by weight of catalyst, and from about 0 to less than 70 parts by weight of the crosslinking agent.

Optionally, solvent comprises of a suitable solvent from the groups including ethers such as di-n-butyl ether and tetrahydrofuran as well as aromatic and aliphatic hydrocarbons such as benzene, toluene, and hexane as well as the mixtures thereof.

Optionally, the oligomers or polymers have a number average molecular weight in the range of from about 100 to about 100,000 g/mole.

Optionally, the step of heating is performed for transforming the cross-linked precursors to ceramic material.

Optionally, the temperature during the crosslinking step (first stage) is within a range between 0 °C and 400 °C. The temperature during the second stage can be held within a range between 400 °C and 1500 °C.

Optionally, the temperature during the heating stage can be held at for as long as needed to reach the temperature for performing the desired reaction (e.g. transforming the cross-linked precursors to ceramic material), then the cooling can start.

According to further embodiments the step of heating is performed in the presence of any atmosphere (including oxidizing, reducing gasses and/or vacuum) or an inert atmosphere, in particular with or without hydrogen, CO_2, ammonia, nitrogen, helium, argon, oxygen, air, vacuum or mixture thereof. In particular, the step of heating (e.g. one or both of the heating stages) may be performed without the presence of hydrogen or another reactive atmosphere (ammonia).

Optionally, the ceramic precursors comprise at least one of the following materials: polysilanes, polycarbosilanes, polyborosilanes, polysilazanes, polycarbosilazanes, polysiloxanes, polycarbosiloxanes, polyborosiloxanes, polysilsesquioxanes, polysilsesquiazanes, polysilylcarbodiimides, polysilsesquicarbodiimides, vinylicpolysilanes, polyboranes, polyborazines, polyborazylenes, amine boranes, polyphenylborazanes, carboranesiloxanes, polysilastyrenes, polytitanocarbosilanes, polyaluminocarbosilanes, polyalanes, alumanes, polyalazanes and like materials, as well as mixtures thereof.

Optionally, the solvent comprises Di-n-butyl ether and/or the crosslinking agent comprises divinylbenzene.

The present invention relates also to a porous ceramic product comprising a (ceramic) material, wherein the material is characterized by: a surface area of more than 30 m^2/g, a porous structure comprising a pore volume of greater than about 0.1 $cm^3\ g^{-1}$, an open-pore microporous or mesoporous cell structure, wherein the pores have a mean width of less than 50 nm.

Optionally, the ceramic material has an amorphous (micro)/mesoporous structure and a surface area in excess of 30 $m^2\ g^{-1}$, preferably in excess of 100 $m^2\ g^{-1}$, or within the range of from about 50 to about 1000 m^2/g. The porous structure may comprise a pore volume of greater than about 0.01 $cm^3\ g^{-1}$, preferably greater than 0.5 $cm^3\ g^{-1}$, of the ceramic.

According to further embodiments the porous structure comprises: a ceramic micropore volume of 0.01 to 0.1 cm^3/g; and a ceramic mesopore volume of 0.01 to 0.9 cm^3/g, wherein the volume fraction of micropores in the ceramic product ranges from about 5 % to about 32 %.

Optionally, the porous ceramic product is filler-free.

The present invention relates also to a preceramic intermediate composition comprising a mixture of a ceramic precursor and a solvent, with or without catalyst, with or without crosslinking agent, whose pyrolysis product in any atmosphere (including oxidizing, reducing gasses and/or vacuum) at temperatures of up to less than about 1500 °C gives rise to the porous ceramics of the invention.

Therefore, embodiments solve at least some of the above-mentioned problems by a solvent assisted synthesis of micro/mesoporous ceramics from preceramic polymers.

Embodiments of the present invention can be used for various applications. In particular, the materials produced by embodiments of the present invention are of advantage as:

- electrode materials for energy storage and conversion devices,
- catalyst supports for the use in fuel cells,
- porous membranes in harsh environments and at high temperatures,
- potential candidate material for CO_2 sorption due to tailored porosity and the possibility to introduce basic groups (e.g. -NH-,-NH_2) in the ceramic composition by the appropriate selection of polymeric precursor.
- materials for H_2 storage.
- fillers, namely additives to the materials, which make better some of the properties (e.g. reinforce, increase thermal stability, etc.) or lower the consumption of more expensive binder materials.

Brief description of the figures

Some aspects of the invention will be described in the following by way of example only, and with reference to the accompanying figures, in which

Fig. 1 shows a flowchart of a method according to an embodiment of the present invention; and

Fig. 2 depicts a temperature profile used in further embodiments.

Detailed Description

Various examples will now be described with reference to the accompanying drawings in which some examples are illustrated.

Fig. 1 shows a flowchart for a method for producing porous ceramics. The method comprises: forming S110 a mixture comprising ceramic precursors, a solvent, performing a crosslinking procedure S115; heating S120 the mixture with a predetermined temperature profile; and cooling S130 the heated mixture.

Various polymers or oligomers may be used as ceramic precursors. In particular, PHPS (perhydropolysilazane) - a polysilazane (PSZ) preceramic polymer – can be used for silicon nitride ceramics. HTT-1800 - a polysilazane (PSZ) preceramic polymer available from KiON Specialty Polymers – can be used as a precursor for silicon carbonitride ceramics. In addition, SMP-10 - a polycarbosilane (PCS) preceramic polymer available from Starfire® Systems – can be used as a precursor for silicon carbide ceramics. Finally, SPR-212a - a polysiloxane (PSO) preceramic polymer available from Starfire® Systems – can be used as a precursor for silicon oxycarbide ceramics.

However, the present invention shall not be limited on these particular examples. According to further embodiments of the present invention ceramic precursor materials include oligomers and polymers such as polysilanes, polycarbosilanes, polyborosilanes, polysilazanes, polycarbosilazanes, polysiloxanes, polycarbosiloxanes, polyborosiloxanes, polysilsesquioxanes, polysilsesquiazanes, polysilylcarbodiimides, polysilsesquicarbodiimides, vinylicpolysilanes, polyboranes, polyborazines, polyborazylenes, amine boranes, polyphenylborazanes, carboranesiloxanes, polysilastyrenes, polytitanocarbosilanes, polyaluminocarbosilanes, polyalanes, alumanes, polyalazanes and like materials, as well as mixtures thereof, whose pyrolysis products yield ceramic compositions containing structural units having bond linkages selected from Si-C, Si-N, Si-C-N, Si-B, Si-B-N, Si-B-C, Si-C-N-B, Si-Al-N-C, Si-Al-N, Al-N, B-N, Al-N-B and B-N-C, as well as oxycarbide and oxynitride bond linkages such as Si-O-N, Si-Al-O-N and Ti-O-C. The oligomers and polymers may have a number average molecular weight in the range of from about 100 to about 100,000 g/mole, more preferably from about 400 to about 20,000 g/mole. The chemistry of these oligomeric and polymeric precursors are further disclosed in the monograph "Inorganic Polymers", J. E. Mark, H. R. Allcock, and R. West, Prentice Hall, 1992.

Solvent comprises of a suitable solvent from the groups including organic solvents, preferably an inert organic solvent. It is preferred that the solvent does not react with the silicon containing component nor with any other component in reaction mixture. The solvent comprises an ether such as di-n-butyl ether, tetrahydrofuran, aromatic, aliphatic hydrocarbons such as benzene, toluene, and hexane, xylene, ethylbenzene, diethylbenzene, trimethylbenzene, or triethylbenzene; an alicyclic hydrocarbon solvent such as cyclohexane, cyclohexene, decahydronaphthalene, ethylcyclohexane, methylcyclohexane, p-menthine, dipentene (limonene); or other solvents such as anisole, acetone, 3-pentanone, 2-heptanone, ethyl acetate, n-propyl acetate, n-butyl acetate, ethyl lactate, ethanol, 2-propanol, dimethyl acetamide, propylene glycol methyl ether acetate, solvents having the functional groups C – O – C (ethers), - CO – (ketones), - CO – O (esters), - CO – N – (amides), and solvents which contain a plurality of these functional groups as well as the mixtures thereof. Crosslinking procedure S115 includes at least one or all of the following reactions: a reaction of the polymer with a crosslinking agent, a thermal treatment of the mixture with a predetermined temperature profile, exposition of the mixture to the radiation. Radiation is defined as emission or transmission of energy in the form of waves or particles through space or through a material medium, exemplarily electromagnetic radiation, acoustic radiation, gravitational radiation or particle radiation. Crosslinking procedure S115 takes place with or without the catalyst and leads to the formation of a solid body in a presence of the above mentioned solvent.

According to further embodiments the crosslinking agent may be DVB (divinylbenzene) and the solvent may comprise DNBTETHR (Di-n-butyl ether).

Fig. 2 illustrates the temperature profile used in the step of heating S120 when the polymer crosslinked thermally. According the depicted temperature profile, at the starting time t0 the mixture is heated up to a first temperature T1 until a first time t1. The temperature of the mixture is kept at or approximately around the first temperature T1 for a first time period (first dwell time) t2-t1≥0. At a second time t2 the mixture is again heated up to a second temperature T2 (T_{max}) until a third time t3. After the time t3 the temperature of the mixture stays approximately constant for the second time period (second dwell time) t4-t3≥0. At a fourth time t4 the mixture is cooled until a fifth time t5.

During the first dwell time the ceramic precursors exhibit a crosslinking. The first temperature T1 and the crosslinking agent are selected such to start this process in the mixture. During the second dwell time the polymers or oligomers in the mixture are thermodynamically decomposed into the ceramic material (pyrolysis). The second temperature T2 and the second dwell time are selected such that this process starts and is completed throughout the mixture.

The temperature of the mixture may rise or lower with a predetermined rate. The rate may be such that the processes is initiated/terminated throughout the mixture uniformly (and without causing thermal stress, e.g. during cooling). An exemplary value for the rate of temperature increase/decrease may be in the range of 50 to 500 °C per hour or about 100 °C per hour.

The first temperature T1 and/or the second temperature T2 can be adapted to the concrete materials (see examples below). In addition, during the first dwell time and the second dwell time, the first and second temperatures T1, T2 may also vary (e.g. +/- 10 % or +/-30%) as long as the processes (crosslinking and pyrolysis) are initiated and sufficiently finalized in the mixture to obtain a desired result, i.e. the amorphous (micro)/mesoporous ceramic materials with desired properties.

According to embodiments the resulting amorphous (micro)/mesoporous ceramic materials have a surface area in excess of 30 m^2 g^{-1}, preferably in excess of 100 m^2 g^{-1}, and an open-pore (micro)/mesoporous cell structure wherein the pores have a mean width (diameter) of less than 50 nm and wherein said porous structure, comprises a pore volume of greater than about 0.01 cm^3 g^{-1}, preferably greater than 0.5 cm^3 g^{-1}, of the ceramic.

According to another embodiment, a preceramic intermediate composition comprises a mixture of a ceramic precursor and a solvent, with or without catalyst, with or without crosslinking agent, whose pyrolysis product in inert atmosphere or vacuum at temperatures of up to less than about 1500 °C gives rise to the porous ceramics of the invention.

Therefore, according to embodiments, the process for the preparation or producing of the porous ceramics of the invention comprises the steps:

a) forming an intimate mixture comprising a ceramic precursor oligomer or polymer and a solvent,
b) gradually heating said mixture in the presence of any atmosphere (including inert, oxidizing, reducing gasses and/or vacuum) , and
c) cooling said porous ceramic product.

The ceramic precursor may have greater than 5 up to about 99 parts by weight and/or may have a number average molecular weight in the range of from about 100 to about 100,000 g/mole. The solvent may have from about 1 ppm to less than 95 parts by weight and may be selected from the group consisting of various ethers.

Optionally, the mixture may comprise a catalyst and/or a crosslinking agent. The catalyst may have from about 0 to less than 1 parts by weight, and the crosslinking agent may have from about 0 to less than 70 parts by weight.

Optionally, the gradually heating of the mixture is performed in the presence of an inert, reducing or oxidizing atmosphere (such as hydrogen, CO_2, ammonia, nitrogen, helium, argon, O_2, air, vacuum or mixture thereof). In addition, gradually heating the mixture may further be performed in sequential stages with/without dwell times at intermediate temperatures (see Fig. 2). Further, a maximum dwell temperature (T2) can be in the range of from about 400 °C up to less than about 1500 °C and over a period of total heating. The dwell time may be more than 2 hours to form a porous ceramic product.

The disclosed method gives a possibility to tune the porosity, namely to obtain e.g. only micro/mesopores without macropores etc. The porous ceramics prepared in accordance with embodiments of the invention generally exhibit a surface area within the range of from about 30 to about 1000 m^2/g, and ceramics micropore volumes of 0.01 up to about 0.1 cm^3/g, and ceramics mesopore volumes of greater than 0.01 up to 0.9 cm^3/g, wherein the volume fraction of micropores in the ceramic product ranges from about 5 % to about 32 %.

Advantages of embodiments can be summarized as follows:

The ceramics produced in accordance with embodiments are particularly useful in bulk sorbent applications, as active layers in membrane separation structures, catalyst supports, electrode material for Li/Na-ion batteries, hydrogen storage, CO_2 capture, and as electrode material for Li-S and Li-air batteries. The porous ceramics produced in accordance with embodiments are also useful as fillers, namely additives to the materials, which make better some of the properties (e.g. reinforce, increase thermal stability, etc.) or lower the consumption of more expensive binder materials.

In particular, in contrast to conventional methods, the so-created porosity is stable up to 900-1000 °C in harsh environment, in particular in corrosive, highly oxidative etc. environment. Embodiments further enable the synthesis of low/high carbon content ceramics, e.g. SiCN, SiOC, SiC, with controlled micro/mesoporosity stable from 500 up to 1400 °C pyrolysis temperature with no fillers.

Furthermore, embodiments of the present invention produce ceramics (oxide and/or nonoxide ceramics), wherein during the bond cleavage no gaseous species such as hydrogen, organic compound etc. are formed to obtain the porous character of the ceramic. Especially, embodiments do not use templates, fillers, sacrificial agents, supercritical drying, or the presence of supporting gases such as H_2/NH_3.

The following examples will further illustrate aspects of the invention, but the invention is not limited thereto. Moreover, the indicated values in the examples may also be varied within certain ranges (e.g. +/- 10% or +/- 50 %), while achieving the same result.

sample	Pre-ceramic Polymer	Sol-vent	Crosslinking Agent/T/time	Pyrolysis Gas	Pyrolysis T_{max}	SSA (m^2/g)	Total Pore Volume (cm^3/g)	Micro-pore Volume (cm^3/g)	Porosity Type
PSZ-1	PHPS	yes	DVB/250 °C/3 h	Ar	500 °C	504	0.90	0.08	Meso
PSZ-2	PHPS	yes	DVB/250 °C/3 h	Ar	700 °C	235	0.56	0.01	Meso
PSZ-3	PHPS	yes	DVB/250 °C/3 h	Ar	800 °C	194	0.47	0.01	Meso
PSZ-4	PHPS	yes	DVB/250 °C/3 h	Ar	900 °C	169	0.48	0	Meso
PSZ-5	PHPS	yes	DVB/250 °C/3 h	Ar	1100 °C	104	0.46	0	Meso
PSZ-6	PHPS	yes	DVB/250 °C/3 h	Ar	1400 °C	446	0.72	0.11	Micro / Meso
PSZ-7	PHPS	no	DVB/250 °C/3 h	Ar	1100 °C	13	0	0	Non-porous
PSZ-8	PHPS	yes	DVB/250 °C/3 h	Ar/H_2 (5 vol%)	900 °C	107	0.41	0	Meso
PSZ-9	PHPS	yes	DVB/250 °C/3 h	Ar/H_2 (5 vol%)	1100 °C	106	0.44	0	Meso
PSZ-10	PHPS	yes	DVB/130 °C/10 h	Ar	900 °C	206	0.59	0	Meso
PSZ-11	PHPS	yes	DVB/130 °C/10	Ar	1100 °C	97	0.40	0	Meso

			h						
PSZ-12	HTT-1800	yes	DVB/250 °C/3 h	Ar	900 °C	32	0.10	0	Meso
PSZ-13	HTT-1800	yes	DVB/250 °C/3 h	Ar	1100 °C	31	0.10	0	Meso
PSZ-14	HTT-1800	no	DVB/250 °C/3 h	Ar	900 °C	20	0.06	0	Nonporous
PSZ-15	HTT-1800	no	DVB/250 °C/3 h	Ar	1100 °C	5	0.02	0	Nonporous

Table 1. illustrates the synthesis procedure and porosity characteristics of the resulting ceramics from polysilazane polymers: PHPS and HTT-1800 (if a solvent is used, then DNBTETHR).

EXAMPLE 1

A mixture of 3.375 g of PHPS was dissolved in 11.625 g of DNBTETHR and mixed with 9.260 g of DVB. A concentration of ~10 ppm of Pt catalyst was added to the obtained reaction mixture and crosslinking reaction was initiated by refluxing at 120 °C for 6 hours under Ar. The polymeric crosslinked intermediates were consequently transferred in quartz crucibles to quartz Schlenk tubes and pyrolyzed to the T_{max} of 500, 700, 800, 900, and 1100 °C, respectively, resulting in the ceramic samples PSZ-1 – PSZ-5 (see Table 1). Additionally, a crosslinking step at 250 °C was applied for all samples. The sample pyrolyzed at T_{max} of 1400 °C, PSZ-6, was first pyrolyzed at 1100 °C and subsequently transferred to an alumina crucible and pyrolyzed further in an alumina tube furnace. In order to avoid oxygen/moisture contamination all the preparation steps were performed in the glovebox. The heating and cooling rates were adjusted to 100 °C per hour. The dwelling time at the crosslinking temperature (T1) and T_{max} of pyrolysis was set to 3 h. The Ar flow was kept constant for the whole pyrolysis procedure. Ceramic samples synthesized by solvent assisted route under Ar atmosphere are mesoporous and exhibit Type IV nitrogen adsorption isotherms with specific surface areas (SSAs) in the range of 100-500 m^2/g and total pore volumes in the range of 0.46-0.90 cm^3/g, while the samples synthesized in the absence of solvent are nonporous, e.g., PSZ-7 (see Table 1).

EXAMPLE 2

A mixture of 3.375 g of PHPS was dissolved in 11.625 g of DNBTETHR and mixed with 9.260 g of DVB. A concentration of ~10 ppm of Pt catalyst was added to the obtained reaction mixture and crosslinking reaction was initiated by refluxing at 120 °C for 6 hours under Ar. The polymeric crosslinked intermediates were consequently transferred in quartz crucibles to quartz Schlenk tubes and pyrolyzed under Ar/H_2 mixture (5 vol% of H_2 in Ar, forming gas) to the T_{max} of 900 and 1100 °C, respectively, resulting in the ceramic samples PSZ-8 – PSZ-9 (see Table 1). Additionally a crosslinking step at 250 °C was applied. In order to avoid oxygen/moisture contamination all the preparation steps were performed in the glovebox. The heating and cooling rates were adjusted to 100 °C per hour. The dwelling time at the crosslinking temperature and T_{max} of pyrolysis was set to 3 h. The forming gas flow was kept constant for the whole pyrolysis procedure. Ceramic samples synthesized by solvent assisted route under forming gas are mesoporous and exhibit Type IV nitrogen adsorption isotherms with SSAs of ≈100 m^2/g and total pore volumes ≈0.40 cm^3/g.

EXAMPLE 3

A mixture of 3.375 g of PHPS was dissolved in 11.625 g of DNBTETHR and mixed with 9.260 g of DVB. A concentration of ~10 ppm of Pt catalyst was added to the obtained reaction mixture and crosslinking reaction was initiated by refluxing at 120 °C for 6 hours under Ar. The polymeric crosslinked intermediates were consequently transferred in quartz crucibles to quartz Schlenk tubes and pyrolyzed to the T_{max} of 900 and 1100 °C resulting in the ceramic samples PSZ-10 – PSZ-11 (see Table 1). Additionally a crosslinking step at 130 °C was applied. In order to avoid oxygen/moisture contamination all the preparation steps were performed in the glovebox. The heating and cooling rates were adjusted to 100 °C per hour. The dwelling time at the crosslinking temperature was set to 10h while at the T_{max} of pyrolysis was 3 h. The Ar flow was kept constant for the whole pyrolysis procedure. Ceramic samples synthesized by solvent assisted route under Ar atmosphere are mesoporous and exhibit Type IV nitrogen adsorption isotherms with SSA of 206 m2/g and total pore volume 0.59 cm3/g for PSZ-10 and ≈100 m^2/g and total pore volume ≈0.40 cm^3/g for PSZ-11.

EXAMPLE 4

A mixture of 3.000 g of HTT-1800 was dissolved in 3.000 g of DNBTETHR and mixed with 2.400 g of DVB. A concentration of ~10 ppm of Pt catalyst was added to the obtained reaction mixture and crosslinking reaction was initiated by refluxing at 120 °C for 6 hours under Ar. The polymeric crosslinked intermediates were consequently transferred in quartz crucibles to quartz Schlenk tubes and pyrolyzed to the T_{max} of 900 and 1100 °C, respectively, resulting in the ceramic samples PSZ-12 and PSZ-13 (see Table 1). Additionally a crosslinking step at 250 °C was applied. In order to avoid oxygen/moisture contamination all the preparation steps were performed in the glovebox. The heating and cooling rates were adjusted to 100 °C per hour. The dwelling time at the crosslinking temperature and T_{max} of pyrolysis was set to 3 h. The Ar flow was kept constant for the whole pyrolysis procedure. Ceramic samples synthesized by solvent assisted route under Ar atmosphere are mesoporous and exhibit Type IV nitrogen adsorption isotherms with SSAs of ≈30 m^2/g and total pore volumes ≈0.1 cm^3/g, while the samples synthesized in the absence of solvent are nonporous, e.g., PSZ-13 and PSZ-14 (see Table 1).

Sample #	pre-ceramic polymer	Solvent	Cross-linking agent/ T/time	pyrolysis gas	Pyrolysis T_{max}	SSA (m^2/g)	Total Pore Volume (cm^3/g)	Micropore Volume (cm^3/g)	Porosity Type
PSO-1	SPR-212a	yes	DVB/250 °C/3 h	Ar	900 °C	113	0.13	0.03	Meso
PSO-2	SPR-212a	yes	DVB/250 °C/3 h	Ar	1100 °C	49	0.07	0.01	Meso
PSO-3	SPR-212a	no	DVB/250 °C/3 h	Ar	900 °C	17	0.06	0	Non-porous
PSO-4	SPR-212a	no	DVB/250 °C/3 h	Ar	1100 °C	15	0.04	0	Non-porous

Table 2. illustrates the synthesis procedure and porosity characteristics of the resulting ceramics from polysiloxane polymer: SPR-212a; if a solvent is used, then DNBTETHR.

EXAMPLE 5

A mixture of 6.000 g of SPR-212a was dissolved in 10.333 g of DNBTETHR and mixed with 2.670 g of DVB. A concentration of ~10 ppm of Pt catalyst was added to the obtained reaction mixture and crosslinking reaction was initiated by refluxing at 120 °C for 6 hours under air. The polymeric crosslinked intermediates were consequently transferred in quartz crucibles to quartz Schlenk tubes and pyrolyzed to the T_{max} of 900 and 1100 °C, respectively, resulting in the ceramic samples PSO-1 and PSO-2 (see Table 2). Additionally a crosslinking step at 250 °C was applied. The preparation steps were performed in air. The heating and cooling rates were adjusted to 100 °C per hour. The dwelling time at the crosslinking temperature and T_{max} of pyrolysis was set to 3 h. The Ar flow was kept constant for the whole pyrolysis procedure. Ceramic samples synthesized by solvent assisted route under Ar atmosphere are mesoporous and exhibit Type IV nitrogen adsorption isotherms with SSAs in the range of 50-100 m^2/g and total pore volumes in the range of 0.07-0.13 cm^3/g, while the samples synthesized in the absence of solvent are nonporous, e.g., PSO-3 and PSO-4 (see Table 2).

Sample #	Preceramic Polymer	Solvent	Cross-linking agent/T/time	Pyrolysis Gas	Pyrolysis T_{max}	SSA (m^2/g)	Total Pore Volume (cm^3/g)	Micropore Volume (cm^3/g)	Porosity Type
PCS-1	SMP-10	yes	DVB/250 °C/3 h	Ar	900 °C	68	0.22	0	Meso
PCS-2	SMP-10	yes	DVB/250 °C/3 h	Ar	1100 °C	69	0.22	0	Meso
PCS-3	SMP-10	no	DVB/250 °C/3 h	Ar	900	16	0.07	0	Nonporous
PCS-4	SMP-10	no	DVB/250 °C/3 h	Ar	1100	17	0.07	0	Nonporous

Table 3. illustrates the synthesis procedure and porosity characteristics of the resulting ceramics from polycarbosilane polymer: SMP-10; if a solvent is used,

then DNBTETHR.

EXAMPLE 6

A mixture of 5.000 g of SMP-10 was dissolved in 17.222 g of DNBTETHR and mixed with 14.150 g of DVB. A concentration of ~10 ppm of Pt catalyst was added to the obtained reaction mixture and crosslinking reaction was initiated by refluxing at 120 °C for 6 hours under Ar. The polymeric crosslinked intermediates were consequently transferred in quartz crucibles to quartz Schlenk tubes and pyrolyzed to the T_{max} of 900 and 1100 °C, respectively, resulting in the ceramic samples PCS-1 and PCS-2 (see Table 3). Additionally a crosslinking step at 250 °C was applied. The preparation steps were performed in the glovebox under Ar. The heating and cooling rates were adjusted to 100 °C per hour. The dwelling time at the crosslinking temperature and T_{max} of pyrolysis was set to 3 h. The Ar flow was kept constant for the whole pyrolysis procedure. Ceramic samples synthesized by solvent assisted route under Ar atmosphere are mesoporous and exhibit Type IV nitrogen adsorption isotherms with SSAs of ≈70 m^2/g and total pore volumes ≈0.22 cm^3/g, while the samples synthesized in the absence of solvent are nonporous, e.g., PCS-3 and PCS-4 (see Table 3).

Unless otherwise defined, all terms (including technical and scientific terms) used herein have the same meaning as commonly understood by one of ordinary skill in the art to which examples belong. It will be further understood that terms, e.g., those defined in commonly used dictionaries, should be interpreted as having a meaning that is consistent with their meaning in the context of the relevant art and will not be interpreted in an idealized or overly formal sense unless expressly so defined herein.

It is further to be noted that methods disclosed in the specification or in the claims may be implemented by a device having means for performing each of the respective acts of these methods.

Further, it is to be understood that the disclosure of multiple acts or functions disclosed in the specification or claims may not be construed as to be within the specific order. Therefore, the disclosure of multiple acts or functions will not limit these to a particular order unless such acts or functions are not interchangeable for technical reasons. Furthermore, in some examples a single act may include or may be broken into multiple sub acts. Such sub acts may be included and part of the disclosure of this single act unless explicitly excluded.

Claims

1. A method for producing porous ceramics comprising:

   forming (S110) a mixture comprising ceramic precursors, a solvent;

   performing a crosslinking procedure (S115);

   heating (S120) the mixture with a predetermined temperature profile; and

   cooling (S130) the heated mixture.

2. The method according to claim 1, wherein the ceramic precursors comprise oligomers or polymers from greater than 5 up to about 99 parts by weight of a ceramic precursor and from about 1 ppm to less than 95 parts by weight of solvent, wherein the solvent comprises an ether such as di-n-butyl ether, tetrahydrofuran, aromatic, aliphatic hydrocarbons such as benzene, toluene, and hexane, xylene, ethylbenzene, diethylbenzene, trimethylbenzene, or triethylbenzene; an alicyclic hydrocarbon solvent such as cyclohexane, cyclohexene, decahydronaphthalene, ethylcyclohexane, methylcyclohexane, p-menthine, dipentene (limonene); or other solvents such as anisole, acetone, 3-pentanone, 2-heptanone, ethyl acetate, n-propyl acetate, n-butyl acetate, ethyl lactate, ethanol, 2-propanol, dimethyl acetamide, propylene glycol methyl ether acetate, solvents having the functional groups C – O – C (ethers), - CO – (ketones), - CO – O (esters), - CO – N – (amides), and solvents which contain a plurality of these functional groups as well as the mixtures thereof and from about 0 to less than 1 parts by weight of catalyst.

3. The method according to claim 1 or claim 2, wherein the crosslinking procedure (S115) includes at least one or all of the following reactions:

   a reaction of the polymer with a crosslinking agent, a thermal treatment of the mixture with a predetermined temperature profile,

irradiation of the mixture with radiation, especially with UV, Vis, and Synchrotron radiation.

4. The method according to one of the preceding claims, wherein the cross-linking procedure (S115) takes place with or without a catalyst.

5. The method according to one of the preceding claims, wherein the cross-linking procedure (S115) is performed in inert, oxidizing or reducing atmosphere and/or vacuum or mixture thereof.

6. The method according to claim 1 or claim 2, wherein the oligomers or polymers have a number average molecular weight in the range of from about 100 to about 100,000 g/mole.

7. The method according to one of the preceding claims, wherein the step of heating (S120) is performed using a temperature profile comprising two stages:

a first stage for forming a cross-linking between the ceramic precursors; and

a second stage for transforming the cross-linked precursors to ceramic material.

8. The method according to one of the claims 3 to 7, wherein the radiation is defined as emission or transmission of energy in form of waves or particles through space or through a material medium, in particular electromagnetic radiation, acoustic radiation, gravitational radiation or particle radiation.

9. The method according to one of the preceding claims, wherein the step of heating (S120) is performed in the presence of an inert atmosphere, with or without oxidizing or reducing atmosphere and/or vacuum or mixture thereof or in any atmosphere including oxidizing, reducing gasses and/or vacuum.

10. The method according to one of the preceding claims, wherein the ceramic precursors comprise one of the following materials: polysilanes, polycarbosilanes, polyborosilanes, polysilazanes, polycarbosilazanes, polysiloxanes, polycarbosiloxanes, polyborosiloxanes, polysilsesquioxanes, polysilsesquiazanes, polysilylcarbodiimides, polysilsesquicarbodiimides, vinylicpolysilanes, polyboranes, polyborazines, polyborazylenes, amine boranes, polyphenylborazanes, carboranesiloxanes, polysilastyrenes, polytitanocarbosilanes, polyaluminocarbosilanes, polyalanes, alumanes, polyalazanes and like materials, as well as mixtures thereof.

11. The method according to one of the preceding claims, wherein the solvent comprises Di-n-butyl ether and/or the crosslinking agent comprises divinylbenzene.

12. A porous ceramic product comprising a material being characterized by:

a surface area of 30 to 1000 m^2/g;

a porous structure comprising a pore volume of greater than about 0.01 $cm^3 g^{-1}$;

an open-pore microporous or mesoporous cell structure, wherein the pores have a mean width of less than 50 nm.

13. The porous ceramic product of claim 11, wherein a porous structure comprises:

a ceramic micropore volume of 0.01 to 0.1 cm^3/g; and

a ceramic mesopore volume of 0.01 to 0.9 cm^3/g,

wherein a volume fraction of micropores in the ceramic product ranges from about 5 % to about 32 %.

14. The porous ceramic product of claim 11 or claim 12, which is filler free.

15. A preceramic intermediate composition comprising a mixture of a ceramic precursor and solvent, with or without catalyst, with or without crosslinking agent, whose pyrolysis product in inert or reactive atmosphere or vacuum at temperatures of up to less than about 1500 °C gives rise to the porous ceramics of the invention.

Abstract

A method for producing porous ceramics comprises: forming (S110) a mixture comprising ceramic precursors, and a solvent and a crosslinking procedure (S115); heating (S120) the mixture with a predetermined temperature profile; cooling (S130) the heated mixture.

Fig. 1

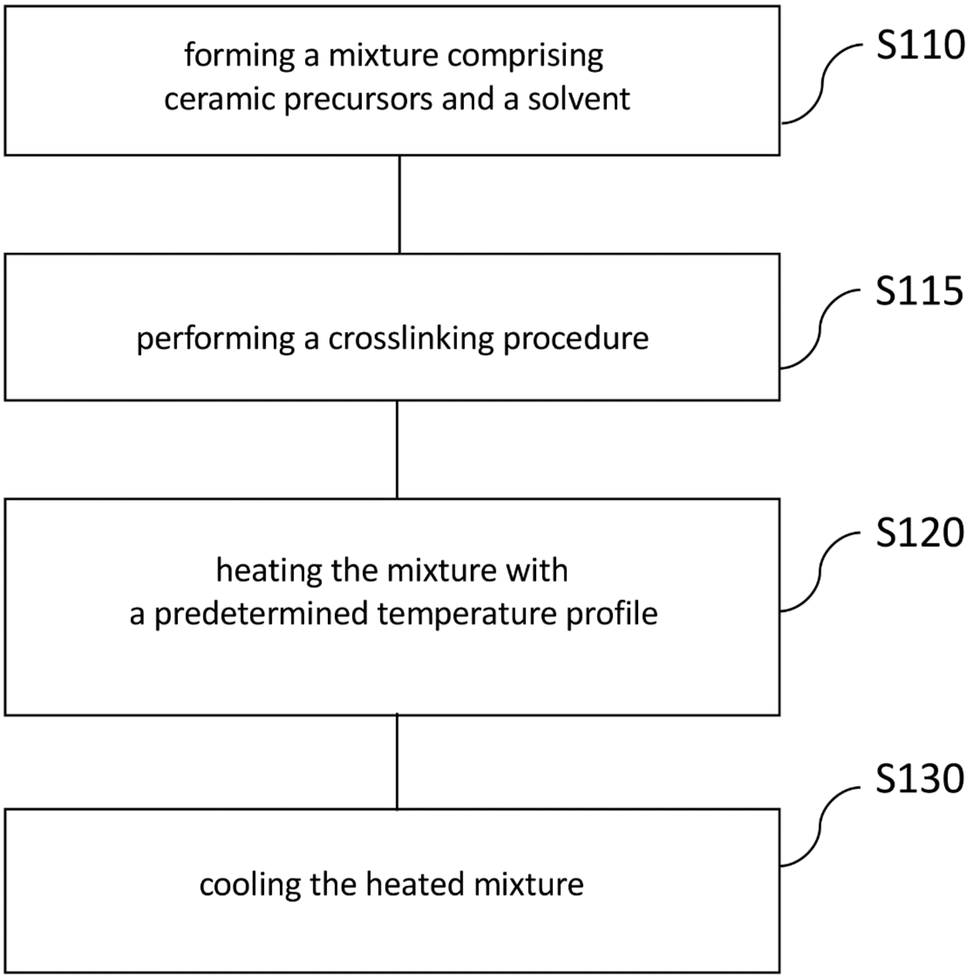
forming a mixture comprising ceramic precursors and a solvent
S110
performing a crosslinking procedure
S115
heating the mixture with a predetermined temperature profile
S120
cooling the heated mixture
S130

Fig. 1

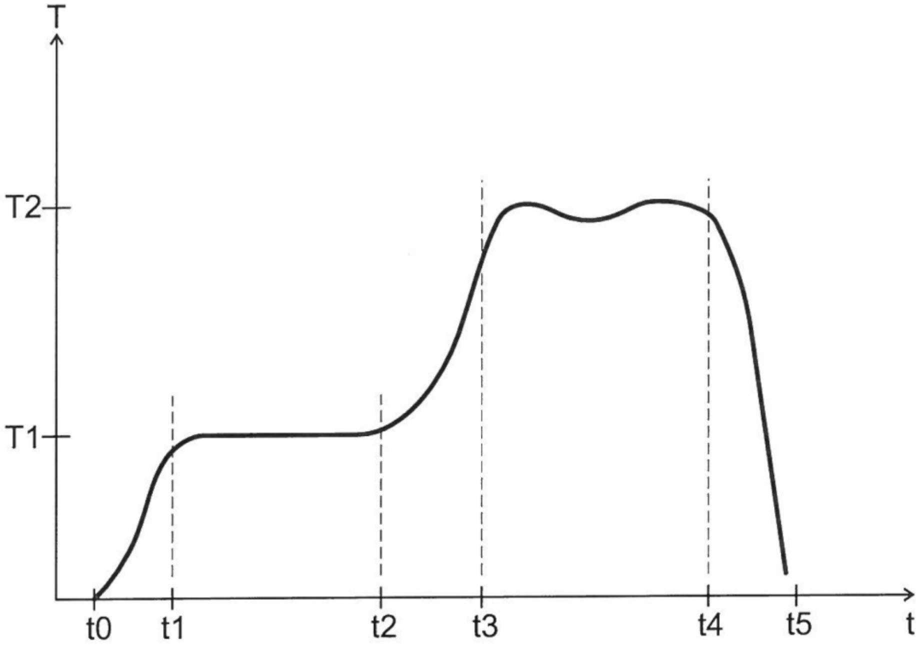

Fig. 2

Acknowledgments

I thank Prof. Dr. Ralf Riedel for the possibility to carry out my research on the fields of lithium-ion batteries and polymer-derived ceramics since I started to work in his group for my internship. I thank him for a constant support, constructive feedback, for his trust and motivation during the entire time.

Prof. Dr. Gian Domenico Sorarù is acknowledged for the second survey of this thesis and for fruitful discussions about porous SiOC materials.

I would like to express my special gratitude to Dr. Magdalena Graczyk-Zajac who supported me at any time during the last four years. I would like to thank her for valuable scientific discussions and advices, for teaching me the critical attitude toward the scientific work and scientific writing.

I want to thank the group of Disperse Feststoffe for the company and the permanent support during my PhD thesis. The special thanks go to Dr. Lukas Mirko Reinold for introducing me to the experimental work and for fruitful discussions, Dr. Cristina Schitco for introducing me to the world of porous materials and gas-sorption techniques, Dr. Jan Kaspar and Dr. Pradeep Vallachira for a company and scientific discussions about LIBs, Christina Stabler for the elemental analysis, Claudia Fasel for the TGA analysis. I also thank Mathias Storch, Kerstin Wissel and Malin Becker for their excellent performance during master/bachelor works and as student research assistants. I thank PD Dr. Emanuel Ionescu for the valuable discussions about PDCs. I specially thank to Prof. Dr. Norbert Nicoloso for valuable advices, helpful discussions and a critical assessment of my scientific writing.

I thank Dr. Jochen Rohrer for a very fruitful cooperation on the material modelling.

I gratefully acknowledge the financial support of the Deutsche Forschungsgemeinschaft DFG within the priority program SPP1473 (Grant No. GR3330/3-1).

Curriculum Vitae

Personal details

First name/Surname	Dragoljub Vrankovic
Address	Kiesstrasse 79 64287 Darmstadt
Date of birth	18.11.1986
Place of birth	Gradiska/Bosnia and Herzegovina

Personal experience and education

present	PhD in Materials Science Technische Universität Darmstadt –Department of Material Science – FG Disperse Feststoffe
10/2014 – 09/2017	Research Assistant Technische Universität Darmstadt –Department of Material Science – FG Disperse Feststoffe
2012 - 2014	Master in Material Science and Engineering Technische Universität Darmstadt Grenoble INP European Master of Science in Advanced Functionalized Materials (FAME) Erasmus Mundus Scholarship
2005 - 2011	Graduated Chemist Faculty of Science and Mathematics – Chemistry Department at the University of Banja Luka, BiH

Complete Publications List

D. Vrankovic, M. Graczyk-Zajac, C. Kalcher, J. Rohrer, M. Becker, C. Stabler, G. Trykowski, K. Albe, R. Riedel, Highly Porous Silicon Embedded in a Ceramic Matrix: A Stable High-Capacity Electrode for Li-Ion Batteries, *ACS Nano*, **11** (2017) 11409.

M. Storch, **D. Vrankovic**, M. Graczyk-Zajac, R. Riedel, The influence of pyrolysis temperature on the electrochemical behavior of porous carbon-rich SiCN polymer-derived ceramics, *Solid State Ionics* **315** (2018) 59.

D. Vrankovic, K. Wissel, M. Graczyk-Zajac, R. Riedel, Novel 3D Si/C/SiOC nanocomposites: toward electrochemically stable lithium storage in silicon, *Solid State Ionics*, **302** (2017) 66.

K. Wissel, **D. Vrankovic**, G. Trykowski, M. Graczyk-Zajac, Synthesis of 3D silicon with tailored nanostructure: Influence of morphology on the electrochemical properties, *Solid State Ionics*, **302** (2017) 180.

M. Graczyk-Zajac, **D. Vrankovic**, P. Waleska, C. Hess, P.V. Sasikumar, S. Lauterbach, H.-J. Klebe, G.D. Soraru**,** On the Li-storage Capacity of SiOC Glasses with and without Mixed Silicon Oxycarbide Bonds, *Journal of Materials Chemistry A*, **6** (2018) 93.

J. Rohrer, **D. Vrankovic**, D. Cupid, R. Riedel, HJ. Seifert, K. Albe, M. Graczyk-Zajac, Novel Si- and Sn-containing SiOCN-based nanocomposites as anode materials for lithium ion batteries: synthesis, thermodynamic characterization and modelling, *International Journal of Materials Research*, **108** (2017) (11) 920.

P. Stein, **D. Vrankovic**, M. Graczyk-Zajac, R. Riedel, B. Xu, A model for diffusion and immobilization of Lithium in SiOC nanocomposite anodes, *Journal of The Minerals, Metals & Materials Society*, **69** (2017) 1524.

D. Vrankovic, L.M. Reinold, R. Riedel, M. Graczyk-Zajac, Void-shell silicon/carbon/SiCN nanostructures: toward stable silicon-based electrodes, *Journal of Materials Science* **51** (2016) (12) 6051.

M. Graczyk-Zajac, **D. Vrankovic**, F.H. Schader, H.R. Fernandes, D.U. Tulyaganov, Influence of external compressive stress on the ionic conductivity of melt-quenched lithium silicate (15Li2O-85SiO2) glass, *Solid State Ionics* **302** (2017) 61.

K. Kawashima, M. Hojamberdiev, C. Stabler, **D. Vrankovic**, K. Yubuta, R. Riedel, K. Domen, K. Teshima, Perovskite $Sr_{1-x}Ba_xW_{1-y}Ta_y(O,N)_3$: Synthesis by Thermal Ammonolysis and Photocatalytic Oxygen Evolution Under Visible Light, *Materials for Renewable and Sustainable Energy*, **6** (2017) 10.

Patent:

D. Vrankovic, M. Storch, C. Schitco, M. Graczyk-Zajac, R. Riedel, Solvent assisted synthesis of micro/mesoporous ceramics from preceramic polymers, German Patent registration DE 10 2016 116 732 A1.

Conference Presentations

9th International Symposium on Nitrides and Related Materials
27.-30. August 2017, Sapporo, Japan
SiCN Ceramics with Tailored Porosity for Stable and Reversible Li-ion storage (O)

18th International Symposium on Silicon Chemistry
06.-11. August 2017, Jinan, China
Silicon-Based Ceramics as a Promising Lithium Ions Host: Performance and Storage Mechanism (O)

21 International Conference on Solid State Ionics
18.-23. June 2017, Padua, Italy
Synthesis and Stabilization of Crystalline Nanostructured Silicon for Highly Reversible Lithium Ion Storage (O)

Materials Science and Engineering 2016
27.-29. October 2016, Darmstadt, Germany
Synthesis and Stabilization of Amorphous/Crystalline 3D Nano Silicon (O)

12th International Symposium on Systems with Fast Ionic Transport

03.-07. July, Kaunas, Lithuania

Synthesis and Stabilization of Amorphous/Crystalline 3D Nano Silicon (O)

18th International Meeting on Lithium Batteries

19.-24. June 2016, Chicago, USA

Carbon-rich Si(O,N)C Ceramics of Controlled Porosity for Storage of Lithium Ions (P)

Lithium Battery Discussions 2015

21.-26. June 2015, Arcachon, France

Benefits of Silicon Carbonitride Matrices on the Cycling Stability of Silicon Anodes in LIBs (O)

Materials Science and Engineering 2014

23.-25. September 2014, Darmstadt, Germany

Benefits of Silicon Carbonitride Matrices on the Cycling Stability of Silicon Anodes in LIBs (P)

65th International Society of Electrochemistry

01.-05. September, Lausanne, Switzerland

Benefits of Silicon Carbonitride Matrices on the Cycling Stability of Silicon Anodes in LIB (P)